Development of Ultrathin Metasurface and Partially Reflective Surface Antennas for Space Applications

Amagoia Tellechea

Department of Electrical and Electronic Engineering
Public University of Navarre

This dissertation is submitted for the degree of
Doctor of Philosophy

Supervisors:
Juan Carlos Iriarte
Ramón Gonzalo

April 2017

upna
Universidad Pública de Navarra
Nafarroako Unibertsitate Publikoa

Zere familia matteari,

Agradecimientos/Acknowledgements

Mientras echo la vista atrás para escribir estas líneas, me invade una sensación de emoción y alegría. Recuerdo perfectamente que cuando comencé esta aventura todos mis pensamientos conformaban un remolino de dudas y miedos. Me gustaría dar las gracias a todas aquellas personas que me han apoyado incondicionalmente desde el primer momento y han creído siempre en mi capacidad tanto profesional como personal para poder realizar esta tesis con éxito. A todos os llevaré siempre en mi corazón, pues habéis sido una parte fundamental en esta etapa de mi vida que llega a su fin.

En primer lugar, como no podía ser de otra forma, quiero dar las gracias a Ramón y Juan Carlos por haberme dado la oportunidad de formar parte del grupo de antenas de la Universidad Pública de Navarra. He aprendido mucho todos estos años y ha sido todo un honor trabajar con vosotros. Sin ninguna duda uno de los mejores consejos que me has dado tú, Juan Carlos, lo llevaré grabado para todos los ámbitos de la vida: "siempre positiva". Nunca me ha faltado una palabra de ánimo, y aunque a veces ha sido difícil, ahora puedo decir que el resultado de estos duros años de trabajo ha merecido la pena. Iñigo y Jorge, gracias por todas las veces que me habéis abierto la puerta de vuestro despacho para resolverme dudas tanto en cuestiones teóricas como experimentales. De todos los demás miembros del grupo no puedo decir más que cosas bonitas. Me acogisteis desde el primer momento y me siento orgullosa del grupo que hemos formado entre todos: Ainara, Belén, David, Inés, Iñigo, Itziar y más recientemente Alicia, Baha, Carlos, Cebrián, Jose Manuel, Miguel, Pablo, Unai y Víctor. No me puedo olvidar de los miembros de Anteral: Aitor, Asier, Gonzalo, Víctor y todos los demás. Me alegro de haber compartido estos años con todos vosotros y espero que compartamos más éxitos profesionales en el futuro. Muchas gracias.

De la universidad también me llevo amigos de otros grupos de investigación: Abián, Aitor, Adrián, Jon, Juanjo, Laura, Nerea y el resto de compañeros de despacho y departamento. Me da pena no haber podido disfrutar de más Juevintxos, pero espero poder ir más a partir de ahora.

Questa tesi non sarebbe quello che è se io non fossi stata a Siena. Sono andata lì per tre mesi ma alla fine sono diventati nove. Ho dei ricordi incancellabili di quel periodo. Grazie di tutto, Stefano, anche se sei un eminenza nel mondo delle metasuperfici m´hai accolto sin dal

upna
Universidad Pública de Navarra
Nafarroako Unibertsitate Publikoa

primo minuto come una di voi. Non potrei dimenticare te, Enrica, una donna fantastica sia sul piano professionale che su quello personale. Ricordo che una volta mi hai raccontato che disegnare delle metasuperfici è proprio arte. Oggi capisco più di mai quella frase e provo una profonda ammirazione per tutto il lavoro che voi fate. Grazie di cuore a tutti di essere stati così bravi con me: Cristian, David, Francesco, Gabriele, Maddalena, Marco, Mario, Santi, Valentina e sopratutto te, Alice, una persona meravigliosa con la quale sin dall´inizio ho provato una grande sintonia e che poi m´ha dimostrato di essere una grande amica. Thanks also to the people from the refugio, Guillen, Alexia and Abhinav.

I would also like to thank members of the thesis committee for the evaluation and reading of this thesis dissertation: Dr. Peter de Maagt from European Space Agency, Dr. Stefano Maci from Università degli Studi di Siena and Dr. Iñigo Ederra from UPNA.

También quiero trasladar mi agradecimiento a las instituciones que han permitido que esta tésis se pudiese desarrollar: Universidad Pública de Navarra a través del programa de ayudas para la formación de personal investigador y ayudas a la movilidad. COST Action IC1102 y NEWFOCUS por la ayuda aportada para la realización de estancias de investigación.

Por último me queda dar las gracias a las personas que me han apoyado siempre. Estoy segura de que todos los que estéis leyendo estas líneas habréis oído hablar de mi pueblo, Betelu. Sabéis que lo llevo muy presente en cada momento de mi vida por muy lejos que esté de casa. Este pueblito que es tan pequeño para muchos y en cambio tan grande para mí. Portua jeistean nere Mailloak ikustean beti nere paradisura noala sentizen dut. Eskerrik asko lagunei, auzokideei eta azken finean Beteluar guztiei. Eta bereziki, aurreko urtean utzi gintuzun loretxoari, gogoan zaitut.

Ez nintzateke naizena izango nere familia gabe. Amona, osaba-izebak eta lehengusuak. Barkatu iezaidazue lana zela eta momentu garrantzitsuak galdu baditut, atzerantz begiratzean pena gehien ematen didana horixe da. Hala ere, beti presente izan nauzue eta horregatik eskerrak eman nahi dizkizuet. Eta bukatzeko, nere gurasoak, Miguel eta María Jesús. Ama, no tengo palabras para agradecerte todo lo que haces por nosotros, eres la mejor madre del mundo, mi ejemplo a seguir. Aita, beti izan zara langile fina eta ez dut bizitzan beste adibiderik behar izan: nolako egurra halako ezpala. Oihane eta nere anaia Ibaitxo, neretzako guztia zara eta beti izango nauzu behar duzun guztietan. Ikaragarri matte zattuztet. Os quiero muchísimo. A María, Jose Ramón y Lorena infinitas gracias por darme a la persona que me acompaña en este viaje de la vida, Javi, mi kari. No puedo agradecértelo lo suficiente, eres mi mejor amigo, mi compañero, mi amor. Has sido mi gran apoyo durante estos ocho años y espero que alcancemos todos nuestros sueños juntos, tanto a nivel profesional como personal. Te quiero kari.

upna
Universidad Pública de Navarra
Nafarroako Unibertsitate Publikoa

Abstract

Space industry has shown huge interest in the evolution of onboard antennas to lighter, thinner and cheaper designs, looking for an easier way to integrate them in satellites and to reduce launching costs. New alternative technologies, such as Partially Reflective Surface (PRS) and metasurface (MTS) have emerged in the recent years and they have shown their applicability for satellite applications. These technologies present a great opportunity for engineers to develop innovative solutions, but it is still necessary to carry out an important work to cover all the satellite antenna specifications.

In this thesis dissertation, different planar technologies have been employed to develop flat and light satellite antennas. On one hand, the PRS technology has been employed to optimize a dual band circularly polarized antenna working at C band. On the other hand, a Ku band dual circularly polarized broadside beam MTS antenna has been designed and fabricated.

This thesis was born as a continuity of the work carried out in the antennas group in Public University of Navarra in collaboration with EADS Astrium Casa Espacio (Spain) and European Space Agency (ESA), for the development of a PRS antenna to meet the on board requirements of a TT&C application working at 3.7GHz. Although previous works consolidated this technology as a feasible light alternative to conventionally employed bulky solutions, its multiband behavior capacity has not been deeply studied. Due to this fact, the second chapter of the thesis has been focused on the design of a PRS for TT&C application working at two close frequencies at C band, 3.7GHz and 4.2GHz. In PRS antennas, also called Electromagnetic Band Gap (EBG) or Frequency Selective Surfaces (FSS) antennas, a resonant cavity is created between the ground plane of source and the PRS placed around half a wavelength distance. The characterization of the PRS is realized by means of the scattering matrix analysis of a plane wave impinging the structure considering two working frequencies. The challenge of the proposed solution is related with the close working frequencies relation (f_2/f_1=1.13). The implementation of this dual band PRS antenna has been realized by introducing a second FSS layer (composed by Jerusalem cross shaped elements inside metallic rings) below the EBG superstrate (composed by a metallic sheet with holes which has been employed in previous works for single band response). The structure is excited by

upna
Universidad Pública de Navarra
Nafarroako Unibertsitate Publikoa

a simple 2x2 circularly polarized array of patches. The work concludes demonstrating the suitability of the proposed light configuration to substitute a conventional array antenna with 27 patch elements with the consequent simplification of the beam forming network.

The second part of this thesis dissertation is the most extensive and it is related with the development of MTS antennas. Due to the great interest shown by the spatial industry in the development of high gain satellite antennas based on this light ultrathin technology, the dissertation was focused in this emerging technology. As it could be found in the literature, MTS technology offers the opportunity to implement solutions with complex radiation patterns and with good circular polarization control. Nevertheless, the capability to provide dual circular polarization or dual band response with a single MTS antenna is still a challenge.

In this thesis, for the first time, the modeling, implementation and measurement of a single layer MTS antenna able to provide both right-hand circular polarization (RHCP) or left-hand circular polarization (LHCP) in broadside direction at 13.5GHz is presented. Theoretical deep study has been realized and the basics for the proposed solution has been developed. Two transverse magnetic and electric surface waves are launched matched in phase and balanced in amplitude. The characterization of the required equivalent surface impedance is explained in detail and the dispersion analysis of several subwavelength elements have been carried out in order to synthetize the MTS. Furthermore, the required feeding system is presented in detail, which has been implemented by a septum orthomode transducer polarizer. The simulation results proves the basics. The solution has been fabricated and the measurement results are shown.

The last part of the thesis establishes characterizes the capability of single layer MTS antennas for multiband applications. Three different MTS configurations able to radiate with different patterns and with circular polarization at 13.5GHz and 16GHz frequencies have been analyzed. The first design provides backward isoflux radiation pattern in the lower band and broadside beam at the upper band. The second design is a dual band isoflux atenna with backward and forward radiation, respectively. The last system radiates in broadside direction in the lower band, while in the upper band isoflux radiation is obtained by means of the contribution of two modes inside the visible region. Main limitations of the proposed configurations are discussed and possible improvements are mentioned.

As a results of this Ph.D., 3 papers have been published in international journals, 12 communications in international conferences (5 of them invited) and 5 national conferences have been presented.

upna
Universidad Pública de Navarra
Nafarroako Unibertsitate Publikoa

Resumen

La industria espacial ha estado siempre muy interesada en la evolución de las antenas que se integran en los satélites. Se buscan soluciones que además de ser ligeras y compactas, tengan un coste reducido. De esta forma se facilita su integración en los satélites y se reduce el coste en el lanzamiento de todo el sistema. Los avances en las diferentes tecnologías han demostrado su viabilidad para cumplir con los requerimientos especificados, como lo son la tecnología de superficies parcialmente reflectivas (PRS) o las metasuperficies (MTS). Aunque estas tecnologías ofrecen a los ingenieros múltiples posibilidades, queda todavía por realizar un gran trabajo para cumplir con todos los requerimientos de las antenas embarcadas en satélites.

Por un lado, se ha empleado la tecnología de PRS para optimizar una antena trabajando en doble frecuencia en banda C. Por otro lado, se ha diseñado y fabricado una antena basada en MTS, con radiación broadside y doble polarización circular en banda Ku.

Esta tesis nació como continuación del trabajo realizado en el Grupo de Antenas de la Universidad Pública de Navarra, en colaboración con EADS Astrium Casa Espacio (España) y la Agencia Espacial Europea (ESA), para el desarrollo de una antena PRS que cumpliese las especificaciones de una antena embarcada de una aplicación TT&C (Tracking, Telemetría y control) a 3.7GHz. Trabajos anteriores consolidaron esta tecnología como una alternativa ligera a las soluciones pesadas y voluminosas utilizadas convencionalmente. No obstante, la mayoría de estas soluciones se han centrado en aplicaciones que funcionan en una sola frecuencia. Falta un estudio más exhaustivo de las configuraciones con doble frecuencia de funcionamiento. El trabajo realizado en esta tesis se ha centrado en el diseño de una antena PRS para el cumplimiento de los requerimientos de una aplicación TT&C en dos frecuencias en la banda C, 3.7GHz y 4.2GHz. En las PRS, también llamadas antenas de band gap electromagnético (EBG) o superficies selectivas en frecuencia (FSS), se genera una cavidad resonante entre el plano de masa donde está la fuente y el superestrato situado a una distancia de media longitud de onda. La caracterización de la PRS se ha realizado mediante el estudio de la matriz de reflexión de una onda incidente en la estructura teniendo en cuenta las dos frecuencias de interés. La dificultad de la solución propuesta se centra en la cercanía de ambas frecuencias, ya que la separación entre ellas es de 1.13%. La implementación de la

upna
Universidad Pública de Navarra
Nafarroako Unibertsitate Publikoa

antena PRS en doble banda se ha realizado introduciendo de forma adecuada una segunda capa de FSS (compuesta por cruces de Jerusalem dentro de anillos metálicos) en la parte inferior de una capa EBG (compuesta por un plano metálico con agujeros en su interior y que se suele emplear para soluciones en una única banda). El sistema de alimentación es sencillo y se compone de un array de 2x2 parches circularmente polarizado. El trabajo concluye demostrando que la configuración propuesta podría ser empleada para sustituir un array de antenas parche de 27 elementos que requiere un sistema de alimentación complejo.

La segunda parte de la tesis es la más extensa y se centra en el desarrollo de antenas de metasuperficie (MTS). Debido al gran interés mostrado por la industria espacial en esta tecnología extremadamente compacta y ligera, la tesis se centró en esta tecnología emergente. Como se muestra en la literatura, las MTSs se pueden emplear para implementar soluciones con diagramas de radiación complejos y buena polarización circular. Sin embargo, hay ciertos aspectos que hoy por hoy todavía suponen una limitación, como pueden ser la capacidad de proveer doble polarización circular o respuesta multibanda.

En esta tesis se presenta por primera vez, el modelado teórico, la implementación práctica y las medidas de una antena MTS compuesta por una única capa capaz de proveer radiación en broadside a 13.5GHz tanto con polarización circular a derechas como a izquierdas. Para ello se ha realizado un estudio profundo sobre la tecnología MTS y se ha desarrollado la base teórica de la solución propuesta. En esta estructura, se excitan dos modos transversales, de tipo magnético y eléctrico, balanceados tanto en fase como en magnitud. Además, se explica en profundidad la caracterización de la impedancia superficial requerida en la MTS y se han realizado el estudio de dispersión de distintos pixeles para la implementación de la misma. Por otro lado, también se explica el sistema de alimentación necesario y se presenta el septum fabricado. Los resultados de simulación corroboran el comportamiento esperado según la teoría desarrollada. El sistema completo ha sido fabricado y se muestran los resultados experimentales.

En la última parte de la tesis se ha desarrollado la base teórica para la caracterización de antenas de MTS de una única capa para aplicaciones multibanda. Se han presentado tres configuraciones con distintos diagramas de radiación a las frecuencias de 13.5GHz y 16GHz, con polarización circular. El primer diseño radia con forma isoflux en dirección backward en la banda baja mientras que en la alta radía en dirección broadside. La segunda configuración es capaz de radiar con forma de isoflux en ambas bandas. Por último, el tercer diseño radia en dirección broadside en la banda baja y en la alta con isoflux, gracias a la contribución de dos modos dentro del región visible. Además, se presentan las limitaciones de las configuraciones propuestas y las posibles mejoras a realizar.

upna
Universidad Pública de Navarra
Nafarroako Unibertsitate Publikoa

Como resultado de este trabajo, se han publicado 3 artículos en revistas indexadas, se han presentado 12 comunicaciones en conferencias internacionales (5 de ellas invitadas) y 5 nacionales.

upna
Universidad Pública de Navarra
Nafarroako Unibertsitate Publikoa

Contents

upna
Universidad Pública de Navarra
Nafarroako Unibertsitate Publikoa

upna
Universidad Pública de Navarra
Nafarroako Unibertsitate Publikoa

upna
Universidad Pública de Navarra
Nafarroako Unibertsitate Publikoa

List of figures

upna
Universidad Pública de Navarra
Nafarroako Unibertsitate Publikoa

upna
Universidad Pública de Navarra
Nafarroako Unibertsitate Publikoa

upna
Universidad Pública de Navarra
Nafarroako Unibertsitate Publikoa

upna
Universidad Pública de Navarra
Nafarroako Unibertsitate Publikoa

upna
Universidad Pública de Navarra
Nafarroako Unibertsitate Publikoa

List of tables

upna
Universidad Pública de Navarra
Nafarroako Unibertsitate Publikoa

Nomenclature

Symbols

α	Attenuation constant
β	SW wavenumber
c	Free space velocity
d	Modulation periodicity
$\Delta\beta$	Surface wave wavenumber shift
Δph	Phase shift over the unit cell
ε_0	Vacuum permittivity
ε_r	Dielectric relative permittivity
η	Average surface impedance normalized with free space
Γ	Reflection coefficient matrix
h	Substrate thickness
I	Current
k	Free space wavenumber
λ_{sw}	SW wavelength
μ_0	Vacuum permeability
μ_r	Dielectric relative permeability
v_g	Group velocity

upna
Universidad Pública de Navarra
Nafarroako Unibertsitate Publikoa

v	Phase velocity
ω	Angular frequency
ϕ	Surface wave incidence angle
Φ	LW pointing angle at dispersion diagram
ψ	Patch rotation inside the unit cell
$\boldsymbol{\rho}$	Radial unit vector in cylindrical coordinates
θ	LW pointing angle
u	Unit cell length
$\boldsymbol{\varphi}$	Azimuth unit vector in cylindrical coordinates
ϑ	Transformation matrix rotation angle
k_t	Wavenumber tangential to MTS
X	Surface reactance
X_{cc}	Grounded slab reactance
X_S	Sheet reactance
$\bar{\bar{\mathbf{Z}}}$	Surface impedance tensor
$\mathbf{z}$	Unit vector transversal to MTS
$\bar{\bar{\mathbf{Z}}}_{\mathbf{cc}}$	Grounded slab impedance tensor
ζ	Free space impedance
$\bar{\bar{\mathbf{Z}}}_{\mathbf{S}}$	Sheet impedance tensor

Acronyms / Abbreviations

AR	Axial Ratio
BW	Backward
CO	Co polar
CP	Circular Polarization

upna
Universidad Pública de Navarra
Nafarroako Unibertsitate Publikoa

EoC	Edge of Coverage
FM	Floquet Mode
FW	Forward
LW	Leaky wave
MoM	Method of moments
MTS	Metasurface
OMT	Orthomode transducer
PRS	Partially Reflective Surface
SW	Surface wave
TE	Transverse Electric
TM	Transverse Magnetic
TRE	Transverse Resonance Equation
XP	Cross polar

upna
Universidad Pública de Navarra
Nafarroako Unibertsitate Publikoa

Chapter 1

Introduction

1.1 Background

During last years spatial industry has been interested in the evolution of antenna design towards new technologies which could offer lighter, thinner and more compact configurations. At the same time, the reduction on the number of radiating elements guides designers to dual frequency, multifrequency or broadband configurations. Deep impact in this reduction is due to the boom of small satellites. The reduction in size and weight in these systems is directly related with the reduction of launch and orbit costs. They have marked a turning point towards a new generation of satellite missions, since they bring the possibility for engineers and researches with low budget to explore a new universe of innovative applications. This is the reason why the development of competitive antenna technologies complying with the requirements of conventional bulky systems but providing at the same time the advantage of lightness and compactness represents an appealing research area. This is the case of Partially Reflective Surface (PRS) technology and Metasurface (MTS) antennas.

For 10 years now, PRS technology has been consolidated as a feasible alternative for atennna designers thanks to its applicability in emerging communication frameworks, such as wireless system or satellite communications [1–19]. It was Trentini who introduced for the first time in his pioneering work the PRS antenna approach [20] to obtain gain enhancement based on fabry perot cavity antennas. Gain enhancement is achieved by using a superstrate, also called in the literature Electromagnetic Band Gap (EBG) or Frequency Selective Surface (FSS), placed at half a wavelength ($h \sim \lambda_0/2$) distance from the feeding antenna located on the metallic ground plane.

Different types of PRSs can be used to generate the cavity between the superstrate and the ground plane, as presented in [1–12]. These solutions require a defect in the EBG periodicity and can be excited with single elements or array configurations with linear or circular

upna
Universidad Pública de Navarra
Nafarroako Unibertsitate Publikoa

polarizations. The simplest configurations are obtained placing a FSS layer conforming the superstate over a patch type feeding system [5] and more complex configurations with three or more feeding points show wider bandwidth and maximum achievable gain [6–8]. Kanso et al. present in [9–12] a dual band EBG resonator antenna for satellite applications at Ka-band (f_1=19-20GHz and f_2=29-30GHz) with a relation between working frequencies f_2/f_1=1.5 (see Fig. 1.1). The FSS superstrate is appropriately adjusted to achieve a 2.2% of working bandwidth at lower frequency and a 3.5% in the upper band, with a simulated gains of 19dBi and 22dBi, respectively.

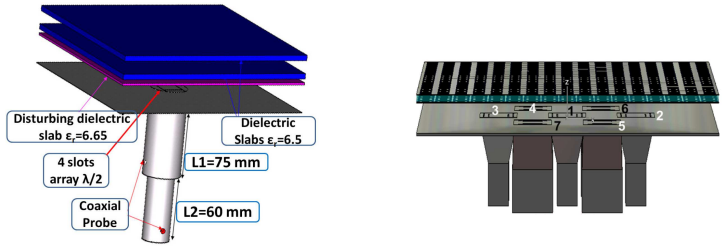

(a) (b)

Fig. 1.1. Dual band EBG resonator antenna for Ka-band satellite applications with (a) single feed ©2009 VDE Verlag GmbH [11] and (b) multifeed ©EuMA 2011 [12].

PRS antennas have been shown as real alternatives to conventional bulky antennas for WAAS (Wide Area Augmentation System) at L_1 band (1575.42 MHz). The work presented in [13–16], was born thanks to a collaboration between the Antenna Group at Public University of Navarra (UPNA, Spain), MDA Corporation (Canada) and European Space Agency. WAAS is a network of geostationary satellites and ground stations that provide GPS (Global Positioning System) signal corrections for better position accuracy. The traditional antenna structures designed for this application are composed by arrays of 9 to 19 helix-shaped array elements fed with complex Beam Forming Networks (BFNs) (see Fig. 1.2). These antennas achieve coverage gain of 16.5dBi over the Earth with good circular polarization purity (low axial ratio AR<1.5dB). One of the design challenges related with this type of antennas is the phase centre stability over the field of view to provide accurate position data. The advantage of the proposed alternative single layer PRS antenna lies in the required simple superstrate design and radiation source, which is composed by a 2x2 element array. The manufactured prototype fulfills all the on board validation tests, such as flight, thermal, multipacting and vibration test.

upna
Universidad Pública de Navarra
Nafarroako Unibertsitate Publikoa

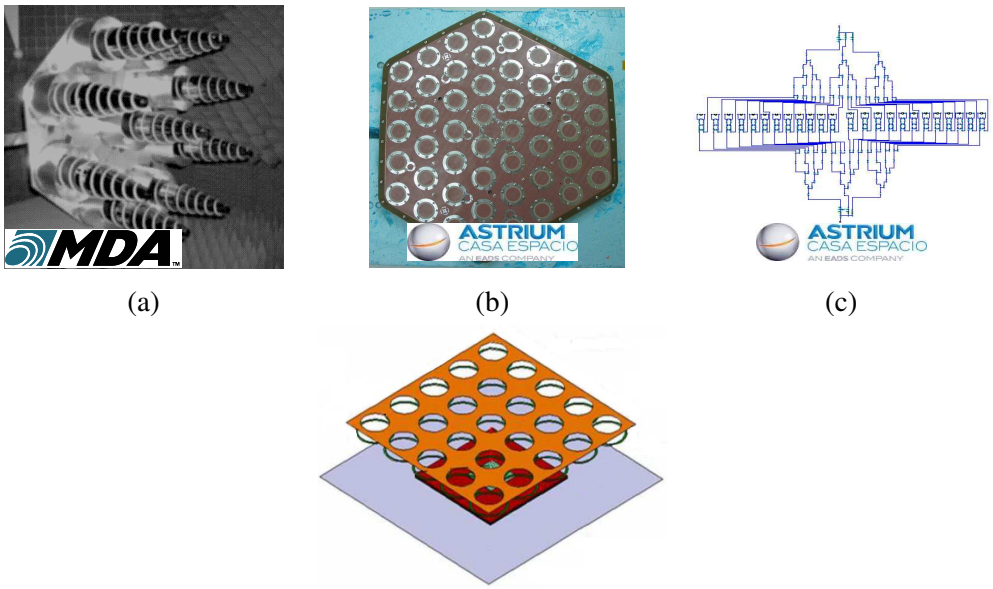

(a) (b) (c)

(d)

Fig. 1.2. (a) 9 helix-shaped element array deployed by MDA for WAAS spatial application at L_1 band ©2006, IEEE [13], [14, 15]. (b) Patch arrays with 27 elements and (c) complex BFN required to excite the antenna proposed by EADS Astrium Casa Spacio and (d) the alternative solution based on EBG-antennas proposed by UPNA ©2009, IEEE [17], [18, 19].

Once single frequency PRS configuration has been proposed to comply real application requirements, the goal was the design of a dual frequency PRS solution [17] to comply with the Telemetry, Tracking and Control (TT&C) antenna requirements at C band (f_1=3.7GHz and f_2=4.2GHz), capable to substitute a 27 patch elements array. The challenging point in the design is the relation between working frequencies f_2/f_1=1.13, resulting in really close one. TT&C functions are vital for successful operation of all satellites since they lead with the satellite management. Their main tasks are related, for instance, with the monitoring of the satellite subsystems and data transmission to satellite control center for routine operational and failure diagnostic purposes. Furthermore, they act as tracking platforms to earth stations, allowing to determine the orbital parameters of a satellite and its assignment in a certain orbital slot. Systems can also receive commands from the control centres to execute several functions over the satellite e.g. power on/off subsystems, change subsystem operating mode, deploy booms, antennas or solar cell arrays. In the carried out work the efforts have been focused on overall volume and mass reduction while complying with RF performances over the required bandwidth at both working frequencies. For this purpose the proposed PRS solution incorporates a second FSS layer below the EBG. Promising results were obtained during the research project.

upna
Universidad Pública de Navarra
Nafarroako Unibertsitate Publikoa

Nevertheless, during the last five years an attractive novel flat and light technology for spatial industry emerged which arouse great interest on research community: the Metasurface (MTS) antennas (see Fig. 1.3). In recent times the Metamaterials have received widespread attention due to the wide range of achievable electromagnetic properties. A good illustration of their application are the inspiring works presented by Engheta, Maci et al. in [21–23]. The greatest appeal of such materials is that by means of the shape and orientation arrangement of the constituent sub wavelength elements at each point of the configuration, they provide extreme control over the electromagnetic properties and they might even exhibit responses that cannot be found in nature. However, the main drawback lies in their complex manufacture. Therefore, the evolution towards two dimensional metamaterials, also called metasurfaces, meant a significant leap forward to open up new possibilities at microwave and optical frequencies. The MTSs are extremely flat configurations, constituted by a single dense layer of sub wavelength metallic patches, also called pixels, printed over a thin dielectric substrate characterized by its thickness ($h \sim \lambda_0/20$) and relative permittivity (ε_r).

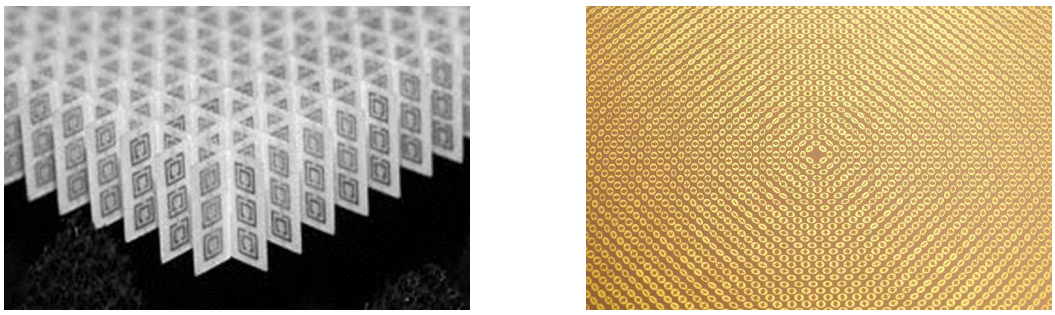

(a) (b)

Fig. 1.3. (a) Metamaterial [24] and (b) Metasurface [25].

Sievenpiper et al. in [26–35] employ the Holography technique with two-dimensional metasurfaces to control the surface wave (SW) wave front. Due to the small size of the pixels in terms of SW wavelength, the homogenized MTS can be described by means of an equivalent surface impedance. The properties of the patch cladding arrangement over the surface are locally modified based on the surface impedance characterization and in this way, the surface wave phase velocity and propagation path is locally modified providing the required electromagnetic properties.

Based on these fundamentals, the metasurfaces have been applied to guide the SWs over the surface (see Fig. 1.4(d)). For instance, Lunenburg or Fish Eye lenses, beam shifters or beam splitters have been implemented by Martini et al. in [35–42].

Besides, MTSs have been also employed to tailor the reactive field close to the structure. In [43–48], Grbic et al. present the design of a near-field plate. In these configurations,

upna
Universidad Pública de Navarra
Nafarroako Unibertsitate Publikoa

non-periodic closely-spaced scatterers are located over a MTS, interacting and focusing the reactive field near to the plate. Moreover, in [49, 50], the radiative field in Fresnel zone is adapted by means of a MTS capable to generate non-diffractive Bessel beams.

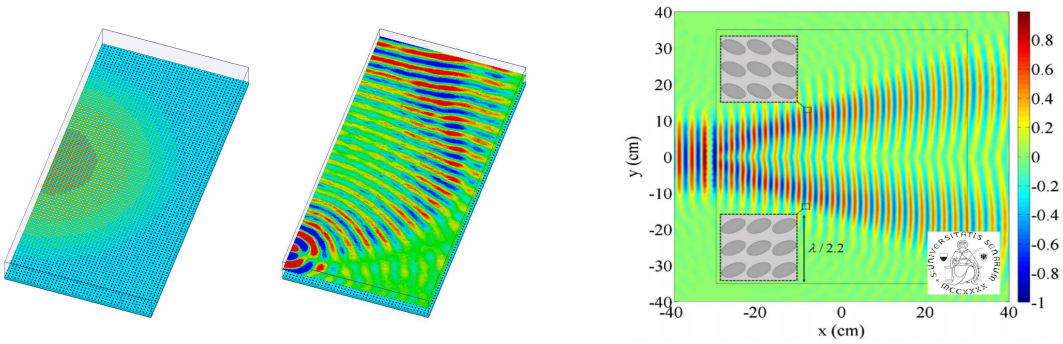

(a) (b)

(c) (d)

Fig. 1.4. Different near-field application devices developed based on MTS technology: (a) Lunenburg lense, (b) SW beam-splitter ©2014, IEEE [37], (c) near-field plate ©2011, IEEE [43] and (d) Bessel beams generating device ©2012, IEEE [50].

On the other hand, MTSs have been also employed for far field applications. For example, Huygen's surfaces are generated in [51]. These are periodic or non-periodic reflectionless surfaces that are employed for beam steering, beam shape, focus or for field polarization manipulation at microwave frequencies, as they allow high control of copolar (CO) and crosspolarized (XP) fields when an incident plane wave propagates through them.

One of the areas in which the development of this innovative, extremely thin and light technology has brought more progress is related with the space antennas, as it allows the design of medium-to-large gain systems with complex shaped radiation patterns and with control over the field circular polarization purity. Ever since the first works were presented by Oliner et al. in [52, 53], significant progresses have been made. Minatti et al. presented in [54–56] the design and implementation of a bidimensional broadside circularly polarized MTS antenna working at 13GHz for mono pulse radar applications (see Fig. 1.5). It is

upna
Universidad Pública de Navarra
Nafarroako Unibertsitate Publikoa

composed by electrically small metallic patches (with a unit cell lattice around $\lambda/8$) printed over a flat grounded slab (thickness $h \sim \lambda/22$). In the presented prototype, the metasurface is characterized by a modulated isotropic surface impedance which traces a sinusoidal profile in radial direction and varies in azimuth following a spiral shape. A single vertical pin excites a single cylindrical TM mode propagating in radial direction with a given phase velocity. When the mode interacts with the sinusoidally modulated reactance (with given average reactance and period values), a leaky wave is generated in broadside direction. The circular polarization is achieved due to the 90 degrees phase shift introduced in the modulation taking into account the azimuth: two sectors separated 90 degrees over the surface contribute to the radiation in phase quadrature, namely, single circular polarization is obtained in broadside. The presented solution provides a gain of 20dBi and 10dBs difference between the CO and XP components. The main disadvantage is the required large surface area (with a radius about $3.7\lambda_0$), which arises due to the low aperture efficiency shown by these antennas (15%-20%).

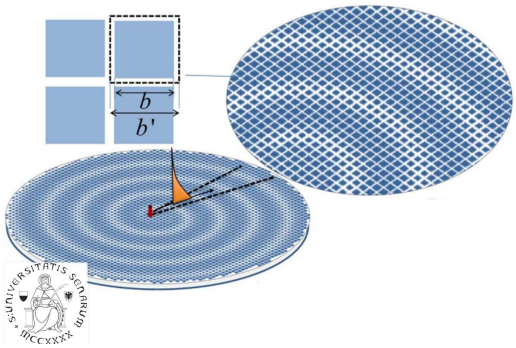

Fig. 1.5. Broadside isotropic MTS satelitte antenna found in literature ©2011, IEEE [56].

Due to the fact that isotropic metasurfaces provide weak polarization control, Faenzi, Minatti et al. in [57–59] take advantage of anisotropic surfaces (see Fig. 1.6). In these solutions, the MTSs are composed by different sized circular pixels with a groove trough the diameter, rotated appropriately with respect to the surface wave impinging angle at each position of the antenna. The broadside beam metasurface antenna presented in [58] is characterized by an anisotropic sinusoidal modulation in radial direction and spiral-shaped distribution of the elements in azimuth. When the TM mode excited with a single vertical pin in the center interacts with the surface, RH circularly polarized broadside radiation is obtained with a maximum directivity of 26dBis and -15dBs XP component. The use of anisotropic pixels increases the aperture efficiency to 35%. Besides, modifying the modulation parameters, it is possible to steer the beam in different directions. A sectorial antenna pointing towards 60 degrees is presented in [59], with a maximum directivity

upna
Universidad Pública de Navarra
Nafarroako Unibertsitate Publikoa

estimation of 23dBs and a XP component of -13dBs. Furthermore, a circularly polarized anisotropic isoflux MTS antenna for LEO applications working at 8.5GHz (X-band) is presented in [57]. The radii of the metallic circular elements above the grounded slab are appropriately modified following a rotationally symmetric sinusoidal impedance radial modulation. Besides, the rotation of the grooves inside the pixels allows to control the field polarization all over the structure. In this example, four vertical pins in sequential phase quadrature are employed to excite the cylindrical TM SW which interacts with the anisotropic modulated surface. The excited leaky wave generates a radiated field with a conical beam, ensuring uniform power reception on the earth within a drop-off angle of 60 degrees. The proposed configuration fulfills the required uniform power coverage with a gain of 9dBs. The main drawback is also given due to the required large dimension (radius of 14λ). Another MTS antenna is presented in [60]. In this case, an optimized high gain sector isoflux antenna is shown, employable for high transmission data rates at 26GHz (Ka-band). The surface is fed from the center and the propagating TM mode interacts with the surface in such a way that some area leaks the field in backward direction providing the required broadside gain level and the area in opposite direction radiates in forward direction towards 65 degrees off-axis.

Therefore, PRS technology and MTSs are attractive alternatives to obtain these flat and light antenna designs demanded by space industry. While PRS technology is a much more mature technology, the MTSs are young and require novel work from research community to impulse their evolution.

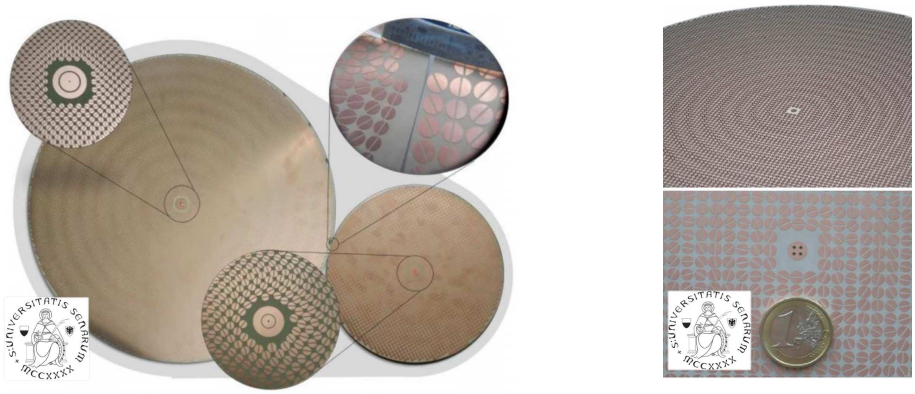

(a) (b)

Fig. 1.6. Circularly polarized anisotropic MTS atennas found in literature, working at X-band: (a) broadside radiation ©2016, IEEE [58], (b) isoflux-shaped beam ©2012, IEEE [57].

upna
Universidad Pública de Navarra
Nafarroako Unibertsitate Publikoa

1.2 Framework of the research and outline of the thesis

This dissertation was born as a continuity of the work realized in the Antenna Group at Public University of Navarra on PRS antennas for satellite applications. Previous prototypes developed in the group in colaboration with ESA and MDA Corporation (Canada) corroborated experimentally the suitability of PRS technology to comply all the on board requirements of a WAAS application working at L_1 single frequency band [13–16]. Although a lot of work could be found in the literature in this topic [1–12], most of proposed systems work at a single frequency or may work at dual band when the ratio between working frequencies is greater than f_2/f_1=1.5. Hence, the design of dual frequency PRS antenna with a working frequency ratio lower that 1.5 was still a challenge. In the first stage of this thesis, the work has been focused on the optimization of an advanced volume and mass reduced EBG antenna capable to comply the specifications of a TT&C application working at two close frequencies at C-band, f_1=3.7GHz and f_2=4.2GHz (f_2/f_1=1.13) [17–19]. Great interest was shown by ESA and EADS Astrium Casa Espacio in this dual frequency developments. Therefore, based on [13–16], a new FSS layer has been appropriately introduced in the configuration. The dual circular polarization purity, gain over coverage, return loss, isolation and mass study of the proposed antenna has been done. It has been demonstrated that PRS technology can be used in dual frequency configurations to substitute a conventional antenna array of 27 patch elements with a complex feeding system. All the design details and simulation results are drawn in chapter 2.

Nevertheless, as aforementioned in the background section, during the realization of this dissertation the MTSs emerged as an attractive novel flat and light technology. It offers the possibility to obtain different radiation patterns, as isoflux ones, which are of great interest to space industry companies. Therefore, it was the natural evolution of the work, as the spatial industry has shown great interest on MTS solutions. In this second stage new objectives were established and a new research thread was open in the research group oriented to the development of satellite MTS antennas.

The following three chapters are devoted to the Metasurface antennas development. Firstly, an important research work has been carried out to strengthen concepts and obtain a good background on this novel topic. Based on the works referenced during this document, chapter 3 summarizes several aspects about the characterization of the MTSs, such as the isotropic or anisotropic nature of the equivalent transparent or opaque impedances. Besides, frequency and spatial dispersion characterization of several pixel geometries have been performed, by means of full wave analysis. The results have been compared with the ones obtained by the method shown in appendix **??**, which is based on closed-form expressions developed by Mencagli et al.[61–63]. Based on the dispersion information, the equivalent

upna
Universidad Pública de Navarra
Nafarroako Unibertsitate Publikoa

surface impedance maps have been calculated following the procedure presented by Martini et al. in [38]. For completeness, in the appendix B, the extracted impedance results using the procedures presented in [38] and [64–69] are compared, from Martini and Patel respectively.

A lot of MTS solutions can be found in the literature. However, there are still challenging designs to contribute to the evolution of MTS antennas. For instance, the ability to provide double circular polarization with a single MTS aperture. Hence, the complete modeling, implementation and measurements of a novel broadside MTS antenna working at Ku-band capable to provide both right-hand circular polarization and left-hand circular polarization is accomplished in chapter 4. The fundamentals of the structure are extended, analyzing the required balanced-impedance boundary conditions to be accomplished not only by the metasurface but also by the necessary feeding system. The study of the pixels to implement the practical configuration is detailed and an efficient compact septum orthomode transducer polarizer has been designed to excite the complete structure. The final antenna is implemented taking into account the manufacturing limitations. The fabricated prototype has been measured and the experimental results have been compared with the simulation analysis. Finally, some conclusions are drawn.

In addition to the circular polarization duality, the fulfilling of the requirements at two different frequencies by means of a single layer MTS means also an important progress for space business. In chapter 5, the capability to cover more than one frequency band with different radiation patterns and with CP control is analyzed. The limitations of the implemented broadside or isoflux-shaped radiation pattern solutions are compared and discussed.

To conclude, the main results of this thesis are summarized in chapter 6 and some guidelines for future research are given.

upna
Universidad Pública de Navarra
Nafarroako Unibertsitate Publikoa

Chapter 2

Dual band Partially Reflective Surface (PRS) antenna for TT&C application

2.1 Introduction

During last decade, aerospace industry has shown great interest on the use of innovative technologies to obtain lightweight and compact designs. This fact has contributed directly on the development of new antenna solutions and broadened the range of employable technologies for their implementation. This is the case, for instance, of the antennas based on Partially Reflective Surfaces (PRS), also called in the literature Fabry Perot resonant cavities, Frequency Selective Surfaces (FSS) or Electromagnetic Band Gap (EBG) structures [1–19]. In these structures, the gain of the source is substantially increased by creating a cavity in between the ground plane of the excitation and a PRS placed around half a wavelength distance. The design of the superstrate is carried out analyzing the scattering matrix of an incident wave impinging the PRS, which can be implemented with different element geometries depending on the application.

The work carried out during the first stage of the dissertation has been focused on the optimization of a PRS compact antenna developed in collaboration with EADS Astrium Casa Espacio (Spain) and European Space Agency (ESA) to meet the on board requirements of a dual band TT&C application. Previous works have demonstrated the suitability of this technology for single band operation [13–16]. Based on the same design, dual frequency behavior is looked for [17–19] to achieve requirements at two close frequencies (f_1=3.7GHz and f_2=4.2GHz, f_2/f_1=1.13). This chapter presents the operating principle of the proposed dual band PRS antenna in which a second FSS sheet has been incorporated to meet the gain over coverage, circular polarization purity, bandwidth, return loss, isolation and mass

upna
Universidad Pública de Navarra
Nafarroako Unibertsitate Publikoa

specifications. Theoretical basics are presented in section 2.2 and details of the design are given in section 2.3. Moreover, simulation results are shown in 2.4. The work concludes in section 2.5, demonstrating the suitability of the proposed solution to substitute a conventional technology array antenna with 27 patch elements and a complex beam forming network (shown previously in Fig. 1.2).

2.1.1 TT&C application requirements

The implementation details of a Partially Reflective Superstrate (PRS) antenna capable to fulfill the on board requirements of a Telemetry, Tracking and Control (TT&C) application provided by European Space Angency (summarized in Table 2.1) are drawn in this section. TT&C systems are the responsible of monitoring the satellite subsystems, ensuring robust communications with on Earth centers to control their position. At C-band, the uplink (UP) communications with TT&C satellites are carried out at 5.9-6.5GHz and the downlink (DL) communications at 3.7–4.2GHz. In this work the design efforts have been focused mainly on obtaining dual band response at two close frequencies for DL, f_1=3.7GHz and f_2=4.2GHz (f_2/f_1=1.13), with a extremely light configuration (mass<800g). Besides, 16.5dBi of gain must be provided in a 80MHz of bandwidth with good circular polarization (cross polar level XP< $-$25dB). The main goal is the design of a PRS solution suitable to substitute traditional patch array antenna configurations from EADS Astrium Casa Espacio, composed by 27 elements and excited with complex beam forming network (shown in Fig. 1.2).

Centre frequency	3.7GHz and 4.2GHz
Bandwidth	80MHz (Goal 120MHz)
Gain over coverage	>16dBi
Edge of coverage (EoC)	9°
Return loss	>18dB
Polarization	Circular (RHCP/LHCP)
Cross polarization	<-25dB
Isolation	>25dB
Power handing	10W
Mass	<800g at 3.7GHz
Envelope	Height<2.5λ_0

Table 2.1 Compact low-mass antenna requirements.

The planar solution is excited by a 2x2 patch array antenna designed by EADS Astrium Casa Espacio (see Fig. 2.9). More details about the feeding system are given in section 2.3.3.

upna
Universidad Pública de Navarra
Nafarroako Unibertsitate Publikoa

2.2 Basic operation principle

The most interesting feature of the PRS technology lies in the fact that it allows to obtain high gain antennas with very compact profile configurations. Besides, as they are usually excited by a reduced number of simple feeding elements, the beam forming networks are extremely simple resulting in a fast and cheap manufacturing.

The gain enhancement phenomena is obtained due to the resonant cavity generated on the structure when a PRS is located at a half a wavelength distance form the excitation point over a ground plane. Equivalent behavior can be obtained by considering a Electromagnetic Band Gap (EBG) dielectric material with a periodicity in one or more directions, as it can be seen in Fig. 2.1(a) [10]. At a certain frequency band, the wave travelling through this material suffers complete reflection and generates a band gap (see Fig. 2.1(c)). However, when a layer is removed introducing a defect in the structures periodicity as depicted in Fig. 2.1(b), an allowed narrow frequency band appears inside the forbidden band gap and energy can be transmitted through the material. Hence, these structures are also known as Frequency Selective Surfaces (FSS) in the literature [1–19]. Taking into account the boundary conditions of the problem, it is possible to relate this behavior with a PRS antenna, in which a partially reflective single layer is located at half a wavelength distance from a feeding point located over a metallic ground plane (see Fig. 2.1(e)).

When the distance between the feed and the PRS is appropriately adjusted ($h \sim \lambda_0/2$), power transmitted in each bounce of the trapped waves inside the Fabry-perot cavity is radiated in phase. Therefore, the directivity is increased as the radiation aperture is raised. This in phase radiation is translated in a broadside radiation pattern with a narrow working frequency band. The phase matching condition in Eq. (2.1) has to be satisfied at the working frequency. Outside the working bandwidth this condition is lost.

$$\phi_{ground} + 2kh_{sup} + \phi_{sup} = 2\pi n \quad n = 0,2,4... \tag{2.1}$$

$\phi_{ground} = \pi$ is the phase shift introduced to the reflected field by the metallic ground plane and ϕ_{sup} is the phase related with the partially reflective superstrate located at h_{sup} distance from the ground plane. $k = 2\pi/\lambda_0$ is the free space wavenumber. It is straightforward to see that as the superstrate is partially reflective ($\phi_{sup} \sim \pi$), the resonant cavity condition is obtained when $h_{sup} \sim \lambda_0/2$ at f_0.

For a given h_{sup}, the resonant cavity condition at two frequencies is obtained when the reflection properties of the superstrate satisfy the following relation at lower (f_1) and upper (f_2) frequencies:

upna
Universidad Pública de Navarra
Nafarroako Unibertsitate Publikoa

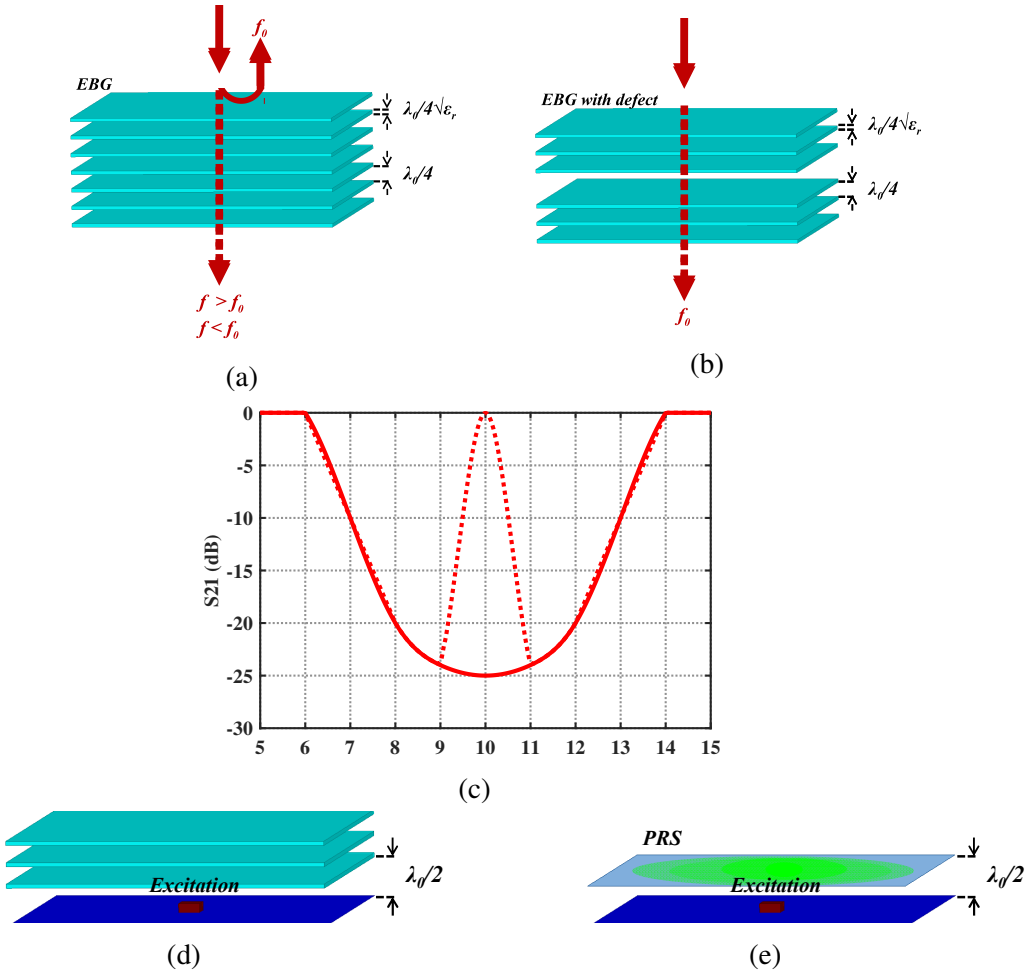

Fig. 2.1. (a) Band Gap generation in a EBG material and (b) inclusion of a defect. (c) Transmission coefficient of a wave impinging a EBG material without defect (continuous line) and with defect (dashed line). (d) EBG antenna. (e) PRS antenna, increase of effective area due to resonant cavity generation is appreciated.

upna
Universidad Pública de Navarra
Nafarroako Unibertsitate Publikoa

$$\phi_{sup_{f_2}} = (\frac{f_2}{f_1}(\frac{1}{2} + \frac{\phi_{sup_{f_1}}}{2\pi}) - \frac{1}{2})2\pi \tag{2.2}$$

It has to be mentioned that both the phase and magnitude of the PRS reflection coefficient must be taken into account for the correct implementation of the antenna. The phase determines the resonant frequency when the PRS is located at h_{sup} distance from the excitation point, while the magnitude determines the achievable effective area. When the size of the structure is large enough, the maximum achievable directivity value is determined by the reflection coefficient magnitude provided by the PRS at the desired working frequency.

2.3 Dual Frequency PRS antenna design

Based on the theoretical basics to meet the resonance cavity condition at two frequencies with a PRS, the complete antenna is characterized in this section. The reflection characterization of the superstrate can be simplified analysing the scattering matrix of its conformal elemental unit cell with symmetry boundary conditions. The cell geometry that best meet the required response has been found based on simulations carried out with ANSYS HFSS commercial solver [70]. The synthesized complete superstrate is located at a given distance from the metallic ground plane, in which a 2x2 patch array excitation is located in the center.

2.3.1 Unit cell reflection characterization

The reflection properties of the superstrate can be analize by studying its elementary unit cell.

Single band response

Fig. 2.2(a) shows the geometry properties of a unit cell composed by a metallic area with a circular hole in the center. Applying appropriate symmetry boundary conditions (see Fig. 2.2(b)), ANSYS HFSS commercial solver provides the reflection coefficient properties of a plane wave impinging the structure (Fig. 2.3).

When the radius of the hole decreases the magnitude of the reflection coefficient increases and the phase approaches the response of a perfect electric conductor (PEC) material ($\phi = \pi$), as it is depicted in Fig. 2.3. The magnitude is related with the field spread on the superstrate surface and therefore determines the illumination, while the phase determines the resonance frequency for a given location h_{sup} of the PRS.

The resonant frequency of the PRS can be extrapolated from a structure composed by two elements located at $2h_{sup} \sim \lambda_0$ distance as shown in Fig. 2.2(c). The S_{11} parameter of

upna
Universidad Pública de Navarra
Nafarroako Unibertsitate Publikoa

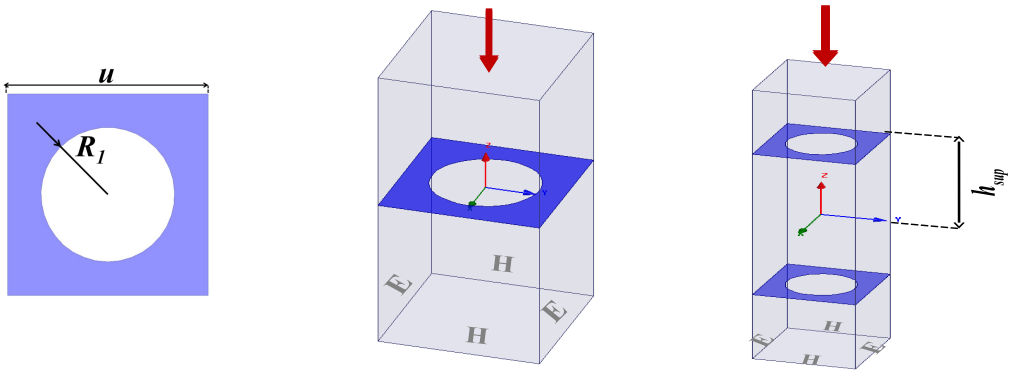

(a) (b) (c)

Fig. 2.2. PRS unit cell composed by metallic area with a hole in the center: (a) geometry details, (b) symmetry conditions for reflection coefficient characterization and (c) structure for resonant frequency characterization.

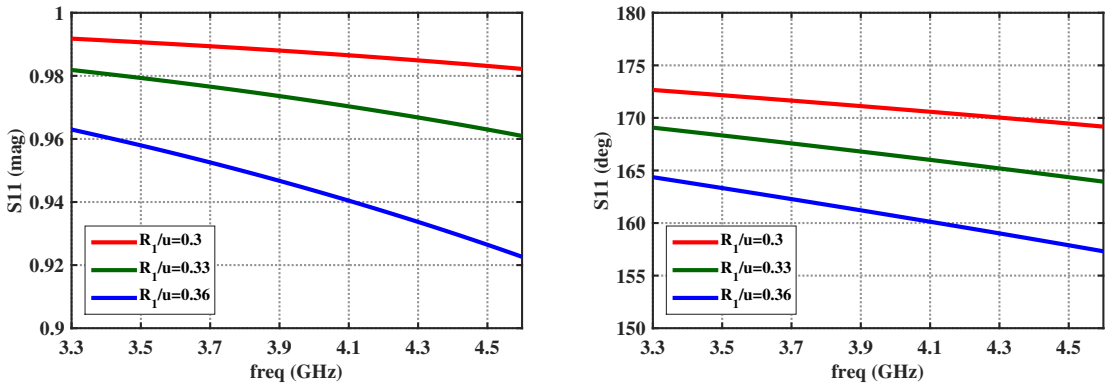

(a) (b)

Fig. 2.3. Reflection coefficient (a) magnitude and (b) phase of a plane wave impinging the unit cell ($u = 26mm = \lambda_1/3.1 = \lambda_2/2.75$) composed by a metallic area with a hole in the center: normalized radii $R_1/u = 0.3(red), 0.33(green), 0.36(blue)$.

upna
Universidad Pública de Navarra
Nafarroako Unibertsitate Publikoa

the configuration shows the frequency were the cavity resonates. Only when fields obtained at this frequencies exhibit a null in the center of the cavity the solution is representative of the complete structure in which the ground plane is placed in that position. Fig. 2.4(a) shows the resonant frequency of the cavity when h_{sup} is located at two different distances ($h_{sup} = \lambda_1/2, \lambda_2/2$) and Fig. 2.4(b) shows the required superstrate phase response to meet the resonance cavity condition at different frequencies when h_{sup} is optimized for a desired working frequency.

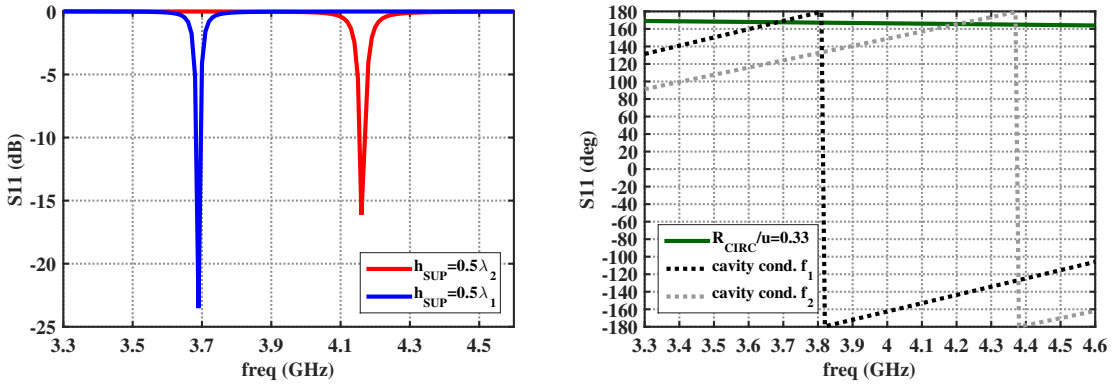

(a) (b)

Fig. 2.4. (a) Resonance frequency of the cavity when the unit cell ($u = 26mm$, $R_1/u = 0.33$) is located at $h_{sup} = \lambda_1/2$ (blue), $\lambda_2/2$ (red). (b) Ideal phase response to meet the cavity condition when h_{sup} is optimized for $f_1 = 3.7GHz$ (black) or for $f_2 = 4.2GHz$ (grey). Unit cell reflection coefficient phase response (green).

The working cavity condition can be turned in frequency adjusting appropriately h_{sup} to $\sim \lambda/2$, as it can be seen in Fig. 2.4(a). Moreover, it can be concluded from Fig. 2.4(b) that the PRS composed by the unit cell presented in Fig 2.2(a) ($u = 26mm$, $R_1/u = 0.33$) can be used to obtain a single frequency band behavior. It is concluded that it is necessary to implement another element geometry to meet the dual band cavity condition.

upna
Universidad Pública de Navarra
Nafarroako Unibertsitate Publikoa

Dual band response

Several geometries have been analyzed to find the most appropriate cell to conform the dual band PRS antenna. A new layer has been introduced close to the previously studied single band element, in order to simplify their printing on both faces of a substrate. The selected cell geometry is shown in Fig. 2.5(a). It is composed by two layers: the metallic cell with a hole in the center (as the one shown previously in Fig. 2.2(a)) is located as the top layer (denoted as CIRC) while the layer on the bottom is composed by a metallic ring (called RING) with a Jerusalem-cross shaped element in the center (denoted as JC).

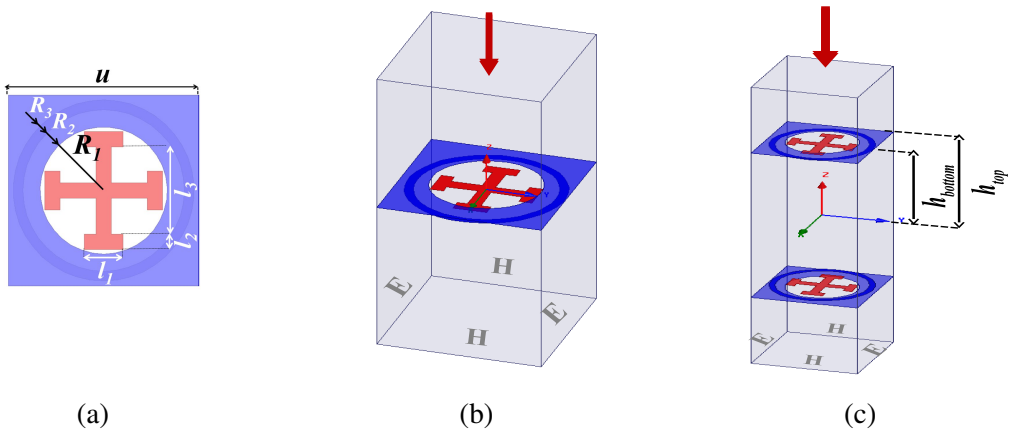

(a) (b) (c)

Fig. 2.5. PRS unit cell composed by two layers: a metallic area with a hole in the center on top layer (CIRC) and a metallic ring (RING) with a Jerusalem-cross shaped element (JC) in the bottom layer: (a) geometry details, (b) symmetry conditions for reflection coefficient characterization, (c) structure for resonant frequency characterization.

The inclusion of a second layer allows the compliment of the resonant cavity condition at two frequencies described in Eq. 2.2. Based on the previous experience in the implementation of a single band PRS antenna [13–16], it is known that the reflection coefficient magnitude required at both bands to meet the gain specification of 16dBi in EoC is close to 0.94-0.96. As shown in Fig. 2.6, when $|S_{11}| < 0.94$ the structure is characterized by a poor aperture efficiency. On the other hand, when $|S_{11}| > 0.96$ diffraction at the edges can be caused due to high reflection of the PRS.

In Fig. 2.7 it can be seen that the inclusion of the RING in the second layer induces a phase jump and consequently enables the dual band resonance of the cavity. Nevertheless, the reflection coefficient magnitude at 4.2GHz is too high ($|S_{11}| = 0.98$). For this reason, the use of the Jerusalem Cross shaped element has been required, which keeps the reflection coefficient phase response but decreases the magnitude at the upper band ($|S_{11}| = 0.96$ at

upna
Universidad Pública de Navarra
Nafarroako Unibertsitate Publikoa

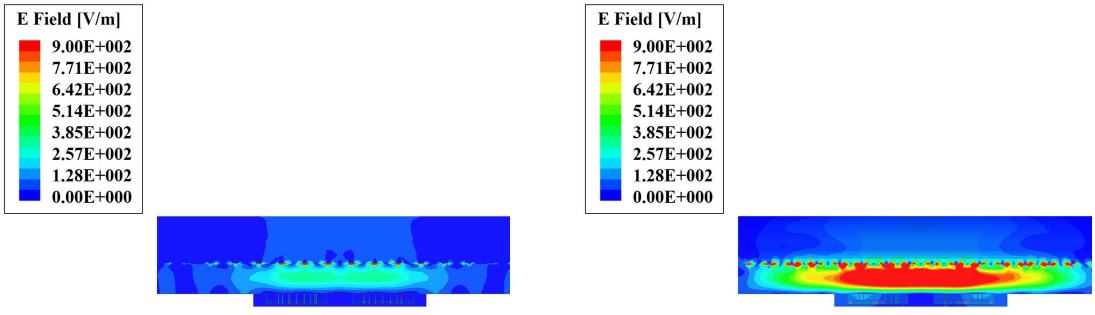

(a) (b)

Fig. 2.6. (a) Poor aperture efficiency due to low PRS reflection ($|S_{11}| < 0.94$). (b) Diffraction at the edges caused due to too high reflection of the PRS ($|S_{11}| > 0.96$).

4.2GHz). Final dimensions of the JC and RING are: $u = 26mm$, $R_1/u = 0.33$, $R_2/u = 0.43$, $R_3/u = 0.48$, $l_1/u = 0.21$, $l_2/u = 0.08$, $l_3/u = 0.47$, $h_{top} = \lambda_1/2.33$ and $h_{bottom} = \lambda_2/2.11$.

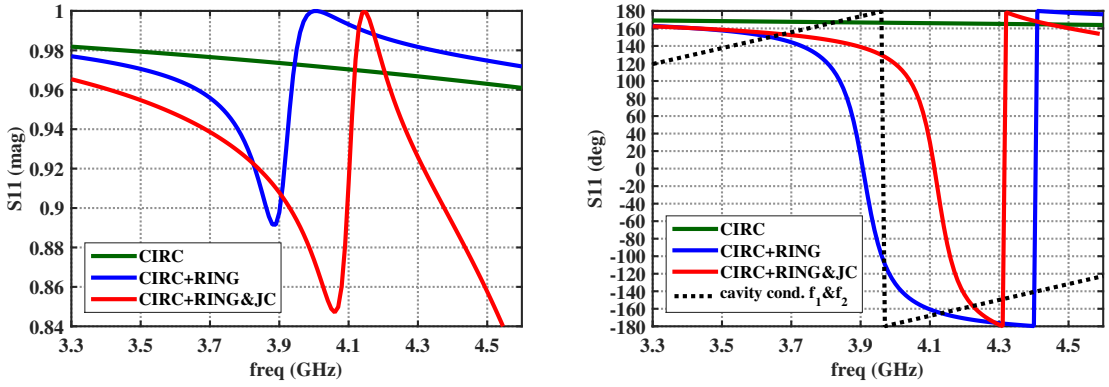

(a) (b)

Fig. 2.7. Comparison of the (a) magnitude and (b) phase of the reflection coefficient when a plane wave impinges the unit cell composed by: a single CIRC layer (green) and by two layers: CIRC(top)+RING(bottom) (blue), CIRC(top)+RING&JC(bottom) (red). Theoretical dual band cavity condition (black). In all the cases $u = 26mm$, $R_1/u = 0.33$, $R_2/u = 0.43$, $R_3/u = 0.48$, $l_1/u = 0.21$, $l_2/u = 0.08$, $l_3/u = 0.47$, $h_{top} = \lambda_1/2.33$, $h_{bottom} = \lambda_2/2.11$.

2.3.2 Synthesis of the complete superstrate

The total dimension of the superstrate is a critical parameter in the design process. It must be large enough to allow the configuration to comply with maximum directivity requirement from Table 2.1. However, at the same time, the prototype must be as light as possible. In

upna
Universidad Pública de Navarra
Nafarroako Unibertsitate Publikoa

the proposed solution, the dimension of the superstrate is set to $15ux15u \quad (5.46\lambda_2 x 5.46\lambda_2)$. Fig. 2.8 depicts the PRS implemented deploying the CIRC(top)+RING&JC(botom) unit cell presented previously in Fig. 2.7, with the top layer located at $h_{top} = \lambda_1/2.33 = 34.72mm$ distance from the ground plane and the RING&JC elements at $h_{bottom} = \lambda_2/2.11 = 33.78mm$. In the fabrication process, each layer should be printed at each side of a foam dielectric sheet ($\varepsilon_r = 1$) with a thickness of 0.94mm.

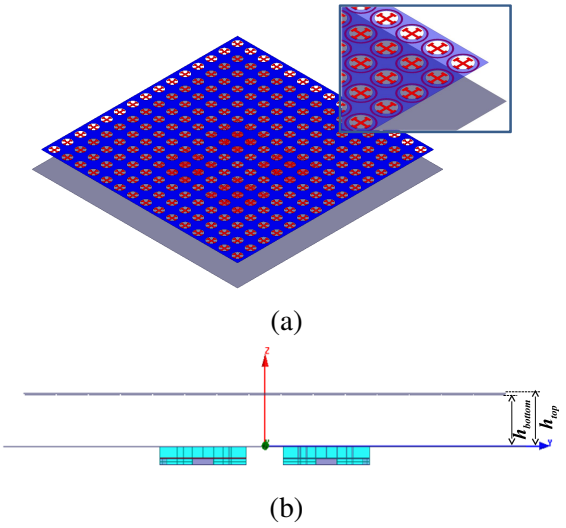

(a)

(b)

Fig. 2.8. Practical implementation of the PRS antenna. Total dimension is $5.46\lambda_2 x 5.46\lambda_2$ and thickness $h_{top} = \lambda_1/2.33$ and $h_{bottom} = \lambda_2/2.11$.

upna
Universidad Pública de Navarra
Nafarroako Unibertsitate Publikoa

2.3.3 Feeding system

Based on the previous works [13–16], it is known that the gain requirement of the TT&C application (Table 2.1) can be obtained employing a single patch designed by EADS Astrium Casa Spacio company.

This patch is composed by 4 microstrip stacked patches fed by two orthogonal striplines. 15 metallic pins connect the different ground planes inside the device. Nevertheless, a sequentially rotated $2x2$ patches array has been introduced in the PRS solution to meet the rigorous axial ratio condition. The two feed ports perpendicularly located at each radiant patch are fed with a 90 degrees phase shift to generate circular polarization. The proposed feed is simpler than the one required to excite the conventional configuration shown in Fig. 1.2(c) with a complex BFN.

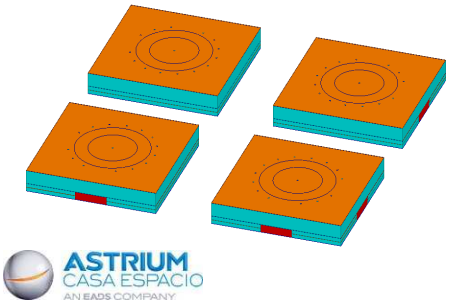

Fig. 2.9. 2x2 patch array feeding system designed by EADS Astrium Casa Spacio deployed to excite the PRS antenna.

Input matching and isolation information as well as the axial ratio provided by the patches are shown in Fig. 2.10. Each patch presents S_{11} parameter lower than -17dB and isolation between ports lower than -22dB in whole working bandwidth (from 3.7GHz to 4.2GHz). Due to the symmetry of the patches the results at both input ports are symmetric. The axial ratio is <1.58dB at two frequency bands (XP<-20dB) in all the EoC.

2.4 Simulation results

Full wave analysis of the antenna presented in Fig. 2.8 has been carried out with ANSYS HFSS commercial solver. The field confined in the cavity at both working frequencies ($f_1 = 3.7GHz$ and $f_2 = 4.2GHz$) is depicted iin Fig. 2.11.

As illustrated in Fig. 2.11, the reflectivity of the PRS has been appropriately implemented to maximize the illumination area and avoid diffraction at the edges.

upna
Universidad Pública de Navarra
Nafarroako Unibertsitate Publikoa

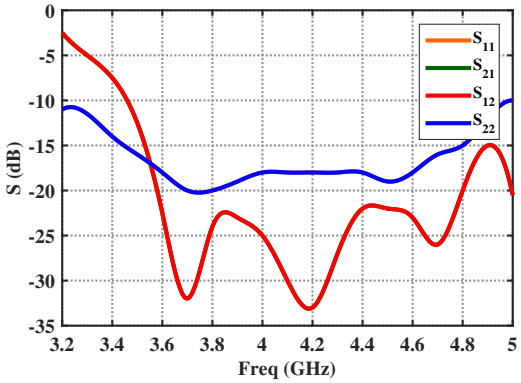

(a)

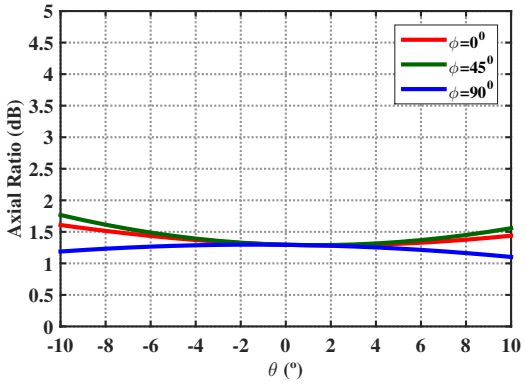

(b)

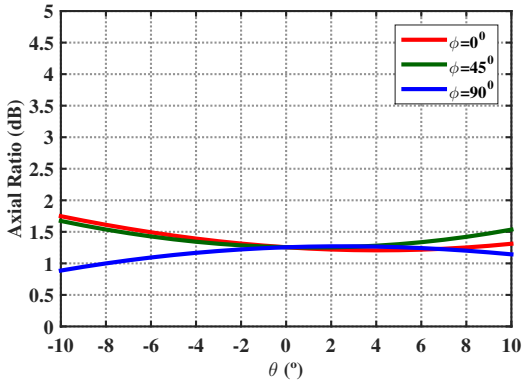

(c)

Fig. 2.10. (a) S_{11} and axial ratio provided by a single patch at (b) 3.7GHz and (c) 4.2GHz.

upna
Universidad Pública de Navarra
Nafarroako Unibertsitate Publikoa

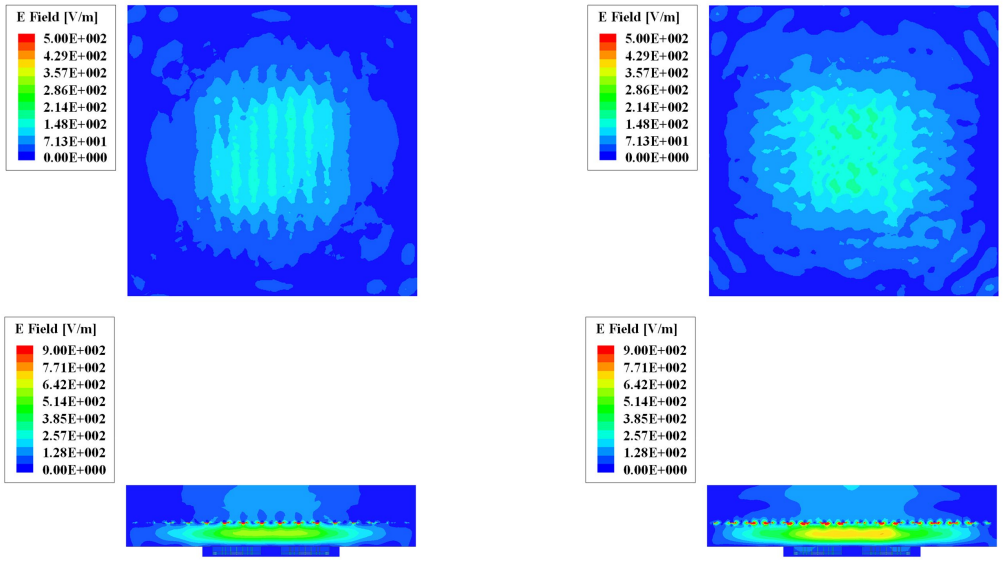

Fig. 2.11. Lateral and top views of the field confined in the cavity at (a) 3.7GHz and at (b) 4.2GHz.

$\varphi = 0°(red), 45°(green), 90°(blue)$ cuts of the simulated gain pattern (LHCP CO and RHCP XP components) obtained with the proposed PRS antenna at low and high frequencies are shown in Fig. 2.12 and Fig. 2.13, respectively. In addition, Fig. 2.14 shows the gain dependence with frequency at broadside ($\theta = 0°$) and at the limit of the required edge of coverage ($\theta = 9°$). A maximum gain of 21.09dBi is obtained at 3.73GHz in the lower band. Gain over 16dBi at the limit of the edge of coverage (EoC $\theta = 9°$) is obtained in a 100MHz of bandwidth (from 3.65GHz to 3.75GHz), complying the requirements given in Table 2.1. Moreover, the maximum achievable gain at the higher frequency (4.2GHz) is 21.7dBi and the bandwidth is 90MHz (4.15GHz to 4.24GHz). The illumination efficiency is 44.2% at f_1 and 39.53% at f_2. Taking into account the losses estimation in Table 2.2, the radiation efficiency is approximately 88%. In conclusion, the calculated total antenna efficiency is of 39.5% in lower band and 35% in the upper band. The losses of the complete structure have been estimated based on EADS Astrium Casa Espacio previous space programs experience and they are summarized in Table 2.1. Total losses have been estimated to be 0.54dBs.

The axial ratio is presented at the central frequencies of both frequency bands (Fig. 2.15).

Fig. 2.15 depicts that the axial ratio requirement (<1dB) is fulfilled at both bands. Equivalently, the XP field level is below 25dBs with respect to CO at each working band. It is clear that the designed PRS antenna complies with the radio frequency requirements.

upna
Universidad Pública de Navarra
Nafarroako Unibertsitate Publikoa

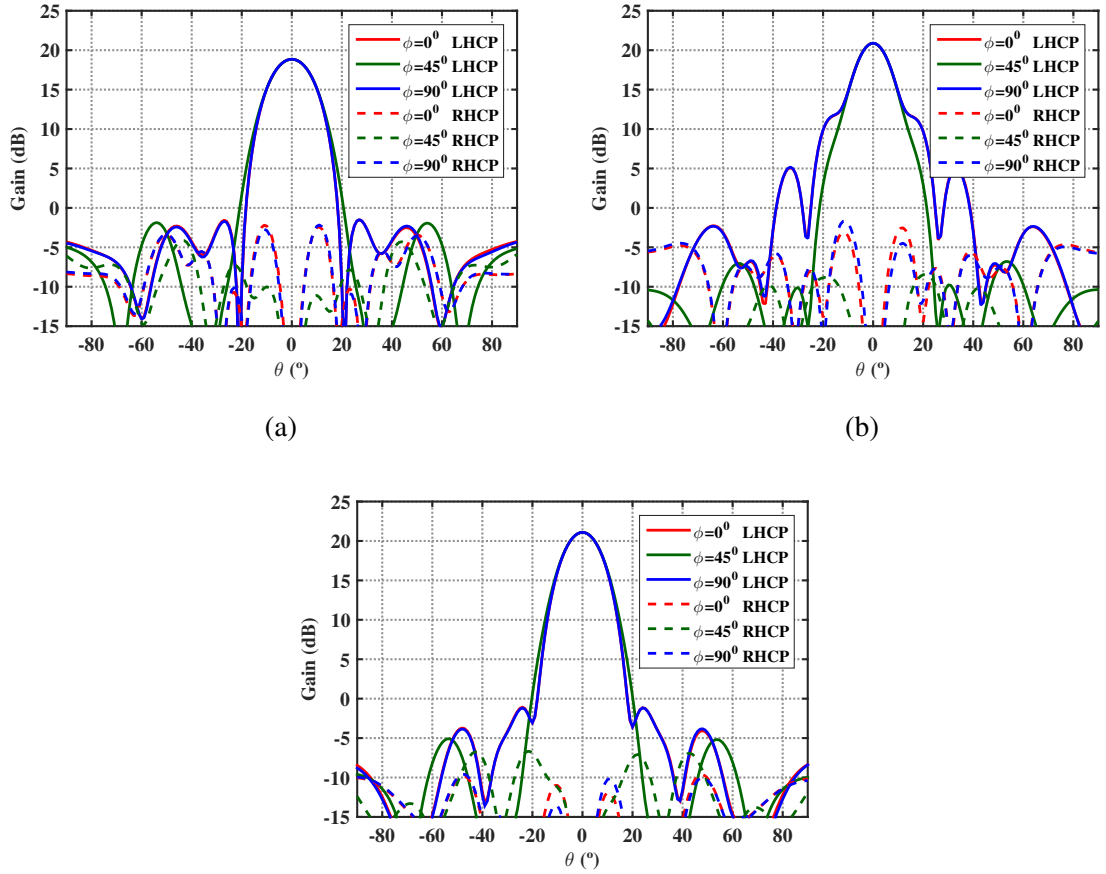

Fig. 2.12. $\varphi = 0°(red), 45°(green), 90°(blue)$ cuts of the simulated gain pattern (LHCP CO continuous lines and RHCP XP dashed lines) at low frequency band: (a) 3.65GHz, (b) 3.73GHz, (c) 3.75GHz.

Ohmic Losses (radiator)	0.15dB
Ohmic Losses (radiator)	0.15dB
Matching Losses	0.04dB
Connector Losses	0.05dB
Transitions between layers	0.20dB
Implementation Margin (including thermal effects)	0.10dB
Total Losses	0.54dB

Table 2.2 Losses estimation.

upna
Universidad Pública de Navarra
Nafarroako Unibertsitate Publikoa

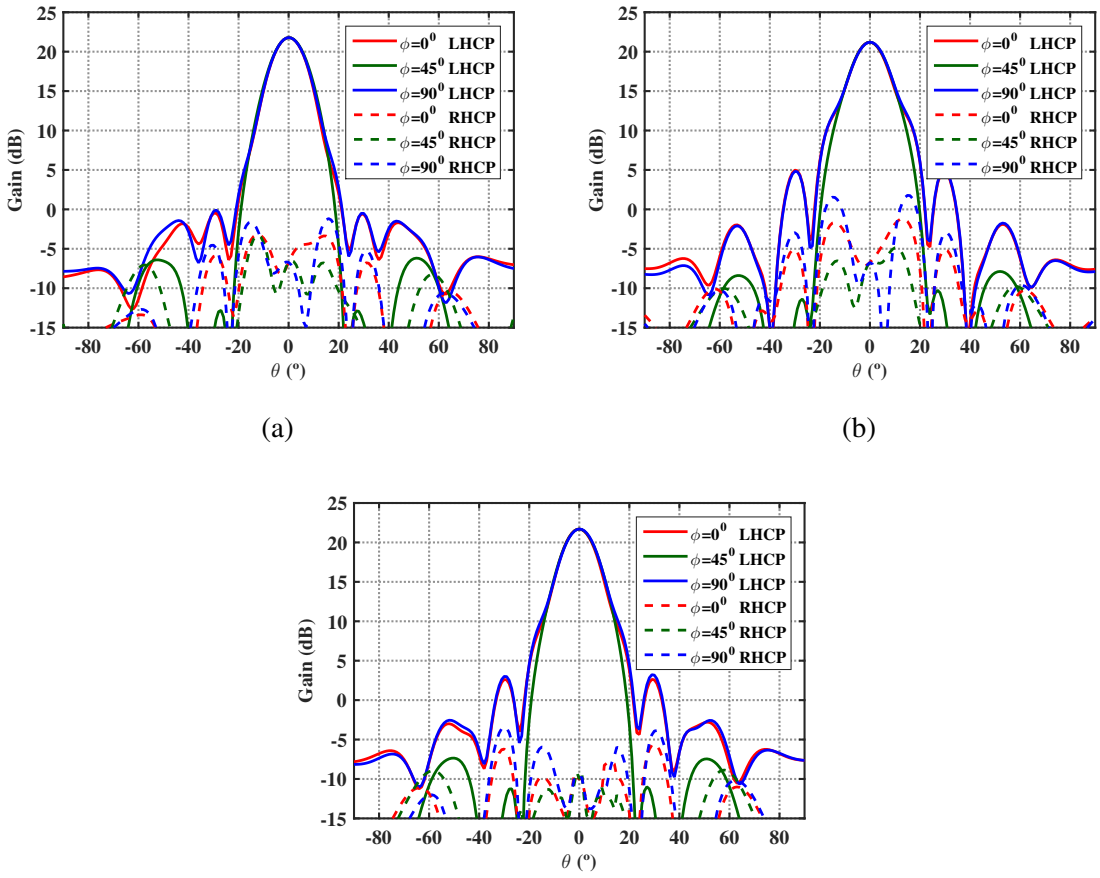

(a) (b)

(c)

Fig. 2.13. $\varphi = 0°(red), 45°(green), 90°(blue)$ cuts of the simulated gain pattern (LHCP CO continuous lines and RHCP XP dashed lines) at high frequency band: (a) 4.15GHz, (b) 4.2GHz, (c) 4.24GHz.

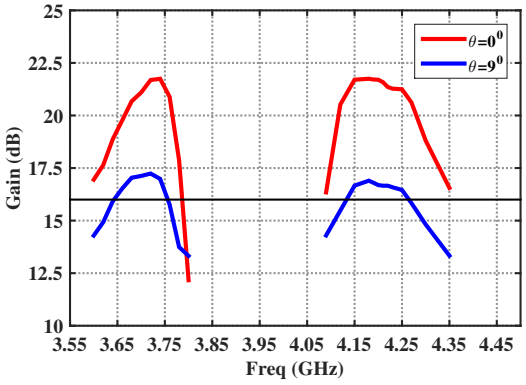

Fig. 2.14. Gain ($\theta = 0^0(red)$, $\theta = 9^0(blue)$) vs. frequency.

upna
Universidad Pública de Navarra
Nafarroako Unibertsitate Publikoa

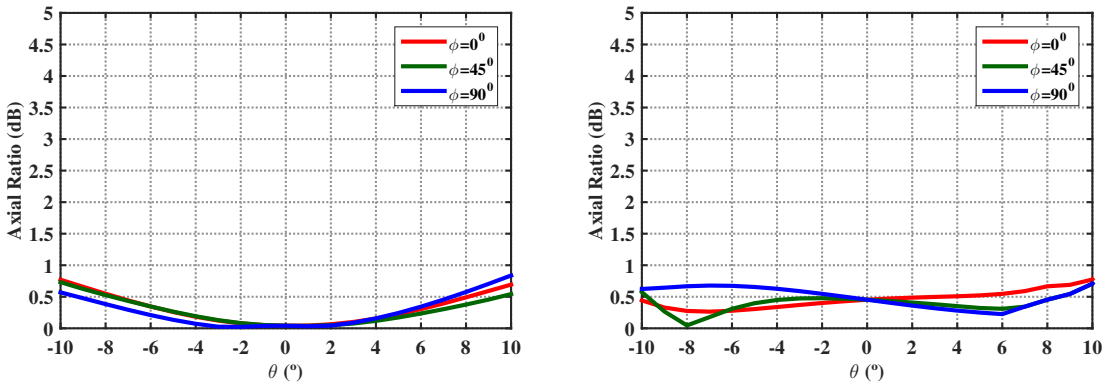

(a) (b)

Fig. 2.15. Axial Ratio ($\varphi = 0°(red), 45°(green), 90°(blue)$ cuts) at: (a) 3.73GHz and (b) 4.18GHz.

Finally, the overall mass of the proposed solution has been estimated. All the constitutive antenna parts have been taken into account, such as the material employed to build the brackets, holders, bolts or nuts with a certain margin for each component. The concluding outcome of the overall mass leads to a estimation of 870g. This value exceeds the mass requirement listed in Table 2.1. The solution lies in the truncation of the structure. As illustrated in Fig. 2.16, it is possible to cut the four edges without affecting to the overall response and ensuring the necessary mass reduction.

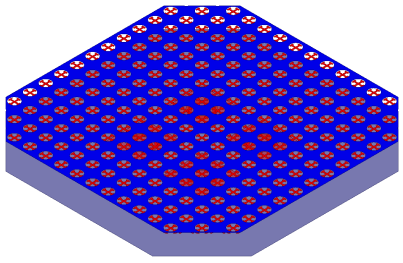

Fig. 2.16. Truncated PRS antenna.

upna
Universidad Pública de Navarra
Nafarroako Unibertsitate Publikoa

2.5 Conclusions

In this chapter the development of a PRS antenna capable to meet the requirements of a TT&C application working at two frequencies (f_1=3.7GHz and f_2=4.2GHz) at C-Band has been carried out.

In contrast to simpler designs employable when the relation between frequencies is larger, the implementation difficulty of the proposed solution concerns the close distance between the working frequencies $f_2 = 1.13 f_1$. Due to the fact a fast variation on the superstrate reflection phase response is required to meet the cavity condition at the two working frequencies, a second layer composed by a metallic ring with a Jerusalem-cross shaped element in the center has been included 0.94mm under the metallic layer with circular holes located at 34.72mm from the ground plane. In addition, the magnitude of the superstrate must be adequately considered to have an optimized illumination efficiency.

The PRS technology solution meets all the flight requirements shown in Table 2.1 and requires a simplified BFN in comparison with traditional technology designs. The low cost and low mass are also key points in favour of the suggested configuration. In conclusion, based on previous designs using PRS technology, the proposed antenna could be included on board of a satellite to substitute more complex conventionally employed bulky antennas.

upna
Universidad Pública de Navarra
Nafarroako Unibertsitate Publikoa

Chapter 3

Metasurface (MTS) antennas development basics

3.1 Introduction

In recent years, space industry has been investing on innovative technologies looking for lower profile and thinner antennas. Particularly, the two dimensional metamaterials [21–23], also called metasurfaces (MTSs), have received widespread attention in the research community. This innovative, thin and light technology has been deployed to implement not only devices to control the propagation of the surface waves (SWs), such us lenses or beam splitters [35–40], but also to design medium-to-large gain satellite antennas [54–60] with complex shaped radiation patterns and having control over the field polarization.

This chapter introduces the classification of different types of metasurfaces and details of their characterization by means of the equivalent surface impedance. All the relevant features of the SWs excited on the structure are described in section 3.2, as well as the properties of the radiated field when the surface impedance is modulated appropriately. Then, in section 3.3, the work is focused on the MTS synthesis by means of subwavelength metallic patches printed on top of a grounded substrate. For this purpose, the spatial and frequency dispersion analysis of different pixels is carried out in section 3.3.1. Besides, the procedure followed to calculate the equivalent surface impedance maps related with several isotropic and anisotropic pixels is detailed in section 3.3.2.

upna
Universidad Pública de Navarra
Nafarroako Unibertsitate Publikoa

3.2 Characterization and classification of the metasurfaces

The MTSs are constituted by a single dense layer of sub wavelength metallic patches, also called pixels, printed over a thin lossless dielectric substrate characterized by its thickness (h) and relative permittivity (ε_r) (see Fig. 1.3(b)) [26–35]. The wave front path of the SW excited on the structure is controlled by means of an equivalent homogeneous surface impedance. Thus, the sub wavelength elements embedded in a uniform periodic arrangement over the grounded dielectric substrate, can vary in their size and rotation at each position of the surface following the characterization of the equivalent homogeneous surface impedance.

When the MTS is uniform, the shape of the pixels composing the surface is repeated all over the structure and it is described by means of a constant equivalent surface reactance. Nevertheless, in some cases it is necessary to introduce a modulation on the characteristic surface impedance and it is synthesized by pixels that differ on size with respect to their adjacent elements (see Fig. 3.1).

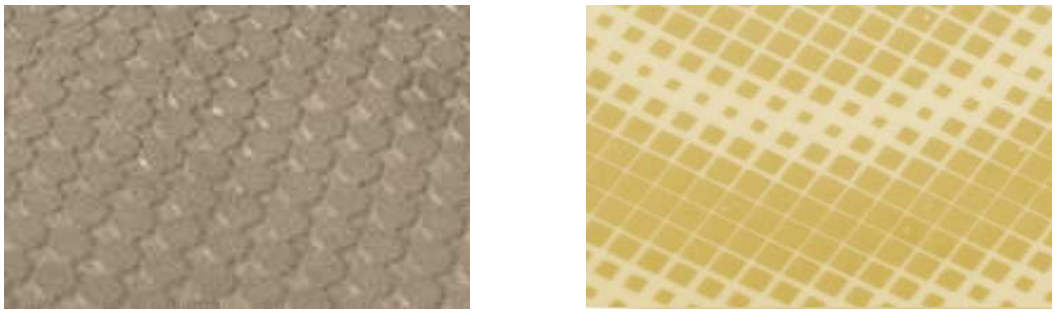

(a) (b)

Fig. 3.1. (a) Isotropic uniform MTS [56]. (b) Isotropic modulated MTS [56].

The isotropic or anisotropic nature of the MTSs is described by means of a scalar or tensorial equivalent surface impedance, respectively [26–35]. When the impedance characterizing the MTS is defined by a scalar quantity dependent only on frequency $Z(\omega)$, it can be synthesized with symmetric patches in all the directions over the surface. However, when the pixels placed at different positions over the MTS contain additional variation on their shape (see Fig. 3.2), the surface reactance is defined by a tensor $\bar{\bar{\mathbf{Z}}}(\omega, \mathbf{k_t})$ [64–72].

Besides, the characteristic impedance related with a MTS can be classified as penetrable or impenetrable. When it considers the contribution of both the patch cladding and the grounded slab, the surface characteristic impedance is called impenetrable or opaque ($\bar{\bar{Z}}$). On the other hand, when the impedance includes only the contribution of the patch cladding sheet, the impedance is called penetrable (or transparent) and it is denoted as $\bar{\bar{Z}}_S$. In both cases, the boundary conditions can be analyzed by equivalent transmission lines [26–35].

upna
Universidad Pública de Navarra
Nafarroako Unibertsitate Publikoa

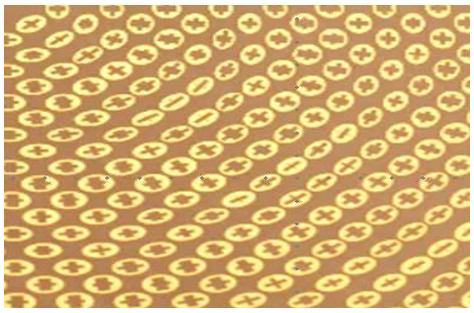

Fig. 3.2. Anisotropic modulated MTS [25]

.

In the following sections, it will be shown how the different characteristic surface impedances are related with the dispersion properties of the SWs propagating on the structure, enabling the guiding of the bounded mode or even the radiation of the field outside the configuration when a leaky wave (LW) is generated.

3.2.1 Uniform isotropic surface impedance

Fig. 3.3 depicts the canonical problem of the isotropic two-dimensional guiding structure, which enables the propagation of a bounded surface wave.

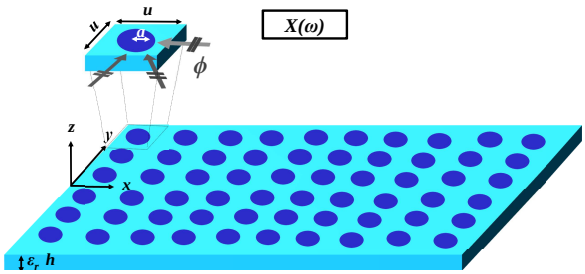

Fig. 3.3. Isotropic uniform MTS.

The uniform isotropic surface is composed by symmetric sub wavelength elements identical at each (x,y) position, printed over a grounded dielectric substrate characterized by its relative permittivity (ε_r) and thickness (h). The surface impedance is characterized by a frequency dependent scalar quantity $Z(\omega)$ [29]. When the unit cell period (u) is small in terms of SW wavelength ($u < \lambda_{sw}$), the homogenization condition is fulfilled and the dielectric and the metal can be considered without losses. Consequently, the surface impedance definition is given by a reactance $Z(\omega) = jX(\omega)$. The tangential electric $\mathbf{E}_t$ and the tangential magnetic $\mathbf{H}_t$ fields at (x,y) position of the air-Metasurface interface ($z = 0^+$) are related as:

$$\mathbf{E}_t \mid_{0^+} = jX(\omega) \cdot \hat{\mathbf{z}} \times \mathbf{H}_t \mid_{0^+} \tag{3.1}$$

upna
Universidad Pública de Navarra
Nafarroako Unibertsitate Publikoa

The mode propagating on the structure can be defined as pure transverse magnetic (TM) or transverse electric (TE) [73]. Fig. 3.4 illustrates the field components of each mode.

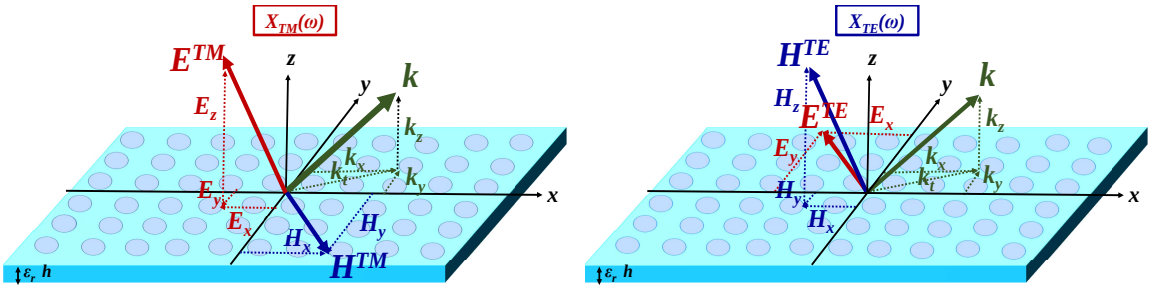

(a) (b)

Fig. 3.4. Surface waves field components: (a) TM, (b) TE.

Due to the periodic nature of the problem and based on the Floquet's theorem [52], it is possible to express the field quantities as a sum of an infinite number of space harmonics:

$$\mathbf{E}_t(x,y) = \sum_{n=-\infty}^{\infty} \mathbf{e}_n(z) e^{-j\mathbf{k}_{tn}\boldsymbol{\rho}} \tag{3.2}$$

A time harmonic dependence ($e^{j\omega t}$) is assumed and suppressed throughout. ρ is the radial position vector in cylindrical coordinates. Each space harmonic has a complex propagation wave number $\mathbf{k}_{tn}$, with different phase constants (β_{tn}) but idem attenuation constant (α):

$$\mathbf{k}_{tn} = k_{xn}\hat{x} + k_{yn}\hat{y} = (\beta_{tn} - j\alpha)\rho \tag{3.3}$$

A SW propagating on the structure, also called proper or slow wave [73–76], is characterized by a real propagation wave number, equal to its phase constant:

$$\mathbf{k}_{t0} = k_{t0}\rho \quad , \quad k_{t0} = \beta = \frac{2\pi}{\lambda_{sw}} \tag{3.4}$$

Moreover, $k_{x0} = \beta\cos\phi$ and $k_{y0} = \beta\sin\phi$ are related with the SW propagation angle, ϕ. The SW wavenumber is greater than the free-space one($k = 2\pi/\lambda$). Equivalently, its phase velocity is less than the speed of light c:

$$\beta > k \rightarrow \quad v = \frac{\omega}{\beta} \quad < \quad c = \frac{\omega}{k} = \frac{1}{\sqrt{\varepsilon_0\mu_0}} \tag{3.5}$$

where $\varepsilon_0 = 8.854187 \cdot 10^{-12} Fm^{-1}$ is the vacuum permittivity or electric constant and $\mu_0 = 4\pi \cdot 10^{-7} N/A^2$ is the vacuum permeability or magnetic constant. The group velocity is defined as:

upna
Universidad Pública de Navarra
Nafarroako Unibertsitate Publikoa

$$v_g = \frac{\partial \omega}{\partial \beta} \tag{3.6}$$

The real part of the n-index higher order harmonics wave vectors in (3.3) are related with the phase constant of the $n = 0$ harmonic (β) as:

$$\beta_{tn} = (\beta + \frac{2\pi n}{u}) \tag{3.7}$$

The wave equation (Eq. (3.8)) establishes the relation between the wavenumbers tangential to the surface (k_{tn}) and the components transverse to it (k_{zn}):

$$k_0^2 = k_{tn}^2 + k_{zn}^2 \tag{3.8}$$

Thus, the transverse wavenumber components can be rewritten as:

$$k_{zn} = \beta_{zn} - j\alpha_{zn} = \sqrt{k_0^2 - k_{tn}^2} \tag{3.9}$$

As the SW possesses a field completely bounded to the interface, the field components in z direction decay exponentially [73–76], thus:

$$\Im(k_{zn}) = -j\alpha_{zn} \quad , \quad \alpha_{zn} > 0 \tag{3.10}$$

3.2.2 Modulated isotropic surface impedance

The isotropic surface reactance of the MTS can be modulated following a given pattern [29, 52]. This modulation can be synthesized by varying the size of the adjacent circular subwavelength pixels inside a periodic cartesian lattice.

Under homogeneous condition assumption, the local equivalent reactance value is related with the reactance given by a periodic isotropic pixel with a fixed geometry and size. When the SW propagating on the structure interacts with the varying cladding pattern, the dispersion properties of the mode at each frequency are locally modified.

upna
Universidad Pública de Navarra
Nafarroako Unibertsitate Publikoa

Guiding the surface wave

Fig. 3.5 illustrates an example of an isotropic surface reactance modulated in $\hat{y}$, the direction transverse to the plane wave (PW) incidence:

$$Z(\omega, y) = jX(\omega, y) \tag{3.11}$$

The boundary conditions imposed by the lossless isotropic modulated MTS reactance on the ratio between the average tangential electric and magnetic field components are described as [36, 37]:

$$\mathbf{E}_t \mid_{0^+} = jX(\omega, y) \cdot \hat{\mathbf{z}} \times \mathbf{H}_t \mid_{0^+} \tag{3.12}$$

The structure is synthesized by sub wavelength circular patches embedded in an uniform rectangular lattice whose radii differ in $\hat{y}$.

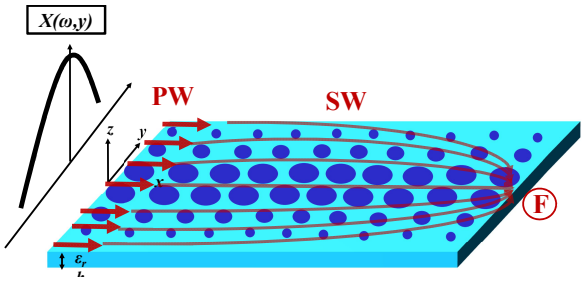

Fig. 3.5. Isotropic modulated MTS guiding a TM SW and focusing the field at F point[36, 37].

The surface reactance modulation affects locally the dispersion properties of the incident PW. The bigger pixels shown at the center of the structure (see Fig. 3.5), provide larger values of reactance and the TM SW phase constant increase. Nevertheless, the smaller pixels provide lower surface impedance values and the local β is decreased. Therefore, the effect of the overall modulated isotropic MTS results on the SW focused at one point (F) [36, 37].

Leaky wave generation

In some cases [52–59, 64–72], the isotropic modulated MTS is characterized by a reactance that follows a sinusoidal function in SW propagation direction (**x**):

$$\mathbf{E}_t \mid_{0^+} = jX_{ave}(\omega)\left(1 + m\sin\left(\frac{2\pi x}{d}\right)\right) \cdot \hat{\mathbf{z}} \times \mathbf{H}_t \mid_{0^+} \tag{3.13}$$

In this case the modulation is defined by three parameters: the normalized average surface reactance value $\eta_{ave} = X_{ave}/\zeta$ (where $\zeta = \mu_0/\varepsilon_0 = 120\pi$ is the free-space impedance), the modulation index m and the modulation periodicity d. In the example drawn in Fig. 3.6, all

upna
Universidad Pública de Navarra
Nafarroako Unibertsitate Publikoa

the parameters are considered constant all over the surface but depending on the application they can also vary [60].

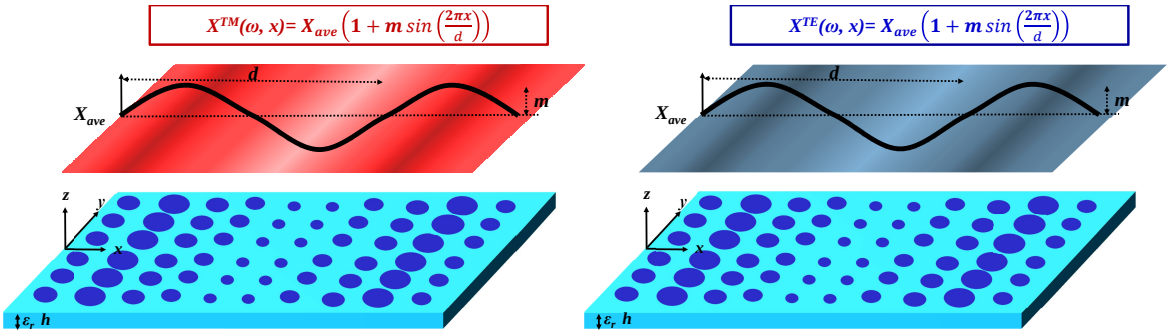

(a) (b)

Fig. 3.6. Isotropic modulated MTS characterized by a scalar surface reactance supporting a: (a) TM mode, (b) TE mode.

The sinusoidally modulated surface in Fig. 3.6 is synthesized varying in $\hat{x}$ the local dimension of the isotropic pixels inside the uniform periodic lattice (with period u). Under homogeneous surface assumption ($u < \lambda_{sw}$), it is possible to match the local reactance with the reactance provided by a certain periodic pixel geometry. When the SW bounded on the structure interacts with this surface, its wavenumber suffers a complex perturbation [52, 77]:

$$\beta \rightarrow k_{t0} = \beta + \Delta\beta - j\alpha \tag{3.14}$$

$\Delta\beta$ describes the phase constant shift due to the surface reactance modulation and α denotes the attenuation constant. The characterization of the propagation characteristics of the waves can be analysed using Oliner's method [52, 77], extended in appendix C. The wavenumbers of the higher order Floquet modes are then written as:

$$k_{tn} = \beta_{tn} - j\alpha = \beta + \Delta\beta + \frac{2\pi n}{d} - j\alpha \quad n = \pm 1, \pm 2... \tag{3.15}$$

As shown in the k vs. β diagram in Fig. 3.7 [78], the negative indexed modes that satisfy the radiation condition ($|\Re(k_{tn})| < k$) enter to the visible region [52]:

$$|\,\beta_{tn}\,| = |\,\beta + \Delta\beta + \frac{2\pi n}{d}\,| < k \rightarrow \quad v = \frac{\omega}{\beta_{tn}} > c = \frac{\omega}{k} = \frac{1}{\sqrt{\varepsilon_0\mu_0}} \tag{3.16}$$

Consequently, a leaky wave (LW), also called improper or fast wave, is generated radiating the field outside the structure (see Fig. 3.8). The transverse components of the field growing exponentially out of the interface are characterized as:

upna
Universidad Pública de Navarra
Nafarroako Unibertsitate Publikoa

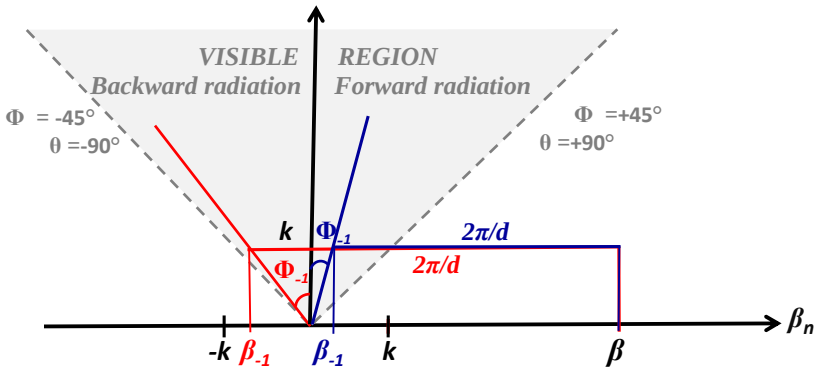

Fig. 3.7. k vs. β diagram illustrating Backward (BW) and Forward (FW) radiation.

$$\Im(k_{zn}) = -j\alpha_{zn} \quad , \quad \alpha_{zn} < 0 \tag{3.17}$$

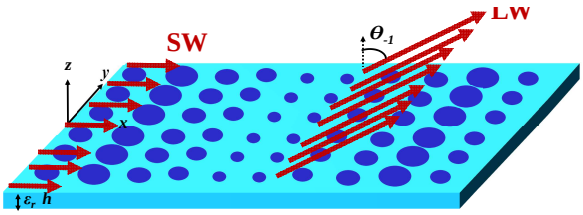

Fig. 3.8. Isotropic sinusoidally modulated isotropic metasurface. A forward leaky wave is generated radiating the field outside the structure towards θ_{-1} direction.

Eq. (3.18) establishes the $\Delta\beta$ and d values that lead to the radiation of the $n-indexed$ higher order space harmonics towards θ_n angles:

$$\beta_{tn} = \beta + \Delta\beta + \frac{2\pi n}{d} = k\sin\theta_n \tag{3.18}$$

θ_n can be related with the Φ_n angle in the k vs. β diagram in Fig. 3.7 as: $\theta_n = \arcsin(\tan(\Phi_n))$. In the examples found in literature [52–59, 64–72], uni-modal regimen is desired and only the $n=-1$ harmonic contributes to the radiation ($|\beta + \Delta\beta + \frac{2\pi n}{d}| > k$ for $n \neq -1$). Under this assumption and considering the phase constant variation effect due to the modulation as $\beta' = \beta + \Delta\beta = 2\pi/\lambda'_{sw}$, the period d can be extracted as:

$$d = \frac{\lambda}{(\frac{\lambda}{\lambda'_{sw}}) - \sin(\theta_{-1})} \tag{3.19}$$

It can be concluded from Eq. (3.19) that the boresight radiation condition ($\theta_{-1} = 0°$) is fulfilled when $d = \lambda'_{sw}$. When the modulation period is larger ($d > \lambda'_{sw}$), forward radiation

upna
Universidad Pública de Navarra
Nafarroako Unibertsitate Publikoa

towards $\mid \theta_{-1} \mid > 0^\circ$ is obtained (see Fig. 3.7). In this case, the beam is directed in the same sense as the SW propagation direction over the structure (the phase and group velocities are in the same direction). On the contrary, when $d < \lambda_{sw}^{'}$, a single beam can be radiated in the opposite sense with respect to the excited SW, i.e., with backward radiation (the phase and group velocities are in opposite directions) [73–76].

3.2.3 Anisotropic modulated surface impedance

The interaction of the excited surface wave with a modulated anisotropic surface modifies locally the dispersion properties of the mode at each frequency, in the same way that in the case of the isotropic modulated configuration described in Fig. 3.8. However, the difference in relation with the isotropic case is that in the anisotropic configuration, the dispersion characterization of the supported mode (which is not pure TM nor pure TE but a hybrid mode) also depends on the SW wavevector ($\mathbf{k_t}$). Depending on the propagation direction of the hybrid mode (ϕ), the anisotropic modulated surface reactance imposes boundary conditions on the average tangential fields which are described by a tensor [26–35, 64–72]:

$$\mathbf{E}_t \mid_{0^+} = \bar{\bar{\mathbf{Z}}}(\omega, x, \mathbf{k_t}) \cdot \hat{\mathbf{z}} \times \mathbf{H}_t \mid_{0^+} \tag{3.20}$$

$$\bar{\bar{\mathbf{Z}}}(\omega, x, \mathbf{k_t}) = \begin{bmatrix} Z_{ee} & Z_{eh} \\ Z_{he} & Z_{hh} \end{bmatrix} \tag{3.21}$$

$e-$ sub-index denotes the TM component whose electric field is oriented along $\hat{\mathbf{k}}_\mathbf{t}$ and $h-$ sub-index denotes the TE component whose electric field is oriented along $\hat{\mathbf{k}}_t^{\perp}$ [38]. In absence of losses the impedance tensor $\bar{\bar{\mathbf{Z}}}$ is anti-Hermitian ($\bar{\bar{\mathbf{Z}}} = -\bar{\bar{\mathbf{Z}}}^{T*} \rightarrow X_{eh} = X_{he}$, where $T*$ denotes conjugate transpose operation). This condition is fulfilled by a real symmetric tensor $\bar{\bar{\mathbf{Z}}} = j\bar{\bar{\mathbf{X}}}$, characterized with real eigenvalues and orthogonal eigenvectors. The representation in the basis of the unit wavevector $\hat{\mathbf{k}}_\mathbf{t}$ is [38]:

$$\bar{\bar{\mathbf{X}}} = \bar{\bar{X}}_{ee}\hat{\mathbf{k}}_\mathbf{t}\hat{\mathbf{k}}_\mathbf{t} + \bar{\bar{X}}_{hh}\hat{\mathbf{k}}_t^{\perp}\hat{\mathbf{k}}_t^{\perp} + \bar{\bar{X}}_{eh}(\hat{\mathbf{k}}_t^{\perp}\hat{\mathbf{k}}_t + \hat{\mathbf{k}}_t\hat{\mathbf{k}}_t^{\perp}) \tag{3.22}$$

Fig. 3.9 shows an anisotropic sinusoidally modulated MTS which is composed by pixels which size and variation vary with respect to the SW propagation direction. The inset in the figure shows details of the employed metallic elliptical shaped element, which is characterized by three parameters: the minor axis (e_a) and major axis (e_b) of the ellipse and the patch rotation inside the cell (ψ). Under homogenization assumption, each local value of the modulated surface impedance is mapped with a certain sub wavelength element, which is

upna
Universidad Pública de Navarra
Nafarroako Unibertsitate Publikoa

considered embedded in a periodic arrangement. Furthermore, the anisotropy of the system is controlled by means of the relation between the rotation ψ and SW propagation angle ϕ. In this way, the anisotropic MTSs enable not only the adjustment of the guiding or radiation properties of the field, but also the control of the radiated field polarization.

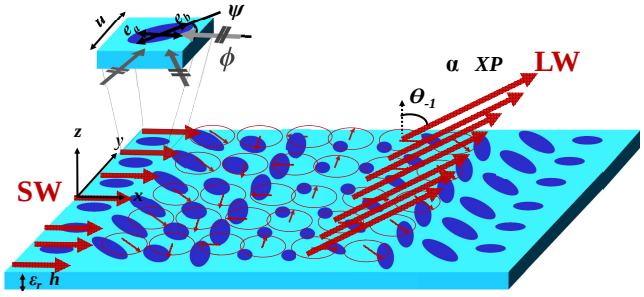

Fig. 3.9. Anisotropic modulated sinusoidal MTS.

A sinusoidal modulation applied to the tensor components of the anisotropic metasurface in Eq. (3.21) allows to radiate the field outside the structure towards a defined direction. Besides, circular polarization purity of the radiated field can be guaranteed taking advantage of the anisotropic nature of the surface[26–35, 64–72].

3.2.4 Opaque vs. transparent impedance

It has been explained in previous sections how the metasurfaces can be modelled by means of an isotropic (Sect 3.2.1) or anisotropic (Sect 3.2.3) surface impedance, which is related with the bounded SW wavevector $\mathbf{k_t}$. In the isotropic case the electric and magnetic average fields at the interface between the air and the MTS are related trough a scalar surface impedance Z (Eq. (3.12)), while for the anisotropic MTS the it is described through a tensor $\bar{\bar{\mathbf{Z}}}$ (Eq. (3.21)). In all the cases, the surface impedance definition, also called impenetrable or opaque impedance in the literature [38], takes into account the contributions of the patch cladding and the grounded slab. The boundary conditions at the MTS can be analysed by means of an equivalent transmission line associated to TM or TE modes [79].

Fig.3.10(a) and Fig.3.10(b) show the equivalent transmission lines related to a MTS characterized by a isotropic impenetrable impedance which supports the propagation of a pure TM and a pure TE mode, respectively. In Eq. (3.23), $Z_0^{TX=TM,TE}$ describes the free-space impedance for the TM or TE modes:

$$\begin{aligned} Z_0^{TM} &= jX_0^{TM} = \zeta \frac{k_{z0}}{k} = \frac{k_{z0}}{\omega\varepsilon_0} \\ Z_0^{TE} &= jX_0^{TE} = \zeta \frac{k}{k_{z0}} = \frac{\omega\mu_0}{k_{z0}} \end{aligned} \tag{3.23}$$

upna
Universidad Pública de Navarra
Nafarroako Unibertsitate Publikoa

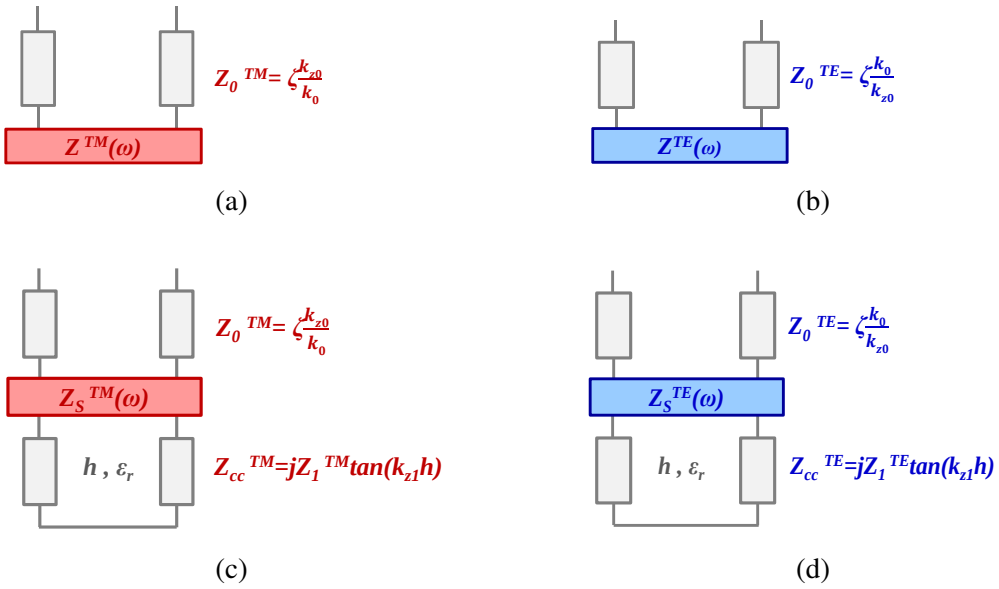

Fig. 3.10. Equivalent transmission lines of an isotropic MTS characterized by an impenetrable impedance supporting a: (a) TM mode, (b) TE mode ; and characterized by a penetrable impedance supporting a: (c) TM mode, (d) TE mode [79].

ζ and k are the free space impedance and wavenumber respectively, the transverse wavenumber k_{z0} fulfills Eq. (3.10) and the wavenumber tangential to the surface k_t agrees with Eq. (3.4). It can be concluded that $X_0^{TM} X_0^{TE} = -\zeta^2$.

Applying the Transverse Resonance Equation (TRE) [26–35, 64–72] it is possible to relate the free-space impedances $Z_0^{TX=TM,TE}$ with the escalar isotropic surface reactance related to each mode:

$$Z^{TX} + Z_0^{TX} = 0 \quad TX = TM, TE \tag{3.24}$$

Hence,

$$\begin{aligned} jX^{TM} - j\frac{\sqrt{k_t^2 - k^2}}{\omega\varepsilon_0} &= 0 \\ jX^{TE} + j\frac{\omega\mu_0}{\sqrt{k_t^2 - k^2}} &= 0 \end{aligned} \tag{3.25}$$

where $X^{TM} > 0$ is inductive and $X^{TE} < 0$ is capacitive. From Eq. (3.25) it is concluded that:

upna
Universidad Pública de Navarra
Nafarroako Unibertsitate Publikoa

$$k_t = k\sqrt{1+\eta_{TM}^2}$$
$$k_t = k\sqrt{1+\left(1/\eta_{TE}\right)^2} \tag{3.26}$$

where $\eta_{TX} = X^{TX}/\zeta \quad TX = TM,TE$ are the normalized surface impedance values for TM and TE modes.

The previous analysis deals with the opaque impedance characterization for isotropic surfaces, which as aforementioned, takes into account the contribution of the patch cladding and the contribution of the grounded substrate. Nevertheless, it is also possible to analyze these structures taking into account only the metallic patch cladding contribution [64–72]. In this case, the MTS is characterized by means of a sheet impedance, also called transparent or penetrable impedance. The equivalent transmission lines of a penetrable isotropic MTS where a pure TM and a pure TE can be supported are depicted in Fig. 3.10(c) and Fig. 3.10(d), respectively. For each case, the MTS is characterized by means of the correspondent sheet impedance $Z_S^{TX=TM,TE}$ and the expression (3.1) is accordingly rewritten as:

$$\mathbf{E}_t\mid_{0^+} = Z_S(\omega,\boldsymbol{\rho})\cdot\mathbf{J}_S\mid_{0^+} \tag{3.27}$$

where $Z^{TX} = Z_S^{TX} \parallel Z_{cc}^{TX} \quad TX = TM,TE$. This model considers for each TM or TE mode the patch cladding contribution separately from the grounded slab contribution. The latter is described by a transmission line with length h terminated in a short circuit:

$$Z_{cc}^{TX} = jZ_1^{TX}\tan k_{z1}h \quad TX = TM,TE \tag{3.28}$$

$Z_1^{TX=TM,TE}$ is the equivalent impedance of the short circuit for each mode: $Z_1^{TM} = Z_1\frac{k_{z1}}{k_1}$ and $Z_1^{TE} = Z_1\frac{k_1}{k_{z1}}$. In the dielectric $Z_1 = \zeta/\sqrt{\varepsilon_r}$ is the impedance, $k_1 = k\sqrt{\varepsilon_r}$ is the tangential wavenumber and $k_{z1} = \sqrt{k_1^2 - k_t^2}$ is the transverse component.

Therefore, dispersion equation (3.24) can be rewritten as:

$$\frac{1}{X_S^{TX}} + \frac{1}{Z_1^{TX}}cot(k_{z1}h) - \frac{1}{X^{TX}} = 0 \quad TX = TM,TE \tag{3.29}$$

The first term in Eq. (3.29) corresponds to the patch cladding contribution, the second term is related with the ground plane contribution and the third one corresponds to the SW mode contribution [62].

The equivalent transmission line model can be also employed to analyze the anisotropic MTSs. When a mode is excited in an anisotropic MTS, it generally suffers hybridization and

upna
Universidad Pública de Navarra
Nafarroako Unibertsitate Publikoa

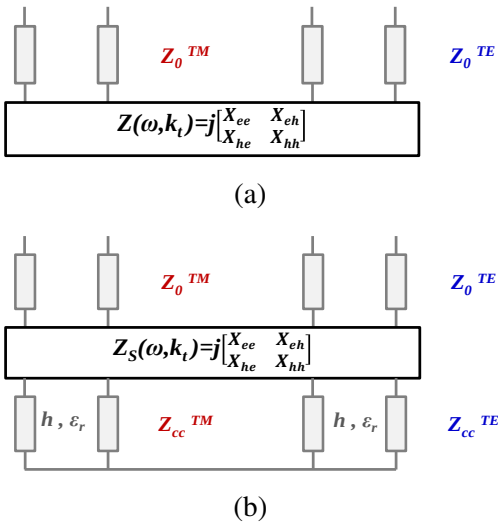

Fig. 3.11. Equivalent transmission lines of the anisotropic MTS characterized by a (a) opaque impedance tensor and by a (b) transparent impedance tensor.

consequently there is coupling between the electric field components. In order to describe this effect, two transmission lines are needed on the equivalent network (see Fig. 3.11(a)).

The dispersion equation can be written taking into account the opaque surface impedance tensor as:

$$\det[\bar{\bar{\mathbf{Z}}}(\omega,\mathbf{k_t})+\bar{\bar{\mathbf{Z}}}_0(\omega,\mathbf{k_t})]=0 \tag{3.30}$$

where

$$\bar{\bar{\mathbf{Z}}}=\bar{\bar{\mathbf{Z}}}_S \parallel \bar{\bar{\mathbf{Z}}}_{cc} \tag{3.31}$$

When the transparent anisotropic MTS is under study (Fig.3.11(b)), the average fields relation is written as:

$$\mathbf{E}_t\mid_{0^+}=\bar{\bar{\mathbf{Z}}}_S(\omega,\boldsymbol{\rho})\cdot\mathbf{J}_S\mid_{0^+} \tag{3.32}$$

And the transparent anisotropic impedance tensor is:

$$\bar{\bar{\mathbf{Z}}}_S(\omega,\boldsymbol{\rho},\mathbf{k_t})=\begin{bmatrix}Z_{See} & Z_{Seh}\\ Z_{She} & Z_{Shh}\end{bmatrix}=\begin{bmatrix}jX_{See} & Z_{Seh}\\ Z_{Seh} & jX_{Shh}\end{bmatrix} \tag{3.33}$$

upna
Universidad Pública de Navarra
Nafarroako Unibertsitate Publikoa

3.3 Synthesis of the metasurfaces

For the synthesis of the MTSs, it is necessary to control the wavefront propagation of the supported SW. For this purpose, the dispersion equation of the dominant mode is locally determined at each point of the structure, related with a theoretical local surface impedance value.

There are different techniques to analyze the SW dispersion properties. For instance, the eigen mode solvers of the commercial simulators such as CST [80] or ANSYS HFSS [70] allow to carry out full wave analysis of any pixel geometry. The main disadvantage of these solvers lie in the required time and resources. For each patch geometry parameterization, several phase shift variations related with the impinging modes must be studied and the mesh of the problem must be sufficiently fine to ensure the convergence of the provided results. Besides, the determination of the TM, TE or hybrid nature of the propagating modes on the structure is not always straightforward.

An alternative rigorous approach to obtain analytically the dispersion properties of a MTS consisting on elliptical patches printed over a grounded slab was presented for the first time by Maci et al. in [21, 81, 82]. In this work the analytic expressions of the patch currents are derived and the reduced spectral method of moments (MoM) matrix is extracted. The calculated MoM matrix is then related with the MTS equivalent surface impedance tensor and frequency-wavenumber curves are derived. Mencagli et al. [61–63] presented closed-form expressions to approximate the frequency dispersion characteristics of the TM mode propagating on isotropic or anisotropic MTSs.

The proposed expressions simplifies the procedure. The solution in low frequency regime can be determined based only in the dielectric properties (ε_r and h) and a quasi-static capacitance. The quasi-static capacitance can be efficiently extrapolated from a single run of the eigen solver provided by commercial simulators. Besides, when the studied pixel geometries are simple (such as circular shaped ones) the procedure is extremely fast because the system can be characterized completely using analytic expressions [83–85].

The dispersion properties of several isotropic and anisotropic pixels obtained from the full wave analysis using the commertial ANSYS HFSS simulator are shown in section 3.3.1. In addition, the comparison of the same patches analyzed combining a single run of the eigenmode solver with the closed-form expressions presented in [61–63] have been included in the appendix A.

Based on the dispersion information, the equivalent surface impedance maps are calculated in section 3.3.2, following the procedure presented by Martini et al. in [38]. Another method presented by Patel et al. [64–69] avoids the use of the eigen mode solver and extracts the equivalent sheet impedance from the scattering matrix information of two plane waves

upna
Universidad Pública de Navarra
Nafarroako Unibertsitate Publikoa

impinging the MTS in normal direction. For completeness, a comparison between the results obtained applying both methods have been included in the appendix B.

3.3.1 Full wave spatial and frequency dispersion analysis

As extended in section 3.2, the SWs propagating on a metasurface are characterized by their wave number. Frequency and spatial dispersion properties of these modes can be analysed by means of k vs. β diagrams [78]. The phase constant and group velocity are defined as the location of a point on the correspondent diagram curve (relating the β at each frequency) and its slope, respectively. To characterize the spatial response of an anisotropic pixel, analysis has to be performed for several SW incidence angles (ϕ).

Eigen mode solvers available in comertial simulators such as CST [80] or ANSYS HFSS allow to calculate the eigenfrequency ω for a given phase delay (Δph) imposed across the unit cell with period u. Taking into account the phase constant definition as $\beta = \Delta ph/u$, a phase delay sweep can be performed to find the $\omega(\beta)$ relation.

Full wave dispersion analysis of different isotropic and anisotropic shaped patches printed over a grounded slab with $\varepsilon_r = 10.2$ and $h = 1.27mm$ have been carried out. Details of the studied geometries are depicted in Fig. 3.12. In all the cases, the periodic unit cell dimension is $u = 3.14mm$. The isotropic circular patch is defined by a normalized radius (a/u) (Fig. 3.12(a)). The anisotropic elliptical shaped patch shown in Fig. 3.12(b) is described with a normalized major axis (e_b/u) and a normalized radius (e_a/e_b). Besides, other anisotropic pixels are composed by circular patches with different apertures in the center: a groove with a normalized width (w/u) (Fig. 3.12(c)); a slot with normalized width (w/u) and length (b/a) (Fig. 3.12(d)); and a cross-shaped aperture characterized also with normalized width (w/u) and length (b/a) (Fig. 3.12(e)). Frequency dispersion curves of TM and TE modes for three different incidence angles: $\phi = 0°$ (red), $\phi = 22.5°$ (green) and $\phi = 90°$ (blue) are shown in Fig. 3.13.

upna
Universidad Pública de Navarra
Nafarroako Unibertsitate Publikoa

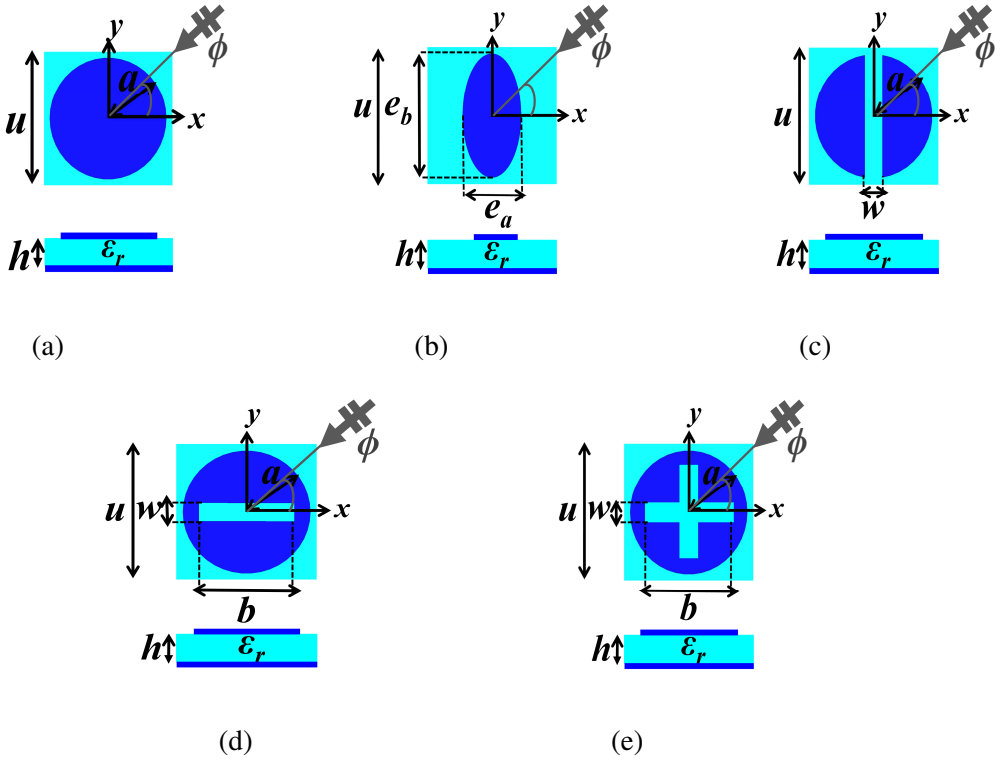

Fig. 3.12. Analyzed patch geometries: (a) circular patch characterized by normalized radius (a/u); (b) elliptical patch characterized by normalized major axis (e_b/u) and axial ratio (e_a/e_b); and circular patches with different apertures in the center: (c) a groove aperture with normalized width (w/u); (d) a slot aperture characterized by normalized width (w/u) and length (b/a); and (e) a cross-shaped aperture characterized by normalized width (w/u) and length (b/a). Dielectric substrate with relative permitivitty ε_r and thickness h. $\phi(^\circ)$ is the SW propagation angle.

upna
Universidad Pública de Navarra
Nafarroako Unibertsitate Publikoa

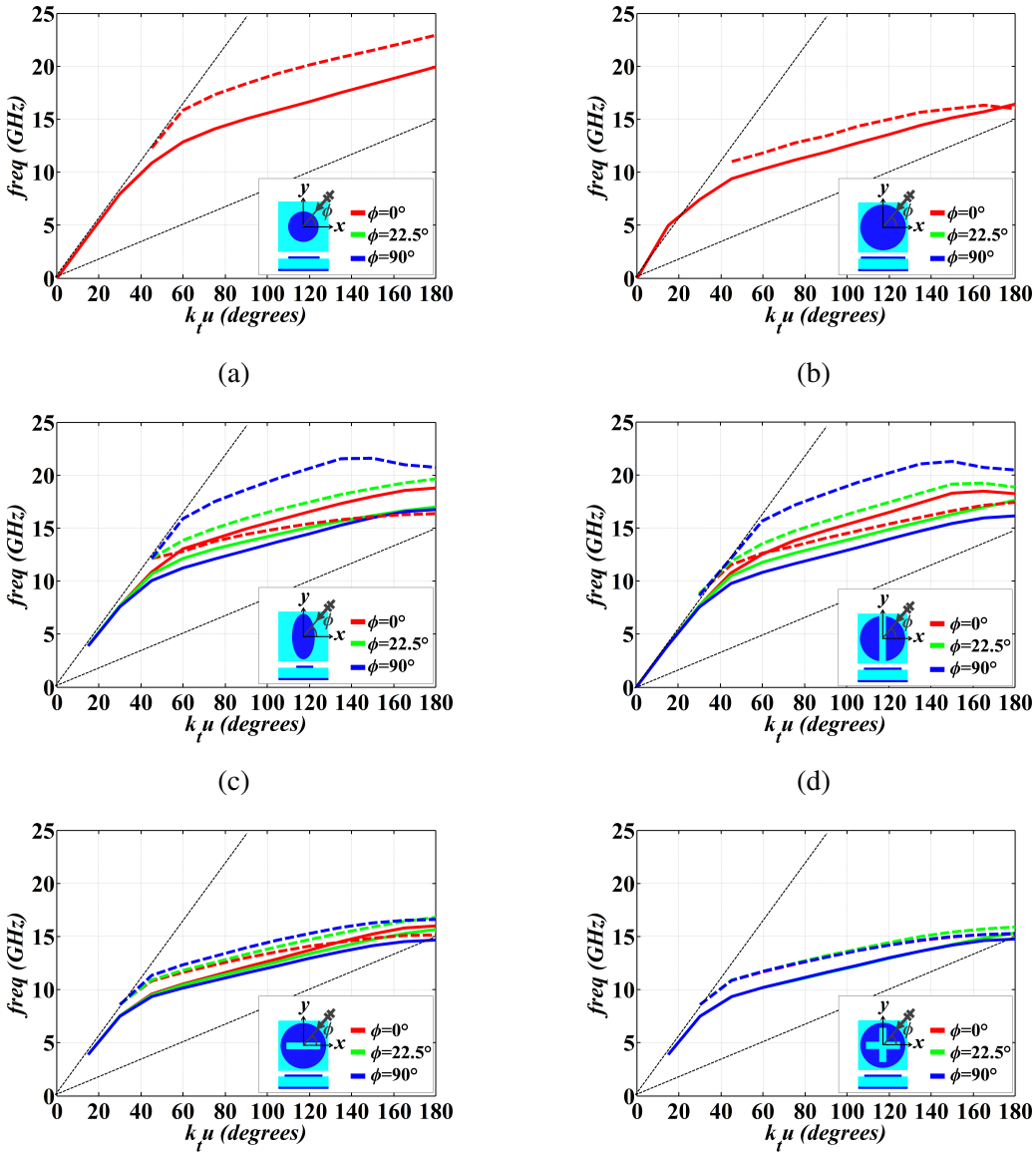

Fig. 3.13. Frequency dispersion curves of TM (continuous lines) and TE (dashed lines) modes for different incidence angles ($\phi = 0°$ (red), $\phi = 22.5°$ (green) and $\phi = 90°$ (blue)) and patch geometries: circular patch with a normalized radius of (a) $a/u = 0.6$ and (b) $a/u = 0.9$; (c) elliptical patch with normalized major axis $e_b/u = 0.9$ and axial ratio $e_a/e_b = 0.6$; and circular patches with different apertures in the center: (d) a groove characterized by normalized width $w/u = 0.3$; (e) a slot with normalized width $w/u = 0.3$ and length $b/a = 0.75$; and (f) a cross-shaped aperture with normalized width $w/u = 0.3$ and length $b/a = 0.75$. $u = 3.14mm$, $\varepsilon_r = 10.2$ and $h = 1.27mm$ for all the configurations.

upna
Universidad Pública de Navarra
Nafarroako Unibertsitate Publikoa

The curves corresponding to the isotropic circular pixels in Fig. 3.13 show that as expected, the wavenumber does not depend on the SW incidence angle ($k_t(\phi) = k_t$). Comparing Fig. 3.13(b) with Fig. 3.13(a) it can be seen that the modes propagating on a structure with electrically bigger metallic patches are characterized by larger k_t values at a given frequency. Therefore, suffered frequency dispersion is steeper. Unlike the TM mode, the TE mode has a cut off frequency and it remains inside the visible region below this value. When the metallic patch size decreases, the cut off frequency of the TE mode increases and the system guarantees unimodal regime.

The other analyzed pixels in Fig. 3.13 show some variation on their geometry and consequently, anisotropic response is shown ($k_t(\phi)$). Comparing Fig. 3.13(c) with Fig. 3.13(b), where the only geometric difference is given by the narrowing of the metallic patch in x-axis, it can be seen that the TM frequency dispersion curve is idem for $\phi = 90^\circ$ while the mode phase velocity is increased trough $\phi = 0^\circ$. On the contrary, Fig. 3.13(c) shows that the wavelength of the supported TE mode is increased when it impinges the elliptical patch towards $\phi = 90^\circ$. Consequently, it can be concluded that both the spatial and frequency dispersion properties of the pixel differ depending on the nature of the supported mode: the TE mode is more frequency and spatially dispersive than the TM as the effect of patch variation or the SW impinging angle is more important.

However, it is possible to obtain similar dispersion properties with different patch geometries. For instance, the circular pixel with a groove oriented towards y-axis in Fig. 3.13(d) shows similar dispersion characteristics than the elliptical pixel with the major axis towards y-axis and characterized by a small ratio shown in Fig. 3.13(c). Moreover, the circular patch with the slot oriented towards x-axis shown in Fig. 3.13(e) show similarities with an ellipse with larger ratio. Due to the symmetry of the circular pixel with the cross-shaped aperture in Fig. 3.13(f), it does not show spatial dispersion.

For completeness, in the appendix A, the full wave frequency dispersion results for TM and TE modes have been compared with the quasi-analytical solutions obtained for the same pixel geometries employing the alternative method developed in [61–63].

The isofrequency curves are also used to show the spatial dispersion characteristics of pixels. In Fig. 3.14 the isofrequency dispersion curves of TM (left column) and TE (right column) modes supported by isotropic pixels characterized by different radii and dielectric properties are shown.

upna
Universidad Pública de Navarra
Nafarroako Unibertsitate Publikoa

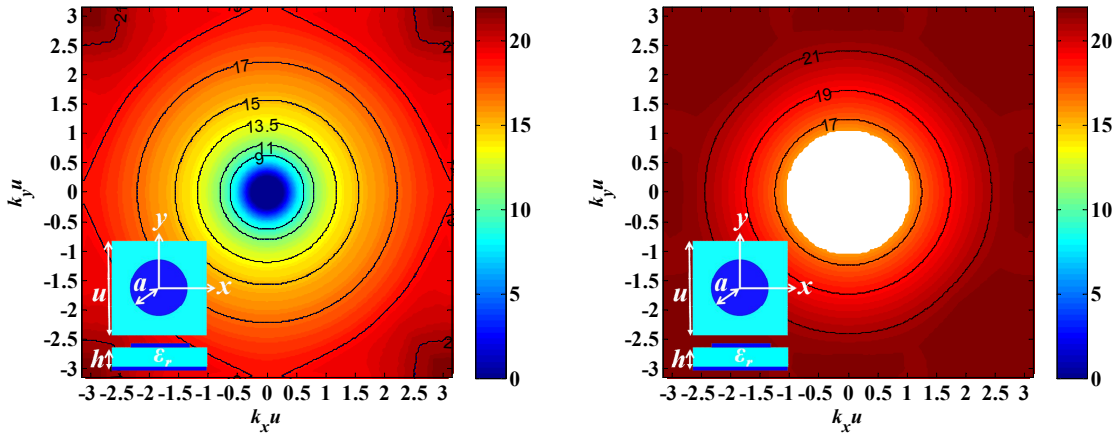

upna
Universidad Pública de Navarra
Nafarroako Unibertsitate Publikoa

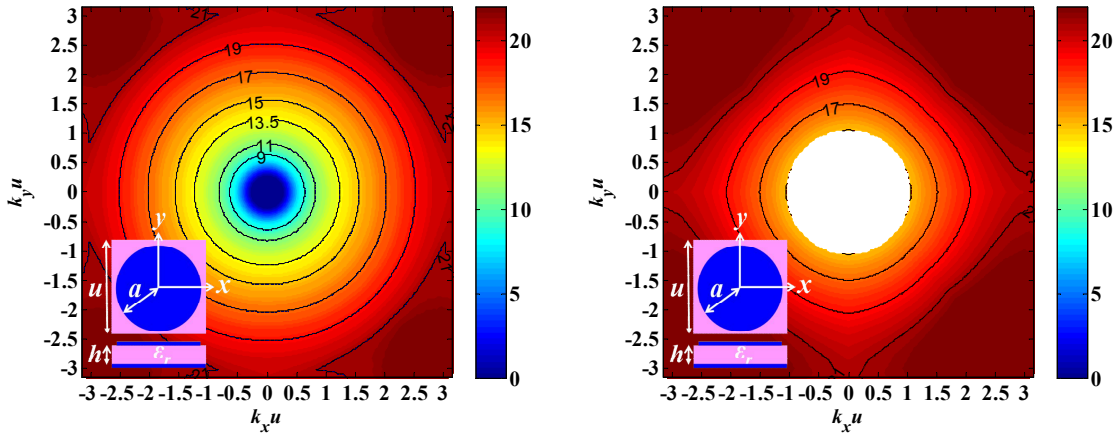

(g) (h)

Fig. 3.14. TM (left) and TE (right) isofrequency curves of circular patches ($u = 3.14mm$) with different radii and dielectric properties. Dielectric with $\varepsilon_r = 10.2$ and $h/u = 0.4$ and radii: (a) $a/u = 0.6$ and (b) $a/u = 0.9$. Radius $a/u = 0.9$ and dielectric with: (c) $\varepsilon_r = 10.2$, $h/u = 0.64$ and (d) $\varepsilon_r = 6.15$, $h/u = 0.4$.

Fig. 3.14 shows that there is no spatial dispersion ($k_t(\phi) = k_t$). It is possible to see in Fig. 3.14(e)-Fig. 3.14(f) that when h is increased, the effective gap between adjacent cells is smaller and the overall TM and TE modes behavior correspond to a electrically larger circular patch with slower phase velocity and lower cut-off frequency of TE mode. Moreover, Fig. 3.14(g)-3.14(h) show that when ε_r is decreased, the pixel behaviour agrees with the electrically smaller patch geometry in Fig. 3.14(a)-3.14(b). It can be concluded from these figures that introducing a modification on the pixel geometry (e.g. increasing the effective size of the patch), frequency and spatial dispersion properties of the TE and TM modes may match for certain frequencies higher than cut-off.

Fig. 3.15 depicts the spatial and frequency dispersion characteristics of the anisotropic pixels composed by elliptical patches. Moreover, Fig. 3.16 illustrates the isofrequency curves related with different anisotropic patch geometries: a circular patch with a cut, a groove or a cross-shaped aperture in the center.

It can be seen at Fig. 3.15 that, at low frequencies close to the visible region, the anisotropic elliptical pixels behave as isotropic patches. Nevertheless, when the frequency increases, the anisotropy of the geometry affects and the dispersion curves show dependency on the propagation direction of the modes: the TM mode wavenumber is larger for the propagation angles within major axis of the elliptical metallic patch and the same occurs for the transverse direction for the TE case. While the TM isofrequency data create elliptical-shaped curves, the TE mode shows stronger spatial dispersion drawing distorted eye-shaped elliptical curves within frequencies outside the visible region. When the frequency is

upna
Universidad Pública de Navarra
Nafarroako Unibertsitate Publikoa

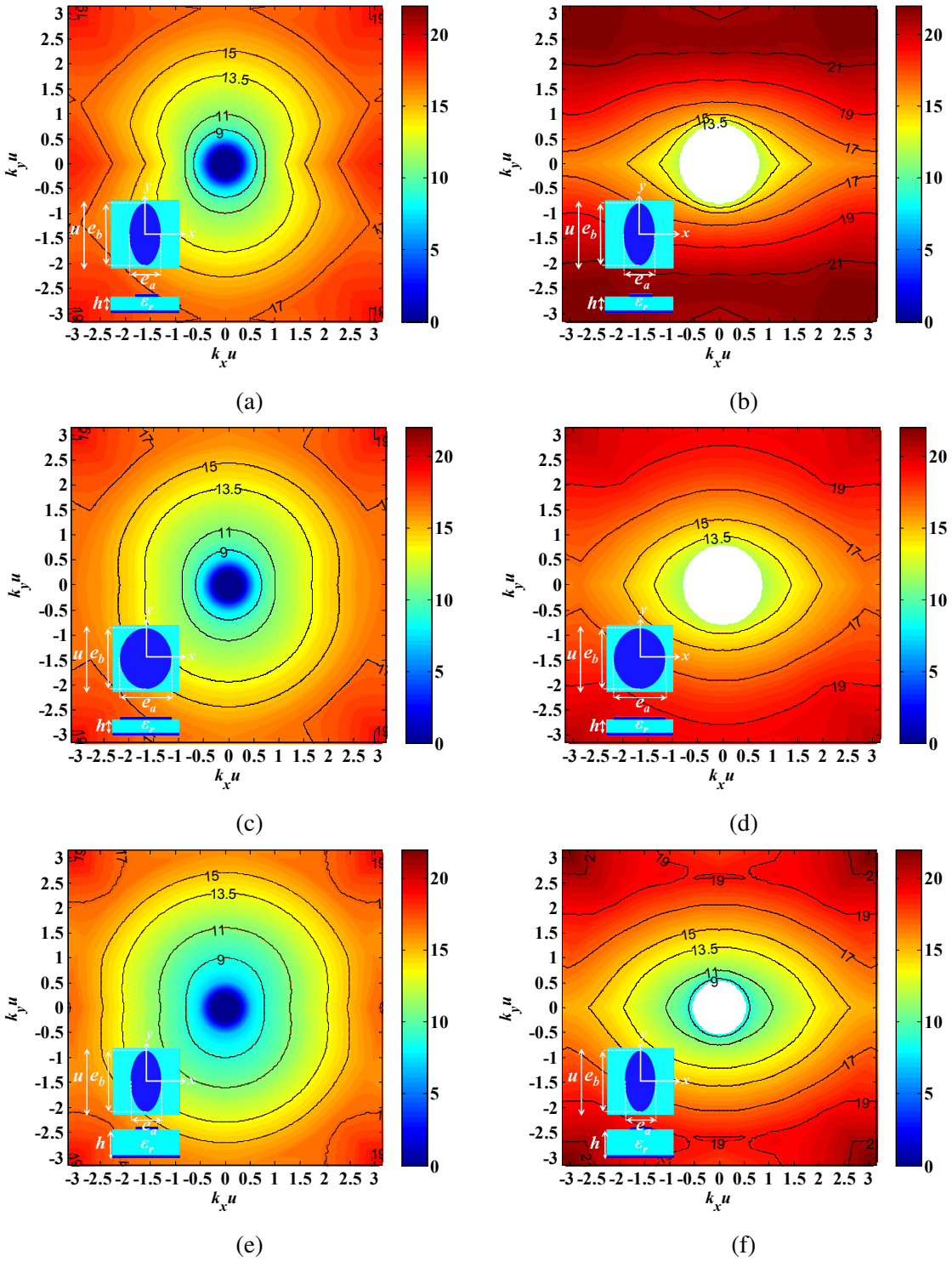

Fig. 3.15. TM (left) and TE (right) modes isofrequency curves of anisotropic elliptical shaped patches with different ratios (e_a/e_b) and substrate thickness (h): (a),(b) $e_a/e_b = 0.6$, $h = 1.27mm$; (c),(d) $e_a/e_b = 0.9$, $h = 1.27mm$; and (e),(f) $e_a/e_b = 0.6$, $h = 2mm$. For all the cases, $u = 3.14mm$, $e_b/u = 0.9$ and $\varepsilon_r = 10.2$.

upna
Universidad Pública de Navarra
Nafarroako Unibertsitate Publikoa

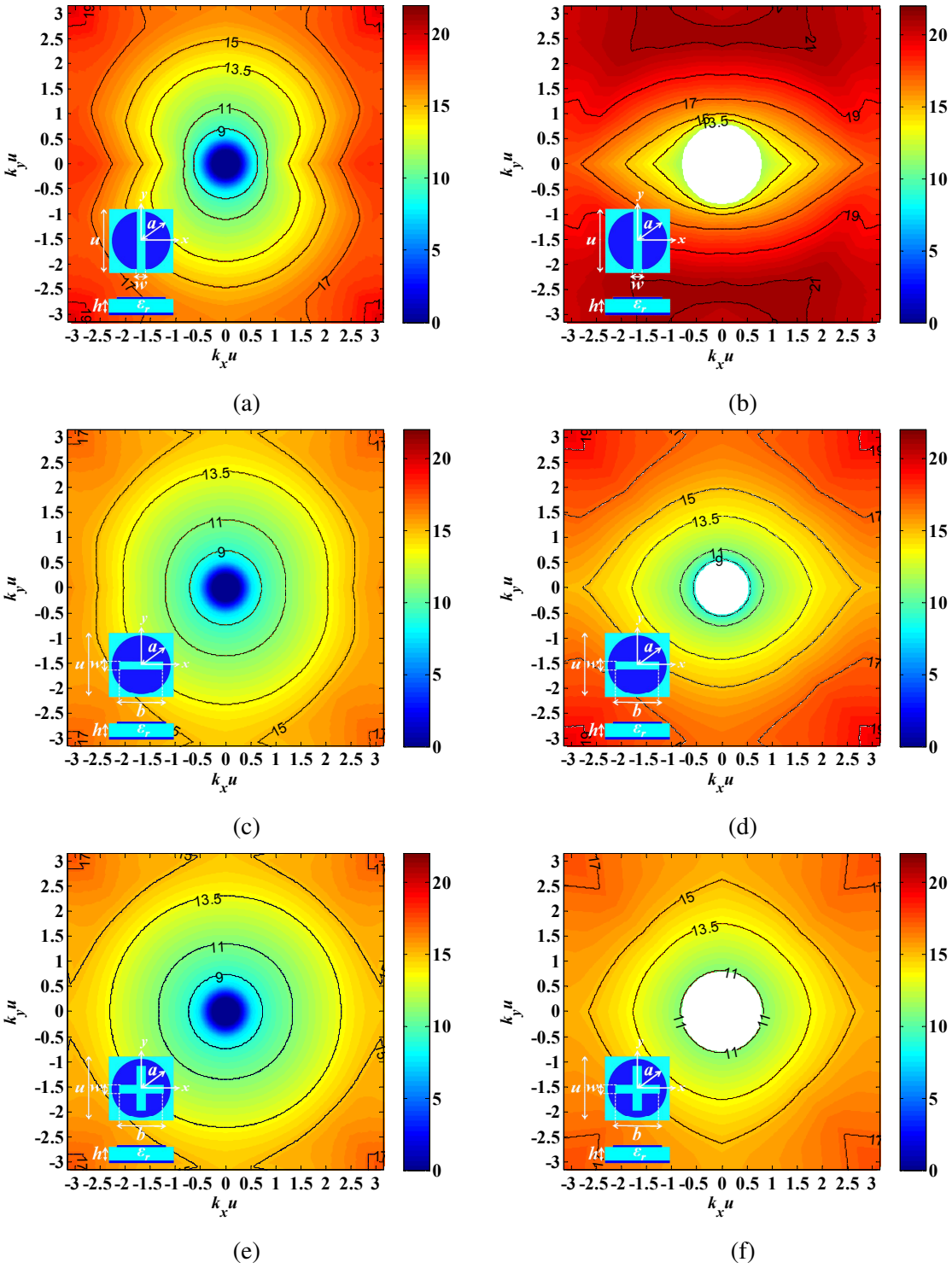

Fig. 3.16. TM (left) and TE (right) modes isofrequency curves of anisotropic pixels composed by a circular shaped patch with an aperture in the center: (a),(b) a cut with $w/a = 0.15$; (c),(d) a groove with $w/a = 0.15$ and $b/a = 0.75$; or (e),(f) a cross-shaped aperture with $w/a = 0.15$ and $b/a = 0.75$. For all the cases, $u = 3.14mm$, $a/u = 0.9$, $\varepsilon_r = 10.2$ and $h/u = 0.4$.

upna
Universidad Pública de Navarra
Nafarroako Unibertsitate Publikoa

considerably increased (the phase delay along the unit cell approximates to $\Delta ph \sim 140°$), the isofrequency curves for both modes start to deform. This effect is due to the fact that at high frequencies the homogenization assumption is not satisfied (i.e. $\lambda_{sw} \sim u$), the unit cell lattice resonates and higher order Floquet modes affect to the overall response. Comparing Fig. 3.15(e) and Fig. 3.15(f) with the figures Fig. 3.15(c) and Fig. 3.15(d) respectively, it can be seen that the effect of increasing the thickness of the dielectric compensates the anisotropy of the pixel geometry (the effective ratio is larger) and the dispersion curves move into lower frequencies.

The circular patch with a groove aligned with y-axis (Fig. 3.16(a)- Fig. 3.16(b)) presents similar TM and TE response than the elliptical patch with its major axis oriented towards y-axis (Fig.3.15) characterized by small ratio. Meanwhile, the circular patch with a slot aligned with x-axis (Fig. 3.16(c)- Fig. 3.16(d)) is comparable to the elliptical patch with larger ratio. On the other hand, when the pixel is composed by a circular metallic patch with a cross-shaped aperture as shown in figures Fig. 3.16(e) and Fig. 3.16(f), the TM and TE modes curves show smooth spatial dispersion. As the dispersion curves move into lower frequencies, the behavior of the pixel with the cross-shaped aperture can be approximated to the behavior of an electrically larger circular patch as the one in figures Fig. 3.15(e) and Fig. 3.15(f).

To complete the study of each pixel, a ψ degrees rotation inside the unit cell has been done to check the effect of the rotation over the dispersion properties of the supported modes. The scheme of each rotated pixels are shown in Fig. 3.17.

upna
Universidad Pública de Navarra
Nafarroako Unibertsitate Publikoa

Different anisotropic patches rotated $\psi = 30^\circ$ have been studied. Their isofrequency dispersion curves are depicted in Fig. 3.18. As it can be seen in the figures, they are in good agreement with the curves obtained in Fig. 3.15 and Fig. 3.16. The difference is that the curves are rotated 30° in concordance with the modification on the patch symmetry axes orientation. Thus, at low frequencies, the spatial dispersion shown by a SW when it impinges a certain pixel from different directions (ϕ) is comparable to the effect of rotating the patch (ψ) through the SW propagation direction, i.e., $\omega(k_t, \phi, \psi) \sim \omega(k_t, 0, \psi - \phi) \sim \omega(k_t, \phi - \psi, 0)$. It has to be mentioned that in the case of the TE mode, this property is maintained in a narrower bandwidth and the effect of the rotation is more important, due to the fact that the mode is more spatially dispersive and patch geometry dependent. While at low frequencies the dispersion curves show the effect of the dominant TM or TE modes, at high frequencies (correspondent to the full wave simulation data with the phase delay along the unit cell larger than $\Delta ph = 130^\circ - 140^\circ$) higher order modes interact with the ground plane and the curves are distorted showing the effect of the cartesian lattice.

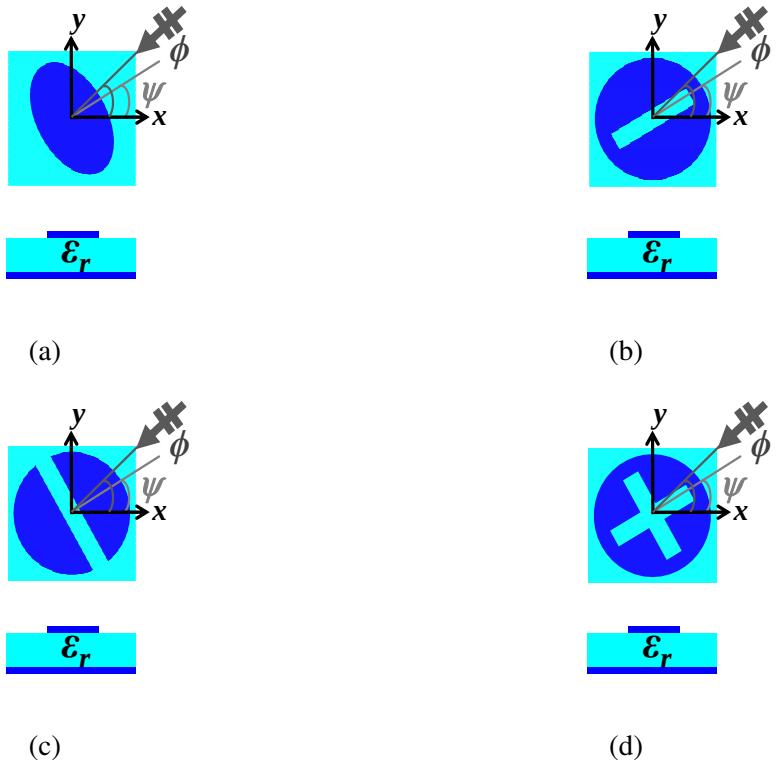

Fig. 3.17. Different anisotropic patch geometries rotated $\psi(^\circ)$ (with respect to x axis): (a) circular patch with (a/u); (b) elliptical patch with (e_b/u) and (e_a/e_b); and circular patches with different apertures in the center: (c) a groove with (w/u); (d) a slot with (w/u) and length (b/a); and (e) a cross-shaped aperture with (w/u) and (b/a). Dielectric substrate with ε_r and h. $\phi(^\circ)$ is the SW propagation angle.

upna
Universidad Pública de Navarra
Nafarroako Unibertsitate Publikoa

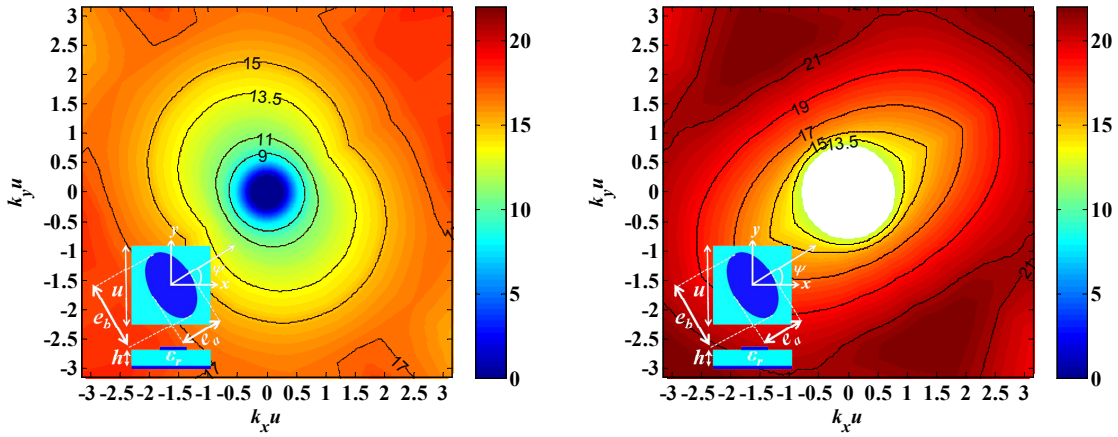

(a)

(b)

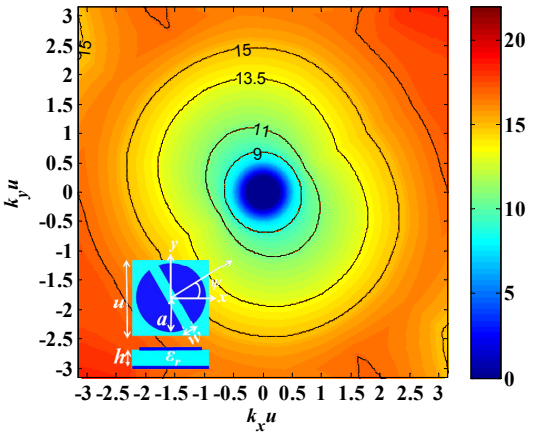

(c)

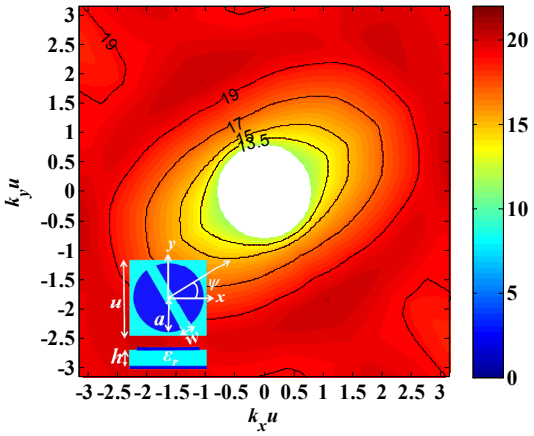

(d)

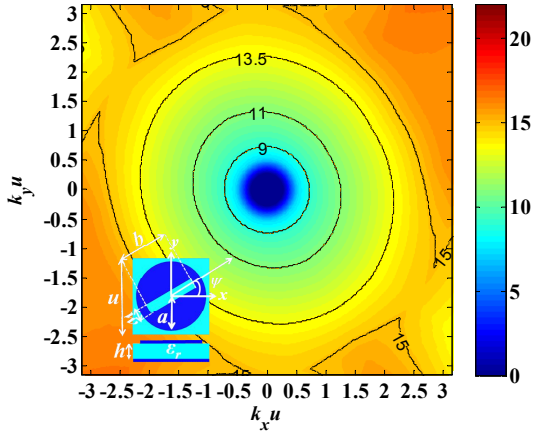

(e)

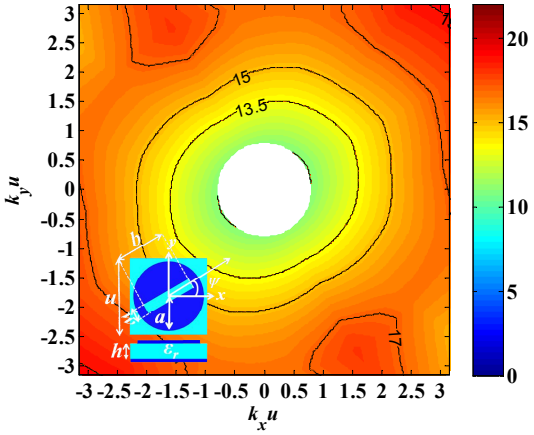

(f)

upna
Universidad Pública de Navarra
Nafarroako Unibertsitate Publikoa

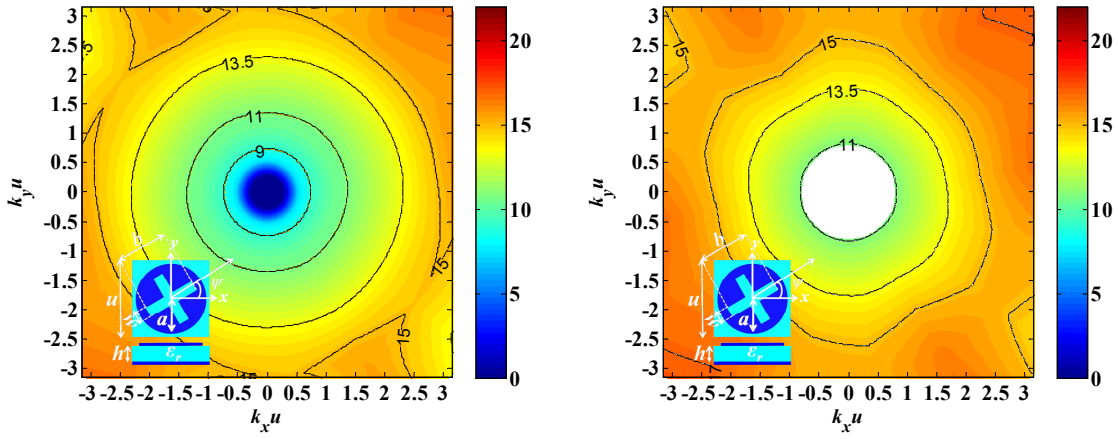

(g) (h)

Fig. 3.18. TM (left) and TE (right) SWs isofrequency curves of different anisotropic patches rotated $\psi = 30°$: (a),(b) elliptical patches with $e_b/4 = 0.9$ and $e_b/e_a = 0.6$; circular patches with different apertures: (c),(d) a groove with $w/a = 0.15$ and $b/a = 0.75$; (e),(f) a slot with $w/a = 0.15$ and $b/a = 0.75$; and a cross-shaped aperture with $w/a = 0.15$ and $b/a = 0.75$. For all the cases, $u = 3.14mm$ and $h/u = 0.4$.

The dispersion analysis provides information not only about the phase velocity dependence with frequency and SW propagation direction, but also about the group velocity, which is related with the power flow direction along the surface. As it can be seen in Fig. 3.19, when the SW impinges the anisotropic pixel towards the patch symmetry axis ($\phi = \psi$), the phase velocity agrees with the group velocity. For different ϕ angles, the group velocity is oriented in perpendicular direction with respect the isofrequency curve.

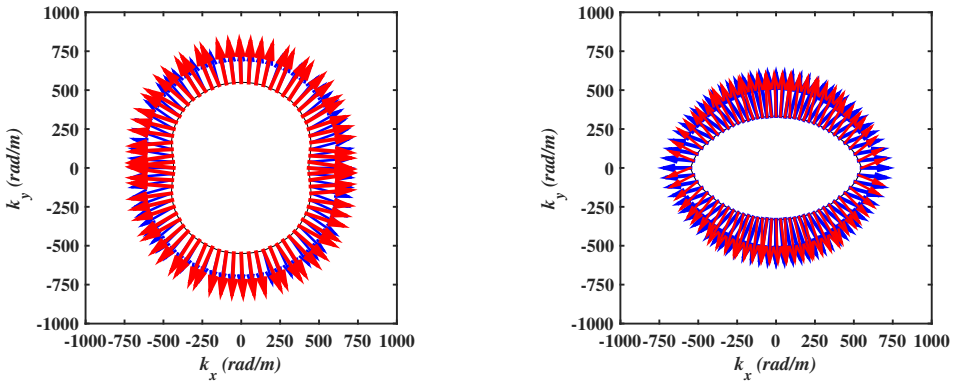

(a) (b)

Fig. 3.19. (a) TM and (b) TE modes phase velocity (blue) and group velocity (red) directions when they impinge an elliptical shaped patch with $e_b/4 = 0.9$ and $e_b/e_a = 0.8$, $u = 3.14mm$ and $\varepsilon_r = 10.2$ and $h = 1.27mm$.

upna
Universidad Pública de Navarra
Nafarroako Unibertsitate Publikoa

To conclude, it has to be mentioned that the full wave analysis gives information about the spatial and frequency dispersion curves for any type of pixel geometry. However, it does not provide straightforward information of the field polarization and possible modes coupling effect when SW incidence is out of the symmetry axes of anisotropic patches. This features have to be studied when synthesizing anisotropic MTS antennas with circular polarization control [57–59]. Therefore, it is necessary to calculate the equivalent surface impedance tensor [38].

3.3.2 Equivalent surface impedance calculation

The method followed in this section for the equivalent surface impedance calculation was presented by Martini et al. in [38]. The equivalent surface impedance tensor, $\bar{\bar{\mathbf{Z}}}$, characteristic of an anisotropic metasurface is related with the wave number through the local dispersion equation in Eq. (3.30):

$$\det[\bar{\bar{\mathbf{X}}}+\bar{\bar{\mathbf{X}}}_0] = (X_{ee}+X_0^{TM})(X_{hh}+X_0^{TE})-X_{eh}^2 \tag{3.34}$$

The components of $\bar{\bar{\mathbf{X}}}$ are given in the basis of the unit wavevector : $\hat{\mathbf{k}}_\mathbf{t}, \hat{\mathbf{k}}_\mathbf{t}{}^{\perp}$ (see section 3.2.3). Nevertheless, as $\bar{\bar{\mathbf{X}}}$ is a real symmetric matrix ($\bar{\bar{\mathbf{Z}}}$ is anti-Hermitian), an equivalent diagonal matrix, $\bar{\bar{\mathbf{X}}}'$, is defined in a second coordinate system with the base vectors $\hat{\mathbf{e}}_1$,$\hat{\mathbf{e}}_2$ oriented towards the symmetry axes of the metallic patch over the grounded slab ($\psi, \psi+\pi/2$). More details are drawn in the appendix D. Both tensors are related as: $[\mathbf{X}] = [\mathbf{Q}^T][\mathbf{X}'][\mathbf{Q}]$, where $[\mathbf{Q}]$ is the transformation matrix and the rotation angle is $\vartheta = (\phi - \psi)$ for the TM mode and $\vartheta = (\phi - \psi + \pi/2)$ for TE mode [38]:

$$\begin{aligned} X_{ee} &= \hat{\mathbf{k}}_t(X_1\hat{\mathbf{e}}_1\hat{\mathbf{e}}_1 + X_2\hat{\mathbf{e}}_2\hat{\mathbf{e}}_2)\hat{\mathbf{k}}_t = cos^2\vartheta X_1 + sin^2\vartheta X_2 \\ X_{eh} &= \hat{\mathbf{k}}_t(X_1\hat{\mathbf{e}}_1\hat{\mathbf{e}}_1 + X_2\hat{\mathbf{e}}_2\hat{\mathbf{e}}_2)\hat{\mathbf{k}}_t{}^{\perp} = sin\vartheta cos\vartheta(X_1 - X_2) \\ X_{hh} &= \hat{\mathbf{k}}_t{}^{\perp}(X_1\hat{\mathbf{e}}_1\hat{\mathbf{e}}_1 + X_2\hat{\mathbf{e}}_2\hat{\mathbf{e}}_2)\hat{\mathbf{k}}_t{}^{\perp} = sin^2\vartheta X_1 + cos^2\vartheta X_2 \end{aligned} \tag{3.35}$$

Depending on whether the mode is TM or TE, X_1 and X_2 elements of the diagonal matrix $\bar{\bar{\mathbf{X}}}'$ are calculated applying Eq. (3.26). When $\hat{\mathbf{k}}_\mathbf{t}$ is oriented towards $\mathbf{e}_1$, there is no coupling between the field components and there is no cross-polar contribution in the tensor. Besides, taking into account that $|\bar{\bar{\mathbf{X}}}| = |\bar{\bar{\mathbf{X}}}'| = X_1X_2$ and the relations (3.23)-(3.24), the dispersion equation in (3.36) can be rewritten as a quadratic equation with the normalized surface impedance value (η) [38]:

$$\det[\bar{\bar{\mathbf{X}}}+\bar{\bar{\mathbf{X}}}_0] = \quad = \eta^2 - \eta\left(\frac{X_1X_2-\zeta^2}{\zeta X_{hh}}\right) - \frac{X_{ee}}{X_{hh}} = 0 \tag{3.36}$$

upna
Universidad Pública de Navarra
Nafarroako Unibertsitate Publikoa

Based on this method [38], TM and TE surface impedance maps of several pixels have been calculated at 13.5GHz, for different geometry variations (previously presented in Fig. 3.12) and patch rotations inside the unit cell (ψ). ARLON AD1000 dielectric has been used, characterized by $\varepsilon_r = 10.2$ and $h = 1.27mm$. In all the cases $u = 3.14mm$.

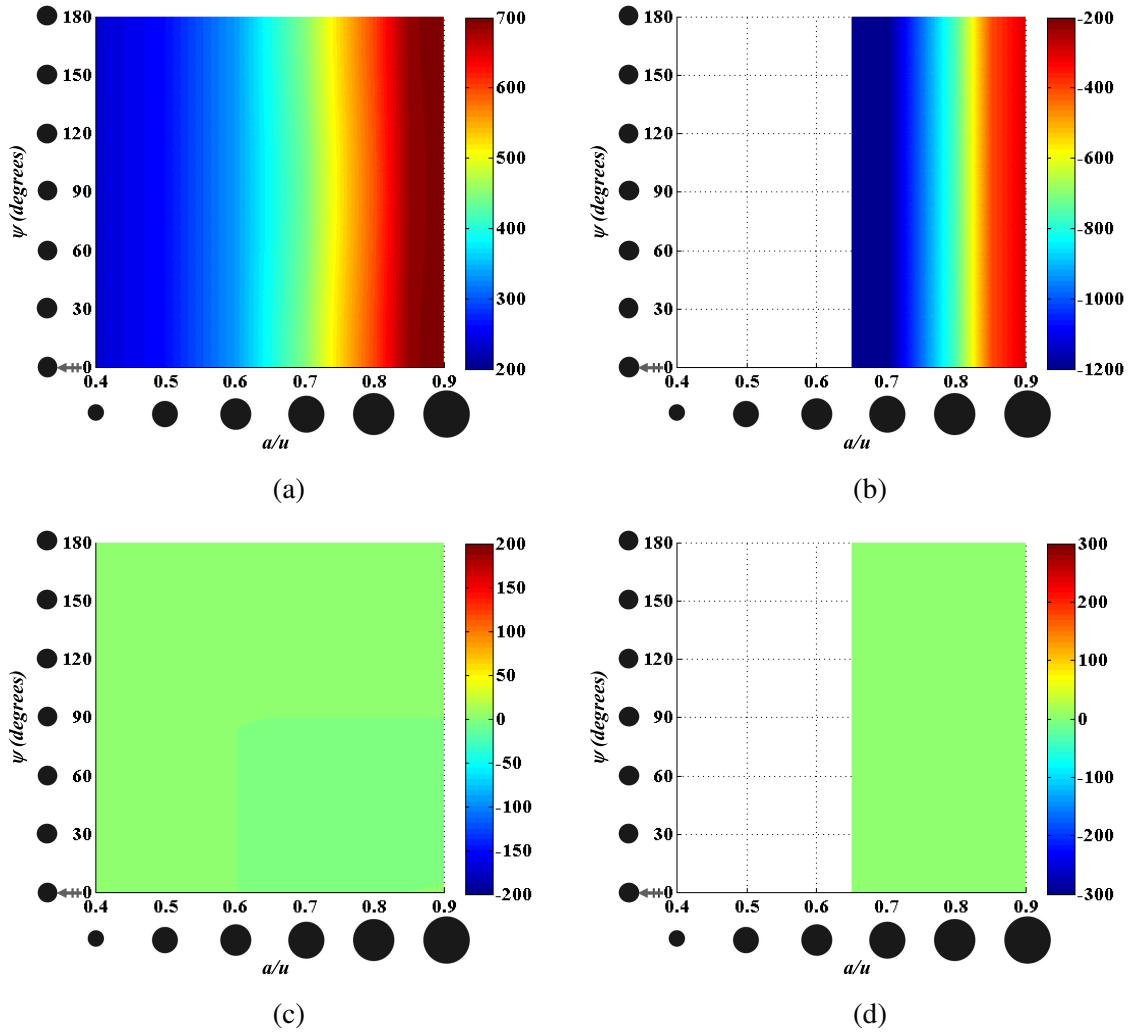

Fig. 3.20. Equivalent scalar surface impedance value and cross-polar contribution for TM SW (a),(c) and TE SW (b),(d) at 13.5GHz, related to isotropic circular metallic patches with different normalized radii (a/u) over a grounded dielectric ($h = 1.27mm$, $\varepsilon_r = 10.2$). ψ denotes the patch rotation angle inside the unit cell. The SW impinges the cell towards $\phi = 0°$.

The equivalent TM and TE impedances related with the circular isotropic patches do not depend on the SW impinging angle, as it has been shown in Fig. 3.20. TM and TE modes are pure (cross-polar components of the tensor are zero) and due to this fact the isotropic metasurfaces synthesized with these pixels do not provide circular polarization control. It

upna
Universidad Pública de Navarra
Nafarroako Unibertsitate Publikoa

has to be mentioned that electrically small patches (in this case the ones with $a/u < 0.65$) do not support TE SW propagation because it is below cut-off at the working frequency (13.5GHz). Electrically larger patches, which support a surface wave characterized by smaller wavelength, provide higher impedance values: higher X^{TM} and smaller $|X^{TE}|$. Depending on the application, high surface impedance values may be required, so in agreement with Fig. 3.14, dielectric substrates with higher ε_r or h values may be needed. Nevertheless, these solutions are limited by the fulfillment of the homogenization condition.

The impedance maps of anisotropic pixels with different geometries (elliptical patch, circular patch with a groove and circular patch with a slot in the center respectively) and rotations (ψ) are shown in Fig. 3.21 to Fig. 3.23. In all the cases $\phi = 0°$. X_{ee}, X_{eh} and X_{hh} components are extracted for TM and TE modes at 13.5GHz.

The calculated equivalent surface impedance maps related with the anisotropic pixels are k_t dependent. The anisotropic pixels composed by elliptical-shaped patches (Fig. 3.21) show that the supported modes are not pure TM neither pure TE, but they are hybrid modes: when the modes impinge the patch towards its symmetry axes ($\phi = 0°, 90°$) the mode purity is kept. However, for different rotation angles modes are coupled and the cross-polar contribution increases. Higher impedance values are obtained when the TM mode impinges the ellipse towards its major axis (higher X_{ee} values when $\phi = 0°, \psi = 90°$). Accordingly, the same behavior is obtained for the TE in the transversal direction (small $|X_{hh}|$ values when $\phi = 0°, \psi = 0°$). It has to be mentioned that the TE mode is more sensitive to the patch dimension variation and also to its rotation, as it is more spatially dispersive than the TM SW.

The equivalent TM surface impedance tensor components for an anisotropic pixel composed by circular metallic patches with a groove aperture in the center are shown in Fig. 3.22. It can be seen that the effect of the groove aperture oriented towards y-axis in the center is negligible for a small a/u relation ($a/u < 0.65$). As the size of the patch increases, the impedance properties are similar to the electrically large elliptical patches (e_b/u) with the major axis oriented towards y-axis and characterized by small ratio (e_a/e_b). It is remarkable that at 13.5GHz the TE mode is below cut-off and remains inside the visible region. This property makes this element appropriate to implement metasurfaces where only single TM mode propagation is required.

Moreover, the surface impedance characteristics of the circular patches with a slot aperture in the center oriented towards x-axis are shown in Fig. 3.23. This pixel geometry shows soft dependence with ψ: when $a/u > 0.8$ the behavior agrees with the results of elliptical patches characterized by big ratio (e_a/e_b) .

upna
Universidad Pública de Navarra
Nafarroako Unibertsitate Publikoa

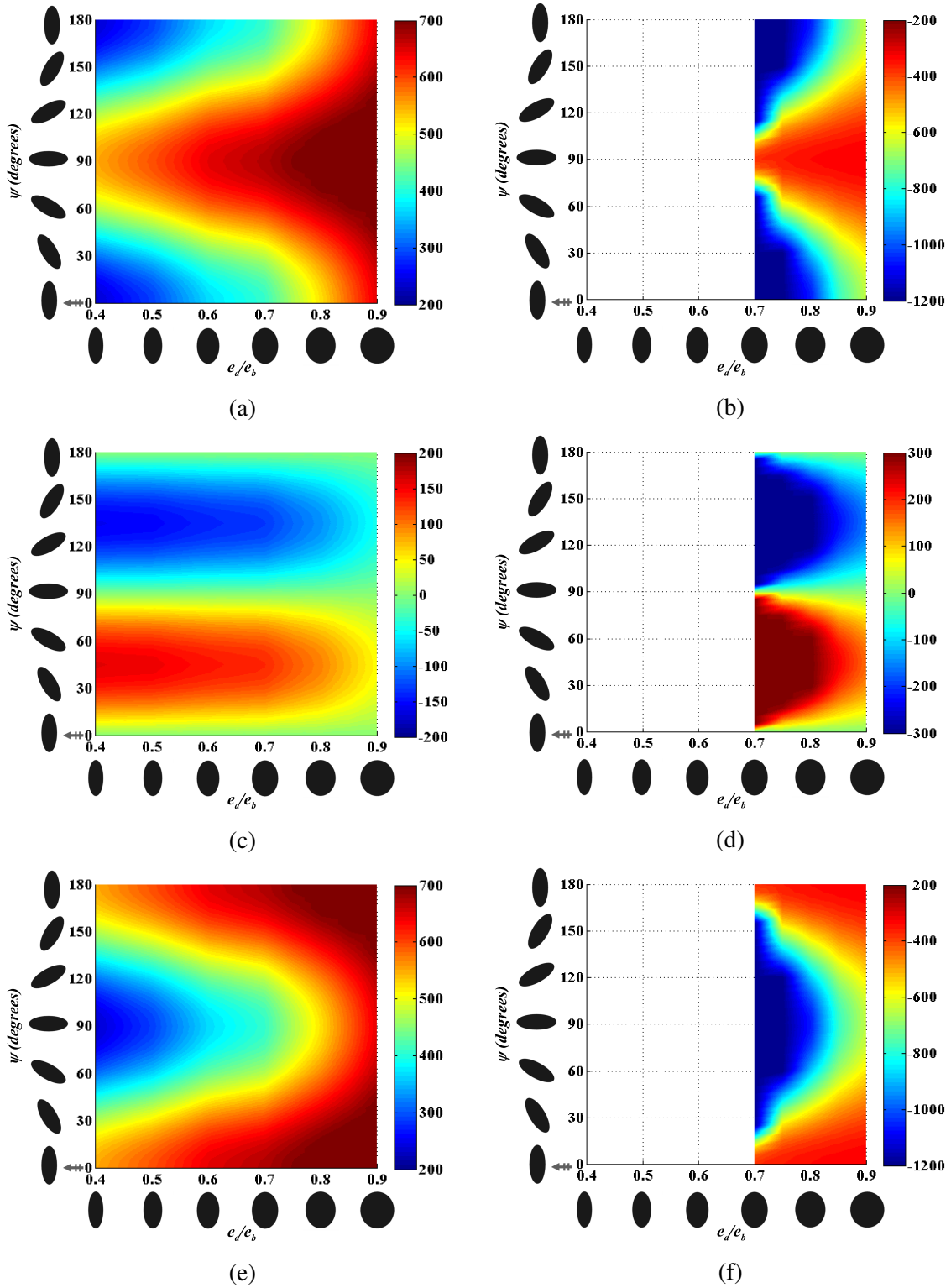

Fig. 3.21. Equivalent TM (left column) and TE (right column) surface impedance tensor components ((a),(b) X_{ee}, (c),(d) X_{eh} and (e),(f) X_{hh}) at 13.5GHz, related to anisotropic pixels composed by: elliptical metallic patches with major axis $e_b/u = 0.9$ and with different ratios (e_a/e_b) over a grounded dielectric characterized by $h = 1.27mm$ and $\varepsilon_r = 10.2$. $\psi(^\circ)$ denotes the patch rotation angle inside the unit cell. The SW impinges the cell towards $\phi = 0^\circ$.

upna
Universidad Pública de Navarra
Nafarroako Unibertsitate Publikoa

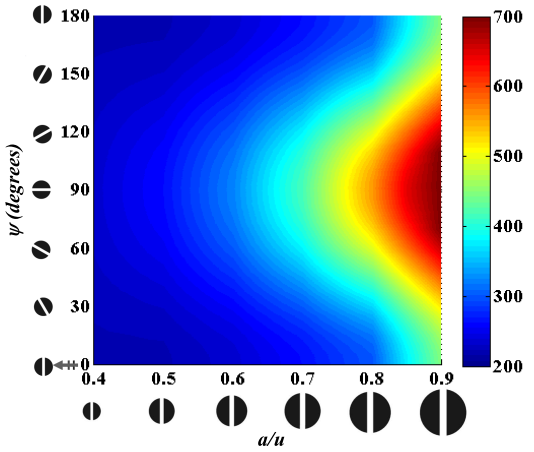

(a)

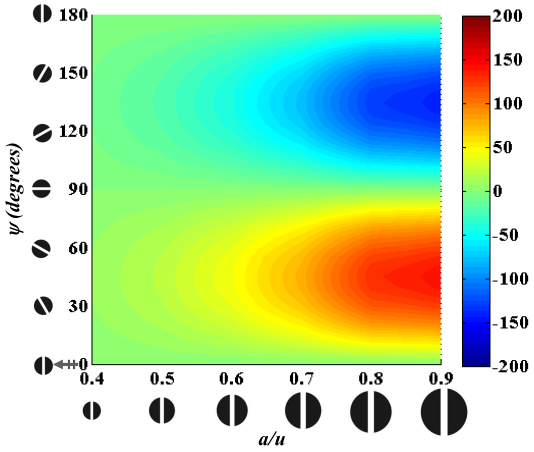

(b)

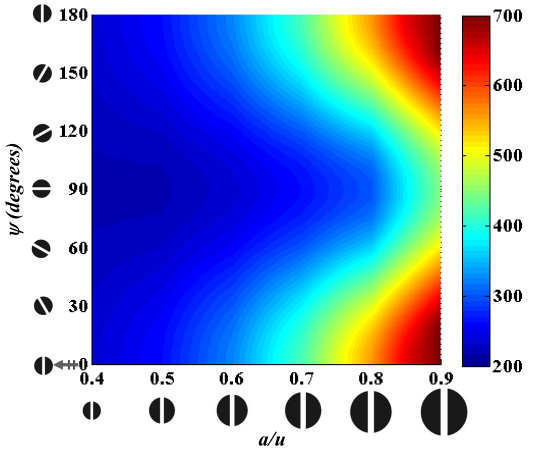

(c)

Fig. 3.22. Equivalent TM surface impedance tensor components ((a) X_{ee}, (b) X_{eh} and (c) X_{hh}) at 13.5GHz, related to anisotropic pixels composed by: circular metallic patches with a groove aperture in the center ($w/a = 0.15$) over a grounded dielectric characterized by $h = 1.27mm$ and $\varepsilon_r = 10.2$. Patches with different radii (a/u) have been analyzed. $\psi(^\circ)$ denotes the patch rotation angle inside the unit cell. The SW impinges the cell towards $\phi = 0^\circ$.

upna
Universidad Pública de Navarra
Nafarroako Unibertsitate Publikoa

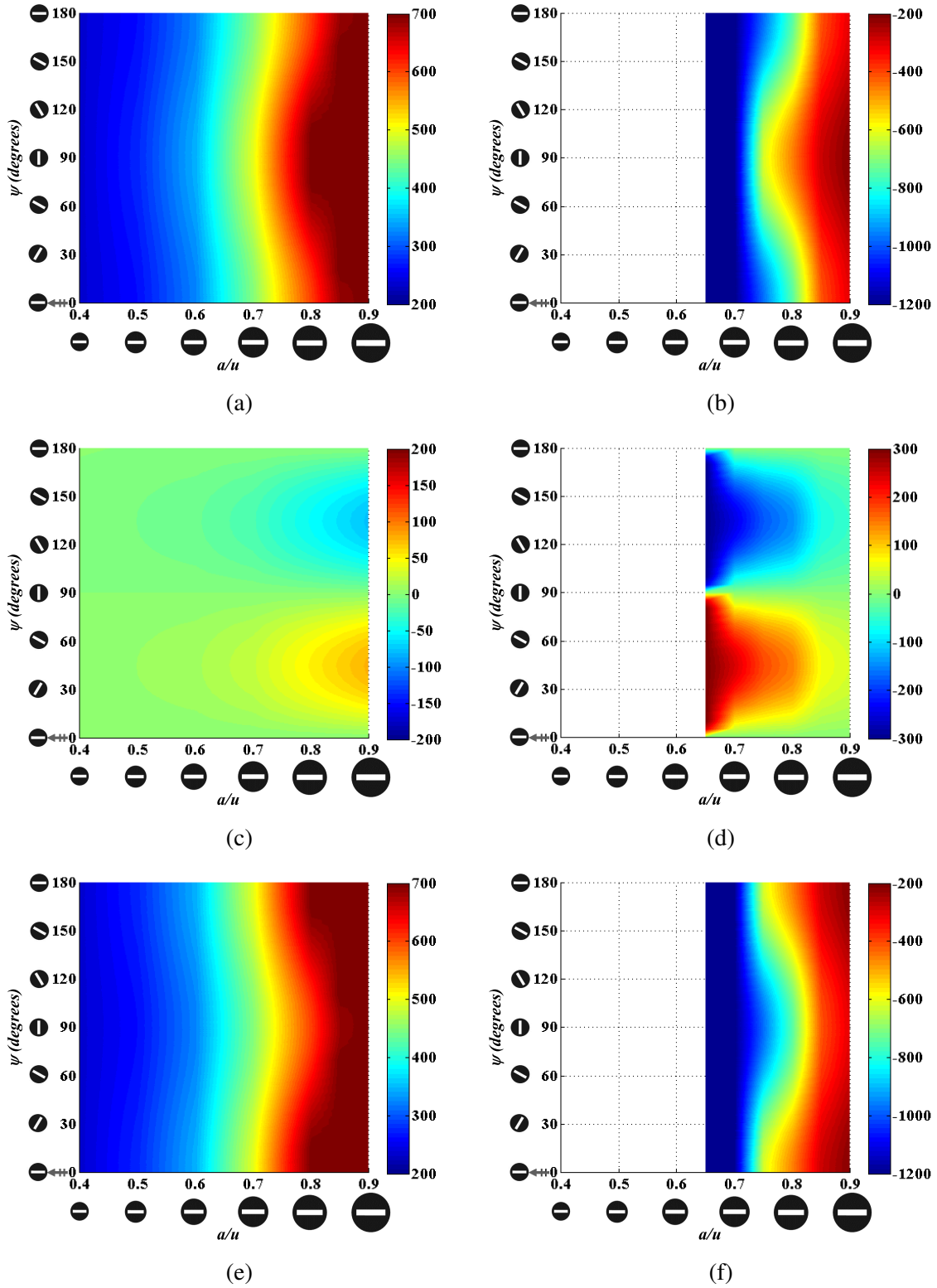

Fig. 3.23. Equivalent TM (left column) and TE (right column) surface impedance tensor components ((a),(b) X_{ee}, (c),(d) X_{eh} and (e),(f) X_{hh}) at 13.5GHz, related to anisotropic pixels composed by: circular metallic patches with a slot aperture in the center ($w/a = 0.15$ and $b/a = 0.75$) over a grounded dielectric characterized by $h = 1.27mm$ and $\varepsilon_r = 10.2$. Patches with different radii (a/u) have been analyzed. $\psi(^\circ)$ denotes the patch rotation angle inside the unit cell. The SW impinges the cell towards $\phi = 0^\circ$.

upna
Universidad Pública de Navarra
Nafarroako Unibertsitate Publikoa

3.3.3 Conclusions

In this section the spatial and frequency dispersion properties of TM and TE modes propagating on different isotropic and anisotropic pixels have been performed based on full wave analysis. It has been concluded that the modes propagating over a structure composed by electrically larger patches printed on top of the grounded slab are characterized by smaller wavelengths. The analysis of several anisotropic pixels show that the TE mode is more spatially and frequency dispersive than the TM mode. As the dependence with the pixel geometry shown by the TE is more important, the effect of the rotation of the pixel inside the unit cell is appreciated in the isofrequency dispersion curves. For high frequencies, where the homogenization condition is not fulfilled, the effect of the cartesian lattice becomes important for both the TM and the TE modes.

The main drawback of the full wave analysis is related with the required time and resources needed for the simulation. Due to this fact, the alternative fast method to calculate the frequency dispersion data from a single run of the eigenmode solver presented by Mencagli et all. [61–63] has been deployed in the appendix A. It has been concluded that the full wave analysis can be efficiently simplified combining it with this alternative method, as the obtained results are comparable for the TM and TE modes until near the end of the transition region. For the TE case, the approximation is more critical but the curves show good agreement at low frequencies. As the work presented in this dissertation is focused on the practical implementation of MTS antennas, the low regime approximation is considered accurate.

At the same time, the equivalent surface impedance maps have been extracted from the dispersion information based on the method proposed by Martini et al. in [38]. The surface impedance tensor components of the anisotropic pixels for all the incidences and rotations have been extrapolated from the SW dispersion characterization carried out trough the symmetry axes of the patch printed on top of the grounded slab, applying appropriately a rotation matrix. Due to the dependence with the pixel rotation, this method is limited for the TE mode within a narrow bandwidth above the cut-off frequency. Besides, at high frequencies (where λ_{sw} is considerably decreased), the method is limited for both the TM and TE modes as the cartesian lattice affects to the dispersion characterization.

For completeness, an alternative method to calculate the sheet impedance maps based on the method proposed by Patel et al. in [64–72] has been presented in the appendix B. The main advantage of this method is that the dispersion characterization of the TM mode is given based on the scattering information on the driven modal solver, which is less time and resource consuming. Nevertheless, the result comparison show some discrepancy between both methods caused by the approximation on the sheet impedance calculation. Due

upna
Universidad Pública de Navarra
Nafarroako Unibertsitate Publikoa

to this fact, the use of the alternative method is limited for low frequencies or dielectrics characterized by low ε_r or thickness values. Furthermore, this method does not allow a straightforward procedure to characterize the TE dispersion properties.

upna
Universidad Pública de Navarra
Nafarroako Unibertsitate Publikoa

Chapter 4

Single layer dual CP broadside MTS antenna at Ku-band

4.1 Introduction

MTS antennas shown in literature [54–60] have established a strong foothold in the spatial business thanks to their lightness and compactness. However, as it is still a technology under evolution, there are challenging designs to face. For instance, nowadays, the capability to provide dual-circular polarization (CP) with a single MTS antenna is still a challenge. These MTS solutions are based on the excitation of a single TM surface wave which interacts with a modulated anisotropic surface and radiates outside the structure RHCP field or LHCP field. Namely, it is not possible to ensure CP in both senses.

This chapter presents, the modeling, implementation and measurements of a single layer MTS antenna which provides both RHCP and LHCP in broadside direction at 13.5GHz. In the structure, for the first time, two simultaneous SWs are launched by the same feed, characterized as TM and TE modes. These modes are matched in phase and balanced in amplitude. Phase matching is ensured by selecting an appropriate anisotropic rotationally symmetric MTS, which allows for almost independent control of the phase velocities of both modes, due to their polarization decoupling. However, amplitude balance is provided by a proper design of the feeding structure.

The chapter is structured as follows. Section 4.2 presents the basic operation principle of the configuration, analyzing the phase matching and polarization balancing boundary conditions. Besides, the required metasurface impedance modulation characteristics are studied. Section 4.3 describes in detail the feeding system needed to obtain dual polarization behavior. Section 4.4 shows the design and implementation of an ideal metasurface, which

upna
Universidad Pública de Navarra
Nafarroako Unibertsitate Publikoa

has been designed based on the previous theoretical analysis. Moreover, the peculiarities of the subwavelength pixel-elements required to synthesize the MTS configuration and the relevant full-wave simulation results are shown. The prototype fabrication details including the metasurface and the design of two septum orthomode transducer polarizers employed to excite the antenna are given in section 4.5. Besides, measurements are shown. To finish, conclusions are drawn in section 4.6.

4.2 MTS antenna with dual CP

4.2.1 Basic operation principle

This antenna operates on the excitation of two cylindrical SWs characterized as TE and TM modes, where $\hat{\mathbf{z}}$ is the normal to the surface. These modes are decoupled in power and present similar dispersion diagrams in a certain frequency band, i.e. , in that frequency range they propagate with approximately the same phase velocity. Furthermore, by employing an appropriate feed, their amplitudes can be also equalized. The SWs interact with a rotationally symmetric anisotropic MTS printed on top of a grounded slab of arlon AD1000 ($\varepsilon_r = 10.2$, $h = 1.27mm$). Modulating the MTS impedance with a period that matches the SW wavelength and employing as the excitation a circular waveguide, field leakage at broadside is obtained with individual control of both polarizations. Namely, properly adjusting the phase shift between the two orthogonal TE_{11} modes of the circular waveguide, RHCP or LHCP can be obtained with the proposed single layer MTS solution.

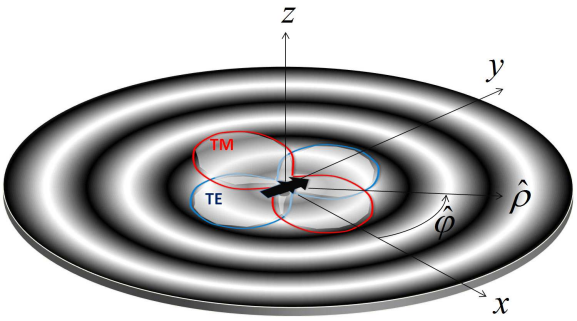

Fig. 4.1. Pictorial representation of the modulated rotationally symmetric reactance with magnetic dipole excitation. The red and blue lines indicate the amplitude pattern of the SW modes launched on the average impedance surface by a magnetic dipole oriented along y, represented by a double black arrow.

As extended in section 3.2.3, the boundary conditions at the observation point $\boldsymbol{\rho}$ on the MTS are described by an anisotropic lossless surface impedance tensor, $\bar{\bar{\mathbf{Z}}}$, which links the

upna
Universidad Pública de Navarra
Nafarroako Unibertsitate Publikoa

tangential electric $\mathbf{E}_t$ and the tangential magnetic $\mathbf{H}_t$ fields at the upper MTS-air interface as in Eq. (3.20) [66–68, 79, 86]. When the modes are decoupled, the surface reactance tensor is defined as:

$$\bar{\bar{\mathbf{X}}}(\boldsymbol{\rho}) = \bar{\bar{X}}_{\rho\rho}\hat{\rho}\hat{\rho} + \bar{\bar{X}}_{\varphi\varphi}\hat{\varphi}\hat{\varphi} \tag{4.1}$$

$(\hat{\rho}, \hat{\varphi})$ are the unitary vectors of the cylindrical coordinate system and $\hat{\mathbf{z}}$ is normal to the interface. $\bar{\bar{\mathbf{X}}}$ presents principal axes along $(\hat{\rho}, \hat{\varphi})$. The $\bar{\bar{\mathbf{X}}}$ components are modulated by an azimuthally symmetric sinusoidal radial function (see Fig. 4.1), with a determined modulation index and radial periodicity.

$\langle\cdot\rangle$ describes the space average operator over the circular surface of radius r where the reactance tensor $\bar{\bar{\mathbf{X}}}$ is defined and the average eigenvalues are given by X_{TM} and X_{TE} values:

$$\langle\bar{\bar{\mathbf{X}}}\rangle = \bar{\bar{X}}_{TM}\hat{\rho}\hat{\rho} + \bar{\bar{X}}_{TE}\hat{\varphi}\hat{\varphi} \tag{4.2}$$

The following lines in this section are focused on the determination of $\langle\bar{\bar{\mathbf{X}}}\rangle$ features to provide the phase balance between the TE and TM modes. Afterwards, the details of the required modulation will be discussed in section 4.2.2.

Phase Matching between TE and TM modes

The boundary condition described by a diagonal tensor like in Eq. (4.1) is ensured by the fact that any lossless MTS is represented by a Hermitian reactance tensor [86]. Due to this fact, $\bar{\bar{\mathbf{X}}}$ always possesses two orthogonal principal axes, that in the proposed design are chosen to be aligned, at any position $\boldsymbol{\rho}$, along the unit vectors of the cylindrical coordinate system. Additionally, $\bar{\bar{\mathbf{X}}}$ depends on both frequency and wavenumber.

Applying the TRE [66–68, 79, 86], the average eigenvalues $X_{TM,TE}$ are related to the magnitude of the radial propagation wavevector $\mathbf{k}_{TM,TE} = \beta_{TM,TE}\hat{\mathbf{k}}_\rho$ of the SWs launched by a point source located at the origin following Eq. (3.26) presented in section 3.2.4.

The key feature of the proposed configuration is the phase-matching between TM and TE modes, namely, they propagate with the same phase velocity. From Eq. (3.26) it can be seen that the *phase matching condition* is fulfilled when:

$$\begin{gathered} \beta_{TM} = \beta_{TE} = \beta \quad \Rightarrow \quad \eta_{TM}\eta_{TE} = -1 \\ \eta_{TM} = \sqrt{(\beta/k)^2 - 1}, \quad \eta_{TE} = -1/\sqrt{(\beta/k)^2 - 1} \end{gathered} \tag{4.3}$$

Therefore, it has to be satisfied that the average surface impedance values of TM and TE modes are inversely proportional to each other and possesses opposite sign (TM has

upna
Universidad Pública de Navarra
Nafarroako Unibertsitate Publikoa

capacitive nature while TE is inductive) (see Fig. 4.2). In practice, this condition can be satisfied using sub-wavelength anisotropic patch elements which allow independent control of both reactances $\eta_{TM,TE}$, guarantying, besides, decoupling of the modes.

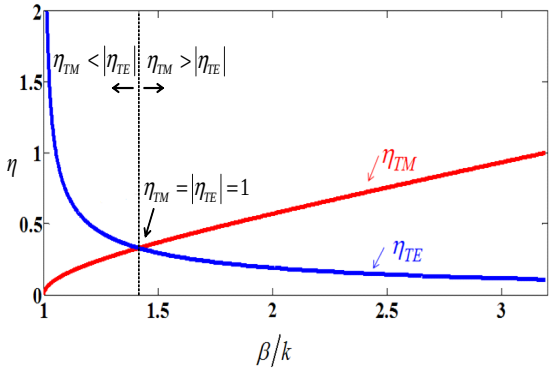

Fig. 4.2. Normalized modal reactances as a function of the normalized propagation constant under phase-matching condition, $\eta_{TM}\eta_{TE} = -1$.

Under the assumption shown in Eq. (4.3) and neglecting modal coupling effects, the driving tangential field supported by the MTS is given by:

$$\begin{aligned} \mathbf{E}_{TM} &= \hat{\rho} E_{TM} = -jX_{\rho\rho} H_{TM} \hat{\rho} \\ \mathbf{E}_{TE} &= \hat{\varphi} E_{TE} = jX_{\varphi\varphi} H_{TE} \hat{\varphi} \end{aligned} \tag{4.4}$$

where both components propagate with the same phase progression. Thereby, the total tangential field in the structure under balanced conditions is given by:

$$\mathbf{E}_{tot} = \mathbf{E}_{TM} + \mathbf{E}_{TE} = -jX_{\rho\rho} H_{TM} \hat{\rho} + jX_{\varphi\varphi} H_{TE} \hat{\varphi} \tag{4.5}$$

Polarization Balance

The anisotropic modulated MTS (characterized by an average reactance tensor satisfying Eq. (4.3)) can be fed by two infinitesimal horizontal magnetic dipoles with equal momentum placed at the center of the structure over the metallic ground. As illustrated in Fig. 4.3, the dipoles are oriented along $\hat{\mathbf{x}}$ and $\hat{\mathbf{y}}$.

The total tangential fields relevant to the dipoles oriented along $\hat{\mathbf{x}}$ and $\hat{\mathbf{y}}$ are described by $\mathbf{E}_{tot}^{(x)}$ and $\mathbf{E}_{tot}^{(y)}$ respectively:

$$\begin{aligned} \mathbf{E}_{tot}^{(y)} &= \mathbf{E}_{TM}^{(y)} + \mathbf{E}_{TE}^{(y)} = -E_{TM}^{(y)} \cos\varphi \hat{\rho} + E_{TE}^{(y)} \sin\varphi \hat{\varphi} \\ \mathbf{E}_{tot}^{(x)} &= \mathbf{E}_{TM}^{(x)} + \mathbf{E}_{TE}^{(x)} = E_{TM}^{(x)} \sin\varphi \hat{\rho} + E_{TE}^{(x)} \cos\varphi \hat{\varphi} \end{aligned} \tag{4.6}$$

upna
Universidad Pública de Navarra
Nafarroako Unibertsitate Publikoa

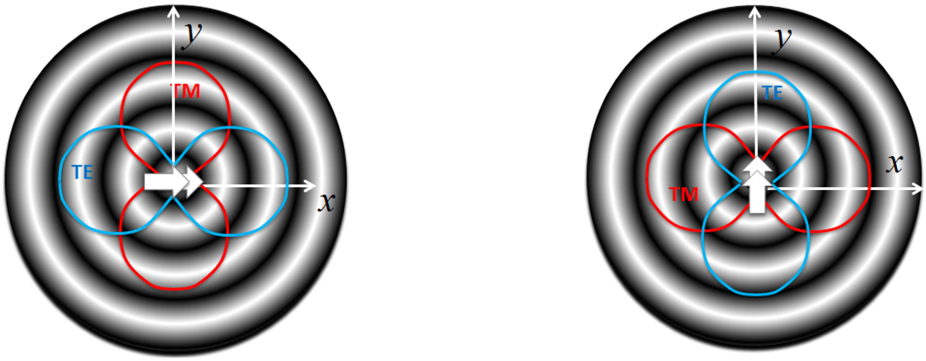

(a) (b)

Fig. 4.3. Excitation of the MTS with an infinitesimal horizontal magnetic dipole over the ground plane oriented along (a) $\hat{\mathbf{x}}$ and (b) $\hat{\mathbf{y}}$.

Taking into account that the MTS is perfectly symmetric in azimuth, $E_{TM}^{(x)} = E_{TM}^{(y)} = E_{TM}$ and $E_{TE}^{(x)} = E_{TM}^{(y)} = E_{TE}$. Therefore, the *polarization balancing condition* is expressed as:

$$E_{TM} = E_{TE} \equiv E_0 \tag{4.7}$$

As a matter of fact, using this latter relationship, expressions in Eq. (4.6) can be simplified to:

$$\begin{aligned} \mathbf{E}_{tot}^{(y)} &= E_0(-\cos\varphi\hat{\boldsymbol{\rho}} + \sin\varphi\hat{\boldsymbol{\varphi}}) = -E_0\hat{\mathbf{x}} \\ \mathbf{E}_{tot}^{(x)} &= E_0(\sin\varphi\hat{\boldsymbol{\rho}} + \cos\varphi\hat{\boldsymbol{\varphi}}) = E_0\hat{\mathbf{y}} \end{aligned} \tag{4.8}$$

A circularly polarized field can be generated by introducing a $\pm 90^\circ$ phase shift between both excitations:

$$\mathbf{E}_{tot} = \mathbf{E}_{tot}^{(y)} \pm j\mathbf{E}_{tot}^{(x)} = E_0(\hat{\mathbf{x}} \pm j\hat{\mathbf{y}}) \tag{4.9}$$

It is important to observe that while *phase matching* is ensured by the condition in Eq. (4.3), which only depends on the MTS properties, the polarization condition in Eq. (4.7) also involves the characteristics of the feed. A discussion on this topic is provided in Sect 4.3.1.

4.2.2 Surface impedance modulation characterization

Once the characteristics of the average MTS are specified by the *phase matching condition* in Eq. (4.3), the modulation is set by an azimuthally symmetric sinusoidal radial function, in such a way to get a broadside radiation thanks to a leaky-wave effect [56–60]:

upna
Universidad Pública de Navarra
Nafarroako Unibertsitate Publikoa

$$\begin{aligned} X_{\rho\rho} &= \zeta\eta_{TM}[1+m_{TM}\cos(2\pi\rho/d_{TM})] \\ X_{\varphi\varphi} &= \zeta\eta_{TE}[1+m_{TE}\cos(2\pi\rho/d_{TE})] \end{aligned} \tag{4.10}$$

The main parameters to be controlled are the average normalized reactances ($\eta_{TM,TE}$), the modulation indexes ($m_{TM,TE}$, here assumed to be constant) and the periodicities ($d_{TM,TE}$) of the sinusoidal radial modulations. Sinusoidal modulation of the surface reactance generates a complex perturbation $\Delta\beta_{TM,TE} - j\alpha_{TM,TE}$ to the wavenumber associated with the average reactance:

$$\beta_{TM,TE} \quad \rightarrow \quad k^{(0)}_{TM,TE} = \beta_{TM,TE} + \Delta\beta_{TM,TE} - j\alpha_{TM,TE} \tag{4.11}$$

The real part of the perturbation, $\Delta\beta_{TM,TE}$, describes the phase shift suffered by the wavenumber of the SW associated with the average reactance, while the imaginary part $\alpha_{TM,TE}$, is the leaky attenuation constant. These perturbations depend mainly on $m_{TM,TE}$ and $\eta_{TM,TE}$. Oliner and Caminita present in [52, 77] the procedure to characterize the complex wavenumber of the modes. This method has been adapted in this section considering an equivalent sinusoidal homogenized penetrable impedance which describes the cladding of the canonical one dimensional problem related with the TM and TE modes: $Z_S = jX_S^{TX} = X_{aveS}^{TX}(1+m_S^{TX}cos(2\pi x/d_S^{TX}))\quad TX = TM,TE$. More details are given in appendix C.

The field and currents over the periodic structure are described in terms of FM with complex wavenumbers $k_{xn} = \beta + \Delta\beta + \frac{2\pi n}{d} - j\alpha, \quad n = 0,\pm1,\pm2...$ and according to the TRE they are related with the pertinent grounded slab spectral TM,TE Green's function $\widetilde{G}_{EJ}^{TX}(k_{xn})$ as:

$$\begin{aligned} E &= Z\sum_n I_{xn}e^{-jk_{xn}x} \\ &= j\zeta\eta_{TX}[1+m_{TX}\cos(2\pi x/d_{TX})]\sum_n I_{xn}e^{-jk_{xn}x} \\ &= \sum_n \widetilde{G}_{EJ}^{TX}(k_{xn})I_{xn}e^{-jk_{xn}x} \end{aligned} \tag{4.12}$$

being

$$\widetilde{G}_{EJ}^{TX}(k_{xn}) = -(Z_0^{TX} \parallel Z_{cc}^{TX}) \quad TX = TM,TE \tag{4.13}$$

Z_0^{TX} and Z_{cc}^{TX} are the free space and grounded slab impedance contributions of the related TM,TE mode, respectively. The numerical solution of (C.2) in terms of the complex

upna
Universidad Pública de Navarra
Nafarroako Unibertsitate Publikoa

wavenumber (k_{xn}) of the supported waves (and therefore the propagation $\beta + \Delta\beta$ and attenuation α constants of the LW) has been obtained rewriting the problem in a continuous-fraction determinantal equation as in [52, 77].

$$\begin{bmatrix} \dots & \dots & \dots & \dots & \dots & \dots & \dots \\ \dots & D_{n-2} & 1 & 0 & 0 & 0 & \dots \\ \dots & 1 & D_{n-1} & 1 & 0 & 0 & \dots \\ \dots & 0 & 1 & D_n & 1 & 0 & \dots \\ \dots & 0 & 0 & 1 & D_{n+1} & 1 & \dots \\ \dots & 0 & 0 & 0 & 1 & D_{n+2} & \dots \\ \dots & \dots & \dots & \dots & \dots & \dots & \dots \end{bmatrix} \begin{bmatrix} \dots \\ I_{n-2} \\ I_{n-1} \\ I_n \\ I_{n+1} \\ I_{n+2} \\ \dots \end{bmatrix} = 0 \tag{4.14}$$

In the matrix D_n is defined as: $D_n = \frac{2}{m_S^{TX}}\left(1 - \frac{\widetilde{G}_{EJ}^{TX}(k_{xn})}{j\zeta\eta_{TX}}\right)$.

Fig. 5.1 shows the normalized-to-k values of $\Delta\beta_{TM,TE}$ and $\alpha_{TM,TE}$ for different modulation indexes $m_{TM,TE}$ and normalized average reactance values $|\eta_{TM,TE}|$. As it is shown, $|\Delta\beta_{TM,TE}|$ and $|\alpha_{TM,TE}|$ increase with $m_{TE,TM}$, but the impact of the modulation indexes is different for the TE and TM cases.

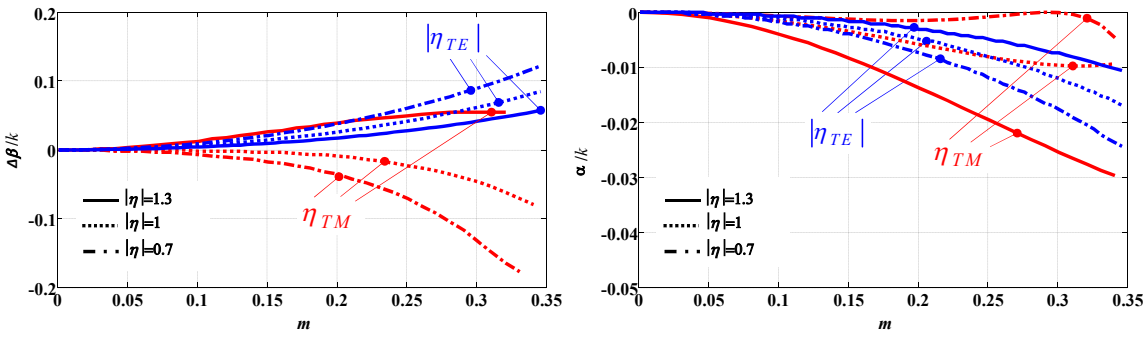

(a) (b)

Fig. 4.4. Variation of $\Delta\beta$ and α (normalized to k) as a function of the modulation index m for three values of the normalized average reactance η, for TM (red lines) and TE (blue lines).

Characterization of the modulation periodicities for broadside radiation

As explained in chapter 3 (section 3.2.2), the *broadside radiation* is strictly related with the choice of the periodicity, which determines the contribution of the $-1-$*indexed* modes of

upna
Universidad Pública de Navarra
Nafarroako Unibertsitate Publikoa

the Floquet expansion of the TM,TE field in the visible region. The wavenumbers of these modes are defined as:

$$k_{TX}^{-1} = \beta + \Delta\beta_{TX} - j\alpha_{TX} - \frac{2\pi}{d_{TX}} \qquad TX = TM, TE \tag{4.15}$$

where $\beta = \beta_{TM} = \beta_{TE}$. The $-1-$*indexed* field must be the only contribution to the far field radiation. Therefore, Eq. (4.15) has to be complemented by the requirement that none of the modes with index different from -1 radiate, namely their wavenumbers are larger than the free space wavenumber k:

$$|\mathrm{Re}(k_{TX}^{n})| = |\beta + \Delta\beta_{TX} + \frac{2\pi n}{d_{TX}}| > k \qquad n \neq -1 \tag{4.16}$$

Broadside radiation of $-1-$*indexed* mode implies vanishing of the real part of wavenumber in Eq. (4.15), which leads to:

$$d_{TX} = \frac{2\pi}{(\beta + \Delta\beta_{TX})} \qquad TX = TM, TE \tag{4.17}$$

Consequently, the period of the modulation must be adjusted taking into account the wavelength of the TE and TM SWs excited on the average surface and accounting also for the polarization-dependent small correction $\Delta\beta_{TM,TE}$. This correction has been proven to be important for large antennas, since small phase shift can cumulate over the surface.

Characterization of the modulation indexes for amplitude matching

In order to equalize the amplitude of the two orthogonal components of aperture field all over the aperture, it must be imposed:

$$\alpha_{TM}(\eta_{TM}, m_{TM}) = \alpha_{TE}(\eta_{TE}, m_{TE}) \tag{4.18}$$

where $\eta_{TM,TE}$ are defined through Eq. (4.3). This condition is referred to as *amplitude matching condition* and it is necessary to ensure the circular polarization. It has been noticed that since the phase matching condition implies different values of average impedance for TE or TM modes and taking into account that the impact of the modulation indexes is different for each of them, different modulation indexes for TE and TM are required to ensure $\alpha_{TM} = \alpha_{TE}$, i.e., polarization balancing all over the surface. However, this condition is not *sufficient*, since it should be complemented by the feed-balancing condition discussed in section 4.3.1.

upna
Universidad Pública de Navarra
Nafarroako Unibertsitate Publikoa

4.3 Feeding system

Apart from the design of the metasurface widely detailed in section 4.2, the dual circular polarization fulfillment of the proposed solution is affected critically by the used feeding system. It must ensure the excitation of the TM and TE modes in the MTS complying the polarization balancing condition described in section 4.2.1. The excitation has been implemented by means of a circular waveguide placed in the center of the structure, in which two mutually orthogonal TE_{11} modes are excited in phase-quadrature. Details of the implemented feeding system are given in the following lines.

4.3.1 Feed balancing: Circular waveguide dimension

As it has been explained in section 4.2.1, circularly polarized field can be obtained in the structure only when the amplitudes of the excited TM and TE modes are balanced. Practical conditions on the required feed can be found by matching the amplitude of the TM,TE Green's function for a magnetic dipole on the ground plane of a grounded slab with an average sheet reactance on the upper interface ($jX_{TX}^{(S)} \quad TX = TM, TE$).

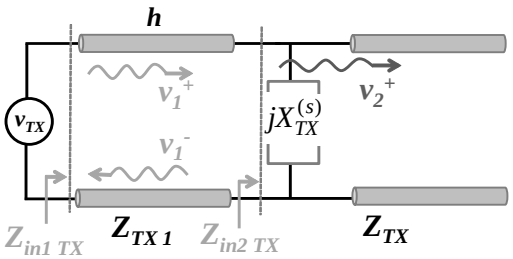

Fig. 4.5. TM,TE transmission line model of the structure.

By using the transmission line network equivalent circuit (see Fig. 4.5), it can be assumed that the TM,TE longitudinal (along $\hat{\mathbf{z}}$) components of the wavenumbers in the dielectric and in air are equalized by the balancing condition:

$$k_{z0} = -j\sqrt{\beta^2 - k^2} \quad , \quad k_{z1} = \sqrt{k_t^2 - \beta^2} \tag{4.19}$$

for both polarizations. Solving the circuit for the voltage v_2 at the interface (which represents the electric field) it is found:

$$v_{2TX} = \frac{2v_{TX}e^{(-jk_{z1}h)}}{1 + e^{(-j2k_{z1}h)}\left(\frac{Z_{TX1}(Z_{TX}^{(S)}+Z_{TX})}{Z_{TX}^{(S)}Z_{TX}}\right)(1 - e^{(-j2k_{z1}h)})} \tag{4.20}$$

upna
Universidad Pública de Navarra
Nafarroako Unibertsitate Publikoa

where $Z_{TM} = \zeta k_{z0}/k$, $Z_{TE} = \zeta k/k_{z0}$, $Z_{TM1} = \zeta_1 k_{z1}/k_1$, $Z_{TE1} = \zeta_1 k_1/k_{z1}$, $k_1 = \sqrt{\varepsilon_r}k$. The conditions for amplitude balancing in Eq. (4.7) becomes $v_{2TM}/v_{TM} = v_{2TE}/v_{TE}$, from which it can be obtained:

$$\frac{v_{TE}}{v_{TM}} = \frac{j\csc(2k_{z1}h)\cot(2k_{z1}h) - \left(\frac{Z_{TE1}(Z_{TE}^{(S)}+Z_{TE})}{Z_{TE}^{(S)}Z_{TE}}\right)}{j\csc(2k_{z1}h)\cot(2k_{z1}h) - \left(\frac{Z_{TM1}(Z_{TM}^{(S)}+Z_{TM})}{Z_{TM}^{(S)}Z_{TM}}\right)} = g(\beta) \tag{4.21}$$

When the excitations are given by simple magnetic dipoles (in practice electrically small slots in the ground plane) the ratio in Eq. (4.21) directly provides the relation needed between the magnetic dipole moments. In general, when the structure is excited by an aperture on a ground plane, Eq. (4.3) is applied to the TE and TM components of the Fourier spectrum of the aperture field, evaluated at $k_\rho = \sqrt{k_x^2 + k_y^2} = \beta$.

If the feeding is implemented by an open ended circular waveguide of radius a excited by a TE_{11} mode, its electric field spectrum $\mathbf{E}_t(\mathbf{k}_t, a)$ (where $\mathbf{k}_t$ denotes the couple of spectral variable k_x, k_y) possesses a closed form $\mathbf{F}_t(\mathbf{k}_t, a)$ written as [87]:

$$\begin{aligned} F_\rho(k_\rho) &= C_1 a J_1(k_\rho a) \\ F_\varphi(k_\rho) &= C_2 \frac{a^2}{x_{11}^{'\,2} - (k_\rho a)^2}(\mathrm{J}_0(k_\rho a) - (\mathrm{J}_2(k_\rho a)) \end{aligned} \tag{4.22}$$

where the variable C_1 in radial spectral component $F_\rho(k_\rho)$ is calculated as $C_1 = \frac{8\pi \mathrm{J}_1(x_{11}^{'})}{k_\rho x_{11}^{'}}$ and the variable C_2 in angular spectral component $F_\varphi(k_\rho)$ is $C_2 = \frac{8\pi x_{11}^{'} \mathrm{J}_1(x_{11}^{'})}{2}$. J_n denotes the Bessel function of the first kind of order n, $\mathrm{J}_n^{'}$ is its derivative and $x_{np}^{'}$ is the p-th zero of $\mathrm{J}_n^{'}$.

In such a case, Eq. (4.21) becomes:

$$\frac{\mathbf{F}_t(\mathbf{k}_t, a) \cdot (\hat{\mathbf{z}} \times \hat{\mathbf{k}}_\rho)}{\mathbf{F}_t(\mathbf{k}_t, a) \cdot \hat{\mathbf{k}}_\rho} = g(\beta) \tag{4.23}$$

The left hand side only depends on $k_\rho = \sqrt{\mathbf{k}_t \cdot \mathbf{k}_t} = \sqrt{k_x^2 + k_y^2} = \beta$. Equation (4.23) establishes, at each frequency, the optimal radius a of the circular waveguide which guarantees perfect amplitude balancing of the two excited TM and TE modes (continuous line in Fig. 4.6).

However, TE_{11} mode aperture has been proven to be inefficient from the SW excitation point of view, since the space-wave radiation affects considerably to the radiation pattern (see Fig. 4.13). Therefore, it is necessary to introduce a corrugated hat on top of the waveguide (see Fig. 4.7), which prevents the flow of currents on top of the metal and consequently

upna
Universidad Pública de Navarra
Nafarroako Unibertsitate Publikoa

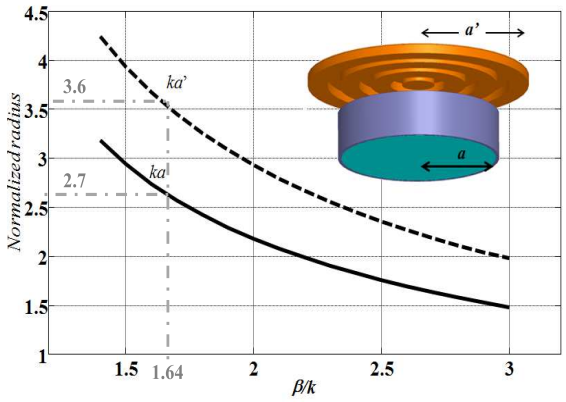

Fig. 4.6. Optimum radius ensuring perfect amplitude balance vs. the normalized SW wavenumber: a open ended waveguide (continuous line), configuration with corrugated hat placed on top of an open ended waveguide (dashed line).

drastically reduces space-wave contribution. Thus, the coupling efficiency from the TE_{11} mode of the circular waveguide to the SWs in the MTS is enhanced thanks to the hat inclusion.

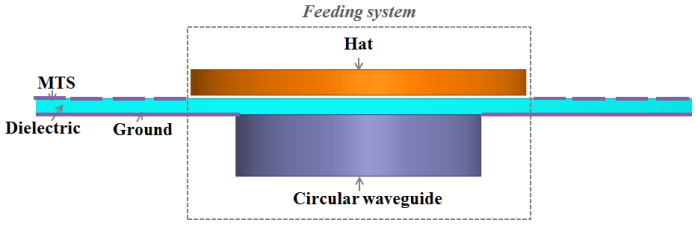

Fig. 4.7. Details of the employed feeding system.

The outer radius dimension of the corrugated hat, $a^{'}$, is a bit larger than the open ended waveguide dimension, a. The relation $a^{'}/a$ can be controlled in order to balance the TM,TE coupling. The global feeding system can be described invoking a patch antenna model: based on the fringe field an equivalent magnetic current ring can be defined, with radius equal to the corrugated disk one and effective width equal to the thickness of the substrate. In order to find the new balance conditions, an appropriate modification must be introduced to the Eq. (4.23), which involves the derivative of the electric field at the rim of the waveguide:

$$\frac{\frac{\partial \mathbf{F}(\mathbf{k}_t,a^{'})}{\partial a^{'}} \cdot (\hat{\mathbf{z}} \times \hat{\mathbf{k}}_\rho)}{\frac{\partial \mathbf{F}(\mathbf{k}_t,a^{'})}{\partial a^{'}} \cdot \hat{\mathbf{k}}_\rho} = g(\beta) \tag{4.24}$$

where,

upna
Universidad Pública de Navarra
Nafarroako Unibertsitate Publikoa

$$\begin{aligned}
\frac{\partial F_\rho}{\partial a} &= C_1 \mathrm{J}_1(k_\rho a) + C_1 a\left(k_\rho \mathrm{J}_0(k_\rho a) - \frac{\mathrm{J}_1(k_\rho a)}{a}\right) \\
\frac{\partial F_\varphi}{\partial a} &= \frac{2C_2 a(\mathrm{J}_0(k_\rho a) - \mathrm{J}_2(k_\rho a))}{{x'_{11}}^2 - (k_\rho a)^2} - \\
&= \frac{C_2 a^2\left(2k_\rho \mathrm{J}_1(k_\rho a) - \frac{2\mathrm{J}_2(k_\rho a)}{a}\right)}{x'_{11} - (k_\rho a)^2} + \\
&= \frac{2C_2 a^3 k_\rho^2(\mathrm{J}_0(k_\rho a) - \mathrm{J}_2(k_\rho a))}{(x_{11}^2 - (k_\rho a)^2)^2}
\end{aligned} \tag{4.25}$$

The corrugated hat radius a' which satisfies Eq. (4.24) is represented in Fig. 4.6 in dashed line.

4.3.2 Feed excitation: CP generation with a Septum-OMT polarizer

Another critical design consideration to take into account for the implementation of the feeding system is related with the circularly polarized field excitation. In order to provide RHCP and LHCP field from the excitation located in the center of the structure, two septum orthomode transducer (OMT) polarizers have been designed.

As the main target of this thesis dissertation is to proof the correct behavior of the dual circularly polarized broadside MTS antenna, the first proposed excitation is a large solution (144mm=6.4λ_0). It is composed by a metallic stepped single ride with 5 steps located inside an air-filled square waveguide. Two lateral flanges are extended to WR-60 waveguide input ports (denoted as port 2 and port 3 in Fig. 4.8). Besides, a taper is included to match the field at the output port of the square waveguide (Port 1) with the circular waveguide (AD1000 filled) at the center of the ground plane of the MTS antenna. More details of the modeling and validation results are drawn in section 4.4.4.

The feeding system has been optimized and a second innovative compact efficient septum-OMT polarizer (Fig. 4.9(a)) has been developed. The main advantage of this solution in comparison with the first design is its reduced dimension (18.73mm=0.8λ_0). Nevertheless, its fabrication and embedding is significantly complicated, which makes this solution more risky. This device possesses two input ports (port 2 and port 3 in Fig. 4.9(b)) located in opposite sides of a circular waveguide and an output port (Port 1) which will be connected with the center of the ground plane of the MTS antenna. In this design, the circular waveguide has a metallic stepped single ride in the center with 4 steps and it is filled with arlon AD1000 ($\varepsilon_r = 10.2$), the same dielectric as the MTS antenna one. From the circular waveguide, two

upna
Universidad Pública de Navarra
Nafarroako Unibertsitate Publikoa

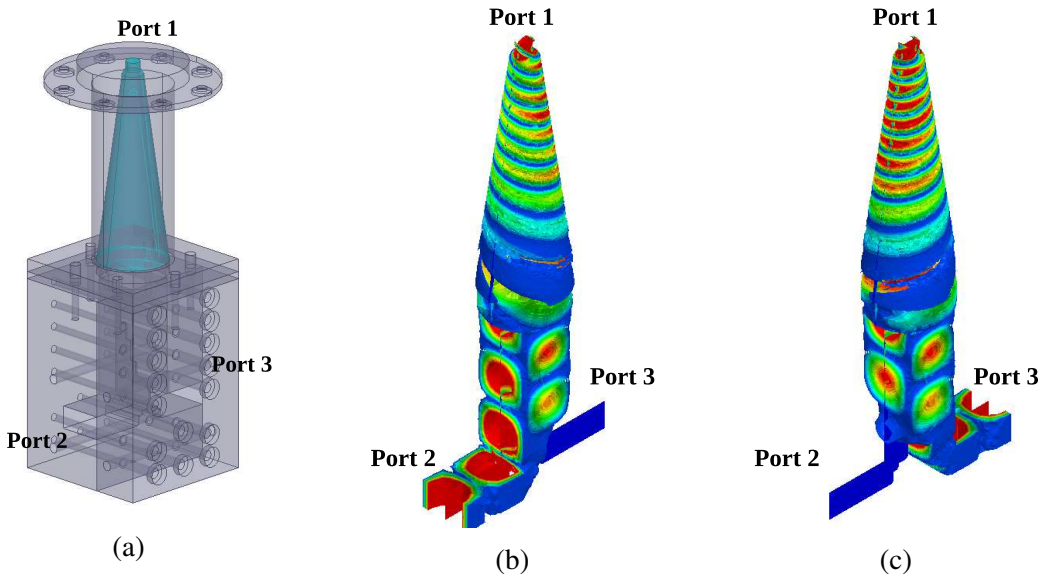

Fig. 4.8. Field excitation on the air-filled septum OMT design: (a) Port 2 on and (b) Port 3 on.

dielectric junctions of arlon AD1000 are extended towards the input ports, in which two SMA connectors are plugged in. As the SMA connectors are teflon-based ($\varepsilon_r = 2.1$), they have been appropriately re-shaped to match and fit with the junctions. Dimension details of the proposed compact solution and its characterization are given in section Fig. 4.4.4.

In both septum-OMT solutions, when one of the input ports is excited, two mutually orthogonal linearly polarized TE_{11} modes are generated at the output port with $\pm 90^\circ$ phase shift, depending on the selected excitation port. Exciting port 3, two TE_{11} modes with a 90° phase shift are excited in Port 1 obtaining LHCP, as it can be seen in Fig. 4.8(c) and Fig. 4.9(c). On the other hand, RHCP is obtained at Port 1 when port 2 is on (see Fig. 4.8(b) and Fig. 4.9(d)).

4.4 Complete antenna design

4.4.1 Ideal MTS design

Based on the previous theoretical considerations, a dual circularly polarized MTS antenna has been designed working at 13.5GHz ($\lambda_0 = 22.2mm$). As a preliminary analysis, the MTS has been modeled by means of an ideal continuous modulated impenetrable anisotropic TM,TE impedance, characterized by the theoretical parameters described in Table 4.1. The

upna
Universidad Pública de Navarra
Nafarroako Unibertsitate Publikoa

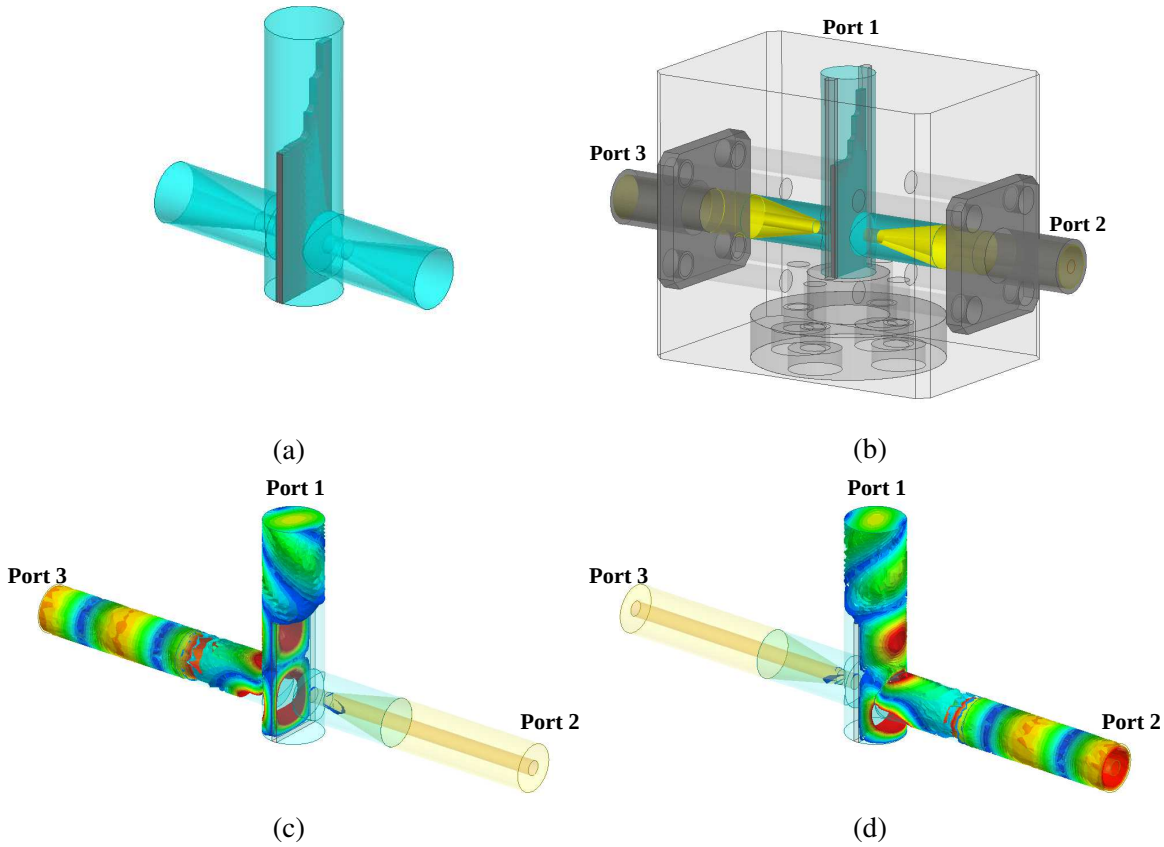

Fig. 4.9. (a) General view of the septum orthomode transducer (OMT) polarizer: stepped ride and arlon AD1000 dielectric ports. b) Details of the input ports (port 2 and port 3) excited with SMA connectors, output port (Port 1) and the septum encapsulation. (c) LHCP is obtained at Port 1 when port 3 is excited. (d) RHCP is obtained at Port 1 when port 2 is excited.

upna
Universidad Pública de Navarra
Nafarroako Unibertsitate Publikoa

distribution properties of the ideal continuous TM,TE impenetrable reactances can be seen in Fig. 4.10.

mode type	η	m	d/λ_0
TM	1.31	0.18	0.61
TE	-0.76	0.34	0.58

Table 4.1 Surface impedance modulation parameters.

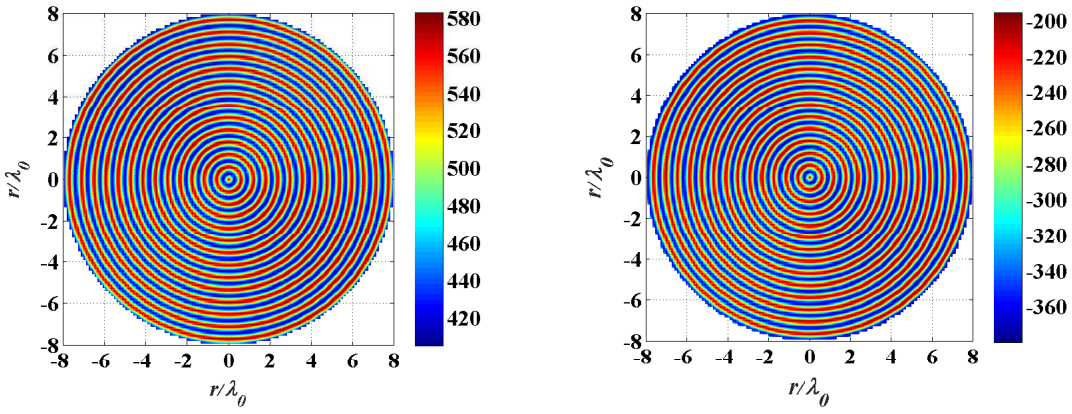

(a) (b)

Fig. 4.10. Distribution properties of the continuous impenetrable reactances: (a) $X_{\rho\rho}$ related with TM mode and (b) $X_{\varphi\varphi}$ with TE.

The analysis of the ideal MTS has been carried out with the commertial software ANSYS HFSS [70], which allows to place an equivalent ideal penetrable anisotropic impedance sheet on top of a grounded dielectric slab. In this configuration, arlon AD-1000 has been used as substrate, characterized by $\varepsilon_r = 10.2$ and thickness $h = 1.27mm = \lambda_0/17.5$. The continuous sinusoidal modulation has been discretised with a cartesian lattice, where the cell size is $u = 3.14mm = \lambda_0/7$. The radius of the complete structure is $r = 177mm = 8\lambda_0$. Due to the circular symmetry of type "body of revolution 1" BoR1 [88] (namely, excited with an azimuthal sine or cosine function), the circular co-pol and cross-pol patterns can be approximated by the linear co-pol and cross-pol cut at $\varphi = 45°$. Therefore, a quarter of the structure with appropriate symmetry boundary condition can be studied and consequently, the simulation time and required resources are significantly simplified.

Furthermore, the feed is designed like the one in Fig. 4.7, with the radius of the circular waveguide set to $a = 9.6mm$ ($ka = 2.7$) and the outer radius of the corrugated hat on top equal to $a^{'} = 12.8mm$ ($ka^{'} = 3.6$) ($\beta/k = 1.64$, green dashed lines in Fig. 4.6).

upna
Universidad Pública de Navarra
Nafarroako Unibertsitate Publikoa

The near field components at 13.5GHz obtained over the quarter of the metasurface excited with a TE_{11} mode oriented towards y-axis in the circular waveguide are shown in Fig. 4.11. As it can be seen in this figure, when the TE_{11} mode is excited towards y-axis, the TM,TE modes contribution generates a linearly polarized field $\mathrm{Re}(E_y)$ and the $\mathrm{Re}(E_x)$ field component is negligible. The results are in agreement with the theoretical basics in Eq. (4.8). Besides, the $\mathrm{Re}(E_y)$ field purity denotes also that both the TM and TE modes are excited on the structure decoupled and with the same amplitude and phase velocities, fulfilling the theoretical balancing conditions for the MTS and feeding system.

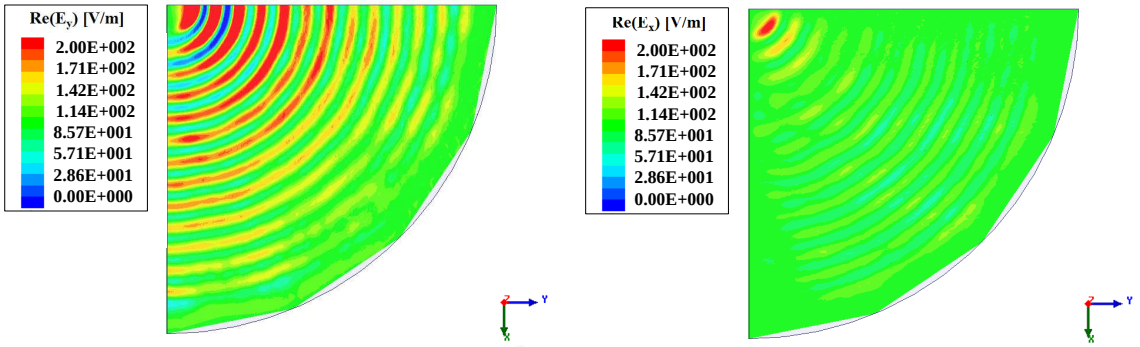

(a) (b)

Fig. 4.11. Near field components of the quarter structure of the ideal MTS at 13.5GHz: (a) $\mathrm{Re}(E_y)$. (b) $\mathrm{Re}(E_x)$. A corrugated hat is located on top of the circular waveguide excited with a TE_{11} mode towards y-axis.

The copolar and crosspolar radiation patterns (in the $\varphi = 45^\circ$ cut) obtained with the ideal metasurface at 13.3GHz (red), 13.5GHz (green) and 13.6GHz (blue) (BW 2.23%) are depicted in Fig. 4.12. A maximum directivity of 31.28dBi is obtained at 13.5GHz (green line in Fig. 4.12(d)). The XP component (DirL3X) is 18dBs below the CO component (DirL3Y) in Fig. 4.12(c). The corresponding aperture efficiency is about 50% at the central frequency. Due to the rotational symmetry of the problem, the complementary result is obtained for the other polarization (TE_{11} in x axis) readjusting the symmetry conditions.

Ideal MTS discussion

Based on the simulation results it is concluded that the theoretical basics developed are valid to obtain the desired broadside dual CP radiation with a single layer MTS antenna.

For completeness, the radiation pattern at 13.5GHz obtained with the same ideal metasurface configuration presented in Fig. 4.12, but in absence of the corrugated top cover is given in Fig. 4.13. The large cupol-type pedestal added to the main beam in Fig. 4.13 illustrates the waveguide direct radiation. This effect reduces significantly the antenna gain since the

upna
Universidad Pública de Navarra
Nafarroako Unibertsitate Publikoa

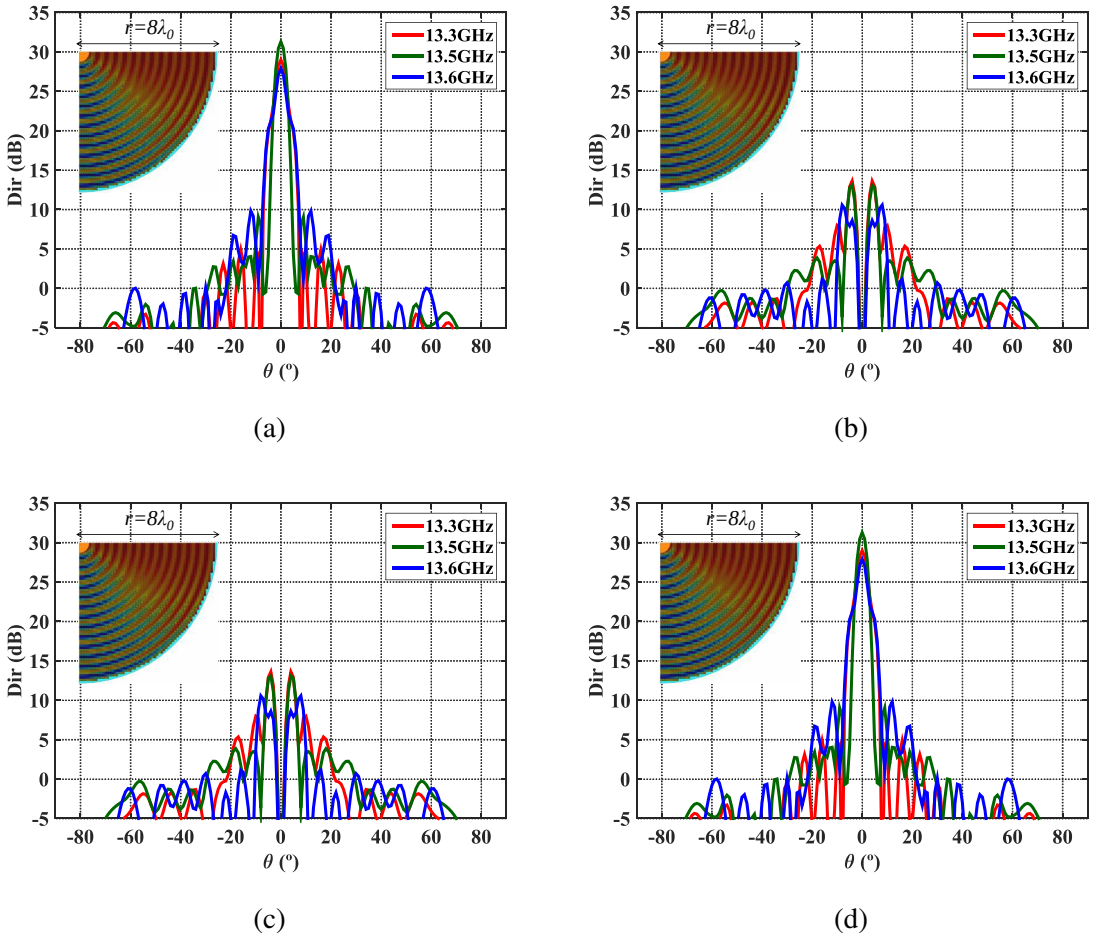

Fig. 4.12. Simulated radiation patterns in the $\varphi = 45°$ cut obtained with the quarter of the ideal MTS at 13.3GHz (red), 13.5GHz (green) and 13.6GHz (blue). TE_{11} mode towards y axis: (a) co-pol (DirL3Y) and (b) cross-pol (DirL3X). TE_{11} mode towards x axis: (c) co-pol (DirL3X) and (d) cross-pol (DirL3Y).

upna
Universidad Pública de Navarra
Nafarroako Unibertsitate Publikoa

space radiation subtracts power to the main lobe and decrease the SW coupling efficiency. This result justifies the inclusion of the corrugated hat on top of the circular waveguide.

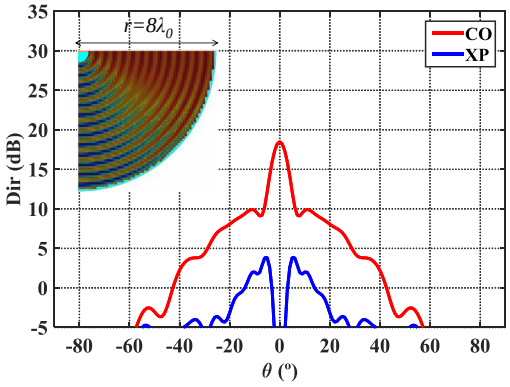

Fig. 4.13. CO (red) and XP (blue) radiation patterns at 13.5GHz on the quarter of the ideal MTS obtained by radiation of the open ended circular waveguide without corrugation hat on top.

4.4.2 Synthesis of the MTS

The proof-of-concept simulation of the ideal MTS presented in the previous section 4.4.1 corroborates the theoretical basics. The next step is the synthesis of the structure using subwavelength printed elements, being able to control the polarization performance. In this section, the properties considered for the pixel selection are described and the followed synthesis procedure is explained in detail. Moreover, simulation results of the MTS implemented with pixels are shown and discussed.

Pixel selection: dispersion analysis and impedance maps calculation

The ideal metasurface shown in section 4.4.1 (see Fig. 4.10), is characterized by a sinusoidally modulated TM,TE surface reactance in radial direction, with a smooth variation. Therefore, the local wavenumber and average reactance values corresponding to each point of the modulation, can be retrieved from a periodic pixel (with given parameters such as size and rotation) that best matches each local reactance value [29].

Establishing periodic boundary conditions in the four vertical walls of a unitary cell composed by the selected pixel geometry, the TM and TE wavenumbers can be extracted using the eigensolver of the commercial ANSYS HFSS[70] software. In order to find the geometry that best fits the surface reactance requirements of the proposed solution, several features have been taking into account:

upna
Universidad Pública de Navarra
Nafarroako Unibertsitate Publikoa

- The desired pixels have to be anisotropic: the geometry must allow independent control of TM and TE contributions.
- The dispersion curves for TM and TE modes should be close to each other around the working frequency to enable the phase-matching condition defined in Eq. (4.3).
- The pixel-elements have to be small enough in terms of wavelength and their axes must be aligned with the wave vector to avoid coupling between modes and consequent introduction of cross-diagonal terms in the reactance tensor.

Taking into account these requirements, the selection of the patch geometry has been made based on the analysis carried out in chapter 3 (section 3.3). The optimum patch, shown in Fig. 4.14, is composed by a elliptical subwavelength element with an asymmetric cross-shaped aperture inside.

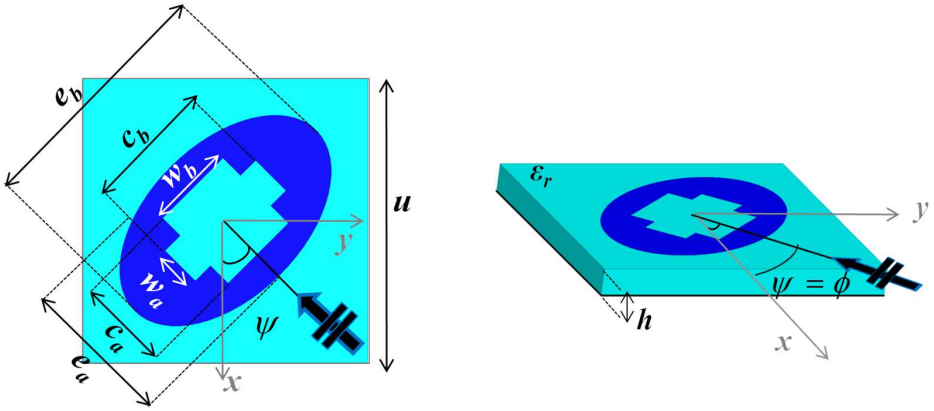

(a) (b)

Fig. 4.14. Unitary cell geometry. (a) Top view: Details of the elliptical metallic element used for the MTS synthesis, ψ denotes its rotation angle inside the unit cell. (b) 3D view, double arrow indicates SW incidence along ϕ.

The geometrical parameters used in the design are: ellipse size normalized to the unitary cell dimension (e_b/u), ratio between the ellipse axes (e_a/e_b) and normalized dimensions of the asymmetric cross aperture (c_a/e_a),(c_b/e_b),(w_a/u),(w_b/u). Several parametric dispersion analyses have been performed to characterize their effect on TM and TE SW propagation. The element rotation inside the unit cell ψ is fixed to be the same as the SW propagation angle ϕ (Fig. 4.14(b)).

As an example, Fig. 4.15 presents the dispersion curves in the case of the most representative pixels with unit cell dimension $u = 3.14mm(\lambda_0/7)$ at the operating frequency (13.5GHz). Employed grounded dielectric slab is arlon AD-1000 with thickness $h = 1.27$mm.

upna
Universidad Pública de Navarra
Nafarroako Unibertsitate Publikoa

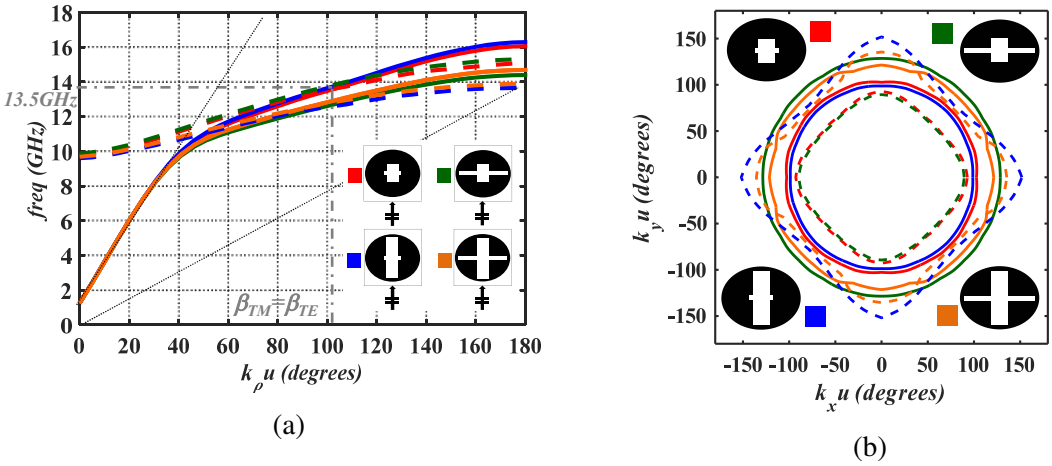

(a) (b)

Fig. 4.15. (a) TM(continuous lines) and TE(dashed lines) dispersion curves as a function of frequency when $\phi = \psi = 0^\circ$ and (b) isofrequency dispersion curves at 13.5GHz when $\phi = \psi$, for 4 different pixels with the following parameters: $(e_b/u) = 0.9$, $(e_a/e_b) = 0.85$, $(w_a/u) = 0.15$,$(w_b/u) = 0.3$; (c_a/e_a),(c_b/e_b) are (0.6,0.6) red lines; (0.6,0.9) green lines; (0.85,0.6) blue lines; (0.85,0.9) orange lines.

As shown in Fig. 4.15(a), for the $\phi = \psi = 0^\circ$ case, the curves associated with TM and TE SWs dispersion cross at the working frequency ($\beta_{TM} = \beta_{TE}$ at 13.5GHz), ensuring the desired phase matching condition expressed in Eq. (4.3). The geometrical variations of (e_b/u) and (c_b/e_b) mostly affect the TM mode. On the other hand, (c_a/e_a) and (w_b/u) mainly affect the TE wavenumber. Therefore, it allows quite independent control over the TM and TE modes dispersion properties, a essential feature to modulate independently the surface impedance corresponding to each mode. It has to be also mentioned that the frequency dispersion is more significant for the TE mode, which works closer to its resonance. Fig. 4.15(b) shows the spatial dispersion characteristics of both TE and TM SWs for different impinging angles (ϕ) at 13.5GHz, for the same pixel geometry dimensions as in Fig. 4.15(a) and setting the rotation of the pixel aligned with each SW incidence angle $(\psi = \phi)$. It is clear that the TE curve is much more spatially dispersive than the TM curve and it depends on the patch rotation.

In conclusion, the main drawbacks of this patch geometry are the fast frequency dispersive nature and the spatial dispersion shown by the TE mode. The first feature impacts on the operational bandwidth of the synthesized MTS because the phase matching of the modes is reached in a very narrow bandwidth. Besides, possible shifting on frequency implies significant cumulative aperture phase error in large structures that reduces directly the achievable gain. Moreover, due to the fact that the TE seems to be sensitive to the patch

upna
Universidad Pública de Navarra
Nafarroako Unibertsitate Publikoa

rotation inside the cell (specially for the larger patch sizes), it is necessary to pay special attention for the MTS synthesis not only in radial direction to meet the required surface impedance modulation, but also in azimuthal direction to compensate locally the TE spatial dispersion.

With this information, the corresponding surface impedance has been calculated following the procedure explained in chapter 3 (section 3.3.2). As the modes impinge the patch towards its symmetry axes, their purity is kept and the crosspolar contribution of the tensor component is negligible.

A data base of the different surface impedance values presented by pixels depending on the geometrical possible variations and different $\phi = \psi$ angles has been obtained. The required surface impedance values corresponding to each (ρ_i, φ_i) position of the discretised MTS structure can be related with a pixel dimension from the data base. Fig. 4.16 and Fig. 4.17 show X_{TM} and X_{TE} values at 13.5GHz for different pixel shapes when $\phi = \psi = 0°$. Higher values of (c_b/e_b) are associated with higher TM reactance levels. A similar trend is found when the pixel-element is larger inside the same cell (i.e., increasing (e_b/u)). On the other hand, higher values of (e_a/e_b), (c_a/e_a) and (w_b/u) increase considerably the TE reactance.

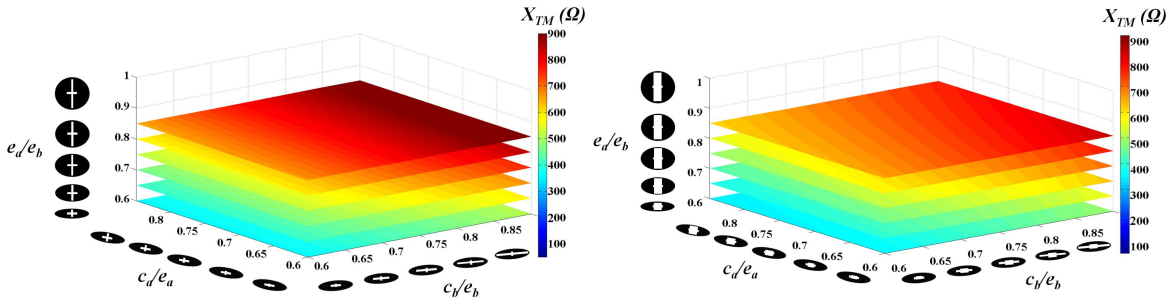

Fig. 4.16. Impedance maps of TM mode at 13.5GHz when $\phi = \psi = 0°$, with different patch geometry parametrization: (e_a/e_b), (c_a/e_a), (c_b/e_b) and (a) $(w_b/u) = 0.15$ and (b) $(w_b/u) = 0.3$. Fixed patch parameters are: $(e_b/u) = 0.9$ and $(w_a/u) = 0.15$.

upna
Universidad Pública de Navarra
Nafarroako Unibertsitate Publikoa

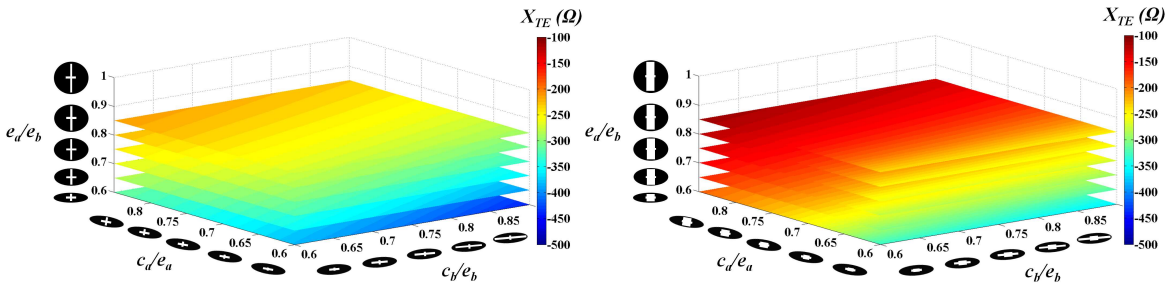

(a) (b)

Fig. 4.17. Impedance maps of TE mode at 13.5GHz when $\phi = \psi = 0°$, with different patch geometry parametrization: (e_a/e_b), (c_a/e_a), (c_b/e_b) and (a) $(w_b/u) = 0.15$ and (b) $(w_b/u) = 0.3$. Fixed patch parameters are: $(e_b/u) = 0.9$ and $(w_a/u) = 0.15$.

Synthesis error

The MTS implementation has been carried out employing the pixel geometries depicted in the previous section (Fig. 4.14). Taking into account manufacturing limitations, the minimum printable dimension of the pixels has been readjusted to $100\mu m$. In such a way, wet-etching effect that appears in the photo lithography process for copper with a thickness of $19\mu m$ is imperceptible. The modulation of the surface impedance has been designed following the ideal MTS reactance distribution for TM and TE modes detailed in Table 4.1. At each (ρ_i, φ_i) position of the antenna, the pixel geometry that best matches the theoretical reactance values is selected, based on the information obtained from the impedance characterization of periodic pixel cells. Fig. 4.18 shows the details of the pixel geometry parameters (c_a/e_b), (c_b/e_b), (w_b/u) and (e_a/e_b) selected to synthesize the MTS. The radius of the circular antenna is $r = 8\lambda_0 = 177mm$.

The predictable TM,TE surface impedance synthesis error related with the implementation proposed in Fig. 4.18 is shown in Fig. 4.19. As it can be seen, the synthesis error can be considered negligible; around $\phi = 45°$ angle the surface impedance synthesis error for the TE rises to 12% due to the challenging high impedance requirement for this mode (high modulation index must be synthesized).

The entire antenna configuration composed by this metasurface assembled with the optimized waveguide and corrugated hat (described in section 4.3) is illustrated in Fig. 4.20.

upna
Universidad Pública de Navarra
Nafarroako Unibertsitate Publikoa

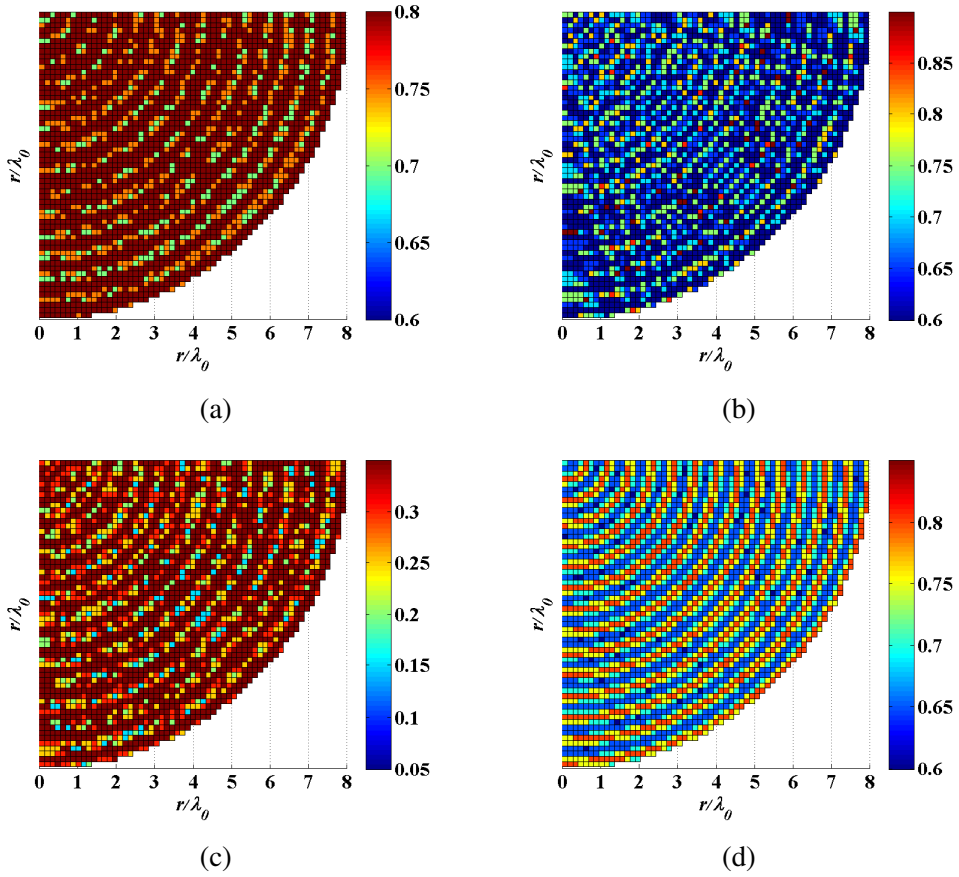

Fig. 4.18. Patch geometry ($u = \lambda_0/7 = 3.14mm$) parametrization details of the synthesized MTS: (a) (c_a/e_b), (b) (c_b/e_b), (c) (w_b/u) and (d) (e_a/e_b), to comply with the required surface impedance at each discretized position.

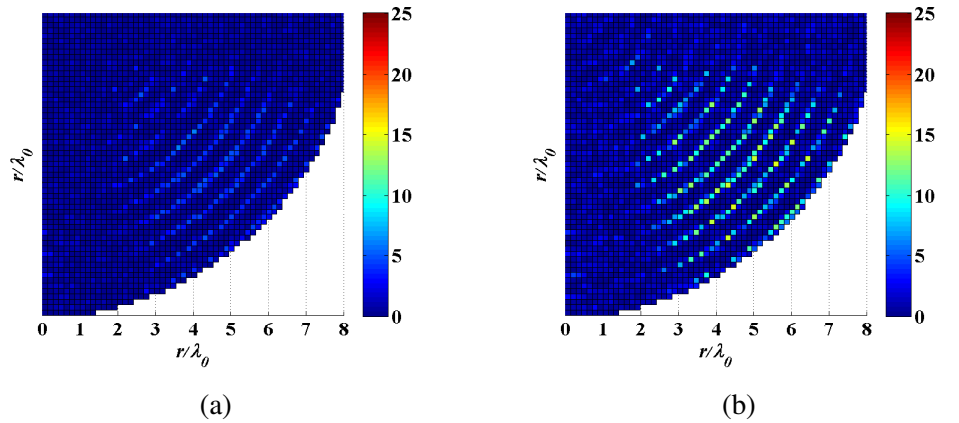

Fig. 4.19. Surface impedance synthesis error (%) of the: (a) TM mode and (b) TE mode.

upna
Universidad Pública de Navarra
Nafarroako Unibertsitate Publikoa

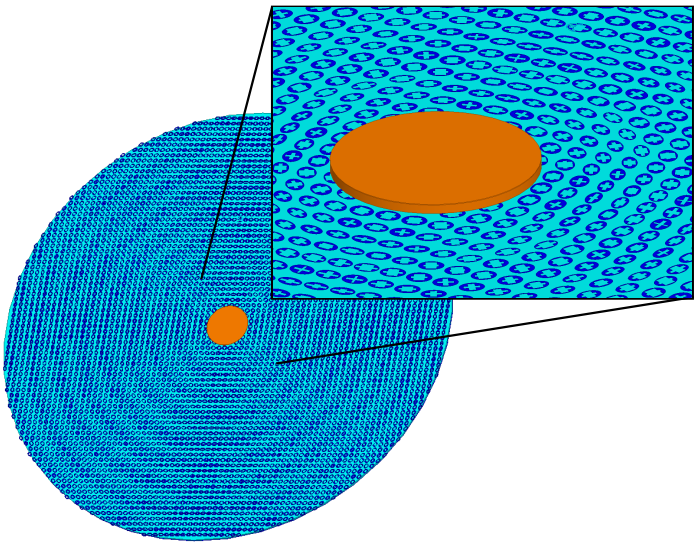

Fig. 4.20. Top view of the complete MTS antenna ($r = 8\lambda_0 = 177mm$) implemented with elliptical pixels with a cross-shaped aperture inside. The inset shows the corrugated hat located on top of the circular waveguide.

Radiation properties

As in the case of the ideal MTS, one quarter of the structure (Fig. 4.20) has been analyzed employing symmetries. The full wave analysis has been launched in the workstation HP Z800, with 192GB RAM, 2 processors at 3.47GHz (X5690 with 12 cores). Converged solution is obtained with a mesh of 2.5 million tetrahedra. The required simulation time is about 3.5 hours for the generation of the metasurface composed by about 3000 patches. Approximately 14 hours for the analysis of the structure and 2 hours to obtain the information at each discrete frequency point have been needed.

The co-polar and cross-polar components cuts (corresponding to the RHCP and LHCP components) of the radiated field at 13.3GHz, 13.4GHz and 13.5GHz are shown in Fig. 4.21(a) and Fig. 4.21(b). Besides, Fig. 4.21(c) shows frequency dependence of the directivity and gain. As it can be seen in Fig. 4.21 a maximum directivity of 27.3dBi has been obtained at 13.4GHz with cross-polar component 21dBs below the CO. The aperture efficiency obtained with this configuration is 21.4%. Gain over 25dBi (radiation efficiency %70) is obtained in a 1.5% fractional bandwidth.

MTS synthesis discussion

A single layer MTS antenna with a broadside radiation beam at Ku-band and dual circular polarization has been implemented, based on the theoretical considerations drawn in section

upna
Universidad Pública de Navarra
Nafarroako Unibertsitate Publikoa

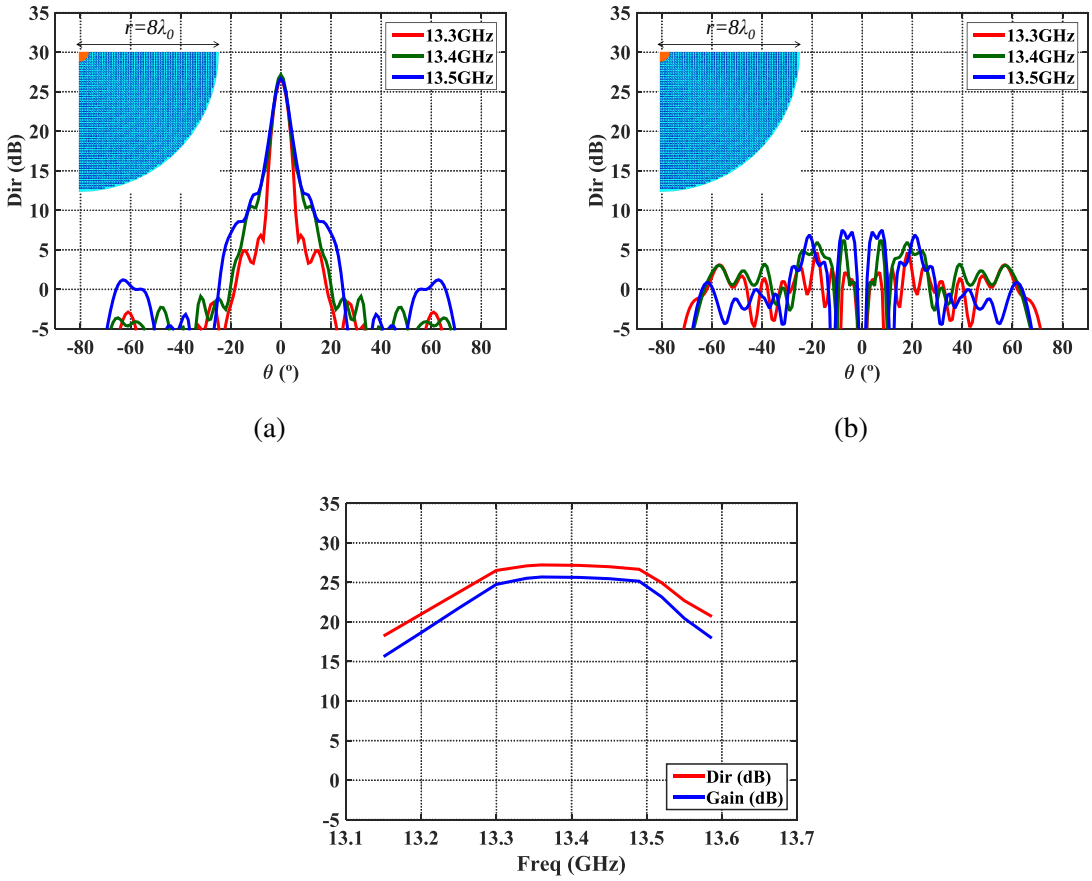

Fig. 4.21. Simulated co-pol (a) and cross-pol (b) radiation patterns($\varphi = 45°$ cut) obtained with the MTS synthesized with pixels and corrugated hat located on top of the circular waveguide, at 13.3GHz (red), 13.4GHz (green) and 13.5GHz (blue). (c) Frequency dependence of directivity and gain.

upna
Universidad Pública de Navarra
Nafarroako Unibertsitate Publikoa

4.2. The feed system is composed by an optimized circular waveguide with a corrugated hat on top shown in Fig. 4.6. A septum-OMT polarizer can be employed to excited the required TE_{11} modes in phase quadrature.

The proposed first implementation for the MTS proves that the theoretical surface impedance characterization of the TM and TE modes detailed in Fig. 4.10 has been carried out following a correct synthesizing procedure and that the employed pixel geometry is appropriate. As expected, the structure operates correctly on the interaction between the two cylindrical-wavefront SWs, ensuring that the modes propagate on the structure decoupled and fulfilling both the phase and amplitude matching conditions. The correct excitation of both modes is also a consequence of the suitable design of the selected circular waveguide, which fulfills the feed balancing requirement. The corrugated hat on top increases the SW excitation efficiency (Fig. 4.22).

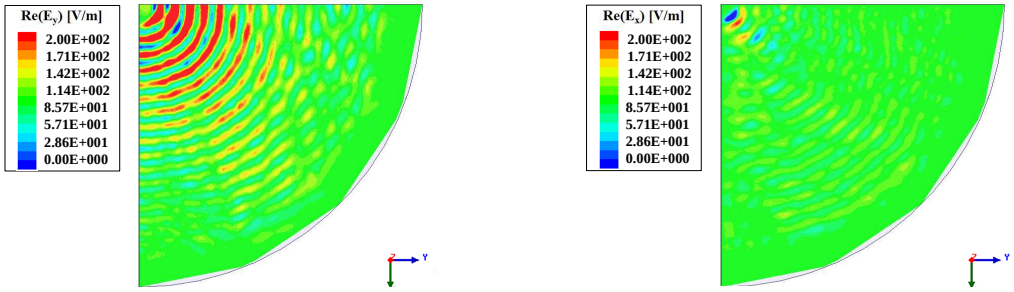

(a) (b)

Fig. 4.22. Near field components of the MTS implemented with pixels at 13.5GHz: (a) $\mathrm{Re}(E_y)$. (b) $\mathrm{Re}(E_x)$. A corrugated hat is located on top of the circular waveguide excited with a TE_{11} mode towards y-axis.

In agreement with the ideal case in Fig. 4.11(a), Fig. 4.22 shows that the only field component excited on the structure synthesized with pixels and excited with the TE_{11} mode (towards y-axis) is $\mathrm{Re}(E_y)$, with a sinusoidal profile in radial direction. In consequence, it can be concluded that the MTS implemented with pixels satisfies appropriately the theoretical phase and polarization balancing conditions.

Nevertheless, as shown in Fig. 4.21, the maximum achievable aperture efficiency with the proposed solution is 21.4%, which denotes a considerable drop in relation to the aperture efficiency of 50% obtained with the ideal configuration (Fig. 4.12). The $\varphi = 0°, 45°, 90°$ cuts of the radiation pattern at 13.4GHz are shown in Fig. 4.23(a). It can be seen that there are differences between $\varphi = 0°$ and $\varphi = 90°$ cuts. Hence, the cause of this drop is related with the beam azimuth asymmetry.

One of the reasons that could lead to the beam azimuth asymmetry in Fig. 4.23(a) and the consequent deterioration of the XP could be the unbalancing of the leakage parameters

upna
Universidad Pública de Navarra
Nafarroako Unibertsitate Publikoa

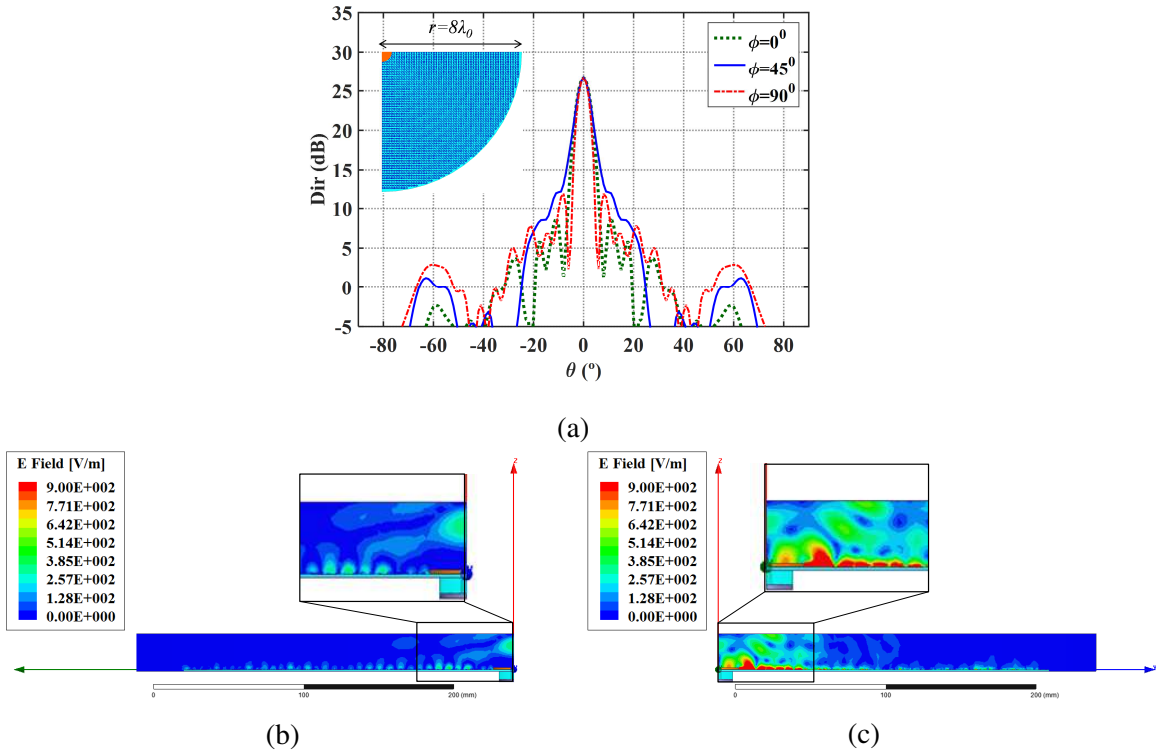

(a)

(b)

(c)

Fig. 4.23. (a) $\varphi = 0°, 45°, 90°$ cuts of the radiation pattern at 13.5GHz. (b) Near E field at *xz*-plane (TE mode contribution). (c) Near E field at *yz*-plane (TM mode contribution). TE_{11} oriented towards *y*-axis is excited at the circular waveguide with a corrugated hat located on top.

upna
Universidad Pública de Navarra
Nafarroako Unibertsitate Publikoa

(α_{TM} and α_{TE}). However, in this configuration the modulation indexes characterization for each TM and TE mode has been carefully considered and the unbalanced radiation effect is avoided. The origin of this problem has been elucidated analyzing the near field components at different planes: Fig. 4.23(b) and Fig. 4.23(c) show the near field at *xz*-plane and *yz*-plane, respectively. Taking into account Eq. (4.6) it is known that when the TE_{11} mode is excited in the waveguide aligned with *y*-axis, the field information at *xz*-plane of the complete structure is related only with the TE mode contribution to the radiation pattern. On the other hand, *yz*-plane field corresponds only with the TM contribution. It can be seen in Fig. 4.23(c) that the introduced corrugated hat, which has been optimized theoretically together with the circular waveguide in the ideal case to increase the SW coupling and aperture efficiency, is affecting the TM mode contribution to the radiation pattern. Therefore, side lobes are generated (see $\varphi = 90^{\circ}$ cut in Fig. 4.23(a)).

The solution to this problem lies in the readjustment of the complete feeding system to obtain a more compact design. The hat and the waveguide radius dimensions have to be redesigned.

4.4.3 Hat and waveguide dimension readjustment

The hat reduction is necessary to minimize its effect in the radiation pattern and improve the efficiency of the proposed solution. It has to be mentioned that the selection of the new hat has been realized considering also the implementation of the septum OMT polarizer. The readjustment must be done considering all the constituent parts, as the response of the whole feeding system must ensure the proper excitation of the TE_{11} modes in phase quadrature and also the balanced excitation of the TM and TE modes in the MTS, as demonstrated in section 4.3.1.

Therefore, the waveguide radius $a = 9.6mm$ (presented previously in Fig. 4.7) has been reduced to a radius $a = 2.54mm$, in order to avoid possible higher order modes interaction when exciting the septum OMT. With the new waveguide dimension, the higher order modes remains below 25dBs. Several minimized hat geometries (see Fig. 4.24) have been placed on top of the circular waveguide with the reduced radius to excite the MTS configuration presented in Fig. 4.18. Near field distributions obtained with the different hats at the working frequency are illustrated in Fig. 4.25. It can be seen that the TM and TE modes contribution is balanced with the minimized cone-type hat with radius $a^{'} = 8mm$ and thickness $6mm$ presented in Fig. 4.24(d). In conclusion, this hat can be employed to substitute the larger corrugated hat model with radius $a^{'} = 12.8mm$ (shown previously in Fig. 4.7).

upna
Universidad Pública de Navarra
Nafarroako Unibertsitate Publikoa

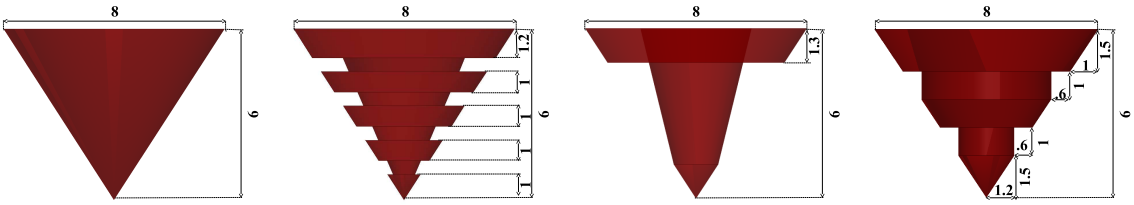

Fig. 4.24. Details of different minimized cone-type hats with: (a) smooth profile, (b) 5 corrugations, (c) a single corrugation and (d) 3 corrugations.

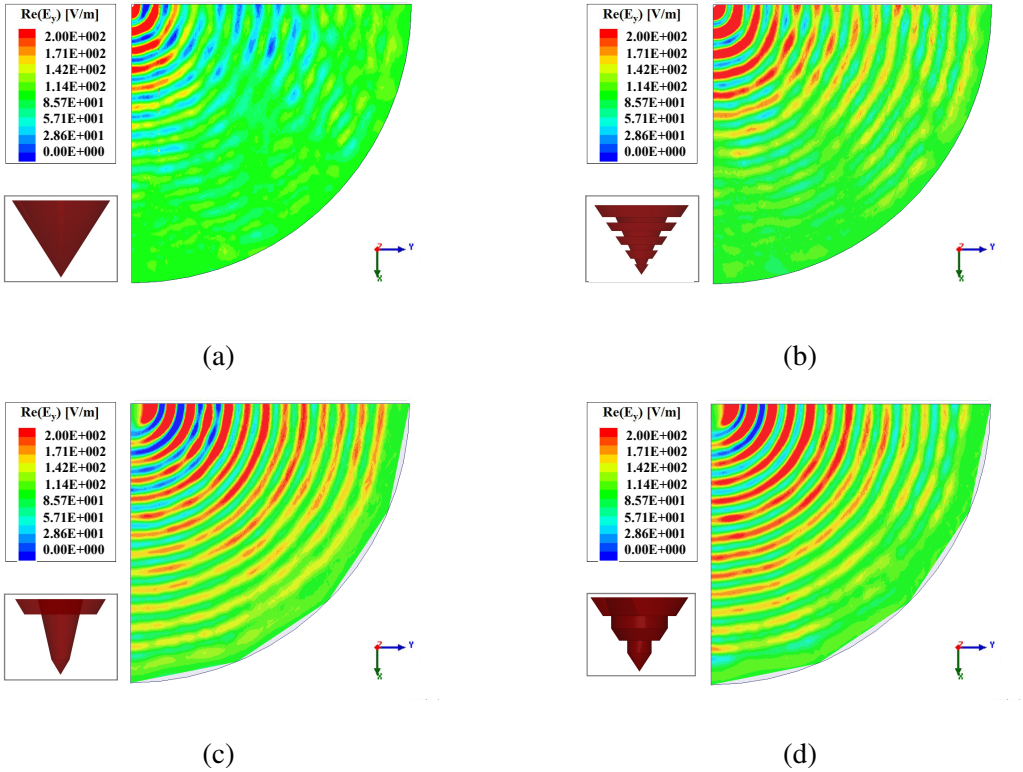

Fig. 4.25. Re(E_y) near field component over the MTS at 13.5GHz, excited with a reduced circular waveguide ($a = 2.54mm$) and different minimized cone-type hats with: (a) smooth profile, (b) a single corrugation, (c) 5 corrugations and (d) 3 corrugations.

upna
Universidad Pública de Navarra
Nafarroako Unibertsitate Publikoa

The complete configuration with a minimized cone-type hat (with 3 corrugations and $a^{'} = 8mm$) placed on top of the reduced circular waveguide ($a = 2.54mm$) employed as the feed is shown in Fig. 4.26.

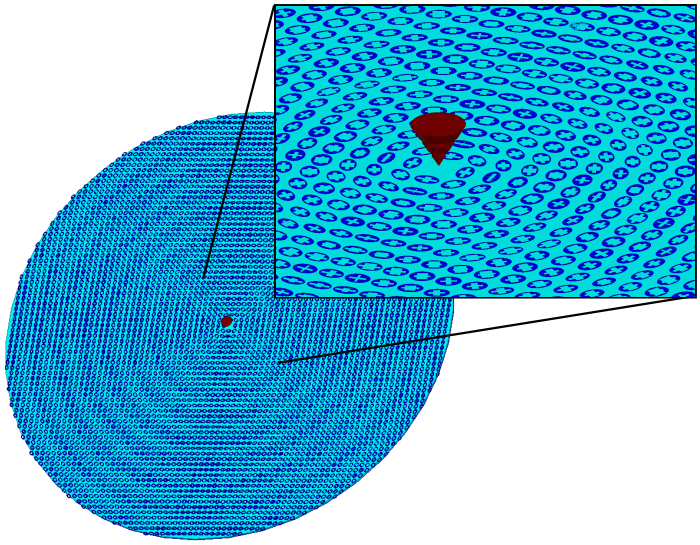

Fig. 4.26. Top view of the complete MTS antenna ($r = 8\lambda_0 = 177mm$) implemented with elliptical pixels with a cross-shaped aperture inside. The inset shows the minimized cone-type hat ($a^{'} = 8mm$) placed on top of the reduced circular waveguide ($a = 2.54mm$).

The full wave reflection coefficient of a quarter of this configuration is shown in Fig. 4.27

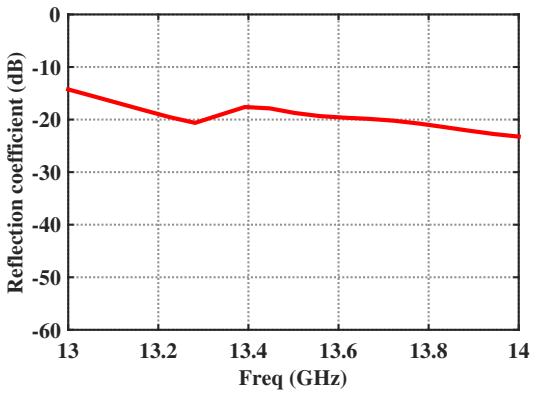

(a)

Fig. 4.27. Reflection coefficient of the MTS antenna with the minimized cone-type hat on top and reduced circular waveguide.

upna
Universidad Pública de Navarra
Nafarroako Unibertsitate Publikoa

The co-polar and cross-polar components of the radiated field at 13.3GHz, 13.4GHz and 13.5GHz are depicted in Fig. 4.28. Besides, the frequency dependence of the directivity and gain are shown.

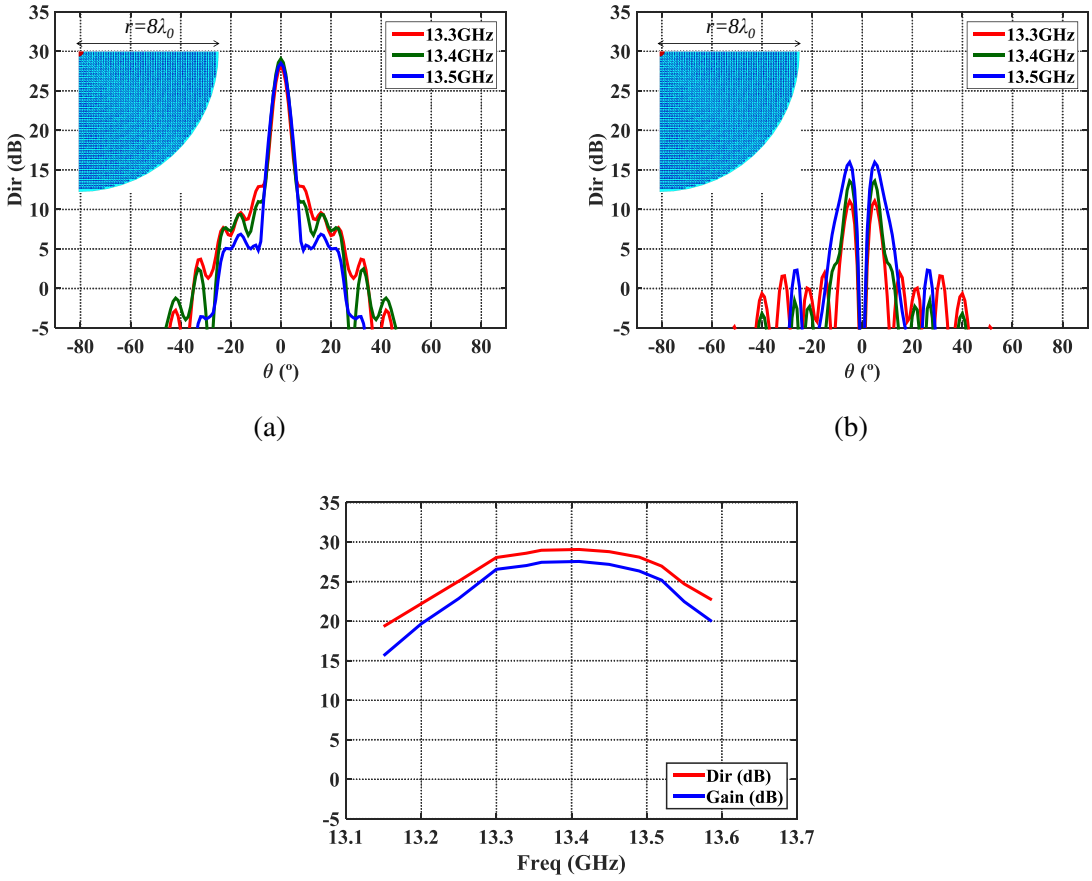

Fig. 4.28. Simulated co-pol (a) and cross-pol (b) radiation patterns in the $\varphi = 45°$ cut obtained with the MTS synthesized with pixels and minimized cone-type hat in the center, at 13.3GHz(red), 13.4GHz(green) and 13.5GHz(blue). (c) Frequency dependence of directivity (red) and gain (blue).

With this configuration a maximum directivity of 29.06dBi is obtained at 13.4GHz (Fig. 4.28). The aperture efficiency is about 32% in a 1.5% fractional bandwidth. The XP component is 13dBs below the copolar contribution. Besides, the gain reaches 27.54dBi, providing a radiation efficiency about 70.5%.

The gain is increased thanks to the hat dimension reduction. In this structure, the diffraction at the hat when exciting the modes at the center (specially TM mode) is avoided.

upna
Universidad Pública de Navarra
Nafarroako Unibertsitate Publikoa

It can be seen in Fig. 4.29 that the beam symmetry is kept at $\varphi = 0°, 45°$ and $90°$ cuts. Therefore, the contribution of both modes to far field is balanced.

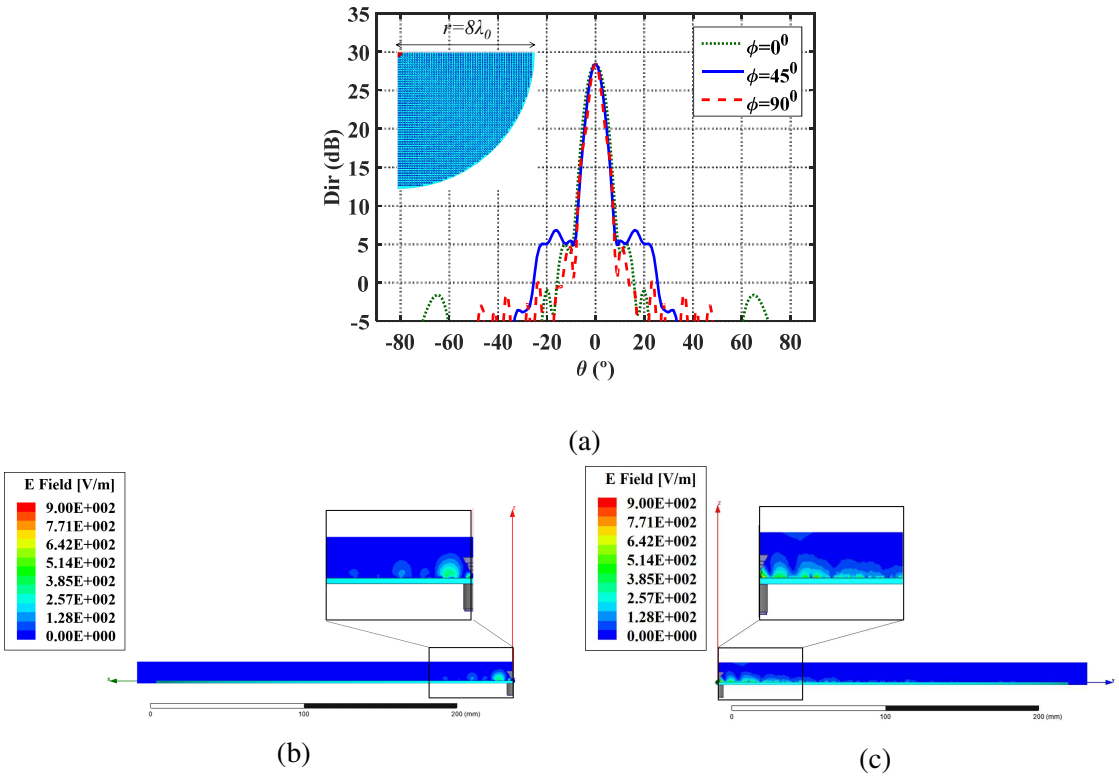

Fig. 4.29. (a) $\varphi = 0°, 45°, 90°$ cuts of the radiation pattern at 13.5GHz. (b) Near E field at *xz*-plane (TE mode contribution). (c) Near E field at *yz*-plane (TM mode contribution). TE_{11} oriented towards *y*-axis is excited at the circular waveguide with a minimized cone-type hat placed on top.

4.4.4 Design of the septum-OMT polarizer

The modeling and validation of the two proposed feeding systems is accomplished in this section. Initially, a large air-filled septum with a taper on top solution is presented. The second design is a more compact, innovative and sophisticated solution, but its manufacturing and assembly is risky.

upna
Universidad Pública de Navarra
Nafarroako Unibertsitate Publikoa

Air-filled septum-OMT

A robust feeding system has been designed to prove the correct behavior of the dual CP broadside MTS antenna. It is composed by two parts. The first part is a metallic septum OMT, which is located inside an air-filled square waveguide. Two lateral flanges to WR-60 waveguide input ports (Fig. 4.45) have been included to feed the OMT. The entire length of this piece is 66.8mm=$3\lambda_0$.

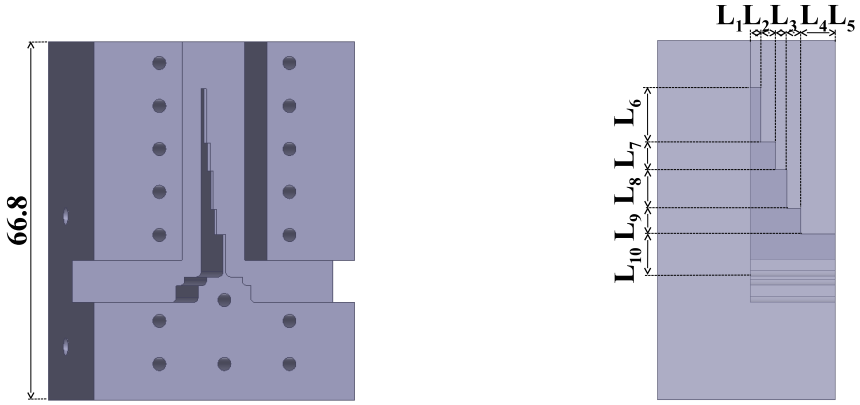

(a) (b)

Fig. 4.30. Septum OMT inside the air-filled square waveguide with lateral flanges to WR-60 waveguide input ports.

	L_1	L_2	L_3	L_4	L_5	L_6	L_7	L_8
Ideal septum	1.97	2.71	2.14	2.58	6.4	10.13	5.17	7.15
Fabricated septum	1.95	2.66	2.13	2.62	6.29	10.00	5.01	7.06
	L_9	L_{10}						
	4.70	6.89						
	4.56	6.80						

Table 4.2 Dimensions (mm) of the stepped septum polarizer inside a square waveguide (air-filled).

The second part is composed by a conical taper, in order to match the field at the output port of the rectangular air-filled waveguide to the arlon AD-1000 based circular waveguide input port of the MTS antenna (see Fig. 4.46). A cone type metallic taper is filled with arlon AD1000 dielectric. This dielectric cone has been designed with an appropriate cone-shaped aperture in the center and its finishes with a diameter of 5.08mm, the diameter of the waveguide which feeds the MTS. A transition from the rectangular waveguide to a circular waveguide (diameter 22.7mm) has been used to connect both parts (Fig. 4.31).

upna
Universidad Pública de Navarra
Nafarroako Unibertsitate Publikoa

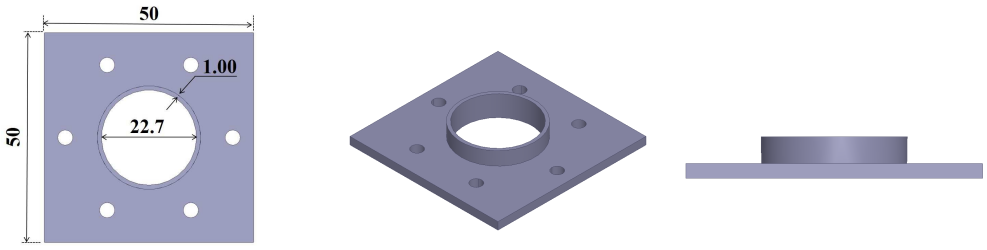

(a) (b) (c)

Fig. 4.31. Metallic transition from the rectangular waveguide to a circular waveguide: (a) top view, (b) isometric view and lateral view.

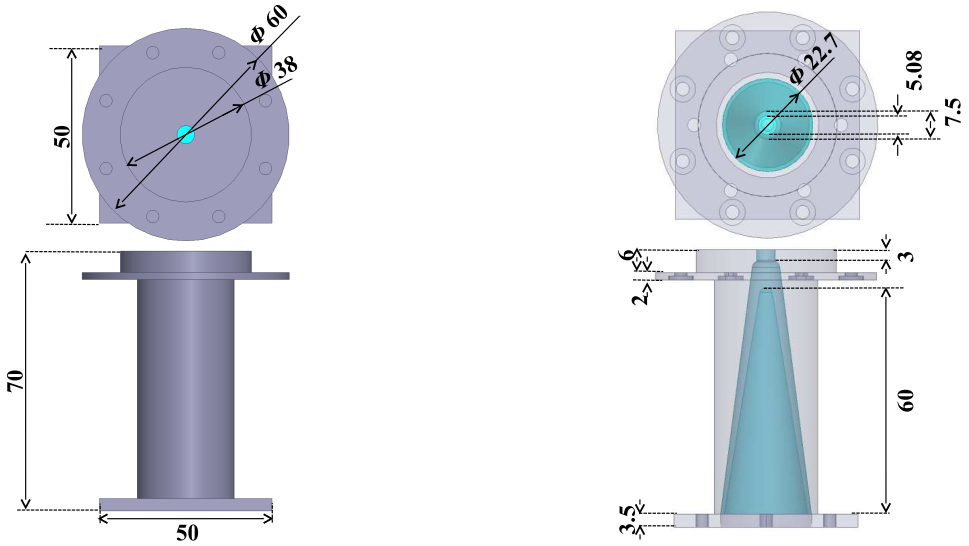

(a) (b)

Fig. 4.32. Taper required to match the field excited at the air-filled septum (diameter 22.7mm) to the MTS antenna (diameter 5.08mm). (a) Exterior details of the metallic encapsulation. (b) Interior details of the conical transition composed by AD1000 dielectric ($\varepsilon = 10.2$) with conical aperture inside.

upna
Universidad Pública de Navarra
Nafarroako Unibertsitate Publikoa

The assembly of both pieces is shown in Fig. 4.33(a) and Fig. 4.33(b). The final configuration (septum+MTS) can be seen in Fig. 4.33(c).

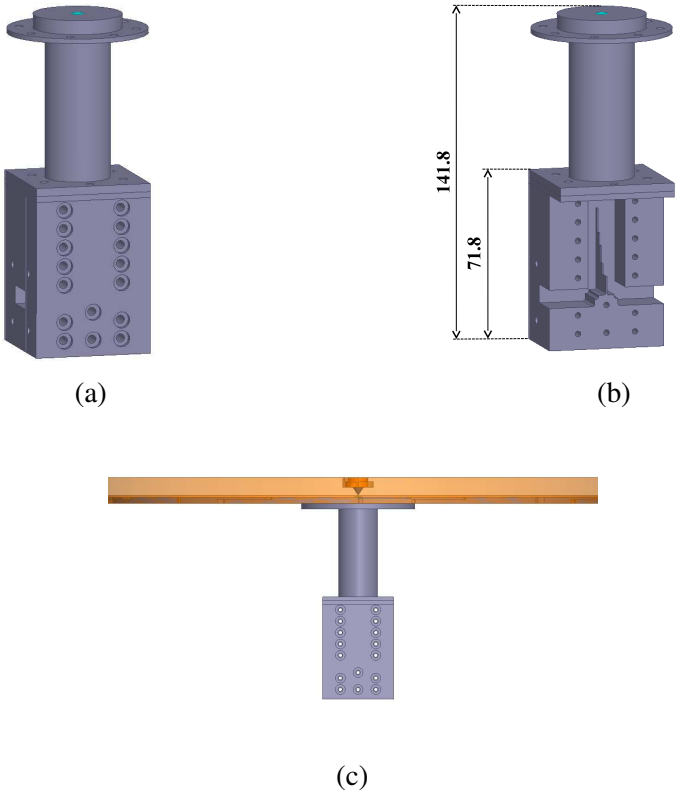

Fig. 4.33. Assembly of the air-filled large septum and the taper to the MTS antenna input port. (a) air-filled OMT and matching pieces. (b) front piece of the septum removed and (c) OMT and MTS assembly.

The analysis of the septum-OMT polarizer (Fig. 4.33) has been done by means of full wave analysis using ANSYS HFSS software. The reflection coefficient, isolation between ports, insertion losses and higher order modes isolation are depicted in Fig. 4.34. As it can be seen, the reflection coefficient is below -20dBs from 12GHz to 14GHz. The isolation between input ports is higher than 17dBs for frequencies higher than 12.9GHz. Besides, the isolation with higher order modes is higher than 20dBs. The insertion loss is -3.6dBs around the working frequency: dielectric losses are -0.6dBs. The phase difference between both modes in the output port (Port 1) is about 94° when port 3 is excited ($-86°$ with port 2 on). In corcondance, the axial ratio is 0.55dB at 13.5GHz. This value will determine the broadside cross polar level of the MTS antenna when it is excited with the proposed feeding system [89–92].

upna
Universidad Pública de Navarra
Nafarroako Unibertsitate Publikoa

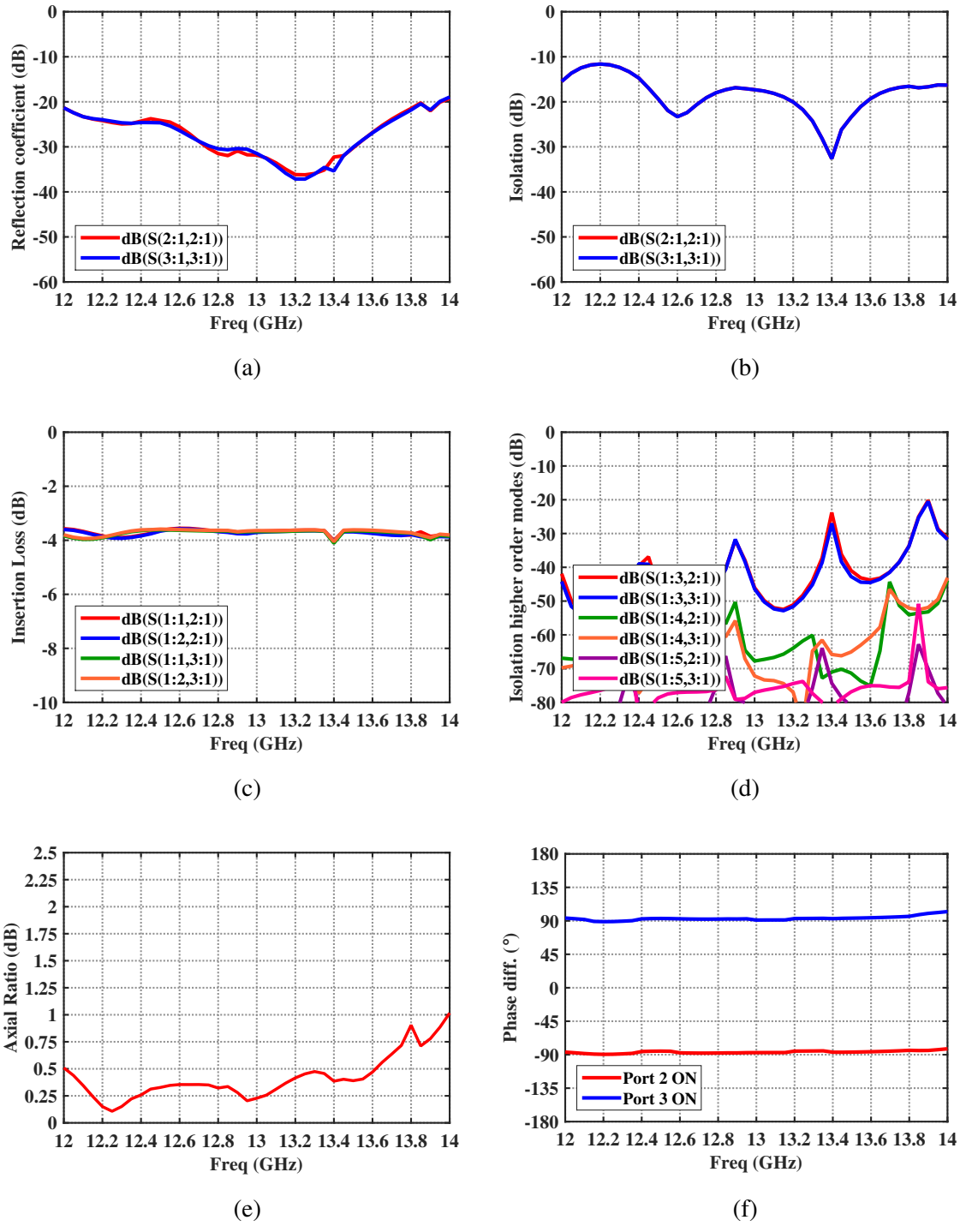

Fig. 4.34. Properties of the ideal septum OMT polarizer inside a square waveguide (air-filled) with a cone type taper on top (filled with AD1000 dielectric with a conical shaped aperture inside). (a) Reflection Coefficient. (b) Isolation. (c) Insertion Loss. (d) Isolation higher order modes. (e) Axial Ratio. (f) Phase difference.

upna
Universidad Pública de Navarra
Nafarroako Unibertsitate Publikoa

Compact AD1000 based septum-OMT

Another OMT has been designed. In this case a much more compact configuration has been used, as it can be seen in Fig. 4.40. Since the circular waveguide of the OMT is filled with arlon AD1000 ($\varepsilon_r = 10.2$), the designed septum results in a extremely compact device with a thickness of $18.73mm = 0.8\lambda_0$.

Ideal septum with sharp edges

The ideal septum design is depicted in figures Fig. 4.35(a) and Fig. 4.35(b). It is composed by a stepped profile, with 4 metallic steps. Dimension details of the proposed solution are gathered in Table 4.3. The circular waveguide is filled with AD1000 to optimize the matching with the MTS antenna. Two lateral AD1000 dielectric junctions shown in Fig. 4.35(c) are necessary to adapt the field excited with the Teflon-based ($\varepsilon_r = 2.1$) SMA connectors. The circular waveguide, metallic septum and the SMA connectors are encapsulated to make the union MTS-septum robust and compact (see Fig. 4.36). The external dimensions of the design are $30mmx26.53mm(1.35\lambda_0 x 1.2\lambda_0)$.

	L_1	L_2	L_3	L_4	L_5	L_6	L_7	L_8	L_9
Ideal septum	0.86	1.95	0.69	0.96	5.08	2.00	2.27	2.16	1.68
Ideal septum (rounded edges)	0.90	1.91	0.69	0.96	5.08	2.00	2.29	2.16	1.66
Fabricated septum	0.92	1.91	0.77	0.84	5.08	2.02	2.28	2.14	1.69
	L_{10}	R_1	R_2	R_3	R_4	R_5	R_6	R_7	R_8
	0.13	-	-	-	-	-	-	-	-
	0.12	0.50	0.50	0.50	0.50	0.50	0.50	0.50	0.50
	0.12	0.54	0.25	0.25	0.50	0.50	0.37	0.25	0.25

Table 4.3 Dimensions (mm) of the stepped septum polarizer.

The scattering matrix of the ideal septum-OMT polarizer shown in Fig. 4.35(a)-Fig. 4.35(b) has been characterized. The reflection coefficient, isolation between ports, insertion losses and higher order modes isolation are depicted in Fig. 4.37. Moreover, the axial ratio and phase difference between the excited TE_{11} modes at the output port (Port 1) are represented.

The reflection coefficient is below -10dBs from 12GHz to 13.6GHz, which comprehend the working frequency of the MTS antenna (the theoretical frequency of the ideal antenna is 13.5GHz, which is shifted to 13.4GHz in the configuration implemented with pixels). The isolation between input ports is higher than 20dBs at this band (-33.5dBs at 13.4GHz) while the isolation with higher order modes is higher than 22dBs. The insertion loss is

upna
Universidad Pública de Navarra
Nafarroako Unibertsitate Publikoa

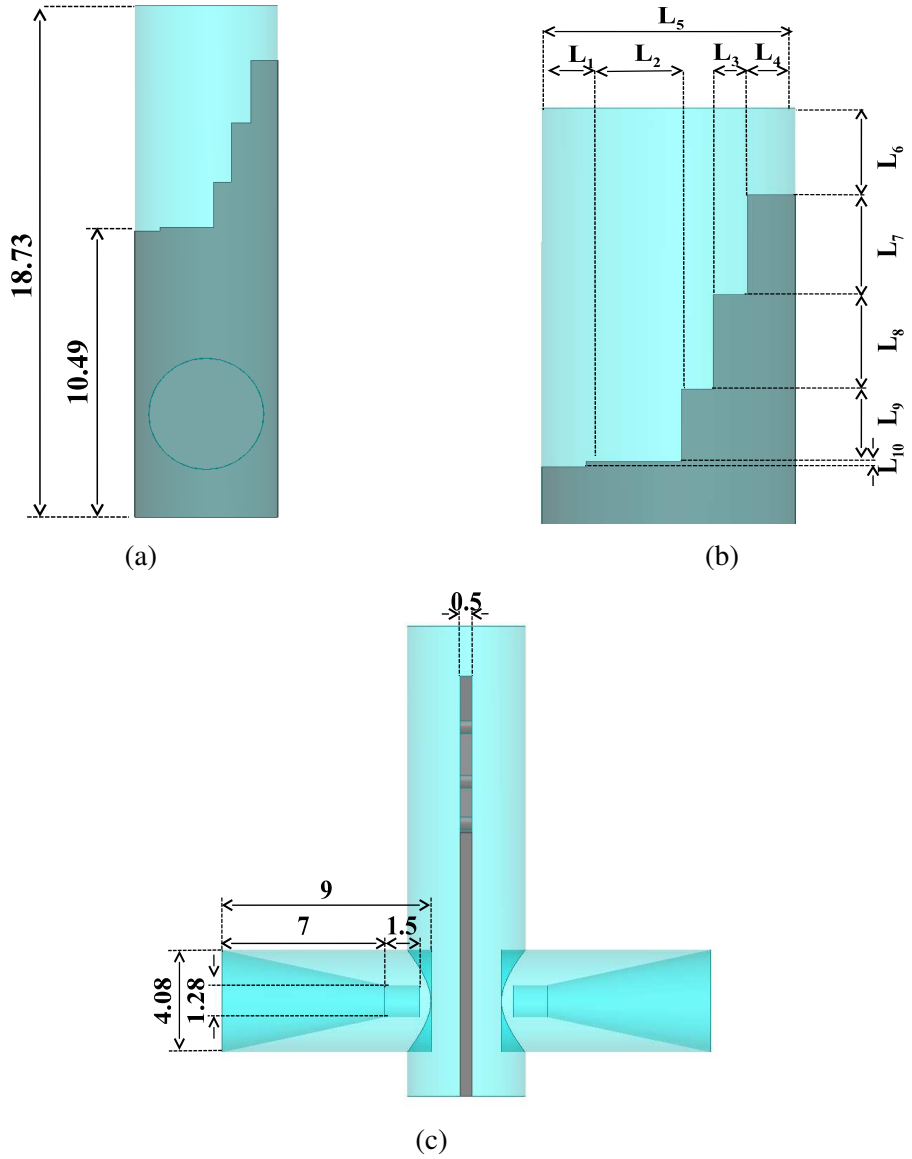

Fig. 4.35. Details of the compact septum OMT polarizer. Ideal design with stepped profile: (a) lateral view, (b) details of the 4 steps in the center and (c) front view of the septum and dielectric inside the circular waveguide, with lateral junctions for matching with the SMA connectors.

upna
Universidad Pública de Navarra
Nafarroako Unibertsitate Publikoa

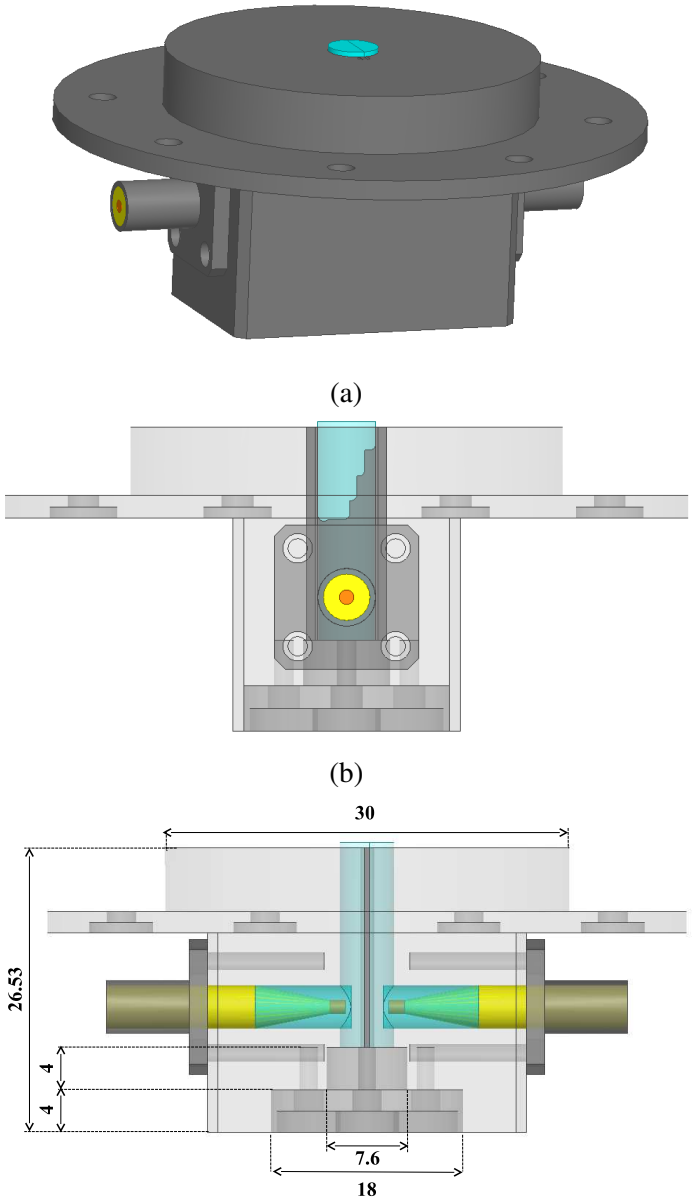

Fig. 4.36. Encapsulation details of the circular waveguide filled with AD1000 dielectric ($\varepsilon_r = 10.2$), the metallic septum-OMT polarizer, 2 lateral AD1000 junctions and 2 teflon-based ($\varepsilon_r = 2.1$) SMA connectors: (a) lateral view and (b) front view.

upna
Universidad Pública de Navarra
Nafarroako Unibertsitate Publikoa

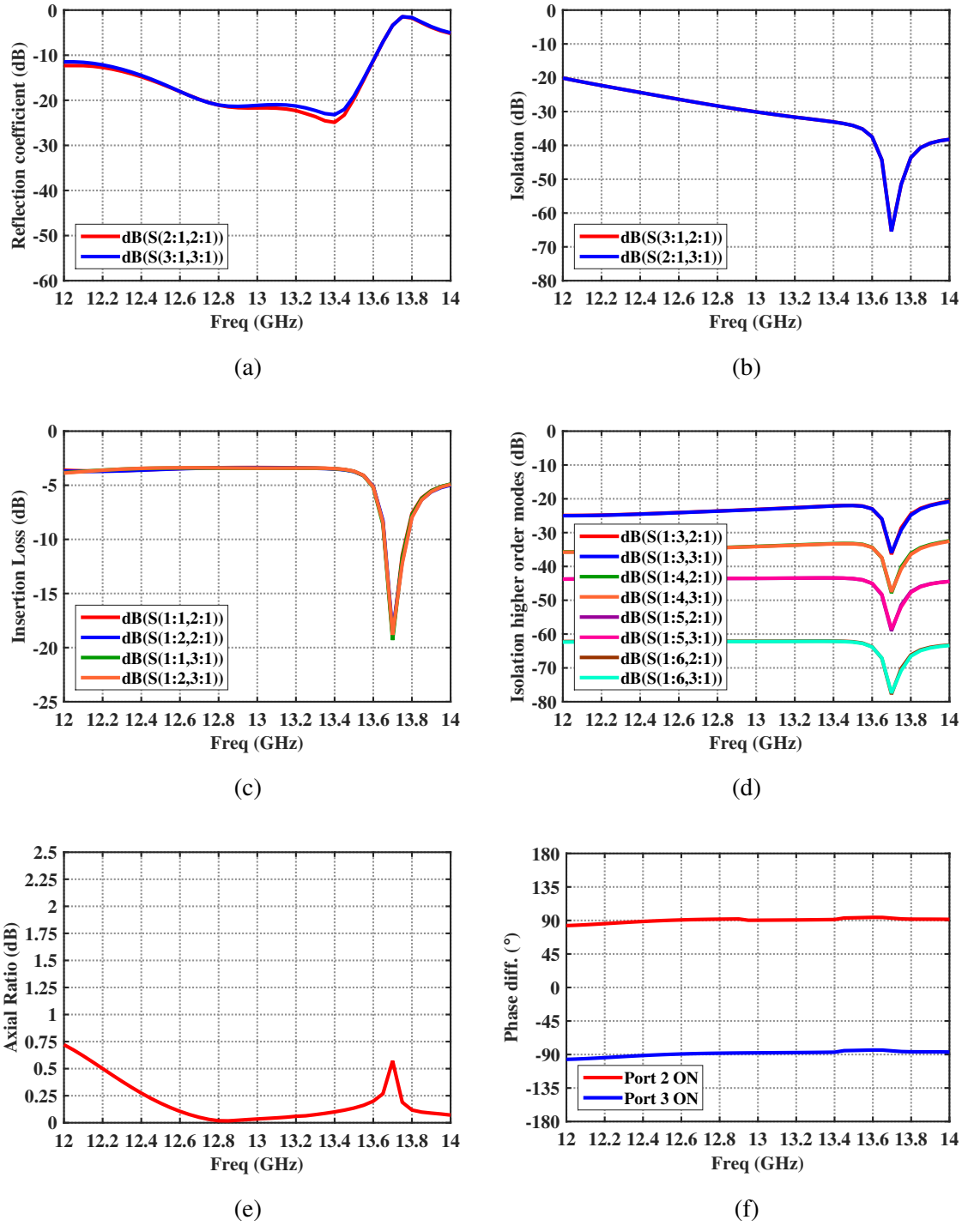

Fig. 4.37. Properties of the ideal septum inside the circular waveguide (radius $a = 2.54mm$) with a stepped single ride in the center, with 4 steps. (a) Reflection Coefficient. (b) Isolation. (c) Insertion Loss. (d) Isolation higher order modes. (e) Axial Ratio. (f) Phase difference.

upna
Universidad Pública de Navarra
Nafarroako Unibertsitate Publikoa

-3.43dBs around the working frequency: 0.43dBs of dielectric losses are expected. The phase difference between the two modes in the output port (Port 1) is about 93° when port 2 is excited (−87° with Port is 3 on), which provides an axial ratio of 0.1dB at 13.4GHz for the ideal septum design. This value will determine the broadside cross polar level of the MTS antenna when it is excited with the proposed feeding system [89–92].

Fig. 4.38 shows how the complete feeding system is fitted with the ground of the MTS antenna and the cone-type hat is placed on top. Two SMA connectors excite the polarizer, which provides CP field excitation at the center of the MTS. Final prototype is encapsulated using a foam ($\varepsilon_r = 1$) cover. The cover allows the hat to be placed on top of the antenna.

The complete configuration (MTS+septum OMT) has been studied using ANSYS HFSS software to check the scattering behavior of the whole structure. The inclusion of the septum, which works with CP, requires the simulation of the complete model without using symmetry boundary conditions for the MTS. Therefore, the diameter of the MTS located over the feeding system has been reduced to $7\lambda_0$ (while the real antenna shown in Fig. 4.20 has a diameter of $16\lambda_0$). The full wave analysis has been launched in the workstation HP Z800, with 192GB RAM, 2 processors at 3.47GHz (X5690 with 12 cores). A converged solution is obtained with a mesh of 2.1 million tetrahedra. The simulation time with these properties is about 11 hours.

The scattering properties of the complete model (composed by a $7\lambda_0$ diameter MTS) excited with the ideal septum) are compared with the scattering properties of the ideal septum in Fig. 4.39. While the reflection coefficient of the input ports is not affected by the inclusion of the metasurface and the hat on top (Fig. 4.39(a)), the coupling between the input ports is considerably deteriorated, approximately 17dBs as shown in Fig. 4.39(b). This difference in isolation values shows the impact of the reflection of the MTS antenna. It can be concluded that the field that is not adapted to the MTS from the circular waveguide output, is reflected in the opposite polarization towards the isolated input port.

upna
Universidad Pública de Navarra
Nafarroako Unibertsitate Publikoa

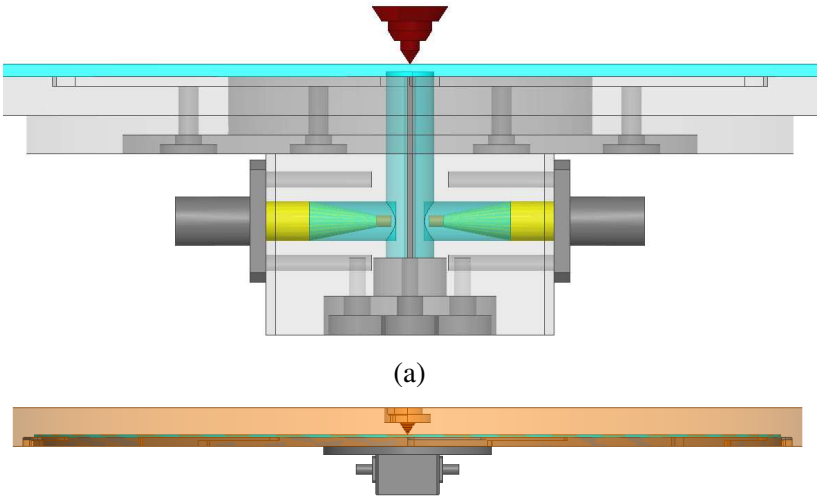

(a)

(b)

Fig. 4.38. Encapsulation of the complete prototype: (a) embedding of the complete feeding system, metasurface and the cone-type hat on top, (b) final prototype with foam covering.

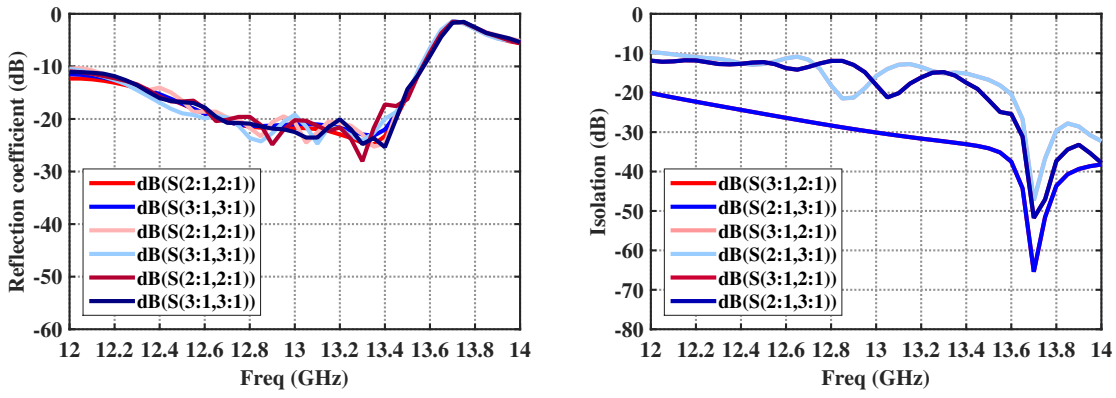

(a) (b)

Fig. 4.39. Comparison of the scattering properties of: ideal septum (red and blue lines), ideal septum+MTS (light red and blue lines) and ideal septum+MTS+cone type hat (dark red and blue lines). (a) Reflection Coefficient. (b) Isolation.

upna
Universidad Pública de Navarra
Nafarroako Unibertsitate Publikoa

Ideal septum with rounded edges

The previous results are related with the ideal septum-OMT polarizer where the metallic steps in the center are characterized by sharp edges (see Fig. 4.35(b)). Nevertheless, due to the fabrication limitations, the edges of the septum must be rounded as in Fig. 4.40(b). As the designed prototype is so compact, a small difference in the geometry parameters can yield an important degradation in the designed response. Due to this fact, considering the manufacturer recommendation, an edge rounding with a radius of 0.5*mm* has been included in the optimization process of the septum design. More details of the geometry modification are summarized in Table 4.3. Full wave simulation results of the ideal and rounded septum models are compared in Fig. 4.41.

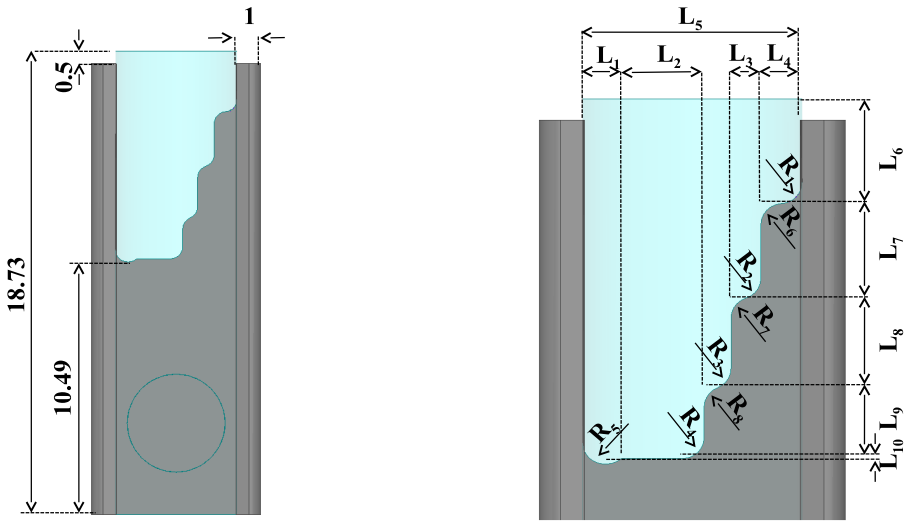

Fig. 4.40. Ideal compact septum OMT polarizer with rounded edges due to fabrication limitations: (a) lateral view and (b) details of the rounded edges.

It can be concluded that the reflection coefficient, insertion losses and higher order modes level are not affected by the edge rounding required due to manufacturing limitations. However, the isolation between the input ports is deteriorated in 5dBs: the ideal septum with sharp edges provides -33dBs at 13.4GHz while the rounded model presents -28dBs. This effect denotes that due to the edge-rounding, some cross-polar field is generated and it is coupled to the isolated input port. Besides, the purity of the circular polarized field excited at Port 1 is also affected: the axial ratio is increased to 0.78dBs. Taking into account that the septum affects directly to the circular field purity at broadside direction of the MTS antenna radiation pattern, a XP level of -26.96dBs is expected.

upna
Universidad Pública de Navarra
Nafarroako Unibertsitate Publikoa

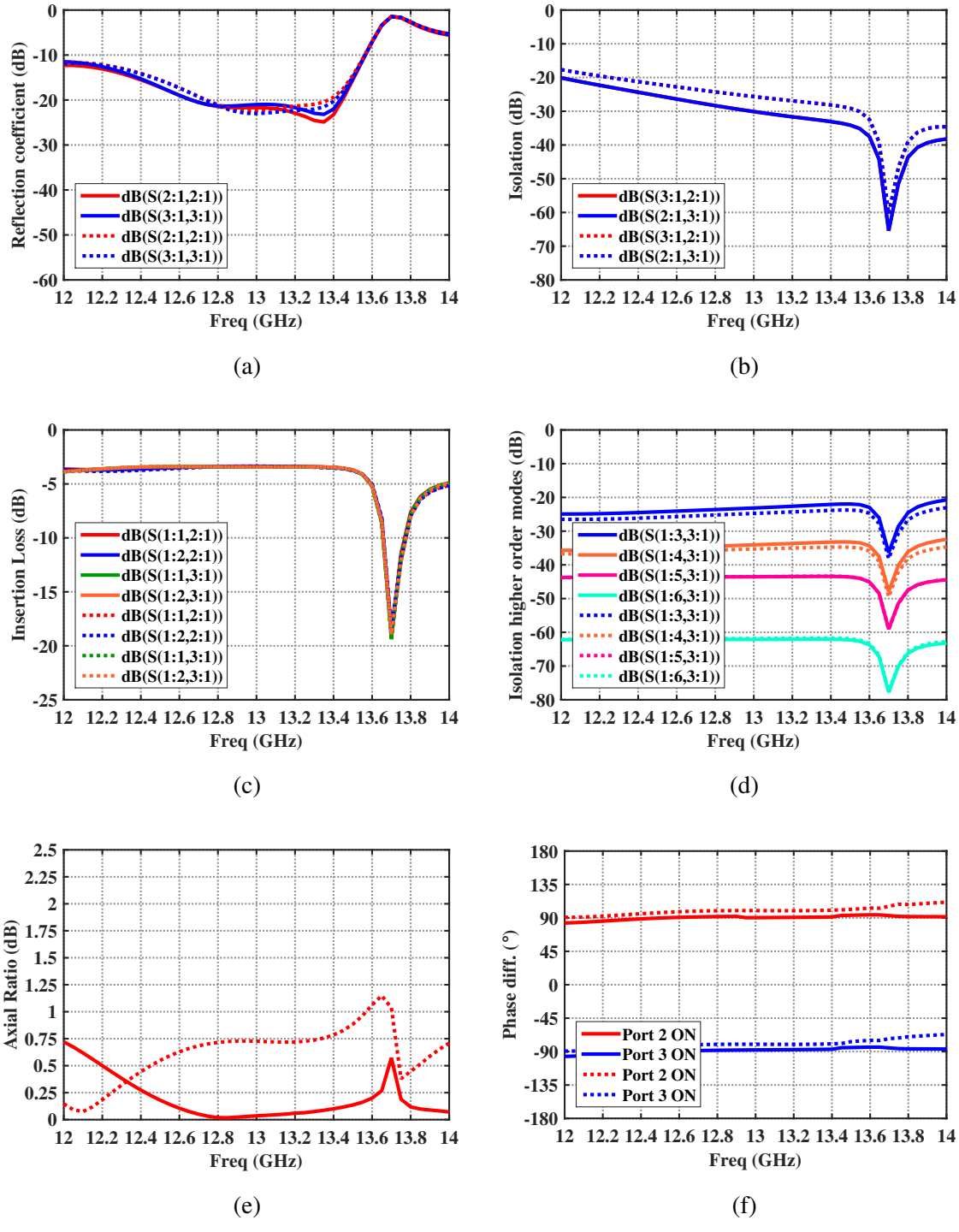

Fig. 4.41. Scattering properties of the ideal septum with a stepped single ride in the center (continuous lines) vs. properties of the septum with rounded edges (dotted lines). (a) Reflection Coefficient. (b) Isolation. (c) Insertion Loss. (d) Isolation higher order modes. (e) Axial Ratio. (f) Phase difference.

upna
Universidad Pública de Navarra
Nafarroako Unibertsitate Publikoa

Finally, the validation of the feeding system with the ideal rounded-edges septum has been corroborated embedding it with the MTS antenna (Fig. 4.42). It is shown that the reflection and isolation properties of the entire configuration (considering the feeding system and the metasurface with the hat) is not especially affected by rounding the septum edges (see Fig. 4.42).

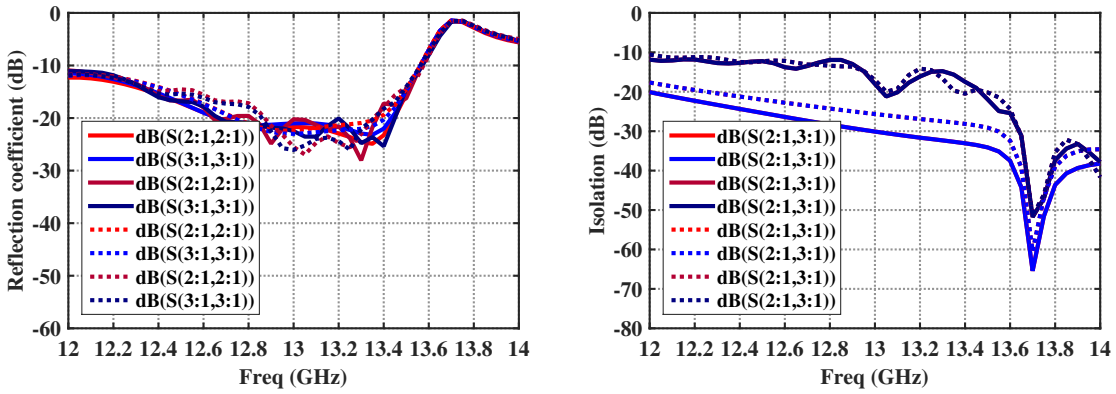

(a) (b)

Fig. 4.42. Comparison of the scattering properties of the configuration excited with the ideal septum (continuous lines) vs. septum with rounded edges (dotted lines): septum (red and blue lines), septum+MTS+cone type hat (dark red and blue lines). (a) Reflection Coefficient. (b) Isolation.

upna
Universidad Pública de Navarra
Nafarroako Unibertsitate Publikoa

4.5 Prototype fabrication and experimental results

Details of the fabricated MTS and both feeding systems are given in this section. Moreover, the measurements carried out to corroborate the dual CP broadside radiation of the designed MTS antenna are presented.

4.5.1 Manufactured MTS

The MTS configuration proposed in Fig. 4.26 has been fabricated by photolitography process. Following the manufacturer recommendation, the minimum printable dimension of the copper elliptical patches with asymmetric cross-shaped aperture has been set to $100\mu m$. This limitation is given by the wet-etching effect that appears in the photolithography process for a $19\mu m$ copper thickness. A $6\mu m$ gold flash coating has been applied to avoid oxidation.

MTS manufacturing has been a challenge since it is necessary to print an important number of different elements (around 13000 patches). Besides, they are characterized by small details and high printing resolution is required. Images of the fabricated pixels captured with a Mitutoyo Hyper MF-U measuring microscope are shown in Fig. 4.43. Really good agreement in dimensions between the fabricated and theoretical pixels has been achieved. Therefore, the wet-etching effect is negligible. The Mitutoyo SJ-410 portable surface roughness tester has been employed to measure the thickness and roughness of the different components: the metallic elements have a measured thickness of $19.637\mu m$ with a roughness of $0.316\mu m$ and the dielectric substrates roughness is $0.334\mu m$. Furthermore, pictures of the fabricated complete metasurface are provided in Fig. 4.44. The prototype is extremely thin ($h = 1.27mm$) and light (mass 320g.). The measured antenna diameter is $355mm$.

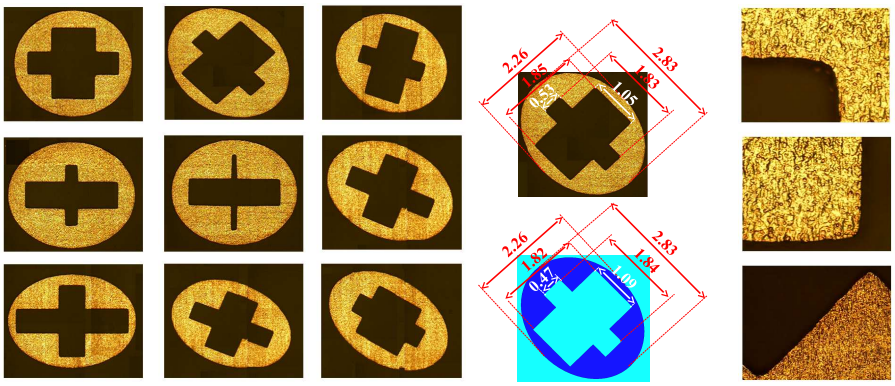

(a) (b) (c)

Fig. 4.43. (a) Microscope images of the manufactured patches. (b) Dimensions of the fabricated (top) vs simulated (botton) pixel. (c) Negligible wet-etching effect.

upna
Universidad Pública de Navarra
Nafarroako Unibertsitate Publikoa

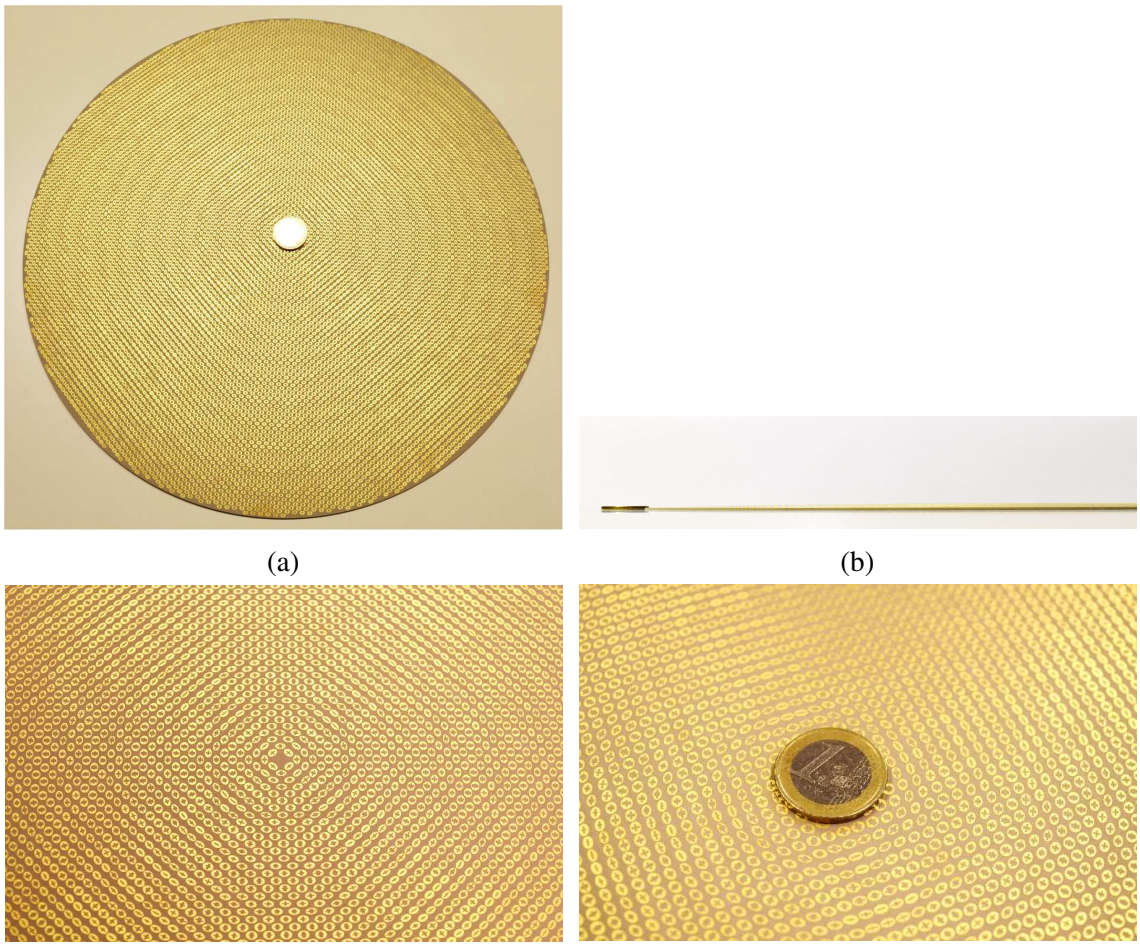

(a) (b)

(c) (d)

Fig. 4.44. Pictures of the fabricated metasurface: (a) top view (diameter 355*mm*), (b) lateral view (thickness 1.27*mm*) and (c),(d) details of the antenna center.

upna
Universidad Pública de Navarra
Nafarroako Unibertsitate Publikoa

4.5.2 Air-filled septum-OMT: fabrication and measurements

Fabrication details

The large air-filled septum has been fabricated in a external company (Fig. 4.45). To join the square waveguide with the septum inside and the MTS antenna, the conical shaped metallic taper shown in Fig. 4.46 has been manufactured. Arlon AD1000 based piece with a cone-type aperture has been inserted inside the metallic taper, as shown in Fig. 4.47. The air filled septum piece and the taper have been connected using a metallic union shown in Fig. 4.48(a). Two WR-60 waveguides are employed to excite the complete feeding, which is embedded with the ground plane of the MTS antenna as illustrated in Fig. 4.50(b).

(a) (b) (c)

Fig. 4.45. Picture of the fabricated septum OMT inside the air-filled square waveguide: (a) front view, (b) front cover piece and (c) lateral view.

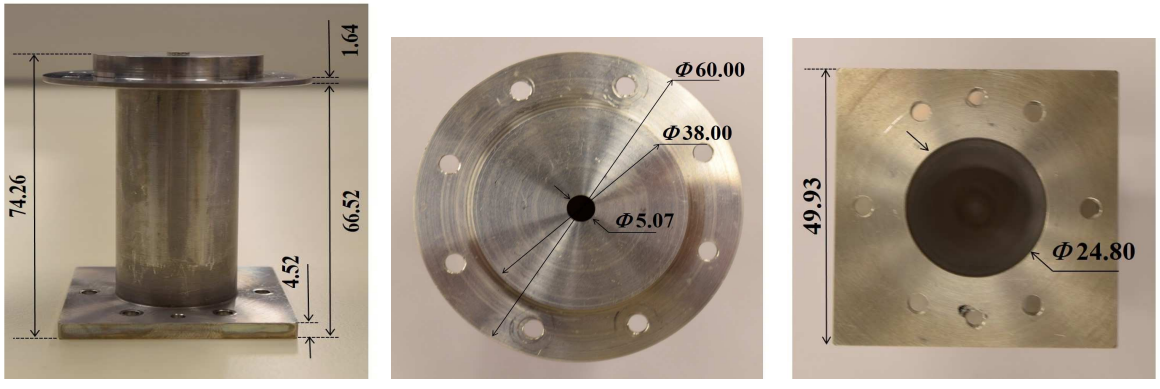

(a) (b) (c)

Fig. 4.46. Picture of the fabricated metallic taper to unite the air-filled septum with the ground plane of the MTS antenna: (a) lateral view, (b) top view and (b) bottom view.

upna
Universidad Pública de Navarra
Nafarroako Unibertsitate Publikoa

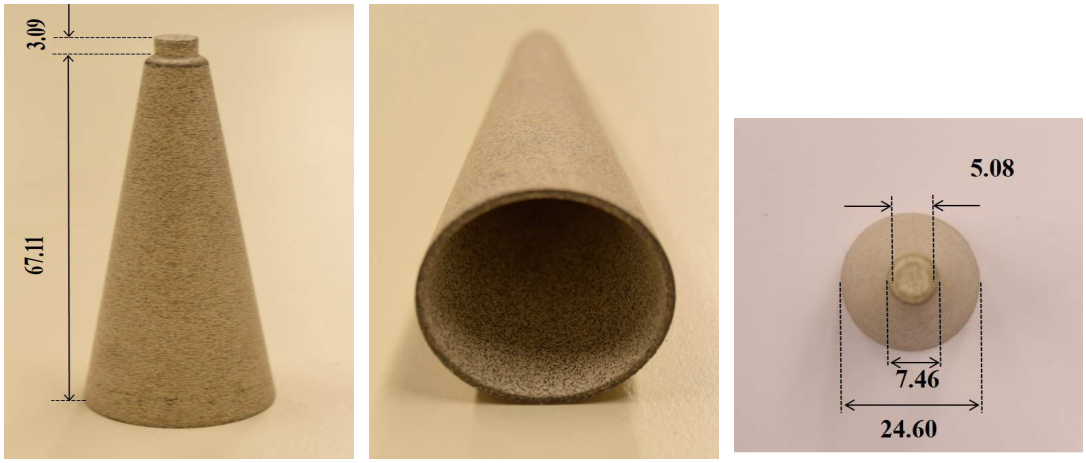

(a) (b) (c)

(d) (e) (f)

Fig. 4.47. Pictures of the arlon AD1000 based taper with a cone-type aperture in the center: (a) lateral view, (b) bottom view and (c) top view. Inclusion of the dielectric piece inside the metallic taper: (d) lateral view, (e) top view and (f) bottom view.

upna
Universidad Pública de Navarra
Nafarroako Unibertsitate Publikoa

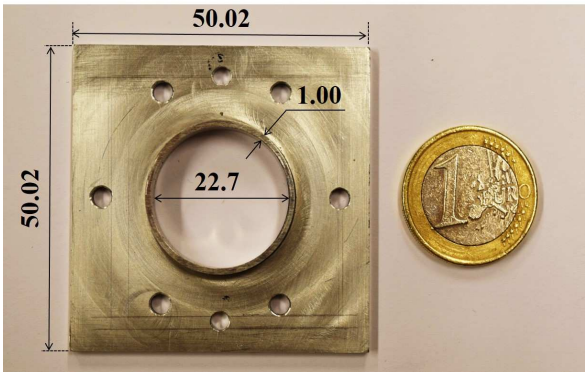

(a)

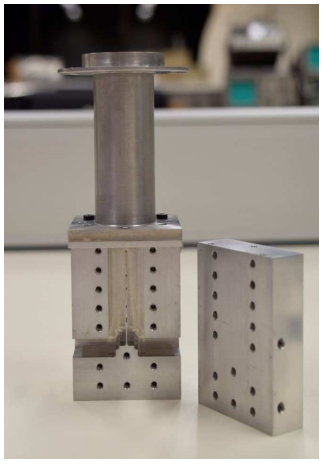

(b)

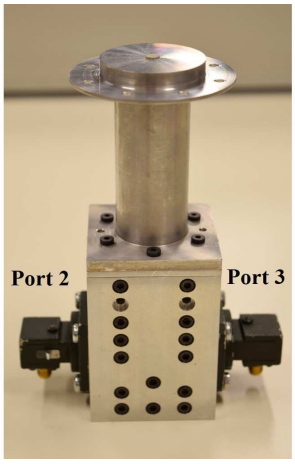

(c)

Fig. 4.48. (a) Metallic piece used to join the square waveguide with the metallic taper, (b) isometric view of the complete feeding system and (c) assembling with the WR-60 excitation waveguides.

upna
Universidad Pública de Navarra
Nafarroako Unibertsitate Publikoa

The minimized cone-type hat has been also fabricated (Fig. 4.49). The measured dimensions are in good agreement with the design.

(a) (b)

Fig. 4.49. Pictures of the manufactured cone-type hat: (a) lateral view and (b) bottom view.

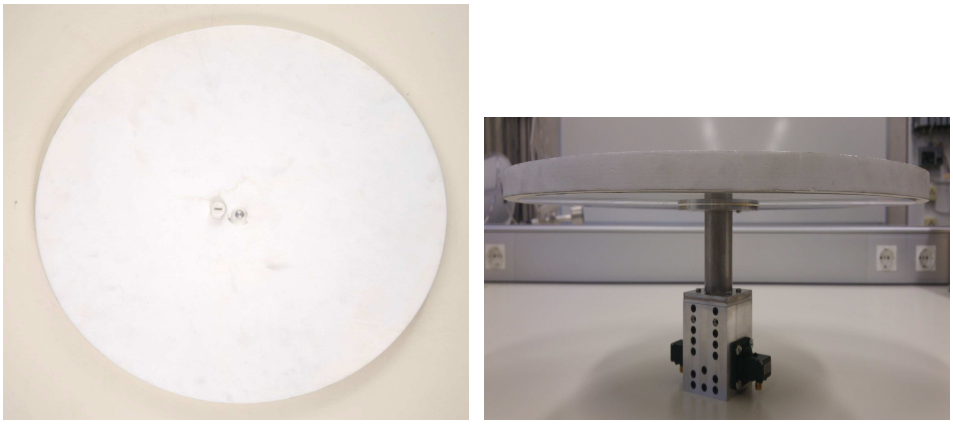

(a) (b)

Fig. 4.50. (a) A foam ($\varepsilon_r = 1$) layer covering the MTS and hat. (b) Lateral view of the complete configuration with the MTS antenna and the air-filled feeding system.

Measurements

The complete antenna (Fig. 4.50(b)) including the MTS (Fig. 4.44), the hat (Fig. 4.49) and the complete feeding system (air-filled septum and the arlon AD1000 based taper in Fig. 4.48(c)) has been characterized. The reflection and isolation properties have been measured at Ku-band (from 12.8GHz to 13.8GHz) using the Vector Network Analyzer (PNA-X N5242A). One of the input ports of the feeding system has been excited by a WR-60 waveguide, while a load is placed in the other port. The same procedure has been followed in both ports to

upna
Universidad Pública de Navarra
Nafarroako Unibertsitate Publikoa

obtain a complete characterization of the configuration. Obtained measurements are shown in Fig. 4.51.

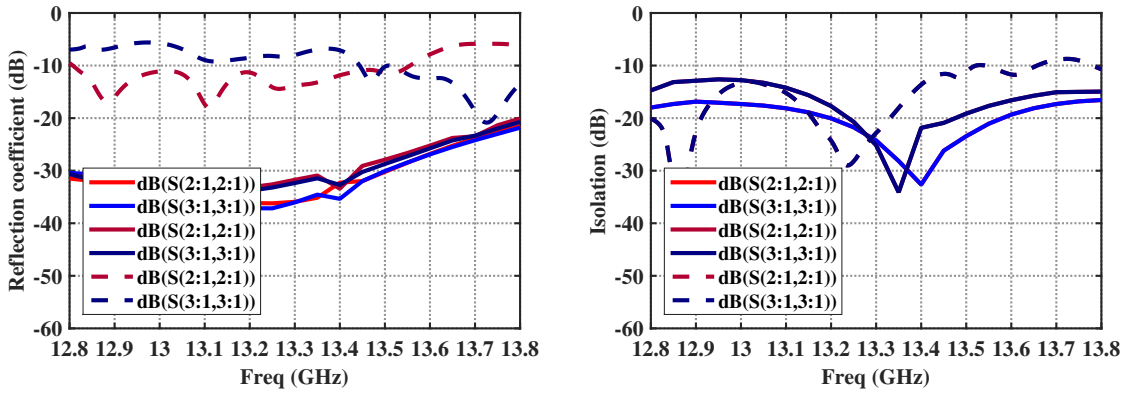

(a) (b)

Fig. 4.51. Comparison of the simulated (continuous lines) and measured (dashed lines) scattering matrix of the fabricated complete feeding system (air-filled septum+taper AD1000) (light lines) and complete feeding system+MTS antenna (dark lines): (a) reflection coefficient and (b) isolation. Port 2 on (red lines) and port 3 on (blue lines).

The measured reflection coefficient is below -10dB when the port 2 is on and below -8dB when the excited port is 3. Besides, the isolation between both input ports remains below -11dBs until 13.5GHz, with a minimum of -30dBs around 13.25GHz. This result agrees with the simulated response and shows that the MTS antenna is appropriately adapted with the manufactured feeding system.

The radiation pattern measurement has been carried out in the anechoic chamber of the Antennas Group (room dimension 4.5mx4.5m) at UPNA. The measurement setup is shown in Fig. 4.52(a). The 17240 standard gain horn from Flann Microwaves has been used as emitter. This horn works from 9.8GHz to 15GHz and it presents a 20dBi gain. As it is linearly polarized, the measurerement of the CP MTS antenna have been done by the composition of the two measured linear components. Firstly, the position of the major and minor axes of the polarization ellipse have been found. Taking the major axis of the ellipse as the reference, the linearly polarized field information (vertical) has been measured at $\phi = 0°, 45°$ and $90°$ cuts, with $1°$ step in θ. Afterwards, the data at the same ϕ and θ cuts with the horn rotated $90°$ has been gathered (horizontal linear polarization). The RHCP and LHCP radiation patterns of the MTS have been composed taking into account the $90°$ phase shift between the linear components. Measured normalized RHCP and LHCP radiation patterns at 13GHz, 13.1GHz and 13.2GHz are shown in Fig. 4.53.

upna
Universidad Pública de Navarra
Nafarroako Unibertsitate Publikoa

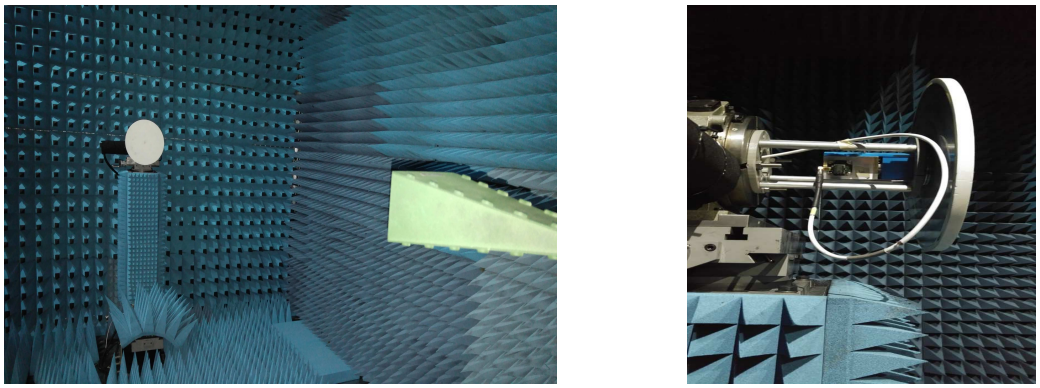

(a) (b)

Fig. 4.52. Radiation pattern measurement setup: (a) complete system and (b) zoom in of the MTS antenna excited with the large feeding system.

Broadside LHCP is obtained by feeding port 2 (Fig. 4.53), while broadside RHCP is achieved feeding port 3. This behavior agrees with the theoretical basics developed in this chapter. The working frequency of the antenna has been shifted from 13.4GHz predicted by HFSS to 13.18GHz. A narrow working bandwidth of 1.52% has been obtained. The radiation patterns within the working bandwidth obtained with both excitation ports are in agreement and show XP levels from -15dBs to -8dBs in broadside direction and of around -5dBs at $\theta = 10^{\circ}$. It is remarkable that the measured XP levels are high in comparison with the simulated results, which shows no contribution of XP field at broadside and around -13dBs at 10° (see Fig. 4.28). The explanation of the XP component increase is extended in the discussion at the end of this section.

Gain and directivity dependence vs. frequency measurements are compared with HFSS predictions in Fig. 4.54. As a linearly polarized standard gain horn has been used, two partial gains have been measured corresponding to each linearly polarized components. Therefore, the total gain of the MTS has been calculated as:

$$G_{MTS} = 10\log_{10}(G_{MTS_H} + G_{MTS_V}) \tag{4.26}$$

where G_{MTS_H} (dB) and G_{MTS_V} (dB) are the linear MTS gain components measured towards the major and minor axes of the polarization ellipse, respectively.

A maximum directivity of 26.6dBs is obtained at 13.2GHz when the MTS antenna is excited with port 2. A drop off 2.46dBs is observed in measurements with respect to the maximum directivity obtained in HFSS at 13.4GHz (29.06dB). In consequence, the aperture efficiency is decreased from 32% to 18.2%. The measured gain is 23.28dBi, which rise to a radiation efficiency of 46.6% when port 2 is used to excited the antenna. On the other hand,

upna
Universidad Pública de Navarra
Nafarroako Unibertsitate Publikoa

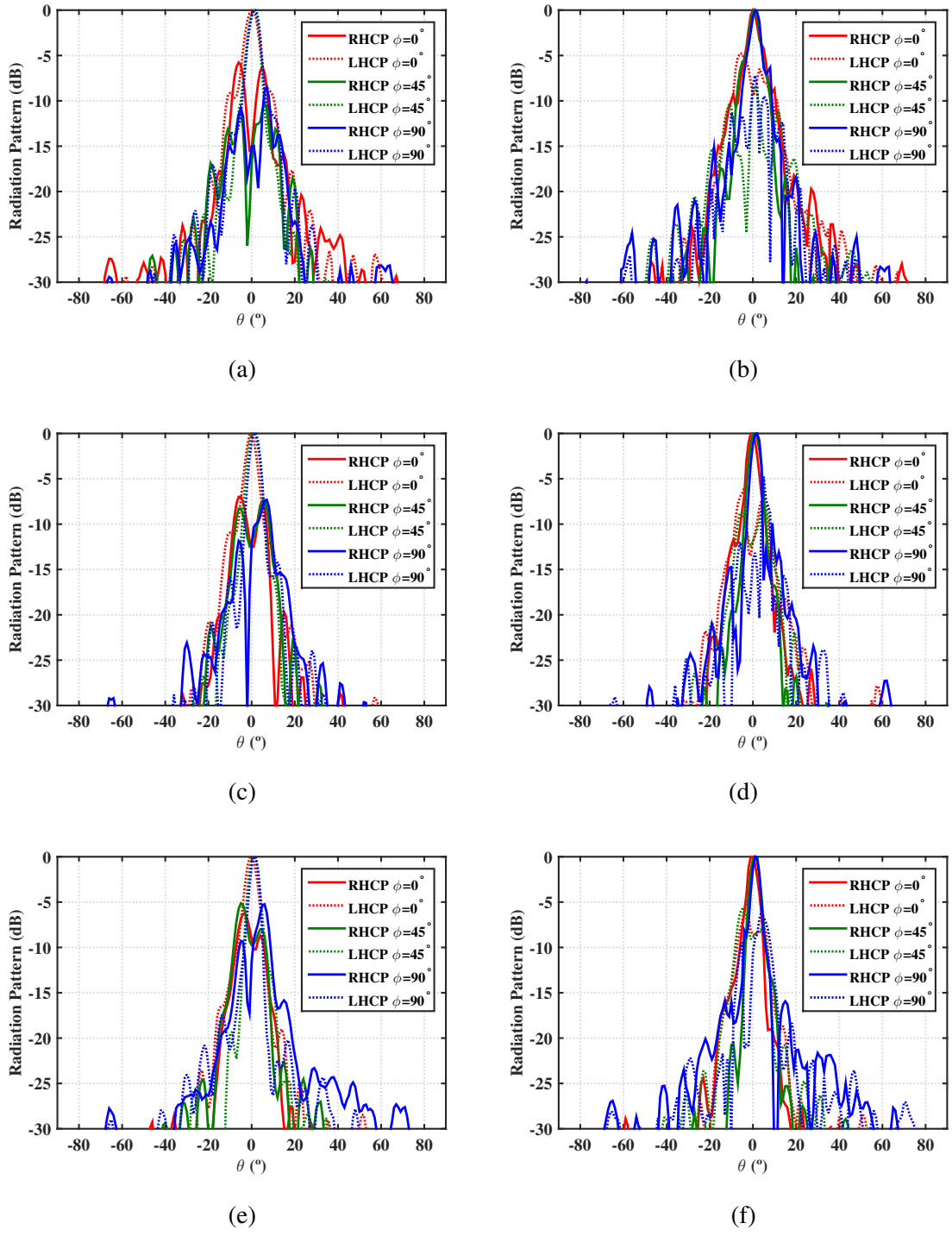

Fig. 4.53. Measured normalized RHCP (continuous) and LHCP (dashed) radiation patterns at $\varphi = 0°(red), 45°(green), 90°(blue)$ cuts obtained with the MTS excited with the large air-filled feeding system port 2 on/ port 3 on at: (a)/(b) 13.05GHz, (c)/(d) 13.1GHz and (e)/(f) 13.2GHz.

upna
Universidad Pública de Navarra
Nafarroako Unibertsitate Publikoa

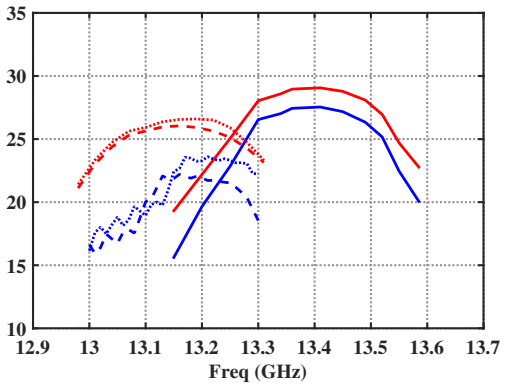

Fig. 4.54. Simulated (continuous lines) vs. measured frequency dependence of directivity (red) and gain (blue) obtained with the MTS antenna excited with the air-filled complete feeding system: port 2 on (dotted lines) and port 3 on (dashedlines lines).

when the structure is fed with port 3, the maximum directivity at 13.2GHz is 25.92dBs and the aperture efficiency is decreased to 15.56%. The measured gain is 22.04dBi, providing a radiation efficiency of 40.9%.

Measured AR is presented in Fig. 4.45 for two different cases: the air-filled septum alone (dotted lines) and considering the complete feeding system (air-filled septum + AD1000 based taper shown in Fig. 4.48(c)) exciting the MTS antenna (dashed lines). The results are compared with simulated AR values (continuous lines) obtained when the MTS antenna is excited with the complete feeding system (Fig. 4.33(a)).

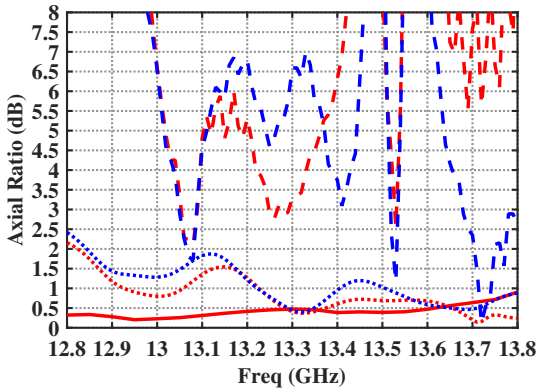

Fig. 4.55. Simulated AR of the complete feeding (septum+taper) (continuous lines) vs. measured AR provided by the air-filled septum (dotted lines) and complete feeding system (dashed lines), when port 2 on (blue) and port 3 on (red).

upna
Universidad Pública de Navarra
Nafarroako Unibertsitate Publikoa

As shown in Fig. 4.55, the AR provided by the manufactured air-filled septum is below 2dBs in the whole working bandwidth. Nevertheless, when the metallic taper with the dielectric inside is assembled, the CP purity of the excited field get worse and AR increases considerably up to 6dBs. Around 13.05GHz the measured AR suffers a fast drop to 1.7dBs. The reason of the AR degradation of the complete feeding system when introducing the upper taper is related with manufacturing tolerances. The fabrication of the cone type aperture inside the metallic taper with such a long length (68mm, see Fig. 4.32(b)) and finished by a small hole (diameter of 5.08mm) has been a challenge for the manufacturers. Indeed, edges rounding inaccuracies in the top of the cone aperture inside of the metallic piece has complicated the embedding of the cone shaped arlon AD1000 part inside. Assembling misalignment also plays an important role for the good response of the device.

upna
Universidad Pública de Navarra
Nafarroako Unibertsitate Publikoa

Manufactured air-filled septum discussion

The experimental results have shown important drop on the obtainable aperture and radiation efficiencies.

The drop on the achievable gain can be related with the dielectric losses. In simulation, the loss tangent of the AD1000 material has been considered to be 0.0023, which introduces insertion losses of 0.6dBs on the feeding system composed by the air-filled septum and cone type taper on top filled with such material (Fig. 4.34(c)). Nevertheless, the insertion losses for the output port of the feeding system (septum+taper) could not be measured. They are expected to be higher than the 0.6dB predicted by HFSS.

The decrease on the aperture efficiency is related with the high XP level measured at broadside. As a rotationally symmetric MTS antenna does not introduce XP contribution at broadside (Fig. 4.28), its origin has been found in the poor CP field purity provided by the manufactured feeding system [89–92].

In the following lines the effect of the excitation CP field purity on the MTS aperture efficiency is characterized. For this purpose, the structure presented in Fig. 4.26 has been simulated excited with two orthogonal TE_{11} type modes with different phase shifts (Δps) on a circular waveguide filled with arlon AD100 (radius $a = 2.54mm$). Thereby, the MTS antenna is excited by several feeds with different AR values (see Fig. 4.56). Besides, the effect on the $\varphi = 0°, 45°, 90°$ cuts of the normalized RHCP and LHCP radiation patterns at 13.35GHz is shown in the figure, when the excitation provides AR values of 0dBs, 1.5dBs, 3dBs, 4.5dBs and 6dBs.

When the feeding system does not provide pure CP field to the rotationally symmetric MTS, it introduces an important XP contribution directly to the broadside radiation (Fig. 4.56). Moreover, it affects to the excitation of the TM and TE SWs on the MTS and consequently, to the CP purity of the field radiated by the complete antenna. When the AR is high, different cuts of the radiation pattern show asymmetries, which are not visible when the azimuthally symmetric MTS is excited with pure CP excitation. As the XP contribution increases, the obtainable maximum directivity and the aperture efficiency decrease.

In conclusion, the lost of CP purity is translated in asymmetries in the radiation patterns and in a loss of directivity, explaining the 2dB difference between predicted values of HFSS and the measurements.

upna
Universidad Pública de Navarra
Nafarroako Unibertsitate Publikoa

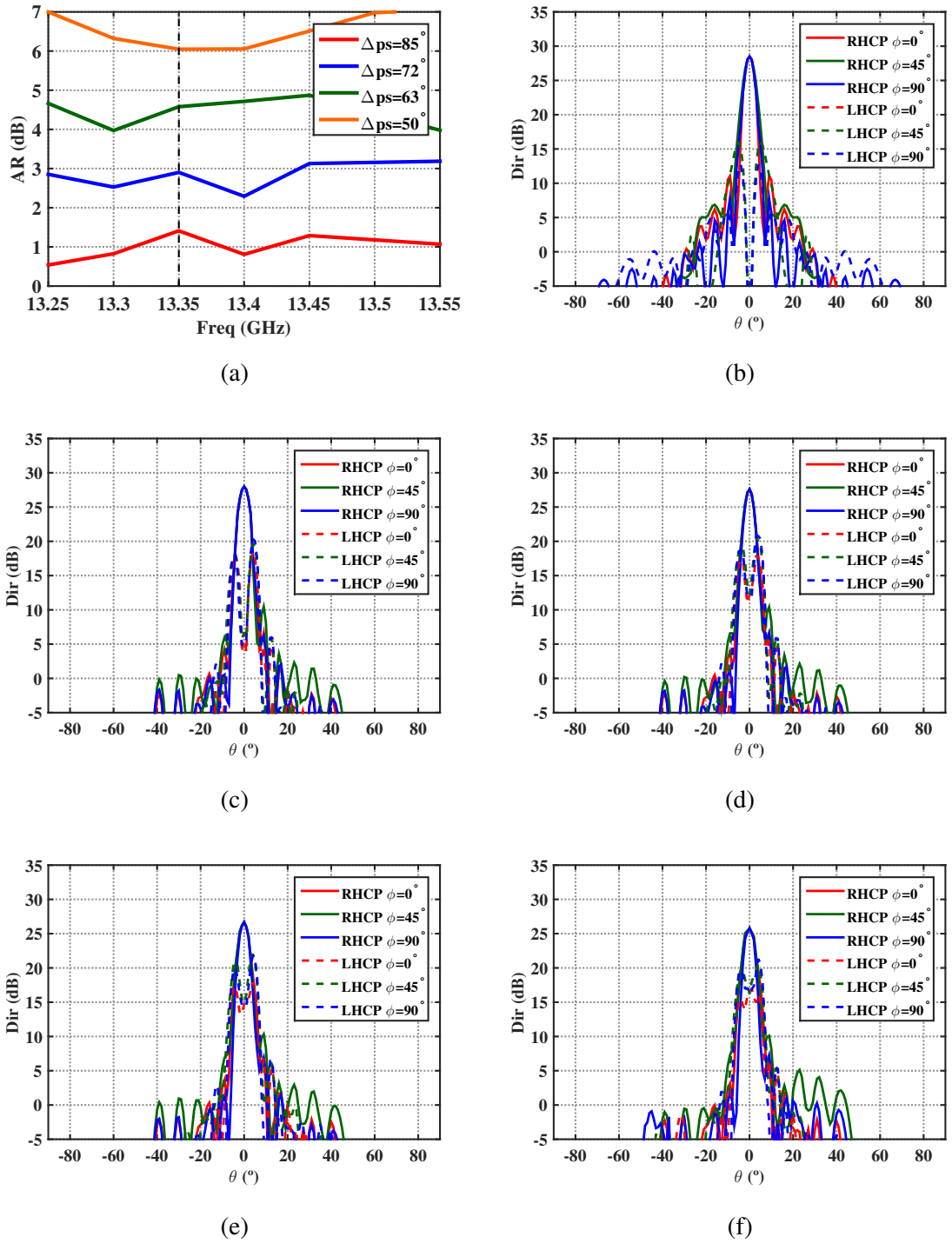

Fig. 4.56. (a) Different phase shifts (Δps) are introduced between the 2 orthogonal TE_{11} modes excited in the feed. $\varphi = 0°(red), 45°(green), 90°(blue)$ cuts of the normalized RHCP (continuous) and LHCP (dashed) radiation patterns at 13.35GHz, when exciting the MTS with a feed characterized by AR values of: (b) 0dB, (c) 1.5dB, (d) 3dB, (e) 4.5dB and (f) 6dB.

upna
Universidad Pública de Navarra
Nafarroako Unibertsitate Publikoa

4.5.3 Compact AD1000 based septum-OMT: fabrication and measurements

Fabrication details

The fabrication details of the compact septum filled with AD1000 dielectric are described in the following lines. For its fabrication, the dielectric part inside the circular waveguide has to be divided in two parts, taking as cutting plane the metallic septum inside the waveguide. Both parts can be seen in Fig. 4.57(a). At the same time, the SMA connectors have to be modified to improve the teflon matching to the AD1000 lateral junctions. A detail of the SMA connector together with the AD1000 cups are shown in Fig. 4.57(b). Measured dimensions of the fabricated metallic septum piece shown in Fig. 4.57(d) are gathered in Table 4.1. Small discrepancies are appreciated between the septum design optimized considering rounded-edges effect and the manufactured device. The fabrication of such a small and complex piece has been a big challenge for the manufactures.

The metallic septum has been introduced in the circular waveguide and it has been encapsulated as shown in Fig. 4.57(c). Besides, the dielectric junctions and matched SMA connectors have been joined with the feeding encapsulation. Special attention has been paid to avoid possible air gaps and misalignment during the assembling process.

upna
Universidad Pública de Navarra
Nafarroako Unibertsitate Publikoa

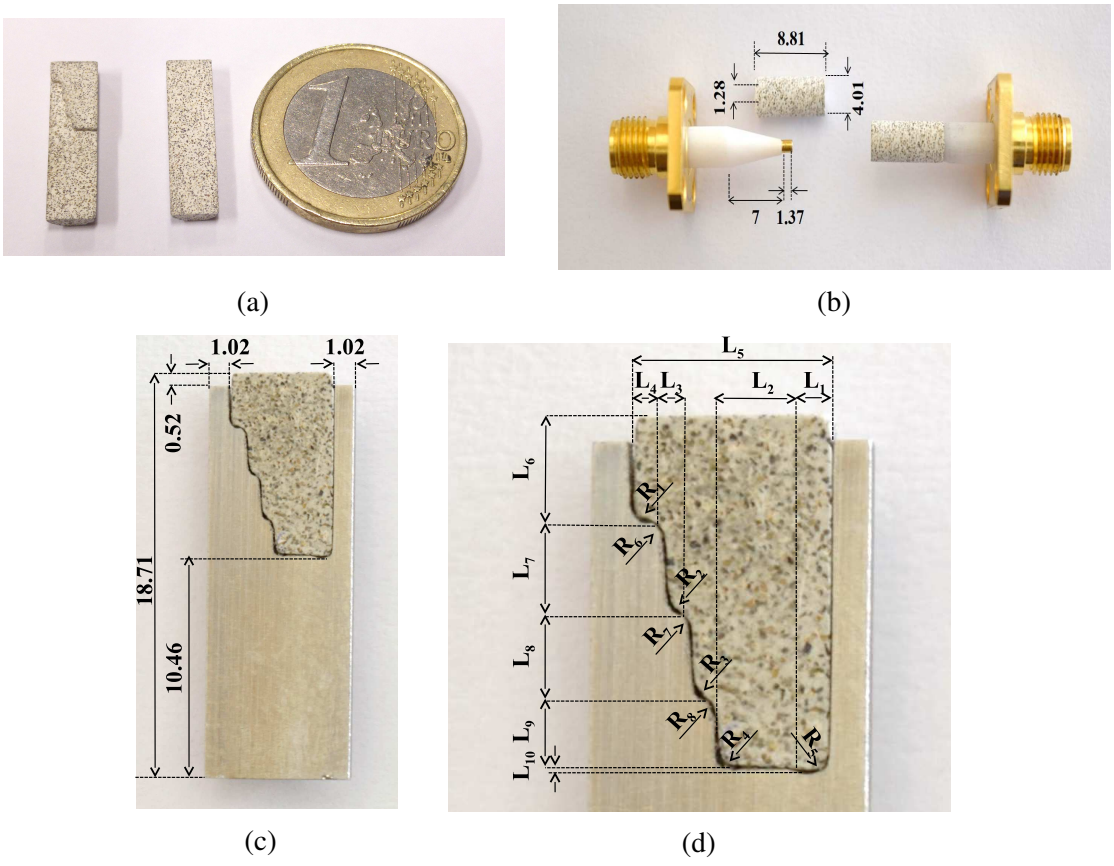

(a) (b)

(c) (d)

Fig. 4.57. Pictures of the fabricated pieces placed inside the feeding system: (a) AD1000 pieces for circular waveguide, (b) lateral AD1000 junctions and teflon-based matched SMA conectors, (c) encapsulation of the septum and dielectric pieces and (d) details of the metallic septum.

upna
Universidad Pública de Navarra
Nafarroako Unibertsitate Publikoa

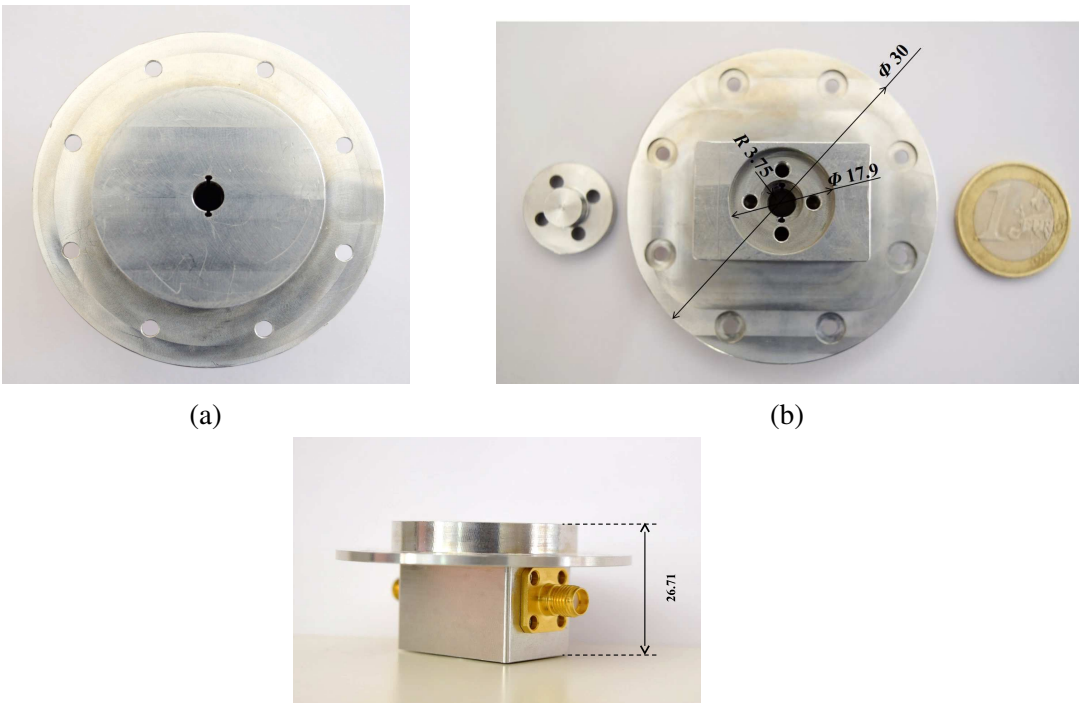

(a) (b)

(c)

Fig. 4.58. Pictures of the manufactured feeding system encapsulation: (a) top view, (b) bottom view and (c) lateral view.

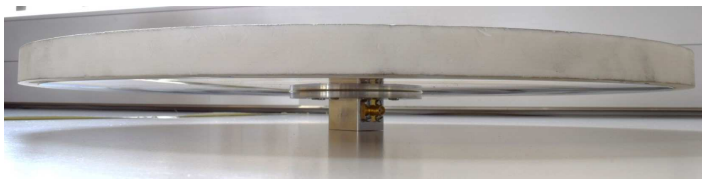

Fig. 4.59. Lateral view of the complete configuration with the MTS antenna and the compact AD1000 based feeding system.

upna
Universidad Pública de Navarra
Nafarroako Unibertsitate Publikoa

Measurements

The complete antenna (Fig. 4.59) including the MTS (Fig. 4.44), the hat (Fig. 4.49) and the compact AD1000 based feeding system (Fig. 4.58) have been characterized. The reflection and isolation properties have been measured at Ku-band (from 12.8GHz to 13.8GHz) and they are compared with the simulation results in Fig. 4.60. When feeding one of the ports a load is placed in the other one.

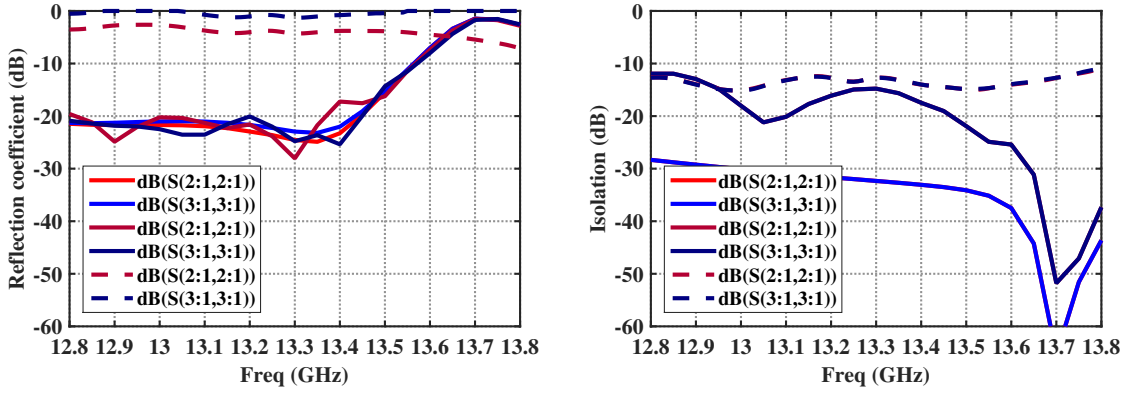

(a) (b)

Fig. 4.60. Comparison of the simulated (continuous lines) and measured (dashed lines) scattering parameters of the fabricated compact AD1000 based feeding system (light lines) and complete feeding system+MTS antenna (dark lines): (a) reflection coefficient and (b) isolation. Port 2 on (red lines) and port 3 on (blue lines).

Measured results show strong disagreement with the simulation, mainly in the reflection coefficient. Port 3 presents a reflection coefficient of -4dBs in the whole band while port 2 is not matched at all (-1dBs). Although the isolation between ports is below -13dBs for both ports, it does not provide accurate information as port 2 is completely mismatched.

The radiation pattern measurement for the MTS antenna excited with the compact feed is shown in Fig. 4.61. Only Port 3 has been used to excite the antenna. Normalized RHCP and LHCP at 13GHz, 13.08GHz and 13.22GHz are shown in Fig. 4.62.

Broadside RHCP radiation is obtained at 13.08GHz when port 3 excites the MTS antenna. The working bandwidth is 1.67%. At 13.08GHz the LHCP level at broadside is -25dB below RHCP, and around $\theta = 10^{\circ}$ is -8dBs. Nevertheless, the XP component increases fast when the frequency is varied: at 13GHz the XP value is -12dBs and at 13.22GHz it is -13.76dBs at broadside. These levels are high in comparison with the simulation results, in which at the working frequency (13.4GHz) the CP purity is ideal at broadside and XP is around -13dBs at 10° (see Fig. 4.28). As concluded in the previous section discussion, the origin of the

upna
Universidad Pública de Navarra
Nafarroako Unibertsitate Publikoa

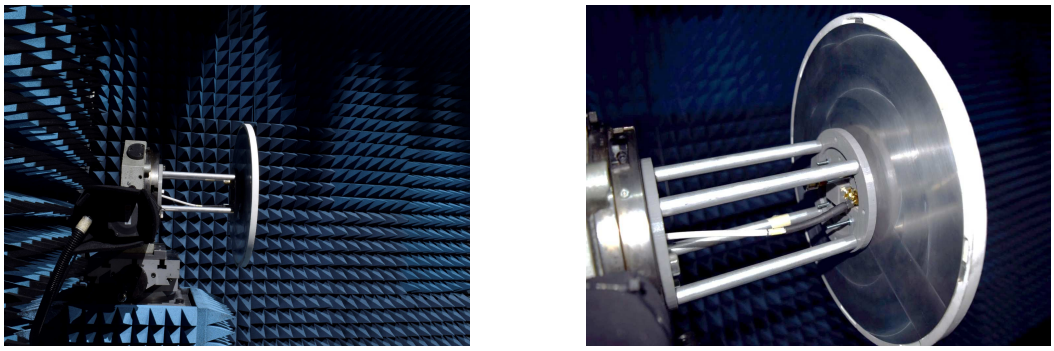

(a) (b)

Fig. 4.61. (a) Radiation pattern measurement setup and (b) zoom in of the MTS antenna excited with the compact feeding system.

measured XP contribution at broadside is related with the loss of CP purity of the excitation when the manufactured feed is employed [89–92].

Measured directivity and gain values are compared with the simulation results in Fig. 4.63. The gain calculation has been realized considering two linear contributions following Eq. (4.26). It has to be mentioned that for the gain calculation, the dependence with the antenna matching has been avoided following the Eq. (4.27), where the received power is corrected ($S_{21}^{'}$) taking into account the reflection coefficient of both antennas:

$$S_{21}^{'}(dB) = 10\log_{10}\left(\frac{|S_{21}|^2}{(1-|S_{11}|^2)(1-|S_{22}|^2)}\right) \tag{4.27}$$

A maximum directivity of 25.3dBs is obtained at 13.2GHz when the MTS antenna is excited with port 3. In consequence, the aperture efficiency is decreased from 32% obtained at simulation to 13.5% in measurements. Experimental gain is 23.8dBi, providing a radiation efficiency of 70.6%.

Measured AR provided by the compact AD1000 filled septum is shown in Fig. 4.64. The AR provided by the manufactured compact feeding system is above 3dBs in the whole band. Nevertheless, there is a fast drop of the measured AR to 0.92dBs at 13.08GHz, which agrees with the working frequency of the MTS antenna. Measured values are higher than predicted ones, with (1dB) and without (0.5dB) rounded edges.

upna
Universidad Pública de Navarra
Nafarroako Unibertsitate Publikoa

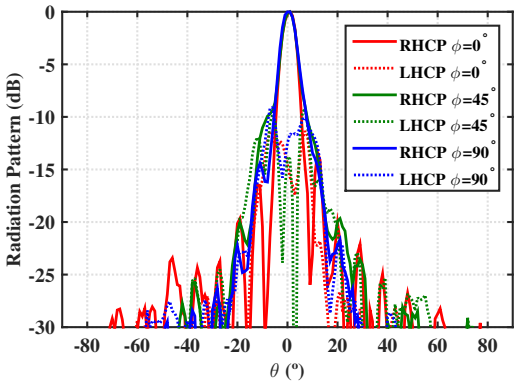

(a)

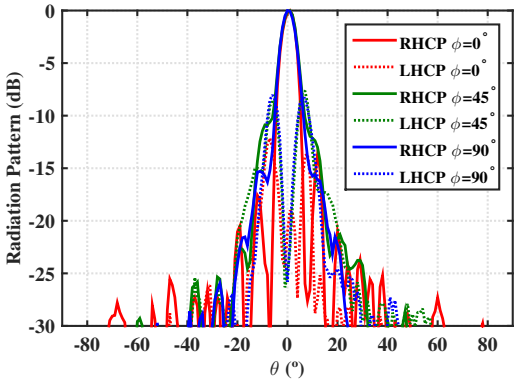

(b)

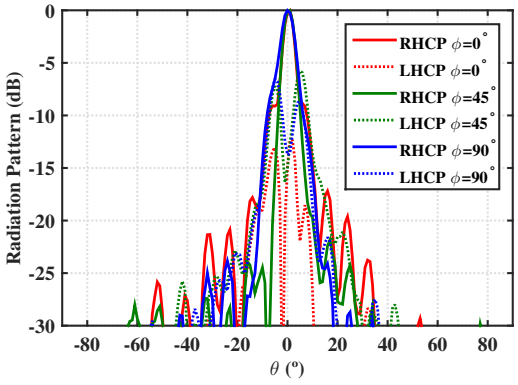

(c)

Fig. 4.62. Measured RHCP (continuous) and LHCP (dashed) radiation patterns at $\varphi = 0°(red), 45°(green), 90°(blue)$ cuts obtained with the MTS excited with the compact AD1000 filled feeding system (port 3 on) at: (a) 13GHz, (b) 13.08GHz and (c) 13.22GHz.

upna
Universidad Pública de Navarra
Nafarroako Unibertsitate Publikoa

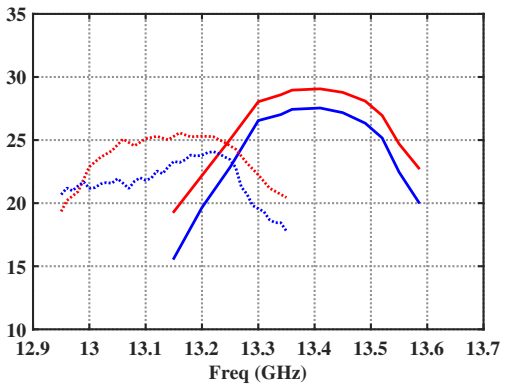

Fig. 4.63. Frequency dependence of measured directivity and gain obtained with the MTS antenna excited with the compact AD1000 filled feeding system.

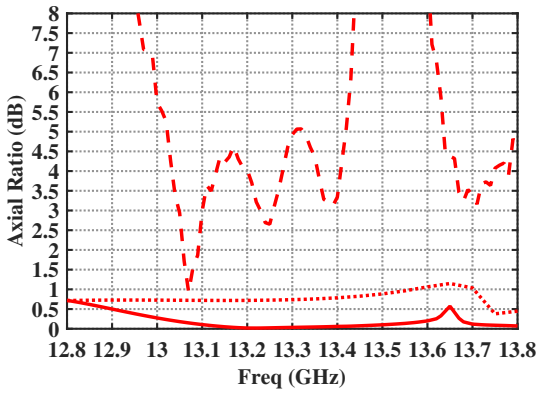

Fig. 4.64. Predicted AR of the ideal septum (continuous lines) and fabricated septum with rounded-edges (dotted lines). Measured AR provided by the compact septum (dashed lines) with port 3 on.

upna
Universidad Pública de Navarra
Nafarroako Unibertsitate Publikoa

Manufactured AD1000 based septum discussion

The manufacturing of the compact AD1000 based septum has been a challenge. For instance, the manufacturing of the AD1000 dielectric junctions with a cone type aperture in the center to match with the SMA teflon parts (Fig. 4.57(b)) has proven to be very complex. Several attempts have been required to obtain consistent fabricated pieces. As a consequence of this mismatch with the SMA connectors, very high return losses are measured in the input ports, which are specially important at port 2. Besides, the feed shows high sensitivity with the embedding between the dielectric parts inside the septum (Fig. 4.57(c)).

As the field provided by the feed (feeding port 3) is not purely CP, it introduces XP field component to the broadside radiation of the complete antenna. It affects also to the excitation of the MTS modes and consequently, to the contribution of all the radiated field polarization. As the XP increases, the contribution of the copolar field component is decreased and the obtainable maximum directivity and aperture efficiency are reduced. It is remarkable that the experimental working frequency of the complete MTS antenna is centered at 13.08GHz, which agrees with the frequency at which the feeding system AR rises its minimum value (0.92dBs). In conclusion, it is expected that an optimization of the feeding system fabrication and assembling will ensure better excitation of the complete MTS antenna with important aperture efficiency increase.

It is remarkable that the MTS antenna is well matched with the feeding system. Possible mismatch between the output port of the feed and the MTS antenna would drive to field reflection from the output port towards the isolated input port with the opposite polarization. If this port is not matched properly (as it is the case of port 2), the field would be reflected again to the output port and in consequence, the provided AR would be completely degraded. As port 3 is exciting the structure appropriately, it can be concluded that the matching betwen the MTS antenna and the feed is correct.

On the other hand, the drop on the measured gain is related with the dielectric losses. In simulation, they are estimated to be 0.43dBs in the septum but experimentally they seem to be higher. As in the previous septum design, insertion losses of the septum could not be measured. The dielectric characterization is required.

upna
Universidad Pública de Navarra
Nafarroako Unibertsitate Publikoa

4.6 Conclusions

Preceding works presented in literature have demonstrated the suitability of the MTS technology to design CP broadside antennas [54–60]. Nevertheless, these solutions provide single CP behavior. In this chapter, a step forward has been given and the implementation of a boresight Ku-band (13.5GHz) MTS antenna capable to provide dual CP has been accomplished. For the first time, two cylindrical wave front SWs of different nature have been excited on a MTS antenna.

The characterization of the equivalent surface impedance modulation must be accomplished taking into account both TM and TE modes. The normalized average values (η_{TX}), periodicities (d_{TX}) and modulation indexes (m_{TX}) have been appropriately adjusted to ensure TM and TE SWs propagation on the structure matched in phase and the generation of a LW in broadside radiation.

The ideal MTS has been a proof-of concept to verify the theoretical basics. Besides, the MTS synthesis has been carried out by a dense texture of anisotropic sub-wavelength elements printed on a grounded dielectric slab of arlon AD1000 ($\varepsilon_r = 10.2$, $h = 1.27mm$). The TM and TE frequency dispersion features shown by the pixel composed by a metallic elliptical patch with an asymmetric cross-shaped aperture make it suitable for the MTS implementation. The simulation results obtained with the synthesized MTS and with a minimized cone-type hat in the center show a maximum directivity of 29.06dB at 13.4GHz. The aperture efficiency is about 32% in a 1.5% fractional bandwidth. The radiation efficiency of this solution is about 70.5%. The fast frequency dispersion of the TE mode impacts on the operational bandwidth of the complete configuration, as the phase matching condition of the modes is fulfilled in a narrow bandwidth. The main reason for the decrease in the aperture efficiency is the Cartesian-lattice discretization carried out for adapting the periodic unit cell to the theoretical, rotationally symmetric, homogeneous surface impedance. While this discretization is not a problem for the TM case (and therefore not a problem for single CP antennas), it is critical for TE mode. There are two reasons that lead to this assumption: on the one hand, the modulation index for the TE mode is high. On the other hand, the isofrequency dispersion curves associated with the TE case are more sensitive to the rotation of the geometry into the square lattice. Therefore, MTS synthesis requires special attention not only in radial direction to ensure the surface impedance modulation but also in azimuthal direction to compensate locally the TE spatial dispersion.

It has to be highlighted that in the proposed dual CP broadside solution the employed feeding system plays an important role. In section 4.3, an in-depth study has been carried out to conclude that, unlike at the single CP broadside MTS antennas [54–60] in which usually one or four vertical pins are required to excite the single TM mode in the structure, at the

upna
Universidad Pública de Navarra
Nafarroako Unibertsitate Publikoa

dual polarization configuration an optimized circular waveguide is necessary. Two septum OMT polarizers have been designed to provide RHCP and LHCP field from the excitation placed in the center of the structure.

The first proposed solution is a large device composed by a metallic stepped single ride with 5 steps located inside an air-filled square waveguide and a conical-shaped taper to match the field to the MTS antenna excitation. The measurements of the MTS antenna excited with such feed has validated the RHCP and LHCP broadside radiation behavior of the proposed MTS antenna solution, depending whether port 2 or port 3 is on. The working bandwidth of the structure is narrow (1.5%) and the antenna efficiency is limited, due to the low aperture efficiency (15.56%-18.2%) and obtained gain (40.9%-46.6%). The maximum directivity is limited by the important XP introduced mainly by the taper. The losses are mainly introduced by the employed dielectric.

The second solution is a compact device, but more risky to fabricate and with a more complex embedding. In this case, the circular waveguide has a metallic stepped single ride in the center with 4 steps and it is filled with arlon AD1000. Only port 3 works properly in the manufactured prototype. The experimental results show an aperture efficiency of 13.5% and radiation efficiency of 70.6%. As in the previous analyzed large feeding system, the aperture efficiency is limited because the excitation is not optimum and the losses are important (about 3dBs).

Improvement on the employed feeding system will rise to a better performance of the complete MTS configuration and increase of the antenna efficiency. It has been demonstrated experimentally that the employment of the proposed rotationally symmetric anisotropic MTS antenna provides dual CP broadside beam radiation and could be employed to substitute two MTS antennas developed based on conventional configurations.

upna
Universidad Pública de Navarra
Nafarroako Unibertsitate Publikoa

Chapter 5

Characterization of a single layer MTS antenna for dual frequency band applications

5.1 Introduction

All the MTS antenna solutions found in literature are focused on single frequency applications [54–60]. It can be appreciated that the two main limitations of the MTSs are related with the low aperture efficiency and the provided working bandwidth. Usually, the required surface impedance properties are fulfilled within a narrow bandwidth and it limits the overall response.

The proof-of-concept work developed during this chapter analyses the capability of single layer MTSs to cover more than one frequency band with different CP radiation patterns. The theoretical considerations taken into account for the characterization of modulated anisotropic MTS antennas able to provide broadside or isoflux-shaped radiation patterns at two frequencies at Ku band, f_1=13GHz and f_2=16GHz, (f_2/f_1=1.23) are described in section 5.2. Three different MTS antennas have been synthesized employing the same anisotropic pixel geometry, composed by a circular metallic patch with a groove trough its diameter. The first configuration, which is shown in section 5.3, provides an isoflux-shaped beam at f_1 and broadside radiation pattern at f_2. Afterwards, a second MTS solution is presented radiating with an isoflux-shaped pattern at both frequencies (section 5.4). To finish, the third model presented in section 5.5 provides broadside radiation at f_1 and isoflux-shaped beam at f_2. The chapter ends with the conclusions.

upna
Universidad Pública de Navarra
Nafarroako Unibertsitate Publikoa

5.2 Basic Operation Principle

Based on Eq. (3.20), each position of the rotationally symmetric anisotropic MTS ($\boldsymbol{\rho}$) the tangential electric ($\mathbf{E}_t$) and magnetic ($\mathbf{H}_t$) fields at the upper MTS-air interface are described by means of an anisotropic, lossless anti-Hermitian surface impedance tensor $\bar{\bar{\mathbf{X}}}(\omega,\boldsymbol{\rho},\mathbf{k_t})$ [35]. A single cylindrical TM SW excited from the center of the structure with a vertical pin is hybridized due to the anisotropic nature of the MTS. The electric field components are related with the surface impedance tensor components as:

$$\begin{aligned}\mathbf{E}_\rho &= -jX_{\rho\rho}H_\varphi\hat{\boldsymbol{\rho}}\\ \mathbf{E}_\varphi &= -jX_{\rho\varphi}H_\varphi\hat{\boldsymbol{\varphi}}\end{aligned} \tag{5.1}$$

In the absence of modulation, the uniform surface reactance supports a SW characterized at a given frequency by a real phase constant β_i, which can be related with the capacitive average surface reactance following Eq. (3.26). As described in chapter 3 (section 3.2.4), the SW becomes gradually a LW when it interacts with a surface impedance modulated in radial direction characterized by the modulation index (m_i), the periodicity (d_i) and the average value ($\eta_i = X_i/\zeta$) at each frequency [52].

$$\begin{aligned}X_{\rho\rho_i} &= \zeta\eta_i[1+m_i\cos(2\pi\rho/d_i)]\\ X_{\rho\varphi_i} &= \zeta\eta_i m_i\sin(2\pi\rho/d_i)\end{aligned} \tag{5.2}$$

As explained, this periodic structure generates a complex perturbation to the wavenumber associated with the average reactance and the field is expressed by n-indexed Floquet modes [52]:

$$\begin{aligned}\beta_i \quad &\rightarrow \quad k_i^{(0)} = \beta_i + \Delta\beta_i - j\alpha_i\\ k_{ni} = k_i^{(0)} + \frac{2\pi n}{d_i} &= k_i\sin(\theta_{ni})\end{aligned} \tag{5.3}$$

$\Delta\beta_i$ and α_i can be estimated following the method proposed by Oliner and Caminita in [52, 77] and extended in appendix C. In summary, this procedure characterizes the waves supported by a sinusoidally modulated impenetrable impedance in one dimensional canonical model by means of their complex wavenumbers. Considering the periodic nature of the problem, both the fields and currents over the surface are described in terms of FMs as:

$$E_x = Z_S\sum_n I_{xn}e^{-jk_{xn}x} = \sum_n \widetilde{G}_{EJ}^{TM}(k_{xn})I_{xn}e^{-jk_{xn}x} \tag{5.4}$$

upna
Universidad Pública de Navarra
Nafarroako Unibertsitate Publikoa

where the spectral Green's function $\widetilde{G}_{EJ}^{TM}(k_{xn},0)$ accordingly to the TRE [52, 77] is defined as:

$$\widetilde{G}_{EJ}^{TM}(k_{xn}) = -Z_0^{TM} = -Z_0\frac{k_{zn}}{k} \tag{5.5}$$

where $Z_0^{TM} = \zeta\frac{k_{zn0}}{k}$ and $Z_{cc}^{TM} = jZ_1\frac{k_{zn1}}{k_1}\tan(k_{zn1}h)$ are the free space and grounded slab contributions related with the TM mode. ζ and k are the free space impedance and wavenumber respectively. $Z_1 = \zeta/\sqrt{\varepsilon_r}$ and $k_1 = k\sqrt{\varepsilon_r}$ are the dielectric impedance and wavenumber. h and ε_r are the the grounded slab thickness and permittivity. The numerical solution of the complex wavenumber k_{xn} is obtained finding the solution of the recurrence function relating the infinite unknown modal currents I_{xn} [52, 77]as shown in the appendix C.

Fig. 5.1 shows the $\Delta\beta$ and α (normalized to k) predicted for different modulation indexes (m) and pointing angles (θ_{-1}) when two different normalized average surface reactance values are implemented ($\eta = 0.7, 1.3$).

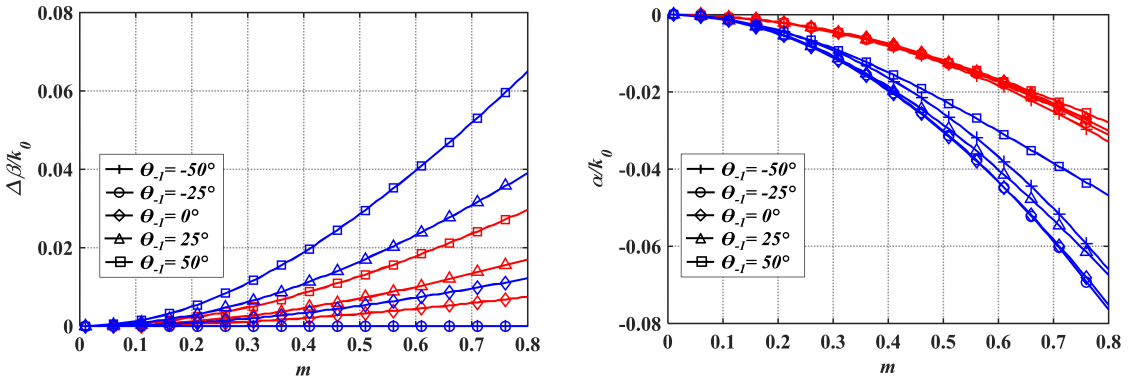

(a) (b)

Fig. 5.1. Variation of (a) $\Delta\beta$ and (b) α (normalized to k_0) as a function of the modulation indexes m for different pointing angles $\theta_{-1} = -50°, -25°, 0°, 25°, 50°$ for two normalized average reactance values: $\eta = 0.7$ (red) and $\eta = 1.3$ (blue).

The modulation index m, which is mainly related with the attenuation constant, determines the size of the radiating surface (see Fig. 5.1). Therefore, the use of higher m values gives rise to a MTS dimension reduction. Nonetheless, the employment of small m is a desirable feature as it simplifies the implementation process: when $m < 0.45$, the perturbation introduced to the SW wavenumber associated with the average surface impedance is purely complex and MTS synthesis can be done with independent control of beam shaping (related with $\Delta\beta$) and the radiation pattern side lobe levels (related with α). On the contrary, large m values require fine readjustment of d to keep the LW pointing angle. This readjustment is more important

upna
Universidad Pública de Navarra
Nafarroako Unibertsitate Publikoa

for FW radiation angles than BW directions. It seems reasonable to think that a variation of m in SW propagation direction, with lower values on the center of the structure and higher close to the edges of the MTS, would allow to generate a uniform illumination over the surface which would increase the overall aperture efficiency. Besides, it is remarkable that structures with higher average impedance values require smaller m to radiate with a given attenuation constant.

The modulation properties are related with the pointing angles of -1 and -2-indexed FMs, $\theta_{-1}(^\circ)$ and $\theta_{-2}(^\circ)$, in Fig. 5.2.

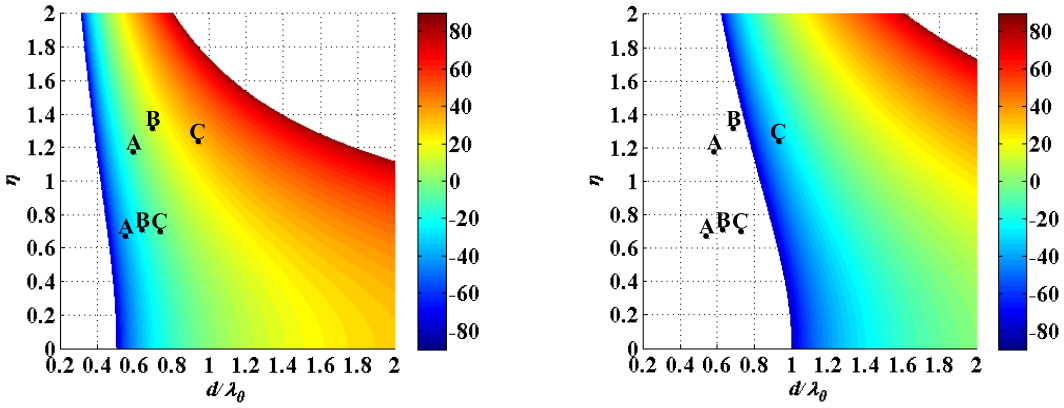

(a) (b)

Fig. 5.2. Relation between the surface impedance modulation parameters (normalized periodicity d/λ_0 and normalized average impedance η values) and n-indexed mode radiation pointing angle θ_{-n}: (a) $\theta_{-1}(^\circ)$ and (b) $\theta_{-2}(^\circ)$. A, B and C denotes the modulation properties of the examples analysed in section 5.3, section 5.4 and section 5.5, respectively.

From Fig. 5.2 it can be concluded that it is also possible to control the MTS radiation properties at two different frequencies, depending on the synthesized d_i and η_i values. Structures with higher average impedance values require smaller d to radiate towards a given angle. The radiation characteristics at two frequencies can be controlled taking into account the inductive nature of the surface supporting a TM SW ($\eta_2 > \eta_1$).

Considering this modulation properties analysis, three different single layer MTSs are characterized in the following sections, capable to provide different shaped radiation patterns at two frequency bands. First, a MTS radiating with an isoflux-shaped beam at $f_1 = 13$GHz and broadside beam at $f_2 = 16$GHz is presented (section 5.3). Afterwards, a second single layer MTS antenna is synthesized with isoflux-shaped patterns at the two frequencies (section 5.4). To conclude, a third configuration radiating in broadside direction at f_1 and with isoflux-shaped beam at f_2 is characterized in section 5.5. In all the aforementioned examples,

upna
Universidad Pública de Navarra
Nafarroako Unibertsitate Publikoa

the CP of the radiated field is ensured exciting the rotationally symmetric anisotropic MTS by 4 vertical pins in phase quadrature.

5.3 Isoflux pattern at f_1 and broadside at f_2

5.3.1 Surface impedance characterization

In this configuration an azimuthally symmetric anisotropic MTS is assumed (Fig. 5.3), characterized by normalized average surface impedance values η_1 and η_2 at two working frequencies, f_1 and f_2. The average impedance values at each band are related with the phase constants of the supported cylindrical TM mode (β_1 and β_2) trought Eq. (3.26).

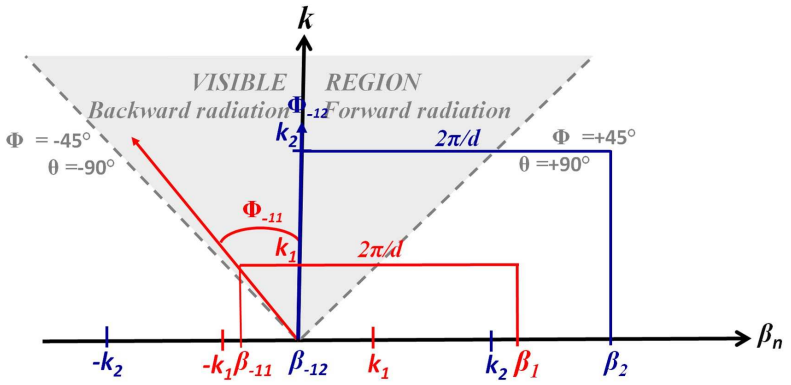

Fig. 5.3. k vs. β diagram describing BW radiation at f_1 (red) and broadside radiation at f_2 (blue). $\theta_{ni} = \arcsin(\tan(\Phi_{ni}))$ and $d_i = d$.

With the appropriate surface impedance characterization it is possible to obtain an isoflux-shaped radiation pattern at f_1 (see Fig. 5.3). The beam in the lower band is radiated in BW direction ($\theta_{-11} < 0°$). Moreover, it can be seen also in the figure that in the upper band the beam is directed in broadside direction ($\theta_{-12} = 0°$). It is straightforward to conclude from Eq. (5.3) that these radiation properties can be obtained when the impedance modulations periodicities at each band are equal ($d_i = d$)and it meets:

$$d = \frac{\lambda_1}{(\lambda_1/\lambda_{sw_1}) + \sin(|\theta_{-11}|)} = \lambda_{sw_2} \tag{5.6}$$

where λ_i and λ_{sw_i} are the free space and SW wavelengths at each frequency band and θ_{-11} is the pointing angle of the radiated -1 indexed mode at f_1.

Considering the aforementioned theoretical basics, a single layer rotationally symmetric modulated anisotropic MTS has been implemented with BW isoflux radiation pointing towards $\theta_{-11} = -35°$ at f_1=13GHz and with broadside radiation $\theta_{-12} = 0°$ at f_2=16GHz

upna
Universidad Pública de Navarra
Nafarroako Unibertsitate Publikoa

(see *A* marker in Fig. 5.2). The surface impedance modulation at each frequency is described following Eq. (5.2). In this example, the surface impedance average values and modulation indexes have been specified as: $\eta_1 = 0.65$, $m_1 = 0.2$ at 13GHz and $\eta_2 = 1.15$, $m_2 = 0.2$ at 16GHz. The modulation periodicity is $d = 0.57\lambda_1 = 0.69\lambda_2$. The distribution of the anisotropic modulated surface reactance tensor components normalized to free-space impedance are shown in Fig. 5.4.

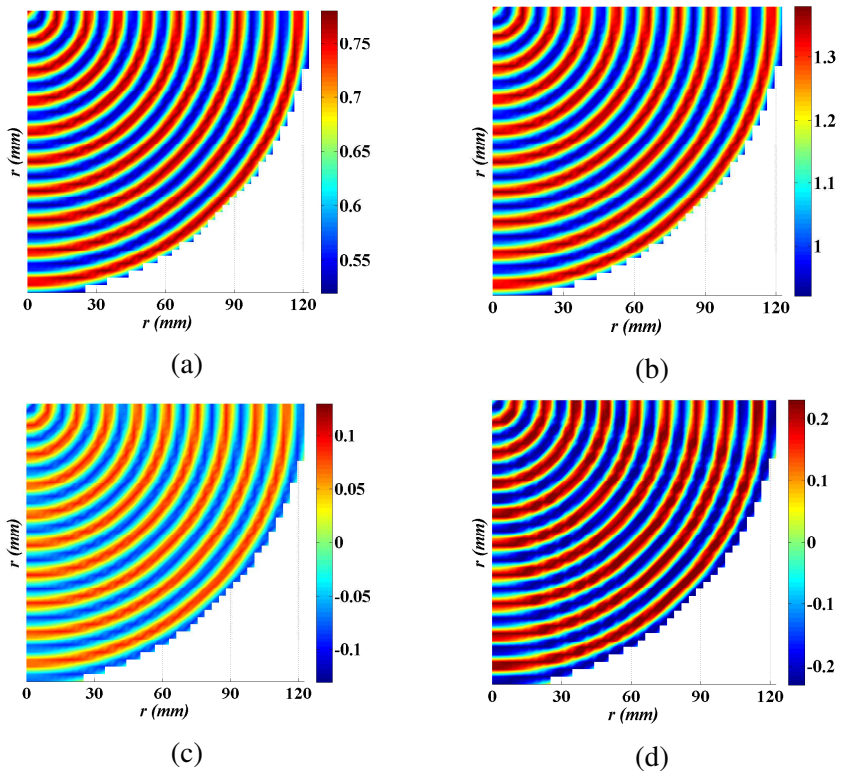

Fig. 5.4. Normalized to free-space impedance components of the surface impedance tensor at f_1=13GHz and f_2=16GHz of the first MTS configuration: (a) $\eta_{\rho\rho_1}$, (b) $\eta_{\rho\rho_2}$, (c) $\eta_{\rho\varphi_1}$ and (d) $\eta_{\rho\varphi_2}$.

5.3.2 Selection of the pixels for MTS synthesis

Based on the extensive background acquired in chapter 3 (section 3.3) on frequency and spatial dispersion characterization of different anisotropic patch geometries and considering the calculated surface impedance maps database, the optimum pixel for the MTS synthesis has been chosen.

The selected anisotropic pixel is composed by a circular metallic patch with a groove trough its diameter (shown in Fig. 3.12(c)). It has a cell dimension of $u = 3.14mm$, a normalized radius (a/u) and a groove with a normalized width (w/u). The patch rotation

upna
Universidad Pública de Navarra
Nafarroako Unibertsitate Publikoa

inside the cell is ψ. This pixel has been printed on top of the grounded dielectric arlon AD1000 with a thickness of $h = 1.27mm$.

The dispersion properties of the pixel for different patch rotations inside the cell are depicted in Fig. 3.16(a) and Fig. 3.18(c) (chapter 3, section 3.3). Moreover, the normalized surface impedance maps for different geometry variations at 13GHz and 16GHz are shown in Fig. 5.5.

The electrically larger patches provide higher impedance values, namely, the surface wave wavelength decreases with larger a/u values or when the SW impinges the patch at the groove direction (see Fig. 5.5). As expected, there is no coupling when the SW impinges the patch through its symmetry axes. For different directions, the cross polar contribution becomes important (maximum when $\psi = 45°$). The inductive nature of the pixel (characterized by $\eta_1 < \eta_2$) ensures the propagation of hybrid mode (dominantly TM) on the MTS at two frequencies.

The continuous modulated surface impedance tensors illustrated in Fig. 5.4 have been discretised at each position of the antenna with a Cartesian lattice (period of $u = 3.14mm$). The implementation has been accomplished selecting the periodic patch with a certain size and rotation that best match the required $\eta_{\rho\rho_i}$ and $\eta_{\rho\varphi_i}$ tensor values at both bands, by means of the minimum mean square error (see Fig. 5.6).

The simulation of the complete structure (with a radius of $r = 5.48\lambda_1 = 6.75\lambda_2$) have been carried out with the ANSYS HFSS. In this structure it is not possible to employ symmetries to reduce the problem and the complete structure must be studied. The full wave analysis has been launched in the workstation HP Z800, with 192GB RAM, 2 processors at 3.47GHz (X5690 with 12 cores). The generation of the MTS composed by 64000 patches takes about 7 hours. A converged solution is obtained with a mesh of 2.8 million tetrahedra. The simulation time with these properties is about 16 hours.

upna
Universidad Pública de Navarra
Nafarroako Unibertsitate Publikoa

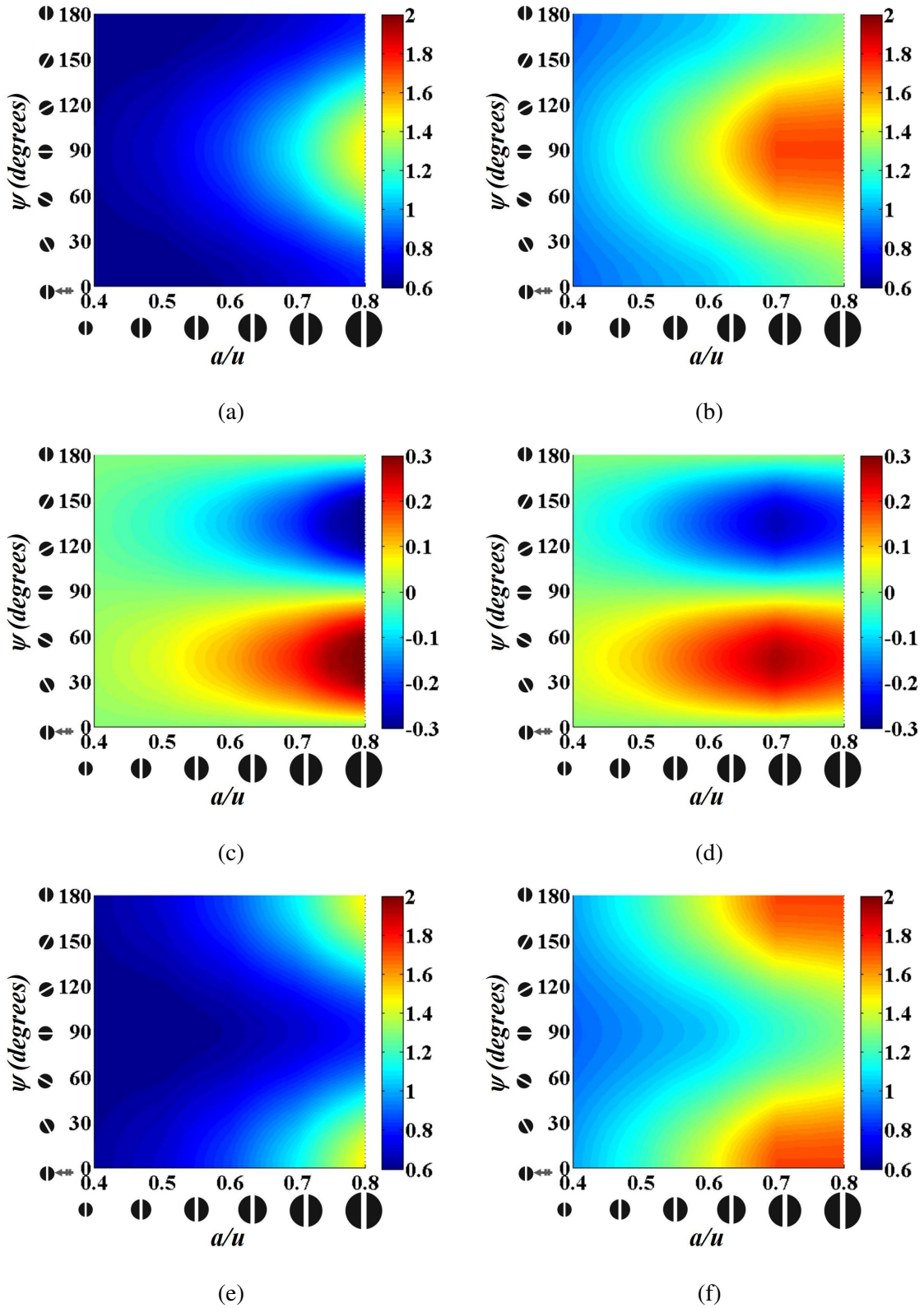

Fig. 5.5. (a),(b) $\eta_{\rho\rho}$, (c),(d) $\eta_{\rho\varphi}$ and (e),(f) $\eta_{\varphi\varphi}$ values at 13GHz (left column) and 16GHz (right column) for patches with different normalized radii (a/u) and rotations ($\psi(^\circ)$). Unit cell dimension $u = 3.14mm$. The SW impinges the cell towards $\phi = 0^\circ$.

upna
Universidad Pública de Navarra
Nafarroako Unibertsitate Publikoa

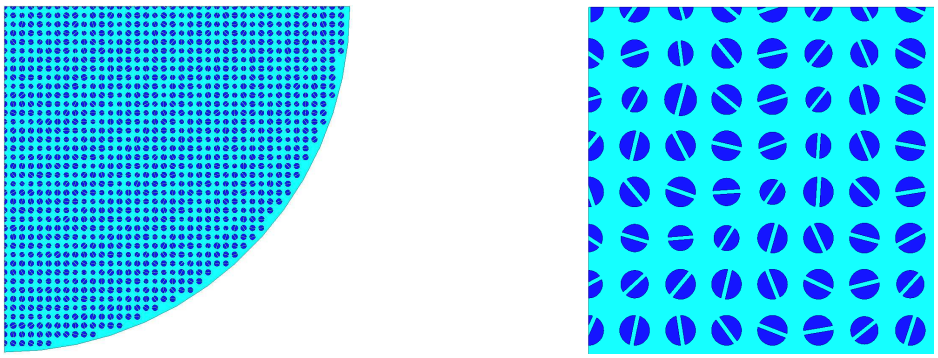

(a) (b)

Fig. 5.6. Implementation details of the first single layer anisotropic MTS: (a) a quarter of the structure with radius $r = 5.48\lambda_1 = 6.75\lambda_2$ and (b) zoom in of the antenna center.

5.3.3 Simulation results

RHCP and LHCP radiation patterns ($\varphi = 45^\circ$ cuts) obtained with the presented MTS configuration at both frequency bands are shown in Fig. 5.7.

With this structure BW isoflux RHCP radiation pattern is obtained at low frequencies (see Fig. 5.7). The working bandwidth is about 3.9% around 12.75GHz. At this frequency, a maximum directivity of 8.6dB is obtained at the edge of coverage (around 33° angle) while in angles close to the broadside ($< |20^\circ|$) the directivity is around 7.7dB. XP component is 20dBs lower than copolar for angles close to broadside but it is considerably deteriorated when pointing far from 0°. For other frequencies in the lower band, the pointing angle varies approximately $\pm 10^\circ$. The main drawback is given by fast drop on the beam around $|25^\circ|$ which could deteriorate the uniform power reception in earth.

In the upper band, around 15.25GHz (3% bandwidth), a maximum directivity of 26.96dBi is obtained in broadside. The estimated aperture efficiency is 27.6% and radiation efficiency is 70.8%. The LHCP component is 22dBs below the RHCP.

upna
Universidad Pública de Navarra
Nafarroako Unibertsitate Publikoa

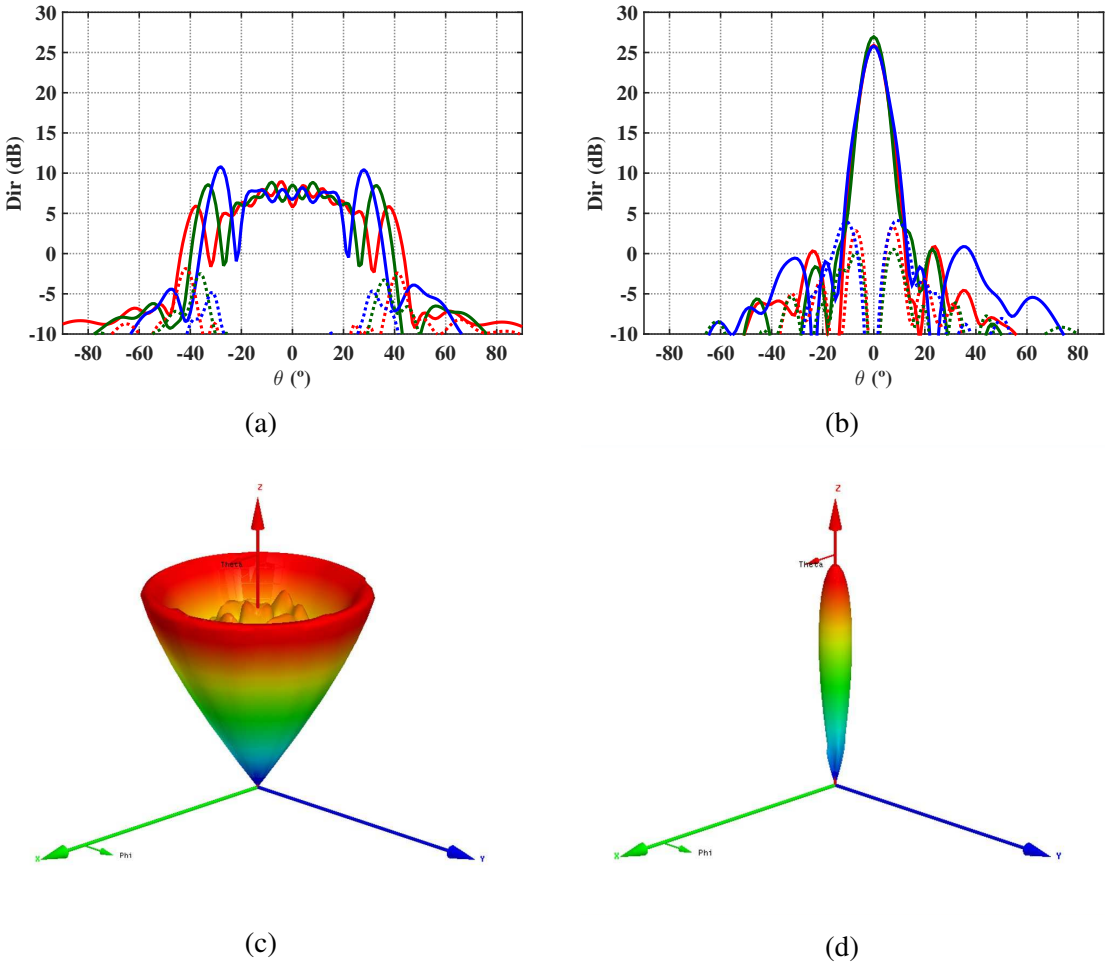

Fig. 5.7. $\varphi = 45°$ cuts of RCHP (continous lines) and LHCP (dashed lines) patterns obtained with the first proposed MTS configuration at: (a) Low band: 12.5GHz (red), 12.75GHz (green) and 13GHz (blue). (b) High band: 15GHz (red), 15.25GHz (green) and 15.5GHz (blue). 3D radiation pattern at (c) 12.75GHz and (d) 15.25GHz.

upna
Universidad Pública de Navarra
Nafarroako Unibertsitate Publikoa

5.4 Dual band isoflux pattern

5.4.1 Modulation details

The viability to implement a single layer cylindrical MTS antenna with dual band isoflux-shaped radiation pattern is analyzed in this section. Increasing the value of d_i while keeping constant the average surface impedance values at each frequency band, the pointing angle can be increased. As it is illustrated in Fig. 5.8, BW radiation is obtained in the lower band while FW radiation is achieved in the upper band.

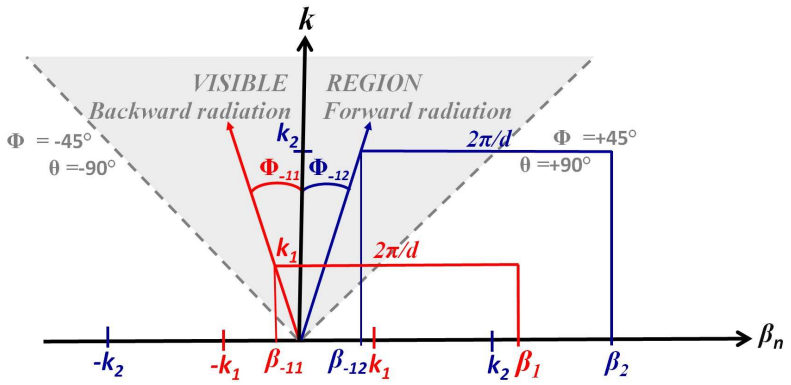

Fig. 5.8. k vs. β diagram describing BW radiation at f_1 (red) and FW radiation at f_2 (blue). $\theta_{ni} = \arcsin(\tan(\Phi_{ni}))$ and $d_i = d$.

Following Eq. (5.3) the modulation period required to ensure this dual band isoflux pattern behavior is established:

$$d = \frac{\lambda_1 + \lambda_2}{\lambda_1/\lambda_{sw_1} + \lambda_2/\lambda_{sw_2}} \tag{5.7}$$

The second studied MTS antenna works also at f_1=13GHz and f_2=16GHz and provides isoflux-shaped radiation pattern at both bands with a drop-off angle of $|\theta_{-11}| = \theta_{-12} = 22°$ (see *B* marker in Fig. 5.2). In this example, the implemented surface impedance modulation parameters are: $\eta_1 = 0.72$, $m_1 = 0.2$, $\eta_2 = 1.3$, $m_2 = 0.2$ and $d = 0.63\lambda_1 = 0.78\lambda_2$ (Fig. 5.9).

upna
Universidad Pública de Navarra
Nafarroako Unibertsitate Publikoa

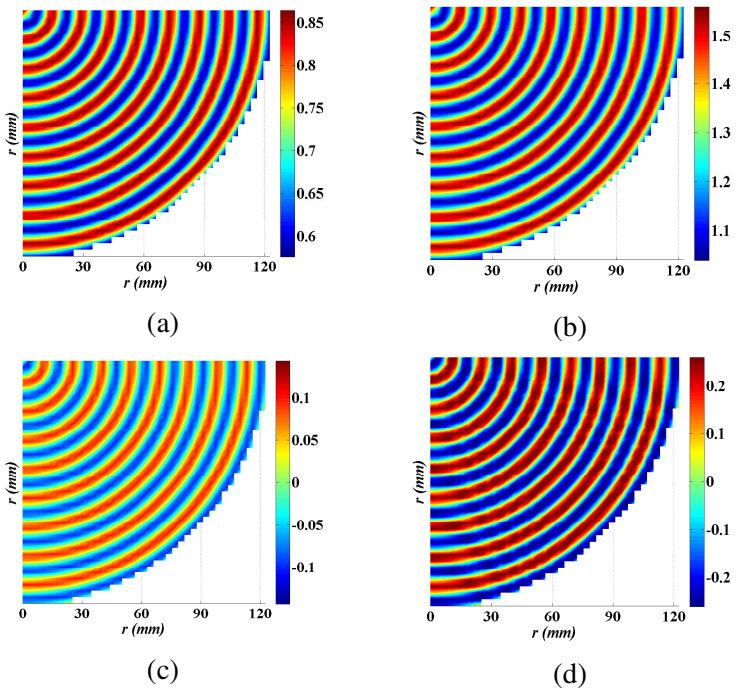

Fig. 5.9. Normalized to free-space impedance components of the surface impedance tensor at f_1=13GHz and f_2=16GHz of the second proposed MTS configuration: (a) $\eta_{\rho\rho_1}$, (b) $\eta_{\rho\rho_2}$, (c) $\eta_{\rho\varphi_1}$ and(d) $\eta_{\rho\varphi_2}$.

5.4.2 Pixel selection for MTS synthesis

The patch geometry selected for the implementation of this second MTS configuration is the same as the one employed in the previous section 5.3.2, as it also provides the desired surface impedance values of this second configuration. The required continuous modulated surface impedance components have been discretised and implemented with the patches that best match the requirements at both working frequencies. Fig. 5.10 shows how the patch geometry and rotation modifies at each position of the surface.

5.4.3 Simulation results

The radiation pattern at $\varphi = 45°$ for RHCP and LHCP obtained with this MTS configuration at both bands are shown in Fig. 5.11.

Fig. 5.11 shows BW and FW isoflux radiation patterns at low and high frequency bands respectively within $|\theta_{-11}| = \theta_{-12} = 22°$. A maximum directivity of 10dBs is obtained at 12.75GHz and 13dBs at 15.25GHz. In both bands, the XP is below -15dBs with respect to the RHCP in the whole edge of coverage.

upna
Universidad Pública de Navarra
Nafarroako Unibertsitate Publikoa

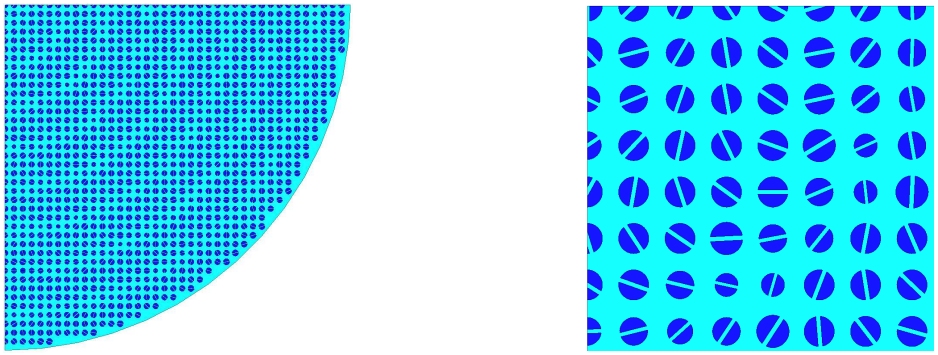

(a) (b)

Fig. 5.10. Implementation details of the second single layer MTS: (a) a quarter of the structure with radius $r = 5.7\lambda_1 = 6.75\lambda_2$, (b) zoom in of the antenna center.

5.5 Broadside pattern at f_1 and isoflux at f_2

5.5.1 Modulation details

The third proposed MTS configuration presents broadside pattern at f_1 and isoflux radiation at f_2 (Fig. 5.12).

Eq. (5.8) establishes a relation between the modulation parameters between both frequency bands to obtain broadside radiation at f_1 and isoflux-shaped beam at f_2. It is remarkable that although in most of the applications unimodal regime is required and consequently the maximum value of d_2 is limited, in this case two modes are contributing to the radiation at f_2: the $-1-$*indexed* Floquet mode contributes to FW radiation while the $-2-$*indexed* mode contributes to BW radiation towards the same pointing angle, $|\theta_{-22}| = \theta_{-12}$ (blue arrows in Fig. 5.12).

$$d = \lambda_{sw_1} = 1.5\lambda_{sw_2} \tag{5.8}$$

5.5.2 Selection of the pixels for MTS synthesis

In this case, the synthesized surface impedance parameters are $\eta_1 = 0.67$, $m_1 = 0.2$, $\eta_2 = 1.23$, $m_2 = 0.2$ and $d = 0.77\lambda_1 = 0.94\lambda_2$ (see Fig. 5.14). In this design, the radiation towards $\theta_{-11} = 0^\circ$ is expected at 13GHz and isoflux-shaped beam towards $\theta_{-12} = \theta_{-22} = |33|^\circ$ is obtained at 16GHz.

upna
Universidad Pública de Navarra
Nafarroako Unibertsitate Publikoa

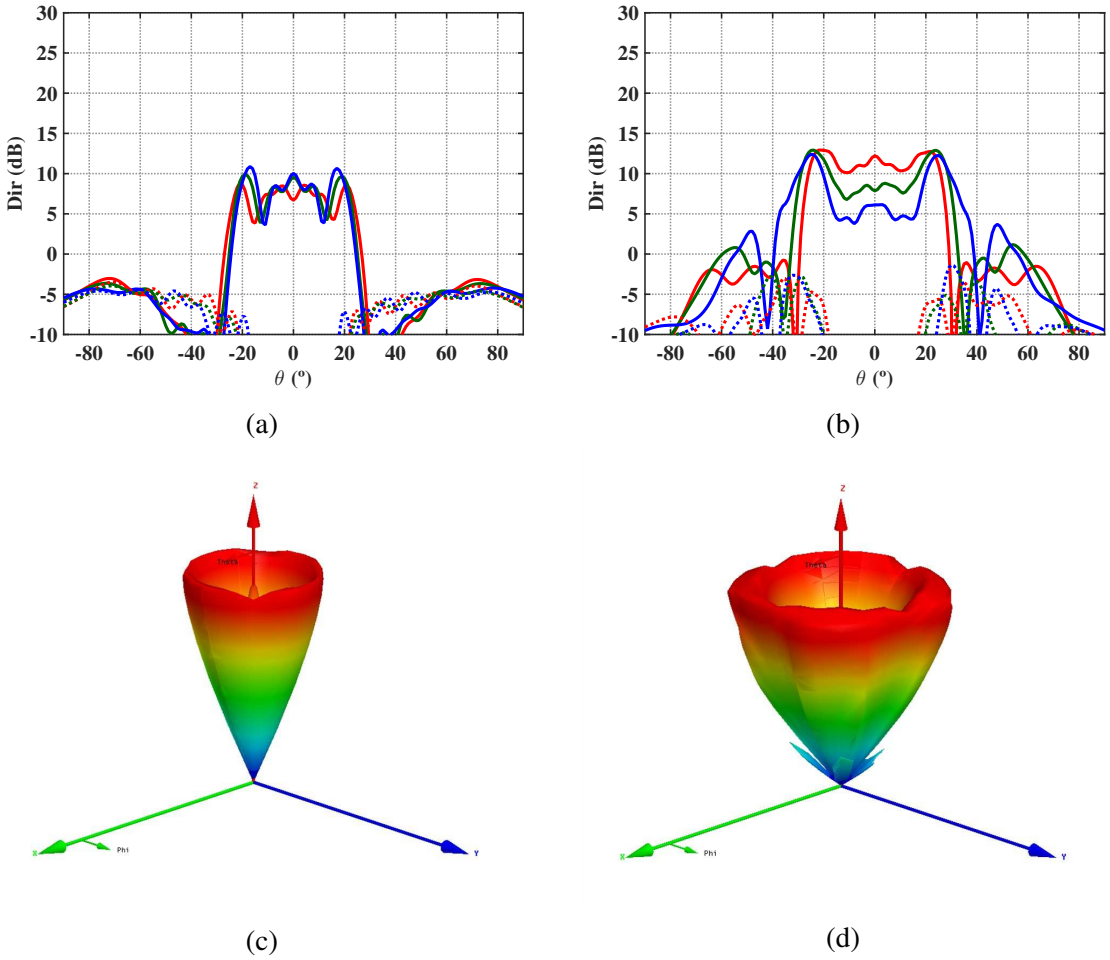

Fig. 5.11. $\varphi = 45°$ cuts of RHCP (continous lines) and LHCP (dashed lines) patterns of the second MTS configuration at: (a) Low band: 12.5GHz (red), 12.75GHz (green) and 13GHz (blue). (b) High band: 15GHz (red), 15.25GHz (green) and 15.5GHz (blue). 3D radiation pattern at (c) 12.75GHz and (d) 15.25GHz.

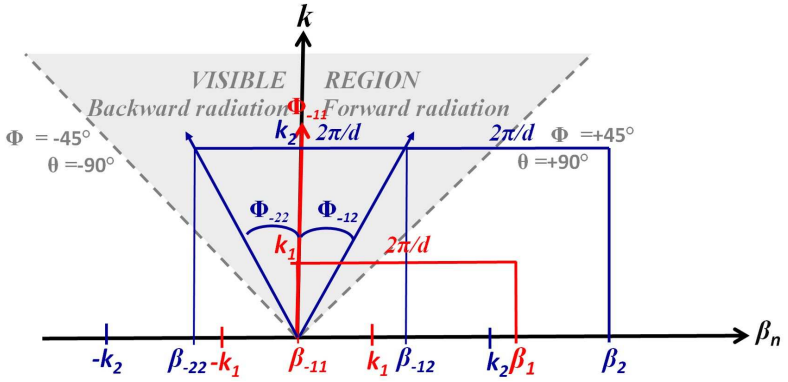

Fig. 5.12. k vs. β diagram describing broadside radiation at f_1 (red) and combination of BW and FW radiation at f_2 (blue). $\theta_{ni} = \arcsin(\tan(\Phi_{ni}))$ and $d_i = d$.

upna
Universidad Pública de Navarra
Nafarroako Unibertsitate Publikoa

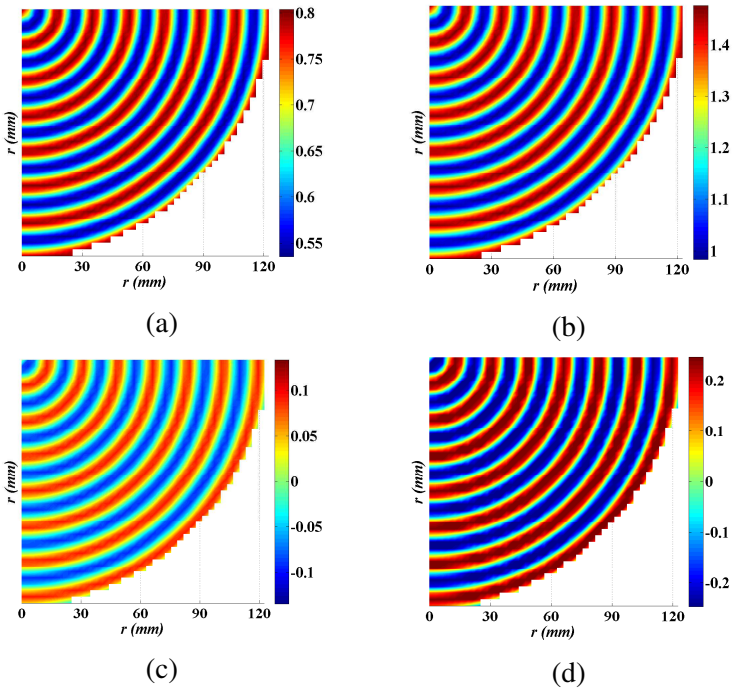

Fig. 5.13. Normalized to free-space impedance components of the surface impedance tensor at f_1=13GHz and f_2=16GHz of the of the third proposed MTS configuration: (a) $\eta_{\rho\rho_1}$, (b) $\eta_{\rho\rho_2}$, (c) $\eta_{\rho\varphi_1}$, (d) $\eta_{\rho\varphi_2}$.

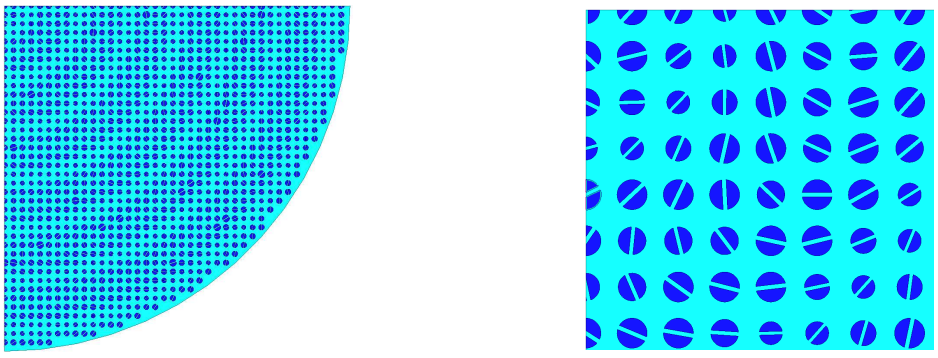

Fig. 5.14. Implementation details of the third single layer MTS: (a) a quarter of the structure with radius $r = 5.7\lambda_1 = 6.75\lambda_2$, (b) zoom in of the antenna center.

upna
Universidad Pública de Navarra
Nafarroako Unibertsitate Publikoa

5.5.3 Simulation results

Fig. 5.15 shows RHCP ($\varphi = 45°$) and LHCP ($\varphi = 45°$) radiation patterns at two working frequency bands.

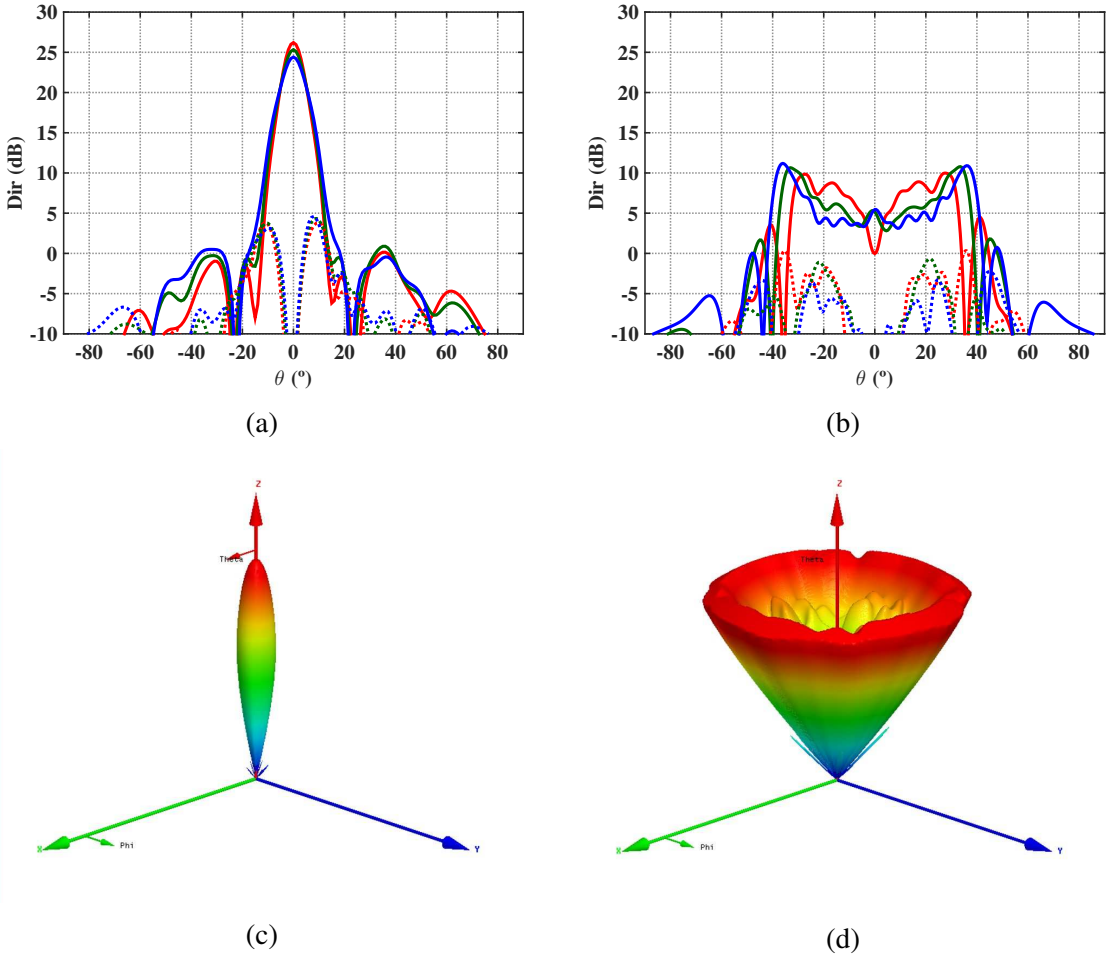

Fig. 5.15. $\varphi = 45°$ cuts of CO and XP patterns with the third MTS implementation at: (a) Low band: 12.5GHz (red), 12.75GHz (green) and 13GHz (blue). (b) High band: 15GHz (red), 15.25GHz (green) and 15.5GHz (blue). 3D radiation pattern at (c) 12.75GHz and (d) 15.25GHz.

A maximum directivity of 26.21dBs is obtained at 12.75GHz (Fig. 5.15). The structure radiates with RHCP and the LHCP component is 21.7dBs below. The aperture efficiency is 35.4% and the calculated radiation efficiency is 70.4% in around 3% of the lower bandwidth. Isoflux radiation pattern is obtained at 15.25GHz in the upper band, within $|\theta| = 33°$ with a directivity of 10dBs. Pointing angle is shifted $\sim 5°$ at close frequencies (from 15GHz to 15.5GHz). The limitation of this structure is given by the XP component, which reaches -6.7dB in the worse case close to $|\theta| = 20°$ angles inside the coverage region.

upna
Universidad Pública de Navarra
Nafarroako Unibertsitate Publikoa

5.6 Conclusion

This paper shows the viability of the single layer MTSs to obtain dual frequency behavior with different radiation patterns at each band. Three different MTS configurations have been synthesized employing circular metallic pixels with a groove through their diameter, with a certain size and rotation at each position of the antenna based on the presented theoretical analysis.

All the structures presented in the chapter provides single circularly polarized radiated field, with RHCP. The first solution shows isoflux radiation pattern at 12.75GHz with a drop-off angle of 33° and LHCP below 20dBs with respect to RHCP. At 15.25GHz RHCP broadside radiation pattern is shown with a maximum directivity of 26.96dBi (aperture efficiency around 27.6%) and XP of -22dBS. The second configuration is a dual band isoflux antenna with BW and FW radiations at each band, with the drop off angle at $|\theta_{-11}| = \theta_{-12} = 22°$. The directivity is about 10dBs and 13dBs and the XP is below -15dBs with respect to the RHCP in all the edge of coverage. The last example shows broadside radiation pattern in the lower band and isoflux radiation pattern at higher frequencies, based on the contribution of -1 and -2 indexed modes to the radiated field. A maximum directivity of 26.21dBs is obtained at 12.75GHz with the LHCP component 21.7dBs below the RHCP. At 15.25GHz an isoflux radiation pattern within $|\theta| = 33°$ is obtained with a directivity of 10dBs. The limitation of this structure is given by the XP component, which reaches -6.7dB in the worse case close to $|\theta| = 20°$ angles inside the coverage region.

The limitations of the proposed configurations are related with the distance between working frequencies (Δf), the working bandwidths at each band and the maximum obtainable pointing angles at FW directions at f_2. These features depend mainly on the selected patch geometry, as it is characterized by particular frequency dispersion properties and it provides a limited surface impedance value. With the selected pixel geometry, ditance between the working frequencies is $\Delta f = 12\%$, the working bandwidth is approximately 3% and the pointing angle is limited to $|\theta| = 33°$. Moreover, low modulation index $m = 0.2$ is applied at the two frequencies to ensure negligible synthesis error which leads to large structures.

Other effects such as the fast drop shown on the beam around $|\theta| = 25°$ at the lower band could deteriorate the uniform power reception in earth. An optimization of the feeding is required to correct this effect. A metallic hat could be located appropriately on top of the 4 vertical pins employed to excited the structure and in this way, the level at the center part of the radiation pattern can be adjusted. An optimization is also necessary at the third configuration in order to decrease the CP effect around $|\theta| = 20°$ angles at the upper band adjusting the modulation parameters to control the XP for pointing angles far from the broadside direction.

upna
Universidad Pública de Navarra
Nafarroako Unibertsitate Publikoa

Chapter 6

Conclusions and open lines

6.1 Conclusions

All the conclusions derived at each chapter are included in this section of the dissertation. The main objective of the thesis was to carry out an in-depth study of the most interesting planar technologies to implement antennas for satellite applications, analysing their strengths and weaknesses, such as compactness, lightness, maximum achievable gain, multiple band response or circular polarization purity. It has been proved that PRS technology can comply with a specific application with dual behavior, being both frequencies really close. At the same time, it has been proposed a novel broadside beam MTS configuration to work with RHCP or LHCP polarization and dual band configurations are presented with different radiation patterns.

During the first stage of the thesis, as a continuation of the work developed in the Antenna Group of the Public University of Navarra, a Partial Reflective Surface was implemented to meet the requirements of Telemetry Tracking and Control application working at two frequencies at C-band (3.7GHz and 4.2GHz). Features such as gain over coverage at established bandwidth, circular polarization purity, return loss, or isolation have been fulfilled with the compact ($\sim \lambda_0/2$) and light solution presented in chapter 2. The obtained simulation results proved that this technology can be deployed as an alternative to the bulky configurations based in conventional technologies.

Following the progress towards even more flat technologies, the later work has been focused on the study of the MTS technology. The main objective has been to carry out in-depth analysis on MTSs to develop an advanced thin MTS antenna with dual circularly polarized broadside radiation pattern at Ku-band. Although different interesting solutions have been already proposed by several authors, which employ MTS to radiate with circular polarization not only in broadside but also with complex shifted beams, they provide only single circular

upna
Universidad Pública de Navarra
Nafarroako Unibertsitate Publikoa

polarization. It is remarkable that the MTS antenna presented in this dissertation works, for the first time, with dual circular polarization.

Chapter 3 describes in a clear way the classification of the different MTSs found in the literature and their properties. The differentiation is given by means of the characteristic surface impedance, which can be uniform or modulated, isotropic or anisotropic, or even can be distinguished as impenetrable or penetrable. For each case, the features of the pixels conforming the MTS are detailed and the characterization of the propagation or radiation properties of the configurations are described. In addition, the full wave dispersion characterization of TM and TE surface waves over different isotropic and anisotropic pixel geometries have been carried out. The same patches have been analysed combining a single run of the eigenmode solver with the closed-form expressions presented by Mencagli et al. in [61–63] and the results are compared in the appendix A. The good agreement between both methods proved that it is possible to efficiently simplify the dispersion characterization which facilitates the implementation of the MTSs. Besides, the equivalent surface impedance of the modes have been calculated by means of the procedure presented by Martini et al. in [38]. The obtained results have been compared with an alternative method presented by Patel et al. in [64–72] which employs scattering information of incident plane waves to extrapolate the surface impedance information. Nevertheless, the comparison of the methods show some discrepancies and in conclusion, the employment of the Patels method has been limited for low frequency regime or when the employed dielectrics are characterized by low ε_r or thickness values.

The knowledge acquired in chapter 3 provided the background to develop a ready-to-use MTS antenna characterized by dual circular polarized broadside radiation at Ku-band. Chapter 4 describes the modelling, implementation and measurements obtained with the designed prototype. The preliminary guide-lines for the design of the proposed solution has been validated by means of full wave simulations. Not only the implementation of the MTS but also the design of a manufacturable feeding system has been a challenge, due to the numerous strict conditions that the different conforming parts of the antenna must met.

On one hand, control of the propagation characteristics of the two SWs of TM and TE types excited over the structure fulfilling the polarization and phase balancing conditions have been accurately carried out. Moreover, by means of a extensively explained appropriate adjustment of the surface impedance modulation parameters, the direction and circular polarization purity of the radiated field have been determined. The implementation of the MTS has been performed deploying a elliptical shaped pixel geometry with an asymmetric cross-shaped aperture in the center, which frequency and spatial dispersion properties and surface impedance characterization have been carried out. These pixels, with a cell dimension

upna
Universidad Pública de Navarra
Nafarroako Unibertsitate Publikoa

about $u = \lambda_0/7$, have been printed over an ARLON AD1000 grounded dielectric ($\varepsilon = 10.2$ and thickness h=1.27mm=$\lambda_0/17.5$) by photolithography technique. The radius of the complete antenna is $r = 8.6\lambda_0$. The structure is ultrathin and light (320g).

On the other hand, the required feed has been proved to be more complex than the vertical coaxial employed usually to excite a TM mode over the single circularly polarized MTS configurations. The design of two feeding systems have been realized, which ensure the correct excitation of two TE_{11} modes in phase-quadrature at the circular waveguide port of the MTS antenna filled with ARLON AD1000 dielectric. The first solution is a large air-filled septum OMT with a AD1000 based taper on top, with a total length of 144mm=$6.4\lambda_0$. The second design is a compact ($18.73mm = 0.8\lambda_0$ length), innovative and sophisticated feed.

The MTS prototype has been tested in the anechoic chamber of the Antennas Group at UPNA. Firstly, the large air-filled feeding system has been employed to excite the MTS configuration. When the MTS is excited with port 2, it radiates in broadside with LHCP, while when port 3 is excited broadside RHCP radiation is obtained. Hence, dual CP behavior is confirmed experimentally, demonstrating the theoretical study carried out during this thesis and validating the proposed MTS design. Therefore, the proposed configuration can substitute two conventional single CP MTS antennas necessary to meet the requirements in two polarizations.

Nevertheless, the measurements have shown also some limitations. The aperture efficiency is about 15.56%-18.2% at 13.2GHz, lower than the 32% obtained at the simulation working frequency (13.4GHz). It has been concluded that the aperture efficiency decrease is related with the poor CP field purity provided by the fabricated feeding system. The measured XP level at broadside is high (from -15dBs to -8dBs) and it increases to -5dBs around $\theta = 10°$. It has been proved that manufacturing optimization of the feed could lead to important improvements on the aperture efficiency of the complete MTS antenna. Besides, the AD1000 dielectric losses are higher than expected and the radiation efficiency is about 40.9%-46.6%. Thus, experimental characterization of the employed dielectric is also required.

On the other hand, the second feeding system composed by a compact AD1000-based septum OMT has been employed to excite the MTS antenna. It has to be mentioned that although the design has been re-adjusted several times taking into account the edges-rounding effect and fabrication limitations, its manufacturing has been difficult and the assembly of all the small pieces is very sensitive to air gaps or possible misalignment. Only one port has been employed in measurements because the other one is mismatched. Broadside RHCP radiation is obtained at 13.08GHz. Measured LHCP level is 25dBs below RHCP broadside, but it increases to -12dBs when frequency is shifted. It has been proved again that this effect

upna
Universidad Pública de Navarra
Nafarroako Unibertsitate Publikoa

is due to the poor AR provided by the feed. The experimental characterization have shown that this single layer MTS antenna prototype meets the requirements of both RHCP and LHCP applications, and with appropriate optimization of the feeding system the efficiency of the solution will increase considerably.

To conclude, the last chapter of the dissertation (chapter 5) analyses the capability of single layer anisotropic MTSs to cover more than one frequency band with different CP radiation patterns. Three different MTS configurations have been synthesized employing circular patches with a groove through their diameter and excited by 4 vertical pins. It has been shown that controlling appropriately the surface impedance modulation parameters, the hybrid mode excited from the center becomes a LW with different shaped beam at two working frequencies. The implemented configurations work at 13GHz and 16GHz and radiate with broadside or isoflux-shaped beams. The limitations of the proposed solutions, such as the frequency separation, the working bandwidth at each band and the maximum beam angles, are related with the dispersion characteristics of the used pixels. Besides, some improvements must be introduced in the modulation to be able to control the XP level when the beam is radiated far from broadside.

As a general conclusion, the thesis has helped to the evolution of MTS technology with innovative designs.

6.2 Open lines

The presented work has opened quite a lot of different possibilities to continue with the design of MTSs and PRSs.

The PRS antenna developed in the first part of the thesis meets all the on board requirements of a dual band TT&C application working at 3.7GHz and 4.2GHz. Due to this fact, the logical continuation of this work would be the fabrication and measurement of the proposed design. Based on the PRS structures shown in literature and previous experience in the group with such antennas, the obtained measurements are expected to be in very good agreement with the simulation results.

The correct behavior of the MTS antenna prototype for dual CP broadside beam radiation at Ku band has been demonstrated experimentally and it could be employed to substitute two single CP MTS solutions designed based on conventional techniques. Nevertheless, in future works the efforts must be focused on the optimization of the feeding systems fabrication because it is limiting considerably the efficiency of the antenna.

To conclude, the work carried out in the last chapter shows that the single layer MTSs beam steering at multiband is limited by the dispersion properties of the pixel geometry

upna
Universidad Pública de Navarra
Nafarroako Unibertsitate Publikoa

employed to synthesize the surface. Due to this fact, the research thread on MTS antennas must be oriented to search new pixels. For instance, active elements could be introduced on the surfaces to modify the modulation period and in consequence, the beam pointing angle. New pixels with appropriate frequency dispersion properties could widen the bandwidth of the proposed solutions. Another possible alternative could be the use of substrates with variable permittivity in order to be able to provide different surface impedance values. To finish, a second layer might be also introduced on the MTS to have more degrees of freedom in the design.

Finally, as high frequencies are getting more and more important nowadays, as millimeter or THz bands, challenging future line will be the design of MTS and PRS antennas in these frequency bands. The main expected difficulty could arise from the fabrication point of view.

upna
Universidad Pública de Navarra
Nafarroako Unibertsitate Publikoa

Appendix A

Alternative frequency dispersion analysis method based on Closed-form representation

The employment of the eigen mode solver of commercial simulators such as CS[80] or Ansys HFSS [70] to calculate full spatial and frequency dispersion properties of the different nature modes propagating on metallic patches printed over dielectric substrate can become a tough and time consuming task, since convergent solutions corresponding to each phase shift must be simulated with refined mesh and the procedure must be repeated for each geometry variation.

Mencagli et all. developed in [61–63] an alternative method to approximate the dispersion characteristics of the dominant TM SW propagating on isotropic or anisotropic spatial and frequency dispersive structures by means on closed-form expressions. This method only requires the determination of the dielectric properties (ε_r and h) and the calculation of one or two quasi-static capacitance depending whether the element is isotropic or anisotropic, respectively. For simple geometry pixels, such as the circular patch one, it is possible to employ analytic expressions to completely characterize the system [83–85] and the proposed procedure is extremely fast. For other geometries, the quasi-static capacitance can be efficiently extrapolated from a single run of the eigen solver provided by the commercial simulators.

These procedure [61–63] defines three regions on the dispersion curves of the TM mode depending on the phase shift (Δph) over the unit cell: the low frequency region (LF) ($\Delta ph = 0^\circ - 40^\circ$), the transition region ($\Delta ph = 40^\circ - 140^\circ$) and the Floquet-Boch (FB) region for higher phase shift values ($\Delta ph = 180^\circ$). The dispersion equation of the dominant TM mode agrees with Eq. (3.29) where the sheet impedance is defined by means of a quasi-

upna
Universidad Pública de Navarra
Nafarroako Unibertsitate Publikoa

static capacitance as follows: $Z_S^{TM} = jX_S^{TM} = -j/\omega C_c^{TM}(k_t)$. The quasi-static capacitance describes the boundary conditions of the metallic patches and it remains constant for all the frequencies (or phase shifts) below the FB region: $C_c(k_t) = C$.

Based on the same idea, the frequency dispersion of the TE SW has been carried out considering $Z_S^{TE} = jX_S^{TE} = -j/\omega C_c^{TE}(k_t)$. Fig. A.1 shows the contributions of the modes, ground plane and patch to the dispersion equation, obtained from the full wave eigen mode results of the pixel geometries shown in Fig. 3.13.

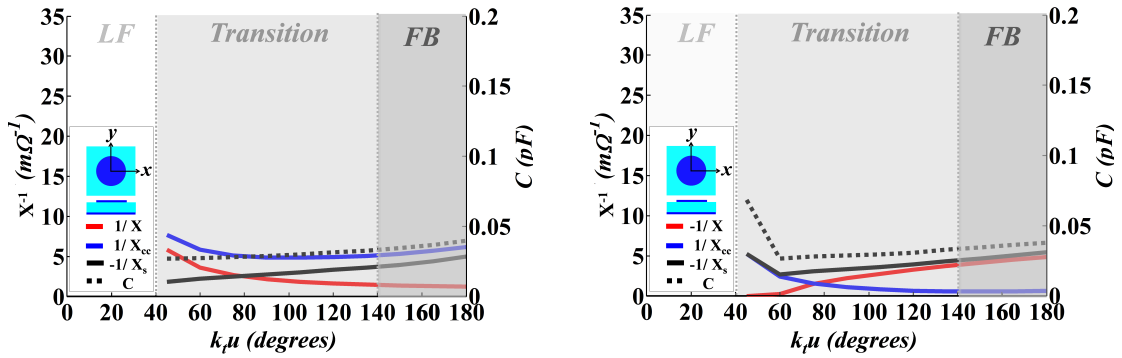

(a)

(b)

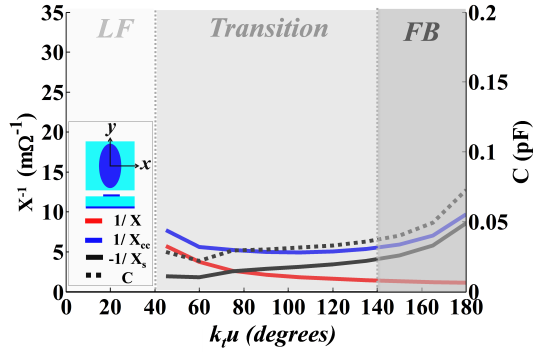

(c)

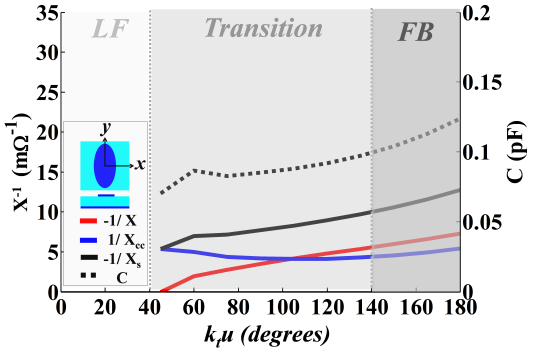

(d)

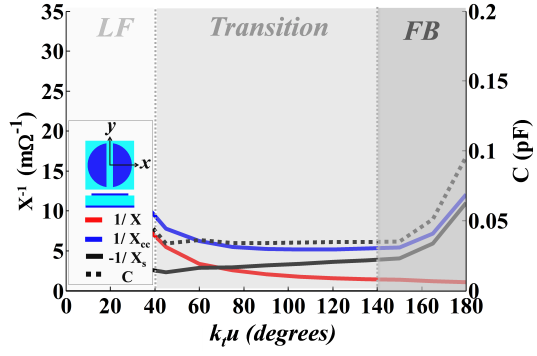

(e)

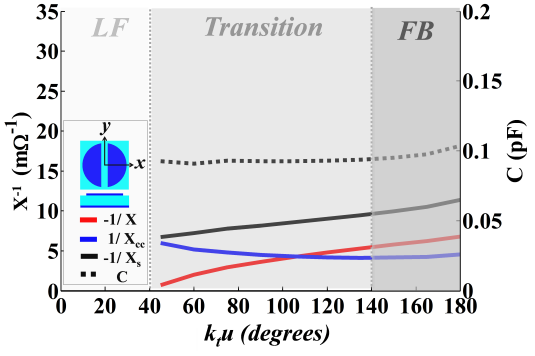

(f)

upna
Universidad Pública de Navarra
Nafarroako Unibertsitate Publikoa

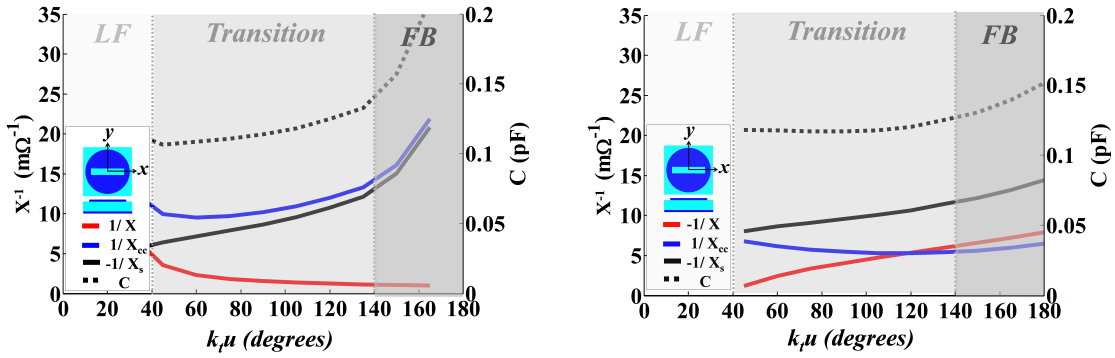

Fig. A.1. Contributions of the TM (left) and TE (right) SWs ($1/|X|$, red line), ground plane ($1/X_{cc}$, blue line) and patch ($1/|X_S|$, black line) to the correspondent dispersion equation as a function of phase shift ($\Delta ph = k_t u$) at three characteristic regions: low frequency (LF), transition and Floquet-Bloch (FB). Extrapolated quasi-static capacitance is depicted in dashed black lines. Different patch geometries has been analyzed: (a),(b) circular patch with $a/u = 0.6$; (c),(d) elliptical patch with $e_b/u = 0.9$ and $e_a/e_b = 0.6$; (e),(f) circular with a groove w/u=0.3; (g),(h) circular with a slot $w/u = 0.3$ and $b/a = 0.75$. In all the cases, $u = 3.14mm$, $\varepsilon_r = 10.2$ and $h = 1.27mm$ and ($\phi = 0°$, $\psi = 0°$).

AT lower frequencies (or phase shifts) the TM dispersion equation is given by the TM SW mode and the short circuit contributions. As it can be seen in Fig. A.1, when Δph values increases, patch contribution becomes more important and it also contributes to the dispersion equation: the sheet contribution varies following a linear increase with frequency and a capacitance C can be defined which does not depend on k_t all over the transition region. Nevertheless, in Floquet-Boch region, the patch capacitance depends on wave number ($C_c(k_t)$) and it can be seen that both the patches and short circuit contributions dominate the dispersion characterization. When the SW wavelength decreases considerably, the homogenization condition ($u < \lambda_{sw}$) is hardly fulfilled and the unit cell lattice resonates, allowing higher order modes to affect.

For the TE mode, the contributions of the elements are different as it shows faster frequency dispersion. From lower frequency until the center of the transition region, both the grounded slab and the patches contribute to the dispersion. As the pixel geometry affects more significantly for this case, the definition of the quasi-static capacitance for the TE case is not as straightforward as it is for the TM case and the accuracy of this approximation may be deteriorated from $\Delta ph > 125°$ at the transition region.

As widely explained in [61–63], the information of a single run of eigen mode solver setting $\Delta ph = 90°$ can be employed in the dispersion equation to extrapolate the wave number

upna
Universidad Pública de Navarra
Nafarroako Unibertsitate Publikoa

information at other frequencies for the TM mode. Comparison between the TM and TE dispersion curves obtained with the proposed procedure and the full wave analysis (see Fig. 3.13) for different pixel geometries are shown in Fig. A.2:

As it can be seen in Fig. A.2, the curves predicted from a single eigen mode solver solution ($\phi = 90°$) agrees adequately with the full wave results for both TM and TE modes until near the end of the transition region. For the TE case, the curves show more accuracy when $\Delta ph < 120° - 125°$ for the different isotropic and anisotropic pixel geometries and two simulations on the eigen mode solver could be run to fit the curves better, for instance at $\phi = 90°$ and $\phi = 120°$. As detailed in [61–63], the curves in the Floquet Bloch region could be fitted extracting from the full wave analysis more information to improve the representation of the $C_c(k_t)$ and taking into account its dependence with the phase shift. Nevertheless, in this thesis the dispersion properties study (and the equivalent surface impedance maps calculated afterwards) is employed to synthesize homogeneous metasurfaces and only the characterization of the transition region is of interest.

upna
Universidad Pública de Navarra
Nafarroako Unibertsitate Publikoa

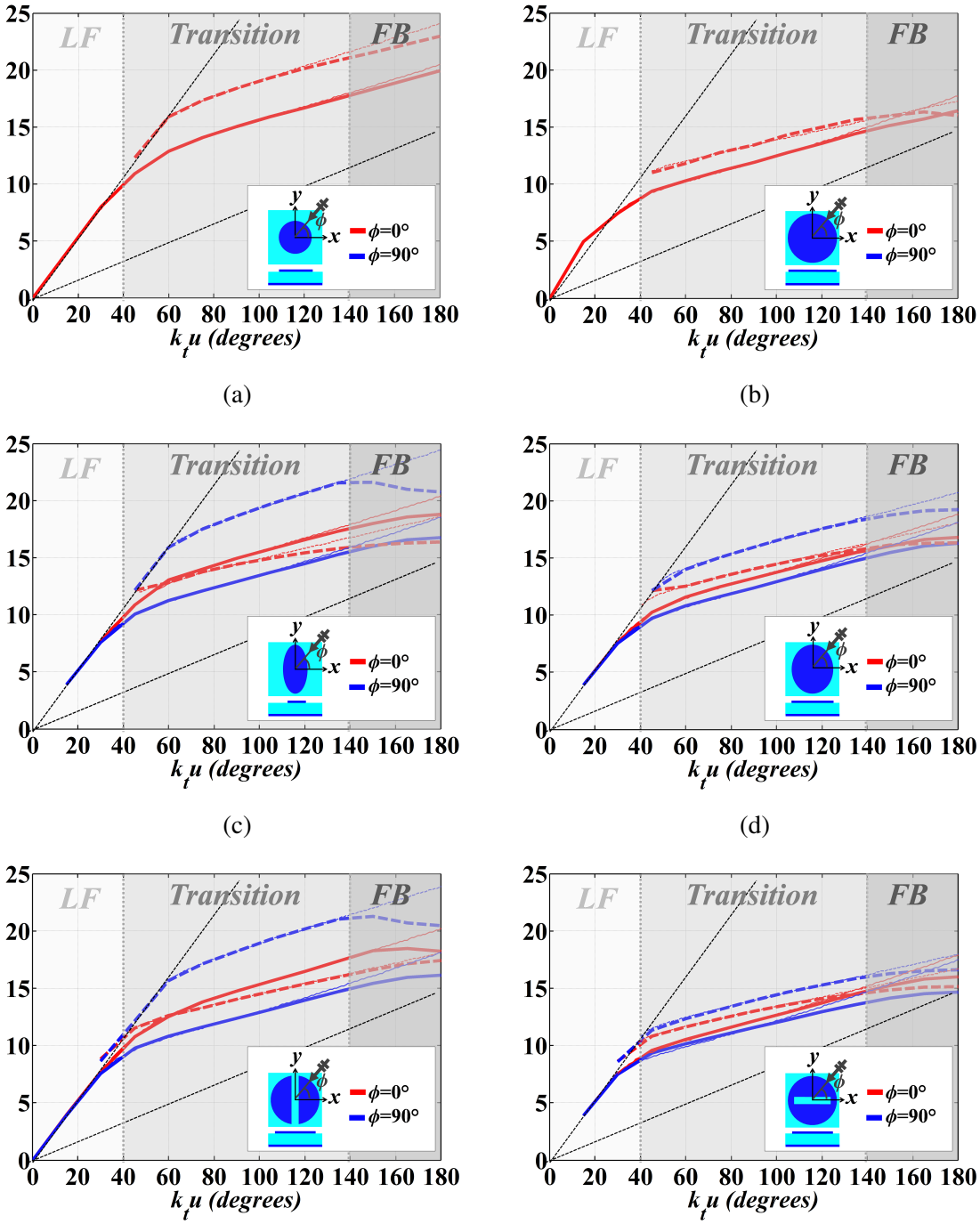

Fig. A.2. Frequency dispersion curves of TM (continuous lines) and TE (dashed lines) modes propagating towards $\phi = 0°$ (red) and $\phi = 90°$ (blue) predicted from a single run of the eigen mode solver setting $\Delta ph = 90°$ (narrow lines) vs. the full wave analysis results (bold lines). Studied patch geometries are: (a) circular patch with normalized radius $a/u = 0.9$; (b) elliptical patch with normalized major axis $e_b/u = 0.9$ and axial ratio $e_a/e_b = 0.6$; and circular patches with an aperture in the center: c) a groove with normalized width $w/u = 0.3$; (d) a slot with normalized width $w/u = 0.3$ and length $b/a = 0.75$. In all the cases, $u = 3.14mm$, $\varepsilon_r = 10.2$ and $h = 1.27mm$.

upna
Universidad Pública de Navarra
Nafarroako Unibertsitate Publikoa

Appendix B

Alternative sheet impedance tensor calculation based on reflection coefficient matrix

An alternative method to calculate the anisotropic surface impedance tensor of a patterned metallic cladding over a grounded dielectric has been presented by Patel et al. in [64–72]. This method relates the reflexion properties of two plane waves (PWs) impinging the structure in normal direction and the propagation properties of a TM SW propagating on it.

The reflection coefficient matrix, Γ, is obtained from two full-wave scattering simulations and the electric and magnetic fields at the air-metasurface interface ($z = 0^+$) are calculated considering the contribution of both the incident and reflected fields:

$$\mathbf{E} = \mathbf{E}^+ + \mathbf{E}^- \quad , \quad \mathbf{H} = \mathbf{H}^+ + \mathbf{H}^- \tag{B.1}$$

Taking into account the relation between the magnitudes of the electric and magnetic fields through the free space impedance, $\mathbf{E} = (-\hat{k} \times \mathbf{H})\zeta$ and $\mathbf{H} = (\hat{k} \times \mathbf{E})\zeta^{-1}$, they can be also described in terms of the reflection coefficient matrix as:

$$\begin{bmatrix} E_x^- \\ E_y^- \end{bmatrix} = \begin{bmatrix} \Gamma_{xx} & \Gamma_{xy} \\ \Gamma_{yx} & \Gamma_{yy} \end{bmatrix} \begin{bmatrix} E_x^+ \\ E_y^+ \end{bmatrix} \tag{B.2}$$

$$\begin{bmatrix} H_y^- \\ H_x^- \end{bmatrix} = \begin{bmatrix} -\Gamma_{xx} & \Gamma_{xy} \\ \Gamma_{yx} & -\Gamma_{yy} \end{bmatrix} \begin{bmatrix} H_y^+ \\ H_x^+ \end{bmatrix} \tag{B.3}$$

upna
Universidad Pública de Navarra
Nafarroako Unibertsitate Publikoa

where the super index $(^+)$ denotes that the incident wave is travelling in $-z$ direction and $(^-)$ denotes that the wave is reflected in $+z$ direction. The (x,y) terms describe the field components of the impinging wave in Cartesian coordinates.

Moreover, the boundary conditions over the surface are described by means of an input impedance tensor:

$$\mathbf{E}\,|_{0^+} = \bar{\bar{\mathbf{Z}}}_{in} \cdot \hat{\mathbf{z}} \times \mathbf{H}\,|_{0^+} \tag{B.4}$$

Considering (B.2), (B.3) and (B.4), the reflection coefficient Γ and $\bar{\bar{\mathbf{Y}}}_{in}$ tensors are related as:

$$\bar{\bar{\mathbf{Y}}}_{in} = Y_0 \begin{bmatrix} 1-\Gamma_{xx} & -\Gamma_{xy} \\ -\Gamma_{yx} & 1-\Gamma_{yy} \end{bmatrix} \begin{bmatrix} 1+\Gamma_{xx} & \Gamma_{xy} \\ \Gamma_{yx} & 1+\Gamma_{yy} \end{bmatrix}^{-1} \tag{B.5}$$

The input impedance is defined as the parallel of the sheet impedance describing the metallic cladding ($\bar{\bar{\mathbf{Z}}}_S$) and the impedance related with the grounded slab contribution, i.e:

$$\bar{\bar{\mathbf{Z}}}_{in} = \bar{\bar{\mathbf{Z}}}_S \parallel \bar{\bar{\mathbf{Z}}}_{cc} \tag{B.6}$$

The boundary conditions related with the plane wave impinging the structure in normal direction imposes that $\beta = 0$ ($k_{z1} = k1$). Taking this relation into account, the short circuit contribution for both TM and TE field components ($TX = TM, TE$) are defined as: $Z_{cc}^{TX} = jZ_1 \tan k_1 h$, being the dielectric impedance $Z_1 = \zeta/\sqrt{\varepsilon_r}$ and the dielectric wavenumber $k_1 = k\sqrt{\varepsilon_r}$. Hence, following this method [64–72] the sheet admittance contribution is extracted as:

$$\bar{\bar{\mathbf{Y}}}_S = \begin{bmatrix} Y_{inxx} - jY_1 \cot(k_1 h) & Y_{inxy} \\ Y_{inyx} & Y_{inyy} - jY_1 \cot(k_1 h) \end{bmatrix} \tag{B.7}$$

Once $\bar{\bar{\mathbf{Z}}}_S$ is determined, the TM surface impedance tensor $\bar{\bar{\mathbf{Z}}}$ is calculated considering the contribution of the previously extracted sheet impedance and the contribution of the grounded slab taking into account its thickness: $\bar{\bar{\mathbf{Z}}} = \bar{\bar{\mathbf{Z}}}_S \parallel \bar{\bar{\mathbf{Z}}}_{cc}$. The characteristic impedance and wave numbers of the TM surface wave are calculated following equation (3.28) shown in Section 3.2.4.

B.0.1 Comparison with full wave analysis results

Based on the Patels method [64–72], the equivalent TM surface impedance maps of several isotropic and anisotropic pixels has been extracted at 13.5GHz. The obtained impedance

upna
Universidad Pública de Navarra
Nafarroako Unibertsitate Publikoa

maps are compared with the ones presented in Section 3.3.1, calculated from the full wave spatial dispersion simulation results. The analyzed pixel geometries have been shown in figure 3.12. The isotropic circular patch is characterized by different normalized radii (a/u) (Fig. 3.12(a)). The anisotropic pixels are the elliptical patch with different ratios (e_a/e_b, $e_b/u = 0.9$) shown in Fig. 3.12(b) and circular patches with different normalized radii (a/u) and with different types of apertures in the center: a groove with a normalized width $w/a = 0.15$ (see Fig. 3.12(c)) or a slot with a normalized with $w/a = 0.15$ and length $b/a = 0.75$ as the one depicted in Fig. 3.12(d). The parameter ψ describes the patch rotation inside the unit cell. The employed dielectric is arlon AD1000 with a thickness of $h = 1.27mm$. In all the cases $u = 3.14mm$.

The TM surface impedance maps of the isotropic circular patches with different normalized radii (a/u) calculated with the method proposed by Patel et al. [64–72] are shown in Fig B.1.

As shown in Fig. B.1, the calculated equivalent TM surface impedance does not depend on SW impinging angle, according to the isotropic nature of the pixel at 13.5GHz. The supported TM mode is pure, as the XP component is null. The relation between the patch size and impedance behavior agrees with the results presented in Fig. 3.20 where the impedance maps are calculated from the full wave dispersion analysis: electrically larger patches provide higher impedance values. Nevertheless, comparing both methods it is remarkable that for the same metallic patch size, the surface impedance calculated with the rbics method (Fig. B.1) is higher.

The impedance maps of the anisotropic pixels composed by elliptical patches and circular patches with different apertures inside (groove and slot) respectively, employing the method presented in [64–72], are shown in Fig. B.2 and Fig. B.3.

Comparing the X_{xx}, X_{xy}, X_{yy} tensor components calculated with Patels method shown in Fig. B.2 and Fig. B.3 with the TM surface impedance tensor componetns X_{ee}, X_{eh}, X_{hh} presented in Fig. 3.21, Fig. 3.22 and Fig. 3.23 it can be seen that the impedance maps trend agrees: the electrically larger patch provide higher surface impedance value and the cross-polar component of the tensor also increases, illustrating the anisotropic behaviour of the analysed pixels. Nevertheless, it can be seen also a noticeable difference in the results taking into account the same metallic patch size. Therefore, with the Patels method the TM mode resonance limit is achieved with smaller patches.

B.0.2 Discussion

The main advantage of this method in comparison with the full wave analysis presented in Section3.3.1 is that here the dispersion characterization of the TM mode is given based

upna
Universidad Pública de Navarra
Nafarroako Unibertsitate Publikoa

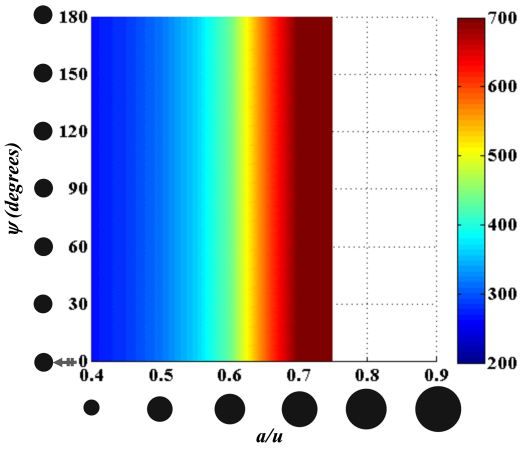

(a)

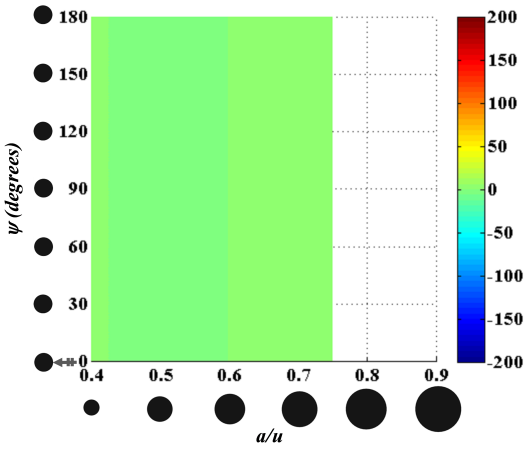

(b)

Fig. B.1. Equivalent scalar TM surface impedance value (a) and cross-polar contribution (b) at 13.5GHz, related to isotropic circular metallic patches with different normalized radii (a/u) over a grounded dielectric($h = 1.27mm$, $\varepsilon_r = 10.2$), calculated from normal impinging PWs scattering information. $\psi(^\circ)$ denotes the patch rotation angle inside the unit cell. The SW impinges the cell towards $\phi = 0^\circ$.

upna
Universidad Pública de Navarra
Nafarroako Unibertsitate Publikoa

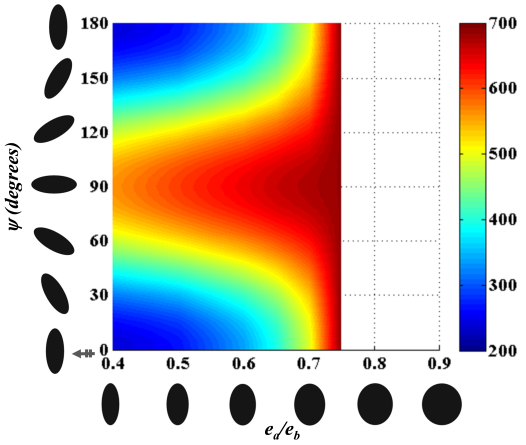

(a)

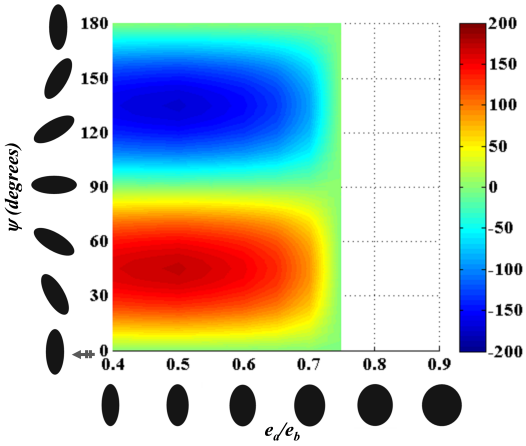

(b)

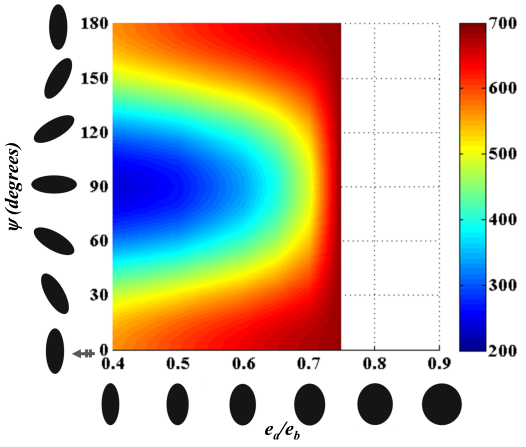

(c)

Fig. B.2. Equivalent TM surface impedance tensor components ((a) X_{xx}, (b) X_{xy} and (c) X_{yy}) at 13.5GHz, related to anisotropic pixels composed by: elliptical metallic patches with different ratios (e_a/e_b, $e_b/u = 0.9$) over a grounded dielectric characterized by $h = 1.27mm$ and $\varepsilon_r = 10.2$, calculated from from normal impinging PWs scattering information. $\psi(^\circ)$ denotes the patch rotation angle inside the unit cell. The SW impinges the cell towards $\phi = 0^\circ$.

upna
Universidad Pública de Navarra
Nafarroako Unibertsitate Publikoa

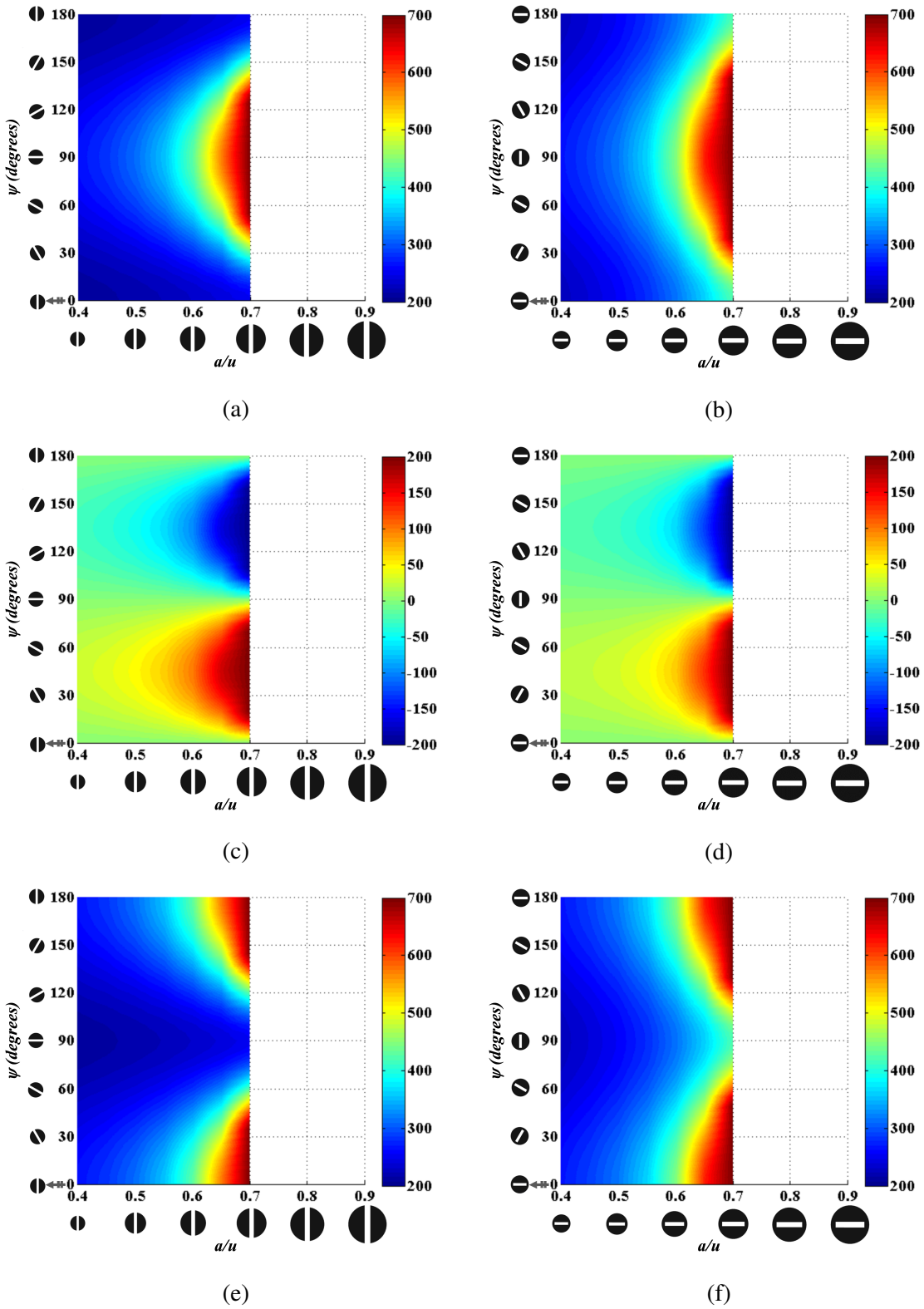

Fig. B.3. Equivalent TM surface impedance tensor components ((a)-(b) X_{xx}, (c)-(d) X_{xy} and (e)-(f) X_{yy}) at 13.5GHz, related to anisotropic pixels composed by circular metallic patches with different apertures in the center: a groove with $w/a = 0.15$ (left column), a slot with $w/a = 0.15$ and $b/a = 0.75$ (right column), over a grounded dielectric characterized by $h = 1.27mm$ and $\varepsilon_r = 10.2$, calculated from normal impinging PWs scattering information. Patches with different radii (a/u) have been analyzed. $\psi(^\circ)$ denotes the patch rotation angle inside the unit cell. The SW impinges the cell towards $\phi = 0^\circ$.

upna
Universidad Pública de Navarra
Nafarroako Unibertsitate Publikoa

on the scattering information on the driven modal solver, which is less time and resource consuming. Nevertheless, it has been shown that there are some drawbacks that limit the accuracy of this method. Comparing the TM surface impedances for isotropic patches shown in Fig. B.1 and anisotropic patches shown in Fig. B.2 and Fig. B.3 with the ones calculated from the full wave dispersion analysis presented in Section 3.3.1 (Fig. 3.20, Fig. 3.21, Fig. 3.22 and Fig. 3.23), it can be seen that there are some significant differences for electrically larger patches, i.e., higher impedances values.

This discrepancy between both methods is related with the sheet impedance extraction method, due to the fact that when it is extracted form normal plane wave scattering information (imposing $\beta = 0$ boundary condition) it does not take into account the grounded slab contribution and in consequence, it provides too high $\bar{\bar{\mathbf{X}}}_S$ impedance approximation (namely too small $|\bar{\bar{\mathbf{X}}}_S|$ value). This method considers the sheet impedance independent of β while the method based on full wave analysis show that this statement is only accurate for low frequencies. For higher frequencies, the frequency dispersive nature of the configuration becomes important and the TM mode is characterized by high β values. Therefore, the sheet impedance also depends on this value and the prediction of the sheet impedance employing this method and subsequent surface impedance calculation is accurate when the analyzed pixel is electrically small, for low frequencies or when the employed dielectric is characterized by low ε_r or thickness values. Otherwise, for electrically large patches, the calculated surface impedance corresponds to larger patches.

On the other hand, it has to be mentioned that with this method it is not clear how to extract the surface impedance information related with the TE mode, which can be also supported on the structure if the electrical size of the patches is large and the working frequency is above its cut off.

upna
Universidad Pública de Navarra
Nafarroako Unibertsitate Publikoa

Appendix C

LW complex wavenumber calculation

When a SW bounded to the structure interacts with a sinusoidally modulated surface, its wavenumber suffers a complex perturbation [52, 77]:

$$\beta \rightarrow k_{t0} = \beta + \Delta\beta - j\alpha \tag{C.1}$$

The real part of the perturbation $\Delta\beta$, describes the phase shift suffered by the wavenumber of the SW associated with the average reactance, while the imaginary part α describes the attenuation constant. The complex perturbation depends mainly on the modulation index (m) and normalized average (η) values. The estimation of the complex wavenumber of a one dimensional model that locally approximates the radial modulation of the impenetrable surface reactance has been proposed by Oliner and Caminita in [52, 77].

Based on the periodic nature of the problem, the fields and currents are described in terms of Floquet modes (FM) with complex wavenumbers $k_{xn} = \beta + \Delta_\beta + \frac{2\pi n}{d} - j\alpha, \quad n = 0, \pm 1, \pm 2...$ (being d the modulation periodicity) as:

$$\begin{aligned} E_x &= Z_{in} \sum_n I_{xn} e^{-jk_{xn}x} \\ &= j\zeta\eta[1 + m\cos(2\pi x/d)] \sum_n I_{xn} e^{-jk_{xn}x} \\ &= \sum_n \widetilde{G}_{EJ}^{TM}(k_{xn}) I_{xn} e^{-jk_{xn}x} \end{aligned} \tag{C.2}$$

The electric field E_x of the TM mode is obtained by weighting each FM component of the current by the pertinent spectral Green's function, $\widetilde{G}_{EJ}^{TM}(k_{xn})$. The transverse (to $\mathbf{z}$) n-th mode voltage V_n can be expressed in the surface interface $z = 0$ as:

upna
Universidad Pública de Navarra
Nafarroako Unibertsitate Publikoa

$$V_{xn}(z=0) = \int_{-d/2}^{d/2} E_x(x) e^{jk_{xn}x} dx = \widetilde{G}_{EJ}^{TM}(k_{xn},0) I_{xn} \tag{C.3}$$

Considering the sinusoidal modulation of the impenetrable reactance towards the TM mode propagation direction (**x**), Eq. (C.3) becomes:

$$V_{xn}(z=0) = j\zeta\eta I_{xn} + j\zeta\eta\frac{m}{2}(I_{xn+1} + I_{xn-1}) \tag{C.4}$$

Transverse resonance equation allows to establish a relation that determines the propagation characteristics of the modes, and consequently the calculation of the complex k_{xn}. It states that at $z=0$ plane, the sum of the impedances for the n-th transverse mode looking toward and outward must be equal to zero:

$$Z_{in} + Z_{out} = 0 \tag{C.5}$$

Thus, the Green function of the TM SW is related with the free-space mode impedance as:

$$\widetilde{G}_{EJ}^{TM}(k_{xn}) = -Z_0^{TM} = -Z_0\frac{k_{zn}}{k_0} \tag{C.6}$$

Combining (C.4) with (C.6), this recurrence function is obtained [52, 77]:

$$I_{n+1} + D_n I_n + I_{n-1} = 0 \quad n = 0, \pm 1, \pm 2... \tag{C.7}$$

where $D_n = \frac{2}{m}\left(1 - \frac{\widetilde{G}_{EJ}^{TM}(k_{xn})}{j\zeta\eta_{TM}}\right)$.

This recurrence relation can be seen as an infinite set of linear homogeneous equations, with infinite unknown modal currents I_n.

$$D_n - \cfrac{1}{D_{n-1} - \cfrac{1}{D_{n-2} - \cfrac{1}{D_{n-3}}}} - \cfrac{1}{D_{n+1} - \cfrac{1}{D_{n+2} - \cfrac{1}{D_{n+3}}}} ... = 0 \tag{C.8}$$

which can be rewritten as:

upna
Universidad Pública de Navarra
Nafarroako Unibertsitate Publikoa

$$\begin{bmatrix} \dots & \dots & \dots & \dots & \dots & \dots & \dots \\ \dots & D_{n-2} & 1 & 0 & 0 & 0 & \dots \\ \dots & 1 & D_{n-1} & 1 & 0 & 0 & \dots \\ \dots & 0 & 1 & D_n & 1 & 0 & \dots \\ \dots & 0 & 0 & 1 & D_{n+1} & 1 & \dots \\ \dots & 0 & 0 & 0 & 1 & D_{n+2} & \dots \\ \dots & \dots & \dots & \dots & \dots & \dots & \dots \end{bmatrix} \begin{bmatrix} \dots \\ I_{n-2} \\ I_{n-1} \\ I_n \\ In+1 \\ I_{n+2} \\ \dots \end{bmatrix} = 0 \tag{C.9}$$

Equation (C.10) has a nontrivial solution if the infinite determinant vanishes:

$$\begin{vmatrix} \dots & \dots & \dots & \dots & \dots & \dots & \dots \\ \dots & D_{n-2} & 1 & 0 & 0 & 0 & \dots \\ \dots & 1 & D_{n-1} & 1 & 0 & 0 & \dots \\ \dots & 0 & 1 & D_n & 1 & 0 & \dots \\ \dots & 0 & 0 & 1 & D_{n+1} & 1 & \dots \\ \dots & 0 & 0 & 0 & 1 & D_{n+2} & \dots \\ \dots & \dots & \dots & \dots & \dots & \dots & \dots \end{vmatrix} = 0 \tag{C.10}$$

The k_{xn} calculation method explained in [52, 77] can be also implemented for the equivalent sinusoidal homogenised penetrable reactance describing the cladding of the canonical problem related with TM and TE modes:
$X_S^{TX} = X_{aveS}^{TX}(1 + m_S^{TX} cos(2\pi x/d_S^{TX}))\quad TX = TM/TE.$

In this case, the field $\mathbf{E}$ at the interface is related with the average electric current flowing in the impedance ($\mathbf{J_S}$) as:

$$\mathbf{E}(x,0) = j\bar{\bar{\mathbf{X}}}_{\mathbf{S}}(\omega,x) \cdot \mathbf{J}_S(x,0) \tag{C.11}$$

It is obtained weighting each FM component of the current by the Green's function of the grounded slab:

$$\widetilde{G}_{EJ}^{TX}(k_{xn}) = -(Z_0^{TX} \parallel Z_{cc}^{TX}) \quad TX = TM, TE \tag{C.12}$$

Therefore, D_n in the matrix (C.10) is rewritten as:

$$D_n = \frac{2}{m_S^{TX}}\left(1 - \frac{\widetilde{G}_{EJ}^{TX}(k_{xn})}{jX_{aveS}^{TX}}\right) \tag{C.13}$$

upna
Universidad Pública de Navarra
Nafarroako Unibertsitate Publikoa

Appendix D

Tensor components coordinate transformation

Consider two-dimensional space with base vectors $\mathbf{e}_1$,$\mathbf{e}_2$. The second order tensor $\mathbf{S}$ can be written in component form as:

$$\mathbf{S} = S_{11}\mathbf{e}_1 \otimes \mathbf{e}_1 + S_{12}\mathbf{e}_1 \otimes \mathbf{e}_2 + S_{21}\mathbf{e}_2 \otimes \mathbf{e}_1 + S_{22}\mathbf{e}_2 \otimes \mathbf{e}_2 \tag{D.1}$$

A second coordinate system can be defined with the base vectors $\mathbf{e}_1^{'}$,$\mathbf{e}_2^{'}$, obtained from the first by a rotation, ϑ. The components of the transformation matrix are:

$$Q_{ij} = \begin{bmatrix} \mathbf{e}_1 \cdot \mathbf{e}_1^{'} & \mathbf{e}_1 \cdot \mathbf{e}_2^{'} \\ \mathbf{e}_2 \cdot \mathbf{e}_1^{'} & \mathbf{e}_2 \cdot \mathbf{e}_2^{'} \end{bmatrix} = \begin{bmatrix} \cos(\vartheta) & -\sin(\vartheta) \\ \sin(\vartheta) & \cos(\vartheta) \end{bmatrix} \tag{D.2}$$

and the components of $\mathbf{S}$ in the second coordinate system are $[\mathbf{S}^{'}] = [\mathbf{Q}^T][\mathbf{S}][\mathbf{Q}]$. Thus,

$$\begin{bmatrix} S_{11}^{'} & S_{12}^{'} \\ S_{21}^{'} & S_{22}^{'} \end{bmatrix} = \begin{bmatrix} \cos(\vartheta) & \sin(\vartheta) \\ -\sin(\vartheta) & \cos(\vartheta) \end{bmatrix} \begin{bmatrix} S_{11} & S_{12} \\ S_{21} & S_{22} \end{bmatrix} \begin{bmatrix} \cos(\vartheta) & -\sin(\vartheta) \\ \sin(\vartheta) & \cos(\vartheta) \end{bmatrix} \tag{D.3}$$

When $\mathbf{S}$ is symmetric, $S_{12} = S_{21}$, the previous system is simplified as:

$$\begin{aligned} S_{11}^{'} &= S_{11}\cos^2\vartheta + S_{22}\sin^2\vartheta + S_{12}\sin 2\vartheta \\ S_{22}^{'} &= S_{11}\sin^2\vartheta + S_{22}\cos^2\vartheta - S_{12}\sin 2\vartheta \\ S_{12}^{'} &= (S_{22} - S_{11})\sin\vartheta\cos\vartheta + S_{12}\cos 2\vartheta \end{aligned} \tag{D.4}$$

upna
Universidad Pública de Navarra
Nafarroako Unibertsitate Publikoa

Bibliography

[1] D. Jackson and N. Alexopoulos. Gain enhancement methods for printed circuit antennas. *IEEE Transactions on Antennas and Propagation*, 33(9):976–987, Sep 1985.

[2] M. Thevenot, C. Cheype, A. Reineix, and B. Jecko. Directive photonic-bandgap antennas. *IEEE Transactions on Microwave Theory and Techniques*, 47(11):2115–2122, Nov 1999.

[3] C. Cheype, C. Serier, M. Thevenot, T. Monediere, A. Reineix, and B. Jecko. An electromagnetic bandgap resonator antenna. *IEEE Transactions on Antennas and Propagation*, 50(9):1285–1290, Sep 2002.

[4] R. Gardelli, M. Albani, and F. Capolino. Array thinning by using antennas in a fabry-perot cavity for gain enhancement. *IEEE Transactions on Antennas and Propagation*, 54(7):1979–1990, July 2006.

[5] L. Moustafa and B. Jecko. Broadband high gain compact resonator antennas using combined FSS. In *2008 IEEE Antennas and Propagation Society International Symposium*, pages 1–4, July 2008.

[6] M. Hajj, E. Rodes, D. Serhal, M. Thevenot, T. Monediere, and B. Jecko. Metallic EBG sectoral antenna for a base station with horizontal polarization. In *The Second European Conference on Antennas and Propagation, EuCAP 2007*, pages 1–5, Nov 2007.

[7] M. Hajj, E. Rodes, D. Serhal, T. Monediere, B. Jecko, and R. Chantalat. Metallic EBG superstrates for dual polarized sectoral base station antenna. In *2009 3rd European Conference on Antennas and Propagation*, pages 2859–2861, March 2009.

[8] M. Hajj, E. Rodes, and T. Monediere. Dual-band EBG sectoral antenna using a single-layer FSS for UMTS application. *IEEE Antennas and Wireless Propagation Letters*, 8:161–164, Jan 2009.

[9] R. Chantalat, C. Menudier, M. Troubat, E. Arnaud, T. Monediere, M. Thevenot, B. Jecko, and P. Dumon. Enhanced two level EBG antenna for a high F/D multibeam reflector antenna in Ka band: Design and characterization. In *The Second European Conference on Antennas and Propagation, EuCAP 2007*, pages 1–7, Nov 2007.

[10] M. Menudier, T. Monediere, and B. Jecko. EBG resonator antennas: State of the art and prospects. In *2007 6th International Conference on Antenna Theory and Techniques*, pages 37–43, Sept 2007.

upna
Universidad Pública de Navarra
Nafarroako Unibertsitate Publikoa

[11] A. Kanso, R. Chantalat, M. Thevenot, T. Monediere, and B. Jecko. Dual band dielectric EBG resonator antenna. In *2009 3rd European Conference on Antennas and Propagation*, pages 3240–3243, March 2009.

[12] A. Kanso, R. Chantalat, M. Thevenot, U. Naeem, S. Bila, and T. Monediere. Multifeed EBG dual band antenna to feed a reflector antenna. In *2011 41st European Microwave Conference*, pages 866–869, Oct 2011.

[13] E. Rodes, M. Diblanc, J. Drouet, M. Thevenot, T. Monediere, and B. Jecko. Design of a dual-band EBG resonator antenna using capacitive FSS. In *2006 IEEE Antennas and Propagation Society International Symposium*, pages 3009–3012, July 2006.

[14] S. Richard, Y. Demers, E. Amyotte, Y. Brand, V. Dupessey, P. Markland, J. Uher, A. Liang, J. C. Iriarte, I. Ederra, R. Gonzalo, and P. de Maagt. Recent satellite antenna developments at mda. In *The Second European Conference on Antennas and Propagation, EuCAP 2007*, pages 1–7, Nov 2007.

[15] J. C. Iriarte, I. Ederra, R. Gonzalo, Y. Brand, A. Fourmault, Y. Demers, L. Salgetti-Drioli, and P. de Maagt. EBG superstrate array configuration for the WAAS space segment. *IEEE Transactions on Antennas and Propagation*, 57(1):81–93, Jan 2009.

[16] Y. Brand, J.C. Iriarte, Y. Cassivi, A. Fourmault, I. Ederra, R. Gonzalo, Y. Demers, L. Salgetti-Drioli, and P. de Maagt. WAAS space segment antenna based on EBG superstrate gain enhancement technique. In *2009 3rd European Conference on Antennas and Propagation*, pages 2613–2617, March 2009.

[17] A. Oses, J.C. Iriarte, I. Ederra, R. Gonzalo, and P. de Maagt. Multiband EBG navigation antenna. In *2009 IEEE International Workshop on Antenna Technology*, pages 1–4, March 2009.

[18] A. Tellechea, J.C. Iriarte, I. Ederra, R. Gonzalo, F. Monjas, S. Arenas, R. Manrique, and A. Montesano. Compact and weightlight electromagnetic band gap superestrate antenna for C-band TTC applications. *Microwave and Optical Technology Letters*, 55(7):1457–1461, Jan 2013.

[19] A. Tellechea, J. C. Iriarte, I. Ederra, R. Gonzalo, F. Monjas, S. Arenas, R. Manrique, and A. Montesano. Dual band compact and light EBG superstrate based antenna for TTC applications. In *2013 7th European Conference on Antennas and Propagation (EuCAP)*, pages 2505–2507, April 2013.

[20] G. V. Trentini. Partially reflecting sheet arrays. *IRE Transactions on Antennas and Propagation*, 4(4):666–671, October 1956.

[21] N. Engheta. *Electromagnetic Metamaterials: Physics and Engineering Explorations*. Wiley-IEEE Press, 2006.

[22] C. Caloz. *Electromagnetic Metamaterials: Transmission Line Theory and Microwave Applications*. John Wiley and Sons, 2006.

[23] F. Capolino. *Applications of Metamaterials*. CRC Press, 2006.

upna
Universidad Pública de Navarra
Nafarroako Unibertsitate Publikoa

[24] R. A. Shelby, D. R. Smith, and S. Schultz. Experimental verification of a negative index of refraction. *Science*, 292(5514):77–79, Jan 2001.

[25] A. Tellechea Pereda, F. Caminita, E. Martini, I. Ederra, J. C. Iriarte, R. Gonzalo, and S. Maci. Dual circularly polarized broadside beam metasurface antenna. *IEEE Transactions on Antennas and Propagation*, 64(7):2944–2953, July 2016.

[26] D. Sievenpiper, J. Colburn, B. Fong, J. Ottusch, and J. Visher. Holographic artificial impedance surfaces for conformal antennas. In *2005 IEEE Antennas and Propagation Society International Symposium*, pages 256–259 vol. 1B, June 2005.

[27] J.B. Pendry, D. Schurig, and D.R. Smith. Controlling electromagnetic field. *Science*, 312(5781):1780–1782, Jun 2006.

[28] U. Leonhardt. Optical conformal mapping. *Science*, 312(5781):1777–1780, Jun 2006.

[29] B.H. Fong, J.S. Colburn, J.J. Ottusch, J.L. Visher, and D.F. Sievenpiper. Scalar and tensor holographic artificial impedance surfaces. *IEEE Transactions on Antennas and Propagation*, 58(10):3212–3221, Oct 2010.

[30] R. Quarfoth and D. Sievenpiper. Simulation of anisotropic artificial impedance surface with rectangular and diamond lattices. In *Antennas and Propagation (APSURSI), 2011 IEEE International Symposium on*, pages 1498–1501, July 2011.

[31] S. Maci, G. Minatti, M. Casaletti, and M. Bosiljevac. Metasurfing: Addressing waves on impenetrable metasurfaces. *IEEE Antennas and Wireless Propagation Letters*, 10:1499–1502, 2011.

[32] O. Vanbésien. *Artificial Materials*. John Wiley and Sons, 2013.

[33] E. Martini and S. Maci. Transformation optics applied to metasurfaces. In *Antennas and Propagation (EuCAP), 2013 7th European Conference on*, pages 1830–1831, April 2013.

[34] R. Quarfoth and D. Sievenpiper. Artificial tensor impedance surface waveguides. *IEEE Transactions on Antennas and Propagation*, 61(7):3597–3606, July 2013.

[35] D. Kwon D. Werner. *Transformation Electromagnetics and Metamaterials*. Springer, 2014.

[36] E. Martini, M. Mencagli, D. González-Ovejero, and S. Maci. Flat optics for surface waves. *IEEE Transactions on Antennas and Propagation*, 64(1):155–166, Jan 2016.

[37] M. Mencagli, E. Martini, D. González-Ovejero, and S. Maci. Metasurfing by transformation electromagnetics. *IEEE Antennas and Wireless Propagation Letters*, 13:1767–1770, 2014.

[38] E. Martini, M. Mencagli, and S. Maci. Metasurface transformation for surface wave control. *Philosophical Transactions of the Royal Society a Mathematical Physical and Engineerring Sciences*, 373(2049):1–20, August 2015.

upna
Universidad Pública de Navarra
Nafarroako Unibertsitate Publikoa

[39] A. Grbic, G. Gok, M.F. Imani, A.M. Patel, C.Pfeiffer, and M. Ettorre. Metamaterial surfaces for near and far-field applications. In *Antennas and Propagation (EuCAP), 2013 7th European Conference on*, pages 3618–3622, April 2013.

[40] E. Martini, M. J. Mencagli, and S. Maci. Addressing surface waves on modulated metasurfaces. In *2013 IEEE Antennas and Propagation Society International Symposium (APSURSI)*, pages 2345–2346, July 2013.

[41] G. Gok and A. Grbic. A printed beam-shifting slab designed using tensor transmission-line metamaterials. *IEEE Transactions on Antennas and Propagation*, 61(2):728–734, Feb 2013.

[42] C. Pfeiffer and A. Grbic. Planar lens antennas of subwavelength thickness: Collimating leaky-waves with metasurfaces. *IEEE Transactions on Antennas and Propagation*, 63(7):3248–3253, July 2015.

[43] A. Grbic, R. Merlin, E. M. Thomas, and M. F. Imani. Near-field plates: Metamaterial surfaces/arrays for subwavelength focusing and probing. *Proceedings of the IEEE*, 99(10):1806–1815, Oct 2011.

[44] A. Grbic and R. Merlin. Near-field focusing plates and their design. *IEEE Transactions on Antennas and Propagation*, 56(10):3159–3165, Oct 2008.

[45] L. Jiang A. Grbic and R. Merlin. Near-field plates: subdiffraction focusing with patterned surfaces. *Science*, 320(1):511–513, April 2008.

[46] M. F. Imani and A. Grbic. Subwavelength focusing with a corrugated metallic plate. In *2009 IEEE Antennas and Propagation Society International Symposium*, pages 1–4, June 2009.

[47] M. F. Imani and A. Grbic. An experimental concentric near-field plate. *IEEE Transactions on Microwave Theory and Techniques*, 58(12):3982–3988, Dec 2010.

[48] M. F. Imani and A. Grbic. Generating evanescent bessel beams using near-field plates. *IEEE Transactions on Antennas and Propagation*, 60(7):3155–3164, July 2012.

[49] M. Ettorre and A. Grbic. Generation of propagating bessel beams using leaky-wave modes. *IEEE Transactions on Antennas and Propagation*, 60(8):3605–3613, Aug 2012.

[50] M. Ettorre, S. M. Rudolph, and A. Grbic. Generation of propagating bessel beams using leaky-wave modes: Experimental validation. *IEEE Transactions on Antennas and Propagation*, 60(6):2645–2653, June 2012.

[51] C. Pfeiffer and A. Grbic. Metamaterial huygens' surfaces. In *Microwave Symposium Digest (IMS), 2013 IEEE MTT-S International*, pages 1–4, June 2013.

[52] A. Oliner and A. Hessel. Guided waves on sinusoidally-modulated reactance surfaces. *IRE Transactions on Antennas and Propagation*, 7(5):201–208, December 1959.

[53] A. M. Patel and A. Grbic. A printed leaky-wave antenna based on a sinusoidally-modulated reactance surface. *IEEE Transactions on Antennas and Propagation*, 59(6):2087–2096, June 2011.

upna
Universidad Pública de Navarra
Nafarroako Unibertsitate Publikoa

[54] G. Minatti, F. Caminita, M. Casaletti, and S. Maci. Leaky wave circularly polarized antennas based on surface impedance modulation. In *ICECom, 2010 Conference Proceedings*, pages 1–4, Sept 2010.

[55] G. Minatti, M. Casaletti, F. Caminita, P. De Vita, and S. Maci. Planar antennas based on surface-to-leaky wave transformation. In *Proceedings of the 5th European Conference on Antennas and Propagation (EUCAP)*, pages 1915–1918, April 2011.

[56] G. Minatti, F. Caminita, M. Casaletti, and S. Maci. Spiral leaky-wave antennas based on modulated surface impedance. *IEEE Transactions on Antennas and Propagation*, 59(12):4436–4444, Dec 2011.

[57] G. Minatti, S. Maci, P. De Vita, A. Freni, and M. Sabbadini. A circularly-polarized isoflux antenna based on anisotropic metasurface. *IEEE Transactions on Antennas and Propagation*, Nov 2012.

[58] M. Faenzi, F. Caminita, E. Martini, P. De Vita, G. Minatti, M. Sabbadini, and S. Maci. Realization and measurement of broadside beam modulated metasurface antennas. *IEEE Antennas and Wireless Propagation Letters*, 15:610–613, 2016.

[59] G. Minatti, M. Sabbadini, and S. Maci. Surface to leaky wave transformation in polarized metasurfaces. In *Electromagnetic Theory (EMTS), Proceedings of 2013 URSI International Symposium on*, pages 298–301, May 2013.

[60] G. Minatti, M. Faenzi, E. Martini, F. Caminita, P. De Vita, D. González-Ovejero, M. Sabbadini, and S. Maci. Modulated metasurface antennas for space: Synthesis, analysis and realizations. *IEEE Transactions on Antennas and Propagation*, 63(4):1288–1300, April 2015.

[61] M. J. Mencagli, E. Martini, F. Caminita, and M. F. S. Maci. Fast approach to the design of planar devices and antennas based on elliptical patch metasurfaces. In *Advanced Electromagnetic Materials in Microwaves and Optics (METAMATERIALS), 2014 8th International Congress on*, pages 379–381, Aug 2014.

[62] M. Mencagli, E. Martini, and S. Maci. Transition function for closed-form representation of metasurface reactance. *IEEE Transactions on Antennas and Propagation*, 64(1):136–145, Jan 2016.

[63] M. Mencagli, C. D. Giovampaola, and S. Maci. A closed-form representation of isofrequency dispersion curve and group velocity for surface waves supported by anisotropic and spatially dispersive metasurfaces. *IEEE Transactions on Antennas and Propagation*, 64(6):2319–2327, June 2016.

[64] A. M. Patel and A. Grbic. Analytical modeling of a printed-circuit tensor impedance surface. In *Microwave Symposium Digest (MTT), 2012 IEEE MTT-S International*, pages 1–3, June 2012.

[65] A. M. Patel and A. Grbic. Dispersion analysis of printed-circuit tensor impedance surfaces. In *Proceedings of the 2012 IEEE International Symposium on Antennas and Propagation*, pages 1–2, July 2012.

upna
Universidad Pública de Navarra
Nafarroako Unibertsitate Publikoa

[66] A. M. Patel and A. Grbic. Transformation electromagnetics devices using tensor impedance surfaces. In *Microwave Symposium Digest (IMS), 2013 IEEE MTT-S International*, pages 1–4, June 2013.

[67] A. M. Patel and A. Grbic. Modeling and analysis of printed-circuit tensor impedance surfaces. *IEEE Transactions on Antennas and Propagation*, 61(1):211–220, Jan 2013.

[68] A. M. Patel and A. Grbic. Effective surface impedance of a printed-circuit tensor impedance surface (pctis). *IEEE Transactions on Microwave Theory and Techniques*, 61(4):1403–1413, April 2013.

[69] A. M. Patel and A. Grbic. The effects of spatial dispersion on power flow along a printed-circuit tensor impedance surface. *IEEE Transactions on Antennas and Propagation*, 62(3):1464–1469, March 2014.

[70] http://www.ansys.com/Products/Electronics/ANSYS HFSS.

[71] A. M. Patel and A. Grbic. A printed leaky-wave antenna with a sinusoidally modulated surface reactance. In *2009 IEEE Antennas and Propagation Society International Symposium*, pages 1–4, June 2009.

[72] A. M. Patel and A. Grbic. Transformation electromagnetics devices based on printed-circuit tensor impedance surfaces. *IEEE Transactions on Microwave Theory and Techniques*, 62(5):1102–1111, May 2014.

[73] R.E. Collin and F.J. Zucker. *Antenna Theory*. McGraw-Hill, 1969.

[74] P. Baccarelli, P. Burghignoli, F. Frezza, A. Galli, P. Lampariello, G. Lovat, and S. Paulotto. Modal properties of surface and leaky waves propagating at arbitrary angles along a metal strip grating on a grounded slab. *IEEE Transactions on Antennas and Propagation*, 53(1):36–46, Jan 2005.

[75] J. Polo. *Electromagnetic Surface Waves: A Modern Perspective*. Elsevier, 2013.

[76] A. Sutinjo, M. Okoniewski, and R. H. Johnston. Radiation from fast and slow traveling waves. *IEEE Antennas and Propagation Magazine*, 50(4):175–181, Aug 2008.

[77] F. Caminita and S. Maci. New wine in old barrels: The use of the Oliner's Method in metasurface antenna design. In *Microwave Conference (EuMC), 2014 44th European*, pages 437–439, Oct 2014.

[78] C. Balanis. *Modern Antenna Handbook*. John Wiley and Sons, 2008.

[79] S. Maci, M. Caiazzo, A. Cucini, and M. Casaletti. A pole-zero matching method for EBG surfaces composed of a dipole FSS printed on a grounded dielectric slab. *IEEE Transactions on Antennas and Propagation*, 53(1):70–81, Jan 2005.

[80] https://www.cst.com/.

[81] M. Mencagli, E. Martini, and S. Maci. Surface wave dispersion for anisotropic metasurfaces constituted by elliptical patches. *IEEE Transactions on Antennas and Propagation*, 63(7):2992–3003, July 2015.

upna
Universidad Pública de Navarra
Nafarroako Unibertsitate Publikoa

[82] D. R. Wilton S. M. Rao and A. W. Glisson. Electromagnetic scattering by surfaces of arbitrary shape. *IEEE Transactions on Antennas and Propagation*, 30(3):409–418, May 1982.

[83] A. Toscano D. Ramaccia and F. Bilotti. A new accurate model of High-impedance surfaces consisting of circular patches. *Progress In Electromagnetic Research M*, 21(21):1–17, Jan 2001.

[84] E. Martini D. González-Ovejero and S. Maci. Surface waves supported by metasurfaces with self-complementary geometries. *IEEE Transactions on Antennas and Propagation*, 63(1):250–260, Jan 2015.

[85] G. Granet O. Luukkonen, C. Simovski and S. A. Tretyakov. Simple and accurate analytical model of planar grids and High-impedance surfaces comprising metal strips or patches. *IEEE Transactions on Antennas and Propagation*, 56(6):1624–1632, June 2008.

[86] Y. R. Samii J. Hoppe. *Impedance Boundary Conditions in electromagnetics*. Washington, DC: Taylor and Francis, 1995.

[87] G. V. Borgiotti. Modal analysis of periodic planar phased arrays of apertures. *Proceedings of the IEEE*, 56(11):1881–1892, Nov 1968.

[88] P. S. Kildal. *Rotationally symmetric antennas*. Foundation of Antenna Engineering, 2015.

[89] C. A. Leal-Sevillano, K. B. Cooper, J. A. Ruiz-Cruz, J. R. Montejo-Garai, and J. M. Rebollar. A 225 GHz circular polarization waveguide duplexer based on a septum orthomode transducer polarizer. *IEEE Transactions on Terahertz Science and Technology*, 3(5):574–583, Sept 2013.

[90] R. A. Hoferer and R. Schwerdtfeger. Development of a wide-band quadrature junction for simultaneous C-band and Ku-band satellite communication applications. In *Antennas and Propagation Society International Symposium, 2002. IEEE*, volume 4, pages 116–119 vol.4, 2002.

[91] W. Hongjian and F. bin. Compact dual polarization feeding system of HY-2 calibration radiometer. In *IGARSS 2008 - 2008 IEEE International Geoscience and Remote Sensing Symposium*, volume 2, pages II–1180–II–1183, July 2008.

[92] A. Tribak, A. Mediavilla, K. Cepero, and J. L. Cano. Compact K/Ka 4-port feed subsystem for dual circular polarisation. In *Microwave Conference (EuMC), 2011 41st European*, pages 1031–1034, Oct 2011.

upna
Universidad Pública de Navarra
Nafarroako Unibertsitate Publikoa

List of publications

Journal Papers

1. **A. Tellechea**, F. Caminita, E. Martini, I. Ederra, J.C. Iriarte, R. Gonzalo, and S. Maci, "Dual Circularly Polarized Broadside Beam Metasurface Antenna", *IEEE Transactions on Antennas and Propagation*, 64(7):2944-2953, 2016.

2. J.C. Iriarte, **A. Tellechea**, J.L. Martinez de Falcon, I. Ederra, R. Gonzalo, and P. de Maagt., "Broadband Radar Cross-Section Reduction Using AMC Technology", *IEEE Transactions on Antennas and Propagation*, 61(12):6136-6143, 2013.

3. **A. Tellechea**, J.C. Iriarte, I. Ederra, R. Gonzalo, F. Monjas, S. Arenas, R. Manrique, and A. Montesano, "Compact and Weighlight EBG Superstrate Antenna for C-band TTC Applications", *Microwave and Optical Technology Letters*, 55(7):1457-1461, 2013.

Invited International Conferences

1. J.C. Iriarte, **A. Tellechea**, I. Ederra, and R. Gonzalo, "Metamaterials for Antennas and RCS REduction Structures", *META15*, New York, EEUU, September, 2015.

2. J.C. Iriarte, **A. Tellechea**, I. Ederra, and R. Gonzalo, "EBG Antenna Technology for Different Applications", *ICEAA*, Turin, Italy, September, 2013.

3. J.C. Iriarte, **A. Tellechea**, I. Maestrojuan, I. Liberal, A. Rebollo, I. Ederra, and R. Gonzalo, "Planar EBG Technology Chessboard Configuration to Reduce RCS in W Band", *EuCAP*, Goteborg, Sweeden, April, 2013.

4. R. Gonzalo, I. Ederra, J. C. Iriarte and **A. Tellechea**, "EBG superstrate based Antennas for Space Applications", *International Congress on Advanced Electromagnetic Materials in Microwaves and Optics*, Burdeos, France, September, 2013.

upna
Universidad Pública de Navarra
Nafarroako Unibertsitate Publikoa

5. J.C. Iriarte, **A. Tellechea**, I. Maestrojuan, I. Liberal, A. Rebollo, I. Ederra and R. Gonzalo, "Chessboard structure evolution for RCS reduction". *META12*, Paris, France, April, 2012.

International Conferences

1. **A. Tellechea**, F. Caminita, E. Martini, I. Ederra, J.C. Iriarte, R. Gonzalo, and S. Maci, "Characterization of a Dual Band Metasurface Antenna with Broadside and Isoflux Circularly Polarized Radiation Patterns", *EuCAP*, Paris , France, March, 2017.

2. **A. Tellechea**, F. Caminita, E. Martini, I. Ederra, J.C. Iriarte, R. Gonzalo, and S. Maci, "Theoretical design considerations for dual circularly-polarized broadside beam metasurface antenna", *EuCAP*, Davos , Switzerland, April, 2016.

3. **A. Tellechea**, F. Caminita, E. Martini, I. Ederra, J.C. Iriarte, R. Gonzalo, and S. Maci, "Dual-pol metasurface antenna supporting transverse magnetic and electric surface waves", *International Symposium on Antennas and Propagation (APSURSI)*, Fajardo , Puerto Rico, July, 2016.

4. **A. Tellechea**, F. Caminita, E. Martini, I. Ederra, J.C. Iriarte, R. Gonzalo, and S. Maci, "Orthogonally polarised modes sharing a single metasurface for dual-pol antennas", *META*, Malaga, Spain, July, 2016.

5. **A. Tellechea**, E. Martini, D. Gonzalez-Ovejero, M. Faenzi, G. Minatti, and S. Maci, "Dual band isoflux ultraflat meta antennas", *EuCAP*, Lisboa, Portugal, April, 2015.

6. **A. Tellechea**, J. C. Iriarte, I. Ederra, R. Gonzalo, F. Monjas, S. Arenas, R. Manrique, and A. Montesano, "Dual Band Compact and Light EBG Superstrate Based Antenna", *EuCAP*, Goteborg, Sweeden, April, 2013.

7. **A. Tellechea**, J. C. Iriarte, I. Ederra, R. Gonzalo, F. Monjas, S. Arenas, R. Manrique, anad A. Montesano, "TTC Applications Dual Band EBG Superstrate Antenna", *IEEE AP-S/URSI-USNC Symposium*, Orlance, EEUU, July, 2013.

National Conferences

1. **A. Tellechea**, F. Caminita, E. Martini, I. Ederra, J.C. Iriarte, R. Gonzalo, and S. Maci, "Development of Metasurface Antennas for Space Applications". *ISC*, Pamplona, Spain, December, 2016.

upna
Universidad Pública de Navarra
Nafarroako Unibertsitate Publikoa

2. **A. Tellechea**, J.C. Iriarte, I. Ederra, R. Gonzalo, E. Martini, D. González-Ovejero, G. Minatti, and S. Maci, "Antena Isoflux Bibanda en Ku basada en MTS de una Capa". *URSI*, Pamplona, Spain, September, 2015.

3. **A. Tellechea**, J.C. Iriarte, I. Ederra, R. Gonzalo, F. Monjas, S. Arenas, R. Manrique, and A. Montesano, "Antena Metamaterial de doble frecuencia para Aplicaciones TTC en Banda C". *URSI*, Valencia, Spain, September, 2014.

4. **A. Tellechea**, J.C. Iriarte, I. Ederra, R. Gonzalo, and P. de Maagt, "Wideband Chessborad AMC Structure Evolution". *URSI*, Elche, Spain, September, 2012.

5. **A. Tellechea**, J.C. Iriarte, I. Ederra, R. Gonzalo, and P. de Maagt, "Dual Band Circularly Polarized Compact Low Mass Antenna in EBG Technology". *URSI*, Elche, Spain, September, 2012.

upna
Universidad Pública de Navarra
Nafarroako Unibertsitate Publikoa